Eduard Gilli

Development of Analysis Methods for Fiber Bonds in Paper

DOCTORAL THESIS

For obtaining the academic degree of
Doktor der technischen Wissenschaften

Doctoral Programme of Technical Sciences
Technical Physics

Graz University of Technology

Supervisor:
Ao.Univ.-Prof. Mag. Dr.rer.nat. Robert Schennach
Institute of Solid State Physics

Graz, August 2011

typeset in LaTeX

Deutsche Fassung:
Beschluss der Curricula-Kommission für Bachelor-, Master- und Diplomstudien vom 10.11.2008
Genehmigung des Senates am 1.12.2008

EIDESSTATTLICHE ERKLÄRUNG

Ich erkläre an Eides statt, dass ich die vorliegende Arbeit selbstständig verfasst, andere als die angegebenen Quellen/Hilfsmittel nicht benutzt, und die den benutzten Quellen wörtlich und inhaltlich entnommene Stellen als solche kenntlich gemacht habe.

Graz, am …… ……..
(Unterschrift)

Englische Fassung:

STATUTORY DECLARATION

I declare that I have authored this thesis independently, that I have not used other than the declared sources / resources, and that I have explicitly marked all material which has been quoted either literally or by content from the used sources.

…… ……..
date (signature)

Abstract

The scope of this thesis is the development of new optical methods and the establishment of methods from other fields of science for the analysis of paper fibers and paper networks. Polarization modulated infrared reflection absorption spectroscopy (pm-IRRAS) has been applied for measurement on paper surfaces, on cellulose thin film systems, and on pure materials. On paper sheets pm-IRRAS has shown a very high sensitivity to chemical fiber treatment that can also be used for quantitative chemical measurement, despite the complex surface structure of paper. This leads to very high correlations between the size of spectral features and chemical treatment of the fibers by different substances, and allows following the chemical process in the fibers. Often a linear correlation is observed, which can be exploited for rapid reliable sensor systems. As a model system the fiber-fiber bond is mimicked by cellulose model films on silicon wafers. This method shall lead to more insight into the surface chemical processes in a fiber bond by chemical modifications and tensile testing of bonded model films. The films are characterized by IRRAS and their thickness can be determined by optical best match simulations. The dielectric functions, necessary for such quantitative analysis of spectra are measured by Kramers-Kronig transformation from pm-IRRAS spectra. Furthermore the optics of a pulp fiber bond in the visible range are modeled and simulated. This leads first to a deeper understanding of polarization microscopy on cellulosic fibers and second to an imaging ellipsometry based method for the optical measurement of bonded area inside a fiber-fiber bond.

Kurzzusammenfassung

Diese Arbeit beschäftigt sich mit der Entwicklung von optischen Messmethoden für Papierfasern und Papier, sowie mit der Etablierung von aus anderen Forschungsbereichen bekannten, aber am Papier noch nicht eingesetzten Methoden. Polarisationsmodulierte Infrarot-Reflektions-Absorptionsspektroskopie (pm-IRRAS) wurde für Messungen an Papieroberflächen, an Zellulose-Dünnschichtsystemen und an Reinmaterialproben angewandt. Auf Papierblatt-Oberflächen zeigt pm-IRRAS, trotz der extrem hohen Komplexität dieser Oberflächen, eine sehr hohe Empfindlichkeit auf chemische Faserbehandlungen die auch für quantitative chemische Messungen eingesetzt werden kann. Die dabei beobachteten Banden weisen sehr hohe, oftmals sogar lineare Korrelationen zu chemischen Faserbehandlungen mit verschiedenen Substanzen auf. Daher lassen sich solche chemischen Prozesse an den Fasern hervorragend mittels pm-IRRAS am Papierblatt nachvollziehen. Die Methode ließe sich auch als schneller, berührungsloser und zuverlässiger Sensor einsetzen. Um genauere Einblicke in die molekularen Eigenschaften einer Faser-Faser Bindung zu bekommen kommen überdies Zellulose-Modellfilme zum Einsatz, mit welchen sich auch Bindungen herstellen lassen. Durch gezielte chemische Modifikationen dieser Oberflächen in Verbindung mit Zerreißversuchen soll ein Zugang zu einzelnen Bindungsmechanismen auf der molekularen Ebene erreicht werden. Diese Dünnschichten werden ebenfalls mittels IRRAS charakterisiert, wobei die Schichtdicke

aus optischen Simulationen ermittelt werden kann. Die dafür nötigen dielektrischen Funktionen der beteiligten Materialien werden mittels Kramers-Kronig-Transformation aus pm-IRRAS Spektren von Reinmaterialproben ermittelt. Des Weiteren wird das optische Verhalten von Zellstofffasern im sichtbaren Bereich modelliert und simuliert. Erstens lässt sich dadurch das optische Verhalten von Zellstofffasern in einem Polarisationsmikroskop detaillierter verstehen, und zweitens wird aus diesem Modell eine auf abbildender Ellipsometrie basierende Methode zur optischen Messung von Faser-Faser-Bindungsfläche abgeleitet.

Contents

Publications this dissertation is based on

Djak, M., Gilli, E., Kontturi, E., and Schennach, R. (2011). *Thickness dependence of reflection absorption infrared spectra of supported thin Polymer films*. Macromolecules, **44**.(7), pp. 1775–1778.

Gilli, E., Horvath, A. E., Horvath, A. T., Hirn, U., and Schennach, R. (2009a). *Analysis of CMC attatchment onto cellulosic fibers by infrared spectroscopy*. Cellulose, **16**.(5), pp. 825–832.

Gilli, E. and Schennach, R. (2010). *Determination of Noise-Free Optical Constants in the Infrared by Kramers-Kronig Troansformation of the Reflectance Ratio in s- and p-Polatization*. Applied Spectroscopy, **64**.(6), pp. 669–681.

Gilli, E. and Schennach, R. (2011). *Imaging ellipsometry based method and algorithm for the analysis of fiber-fiber bonds in a paper network*. Submitted to: Applied Optics,

Gilli, E., Kappel, L., Hirn, U., and Schennach, R. (2009c). *An optical model for polarization microscopy analysis of pulp fibre-to-fibre bonds*. Composite Interfaces, **16**.(5), pp. 901–922.

Gilli, E., Schmied, F., Diebald, S., Horvath, A. T., Teichert, C., and Schennach, R. (2011b). *Analysis of lignin precipitates on ozone treated kraft pulp by FTIR and AFM*. Submitted to: Cellulose,

Gilli, E., Kornschober, M., and Schennach, R. (2011c). *Optical arrangement and proof of concept prototype for mid infrared variable angle spectroscopic ellipsometry*. Submitted to: Infrared Physics & Technology,

List of Publications

Djak, M., Gilli, E., Kontturi, E., and Schennach, R. (2011). *Thickness dependence of reflection absorption infrared spectra of supported thin Polymer films.* Macromolecules, **44**.(7), pp. 1775–1778.

Gilli, E., Horvath, A. E., Horvath, A. T., Hirn, U., and Schennach, R. (2009a). *Analysis of CMC attatchment onto cellulosic fibers by infrared spectroscopy.* Cellulose, **16**.(5), pp. 825–832.

Gilli, E. and Schennach, R. (2009). *Detection of coatings on paper usinf infra red spectroscopy.* Lenzinger Berichte, **87**, pp. 162–167.

Gilli, E. and Schennach, R. (2010). *Determination of Noise-Free Optical Constants in the Infrared by Kramers-Kronig Troansformation of the Reflectance Ratio in s- and p-Polatization.* Applied Spectroscopy, **64**.(6), pp. 669–681.

Gilli, E. and Schennach, R. (2011). *Imaging ellipsometry based method and algorithm for the analysis of fiber-fiber bonds in a paper network.* Submitted to: Applied Optics,

Gilli, E., Kappel, L., Hirn, U., and Schennach, R. (2009c). *An optical model for polarization microscopy analysis of pulp fibre-to-fibre bonds.* Composite Interfaces, **16**.(5), pp. 901–922.

Gilli, E., Schmied, F., Diebald, S., Horvath, A. T., Teichert, C., and Schennach, R. (2011b). *Analysis of lignin precipitates on ozone treated kraft pulp by FTIR and AFM.* Submitted to: Cellulose,

Gilli, E., Kornschober, M., and Schennach, R. (2011c). *Optical arrangement and proof of concept prototype for mid infrared variable angle spectroscopic ellipsometry.* Submitted to: Infrared Physics & Technology,

Gilli, E., Schennach, R., and Kornschober, M. (2011d). *Optical arrangement for ellipsometry.* PCT Patent Application. WO 2011/022745 A1.

Gilli, E., Schennach, R., and Kornschober, M. (2011e). *Optische Anordnung für Ellipsometrie.* AT Patent Application. AT 508 690 A1.

Kappel, L., Hirn, U., Gilli, E., Bauer, W., and Schennach, R. (2010a). *Revisiting Polarized Light microscopy for fiber-fiber bond area measurement - Part I: Theoretical fundamentals.* Nordic Pulp & Paper Research Journal, **25**, pp. 65–70.

Kappel, L., Hirn, U., Gilli, E., Bauer, W., and Schennach, R. (2010b). *Revisiting polarized Light microscopy for fiber-fiber bond area measurement - Part II: Poroving the applicability.* Nordic Pulp & Paper Research Journal, **25**, pp. 71–75.

Schennach, R., Hirschmugl, C., Gilli, E., and Tysoe, W. T. (2009). *A New Method for Performing Polarization-Modulation Infrared Reflection-Absorption Spectroscopy of Surfaces.* Applied Spectroscopy, **63**.(3), pp. 369–372.

Stettner, J., Frank, P., Griesser, T., Trimmel, G., Schennach, R., Gilli, E., and Winkler, A. (2008). *A study on the formation and thermal stability of 11-MUA SAMs on Au(111)/mica and on polycrystalline gold foils.* Langmuir, **25**.(3), pp. 1427–1433.

1. Introduction

1.1. Motivation

Paper is a very important part of everyday life and has been known for more than 2000 years. Over all, the methods of paper production have been improved and upscaled to mass production, but the fundamental process of papermaking has always been the same: An aqueous suspension of fibers is equally distributed on a sieve, and subsequently the water is removed. After drying, the fibers have formed a network, that is held together by fiber-fiber bonds. No kind of glue has to be added for this procedure.

Paper, therefore, is composed of a network of more or less randomly oriented celulosic pulp fibers, which themselves are chemically dissolved cells of wood and consist of a multi-layered anisotropic partially crystalline structure of cellulose, hemicelluloses and lignin.

The strength of a paper network is one of the most important properties when it comes to optimization of the industrial processes, because most of the cost of kraft paper production is caused by the cost of the raw material. This is to a great extend due to the fact that the paper production over the last decades has become an energy neutral and chemically closed process.

At least for european papermakers further reduction of production cost can only be reached by a higher material efficiency, which means a need for stronger paper, or paper of the same strength, employing less fiber material.

Generally speaking, the strength of paper is determined by the geometric properties of the fiber network, the relative bonded area, being the portion of the network made up by bonds, and the specific bond strength being the force per bond unit area necessary to break a bond. There exist means to improve the former two properties, like e.g. the optimization of the machine properties, the swelling time of the fibers, the speed of the dewetting, the pressure applied at sheet forming or the temperature applied at drying. However, the specific bond strength can only be improved further, if the microscopical surface physical mechanisms of the bonding of two fiber walls can be deciphered, and further optimization of paper network properties seems improbable, as long as the micromechanics of paper networks cannot be fully understood in terms of e.g. finite element simulations.

Both approaches, as well the deeper understanding of bonding mechanisms, as the deeper understanding of the interplay between macroscopic tensile strength of paper and the microscopic fiber network characteristics suffer a very general shortcoming: The lack of reliable, accessible, and non-destructive measurement methods.

It is, therefore, the main purpose of the dissertation at hand, to contribute to this

measurement problem. Several methods have been used, and develloped in the course of the work, which can give substantial new input to paper science, in the field of fiber-fiber bonds, as well as in the field of fiber network analysis.

1.2. Background

The morphology of fibers very much depends on their growth parameters, especially the season in which the fiber was grown. Fig. 1.1 depicts an transverse cross section of a timber (Gullichsen and Paulapuro 1999). The annual rings of the wood are clearly

Figure 1.1.: Transverse cross section of a timber with clearly visible annual rings, adopted from (Gullichsen and Paulapuro 1999)

visible. They consist of wood tracheids (wood cells) of different diameters (early wood and late wood fibers) and, therefore, have different colors in the microscopic image. The different tracheid dameters can be seen in Fig. 1.2.

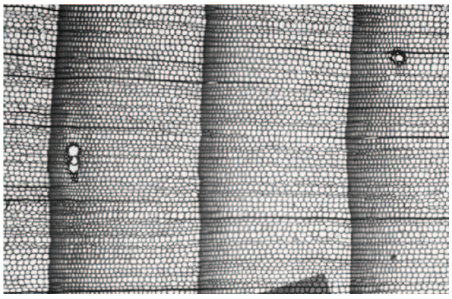

Figure 1.2.: Close up of the annual rings, and the tracheid diameters, adopted from (Gullichsen and Paulapuro 1999)

An image of the layered structure of a wood tracheid is given in Fig. 1.3.

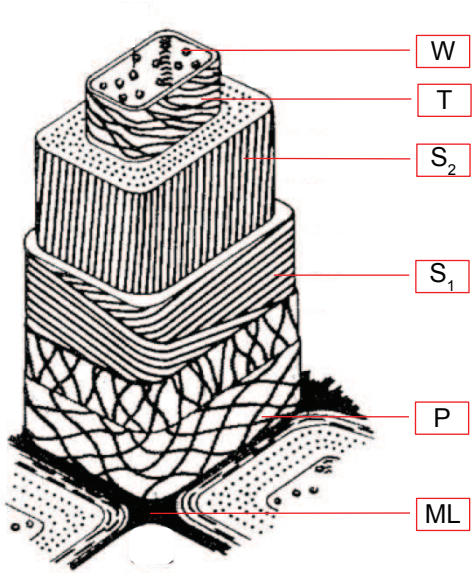

Figure 1.3.: Schematic image of the structure of a Wood tracheid, adopted from (Gullichsen and Paulapuro 2000)

In the raw material wood, the fibers are held together by a middle lamella (ML in Fig. 1.3) which consists of lignin. This lignin has to be dissolved in the pulping process in order to get the pulp fibers for papermaking. The resulting pulp fiber consists of 5 layers of different crystallinity and order, all of them being composed from microfibrils, which themselves are composed of crystalline cellulose. The microfibrils are embedded in a matrix of hemicelluloses and lignin (Sixta 2006a).

The primary wall of the cellulose fiber (P in Fig. 1.3) is the thinnest of all the cell walls and has an unordered structure. The two secondary fiber walls (S1 and S2) show an ordered helical structure of aligned microfibrils, the first of them (S1) being much thinner than the second secondary wall (S2), which makes up the major part of the fiber material (55%-70% of the wall thickness (Sixta 2006a)).

The tertiary wall (T in Fig. 1.3) again is quite thin and unordered. The center of the fiber carries the fiber lumen (W), which has the function of water transport in a living wood cell. It is collapsed at most refined pulp fibers, thus, the fibers in a paper network have a belt-like shape.

Paper is a network material, made from such pulp fibers. The individual fibers in the network are bonded onto each other by processes not fully understood today. An image of two bonded late wood spruce kraft fibers in a polarization microscope is given in Fig. 1.4. The network of a paper sheet now consists of many fibers, which are more or less oriented in the network, and more or less bonded onto each other. These parameters are to a great extend determined by the paper making process. Therefore, it is not exaggerated to say that paper is an extremely complex system, optically as well as mechanically and chemically. An impression of a fiber network is given by Fig. 1.5.

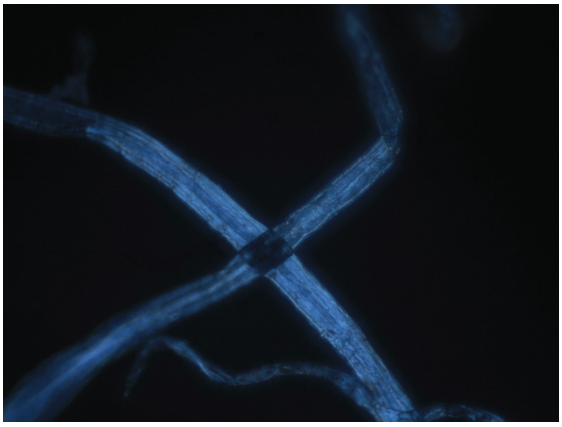

Figure 1.4.: Two bonded pulp fibers in a polarization microscope

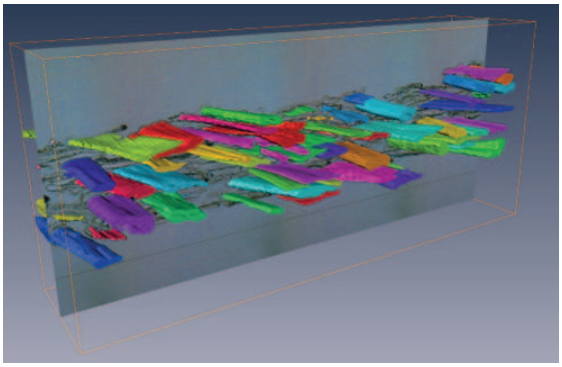

Figure 1.5.: 3D model of a paper network, produced by serial microtome cross sectioning (Wiltsche 2006; Wiltsche et al. 2011)

The image is a 3d model of a kraft paper network and was produced by microtome cross sectioning (Wiltsche 2006; Wiltsche et al. 2011).

A lot of research on mechanical paper properties has been done in the last century, to optimize the papermaking process. This research mostly concentrated on physical and chemical modifications of the process itself and on different forms of fiber treatment, in order to improve parameters like e.g. the fiber flexibility, fiber swelling, and fiber conformability, which all have a major influence on the resulting bonded area. Another widely used strategy of improving paper strength is given by chemical fiber treatment, such as coating the fibers with charged cellulose derivates or polymers in order to increase surface charge, and thus swelling and specific bonding strength (Lindström et al. 2005).

The focus of paper research purely towards application has been due to different reasons, one of them being the lack of reliable microscopic measurement methods, another being the lack on interdisciplinarity.

Only quite recently a tendecy towards interdisciplinary research has come up, because a further optimization of paper properties without a deeper understanding of the microscopic fundamentals of fiber-fiber bonding seems improbable.

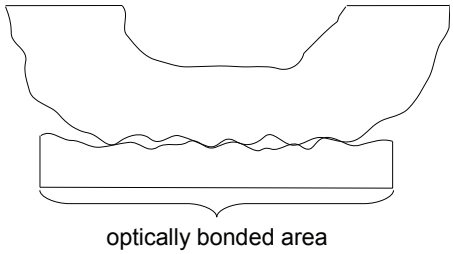

Figure 1.6.: Area in molecular contact vs. optically bonded area of a fiber fiber bond. Adopted from (Lindström et al. 2005)

The actual bonding on the molecular level can only occur at areas which are in molecular contact. From tribology it is known (Persson 1998) that this area mainly depends on the externally applied pressure, the roughness of the surfaces and the indentation hardness. The area in actual molecular contact is much smaller than optically detected area of contact between two fibers, because the optical measurement is limited by the diffraction limit ($\lambda/2$), which is, at least in the visible range much bigger than the range of the molecular bonding mechanisms (see Fig. 1.6). Consequently specific bonding strength can be improved by increasing the area in actual molecular contact, either by applying more pressure (the limits of technical feasability have been reached here), or by increasing fiber conformability, because specific bond strength is defined by the area of optical contact.

If the bond strength per area in molecular contact shall be increased, the fundamental bonding mechanisms have to be taken into account. A set of bonding mechanisms on the molecular level has been proposed by Lindström, Waagberg and Larsson (Lindström et al. 2005). These mechanisms are

- Mechanical interlocking of the two surfaces. This can happen due to wrinkling of the surfaces in the drying process. Additionally to the interlocking effects, the area in molecular contact is increased.
- Hydrogen bonding between the $-OH$-endgroups of the cellulose molecules. This also occurs within the fibers.
- Interdiffusion of individual cellulose molecules from one fibersurface into the other.
- Coulomb bonding (electrostatic forces) due to charged species on the surfaces.
- Van der Waals bonding between the surfaces.

The mechanisms have different ranges and different contributions to the bonding of fibers, however, the contribution of the different bonding mechanisms remains unknown.

On this background, the Christian Doppler Laboratory for Surface Chemical and Physical Fundamentals of Paper Strength (CD-Lab) was founded, initiated by the kraft paper maker Mondi Frantschach, where an interdisciplinary group of researchers approaches this problem from different points of view. Three institutes work together in this research project. The group at the Institute for Paper-, Pulp-, and Fiber Technology at the Graz University of Technology is investigating the morphology of the fiber-fiber bond and the bonded area, develloping a micro tensile testing system for single fiber bond testing, and investigating the interaction between pulp and viscose fibers. The Scanning Probe Microscopy Group at the Institute of Physics at the University of Leoben is investigating the fibers and fiber-fiber bonds by atomic force microscopy, and the Institute of Solid State Physics at the Graz University of Technology investigates the surface chemistry of the fibers by infrared spectroscopy.

After a year of research, the worlds biggest viscose producer, Lenzing AG joined the CD-Lab as a second industrial partner. In the viscose process hemicelluloses are isolated as a byproduct. The interaction between cellulose and hemicelluloses does play a prominent role in fiber-fiber bonding(Sixta 2006b). Therefore, the Lenzing AG has a great interest in the outcome of the CD-Lab. The dissertation at hand was carried out within the Lenzing module of the CD Laboratory for Surface Chemical and Physical Fundamentals of Paper Strength.

It is one of the main objectives of this interdisciplinary research project to employ the findings of the different analysis methods used into a fiber-bonding model on the molecular level. Such a model, should be able to give a clearer answer to the contributions of the different proposed bonding mechanisms.

1.3. Methods

Infrared spectroscopy (especially Fourier Transform infrared spectroscopy) is a tool frequently used in any field of chemistry, due to its selectivity to molecular functional groups and, therefore, its unmatched chemical contrast.

In paper science Fourier Transform infrared spectroscopy (FTIR) is also a very common tool, mainly in its standard form of transmission spectroscopy. Transmission spectroscopy has the dissadvantage of complicated sample preparation, and usually the spectra are not used for quantification. The optical implications of measuring systems with multiple interfaces and the related errors do not seem to be a topic neither in the paper science community nor in the chemistry community.

Other techniques that are commonly used in paper science are diffuse reflectance infrared Fourier Transform spectroscopy (DRIFTS), and attenuated total reflection spectroscopy (ATR). At DRIFTS the diffusely reflected radiation from vertically incident infrared light is collected by a parabolar mirror and integrally measured. This technique has the apparent advantage of high measured intensity, but for the cost of measuring all reflection angles at the same time. Therefore, the possibilities of a geometric interpretation of the data are poor. The method is rather suited for a purely chemical analysis. ATR has the main advantage of no sample preparation and a well defined penetration depth of the radiation into the sample. This can be especially useful for powders or highly absorbing substances.

In the work at hand infra red reflection absorption spectroscopy (IRRAS) was chosen as an approach to measure the chemistry in paper fibers from spectra of paper sheets. At a first glance this seems unusual, because of the rough and irregular surface of a paper sheet. Carried out in the correct way, the obious advantage of IRRAS over DRIFTS is the better defined incidence angle, which allows to find optimal parameters of high chemical sensitivity. The structural sizes of the fibers are in the order of magnitude of the employed wavelengths, which renders a complete understanding of the scattering behaviour of the used surfaces very complicated, if not impossible, due to the very irregular fiber geometry, the multilayered fiber structure, and the irregular distribution and ordering of the fibers in the paper network.

All these influences introduce base-line shifts into the infrared reflection spectra, that have to be dealt with. It turned out, that a very simple method to get rid of this problem is given with polarization modulated IRRAS (pm-IRRAS). Employing a new, and very simple polarization modulation technique(Schennach et al. 2009), it was found that a semiquantitative surface chemical analysis of fibers in paper sheets is possible, with a very high sensitivity.

With this method is is e.g. possible to watch the build up of different charged species, such as carboxylate on the fiber surface (Sec. 3, Ref. (Gilli et al. 2009a)), and thus have an indirect measure of surface charge of the fibers in a paper network by a contact-free spectroscopic measurement. Such methods would be nicely suited to measure different fiber parameters on-line in the paper mill on the running paper. Also the lignin content of a paper can be measured in this way, and the data can be linked to atomic force microscopy (AFM) measurements of the fiber surfaces. The link of pm-IRRAS and AFM yields valuable new information of the reaction kinetics at the fiber surface. This is shown in Sec. 4 (Ref. (Gilli et al. 2011b)).

In order to get a hold on the fundamental processes of fiber-fiber bonding, model systems were employed. This is an approach, very common to surface science. These

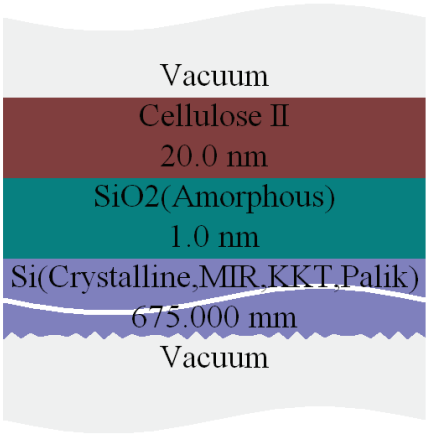

Figure 1.7.: Schematic illustration of the layer system of the employed model films

model systems are amorphos cellulose films on silicon wafer substrates, that can be modified chemically as needed, and employ a simple geometry that can be simulated rather easily. An illustration of the standard setup of these model systems is given in Fig. 1.7. This figure depicts a layer stack for optical simulation of the model system, thus the two vacuum halfspaces above and below the sample. The chioce of silicon as a substrate material is due to two reasons. Firstly, silicon is transparent in the mid infrared region, and therefore, the samples can be measured as well in reflection as in transmission, and secondly, silicon wafers are extremely flat and smooth, and obtainable at low cost.

The cellulose model films on the silicon substrates are prepared by spin coating from trimethylsilyl cellulose (TMSC). The TMSC is subsequently hydrolyzed by hydrocloric acid vapour, to build regenerated cellulose. For thick layers a series of spin coating and subsequent hydrolysis steps is carried out. A detailed description of the process can be obtained from Refs. (Kontturi et al. 2003a; Kontturi et al. 2003b) and a more detailed description of the films and film systems is given by Ref. (Kontturi et al. 2006).

The model systems enable a view on the surface chemical processes, especially the interaction between cellulose and hemicelluloses, that cannot be reached within the network, because there are too many uncontrollable parameters.

Additionally, by introducing different additives, the different bonding mechanisms, as discussed above can be directly influenced, e.g. electrostatic forces can be intoduced by introducing charged species to the cellulose film surface. By mimicing the sheet forming process bonding as between two pulp fibers can be established between two model films. This enables mechanical testing of the bonding strength, and transmission spectroscopy through such a bond between cellulose or hemicellulose surfaces. Mechanical bonding of the films can be carried out as described in the diploma thesis of M. Djak (Djak 2011). The resulting specific bonding strength in this case is much smaller than in real fibers. This can be attributed to the absence of mechanical interlocking, which cannot occur due to the flat surfaces, the reduced conformability, and the absence of charged species

at a pure cellulose surface. Additionally, the higher hardness of the silicon substrates, reduces area of molecular contact.

Systematic studies on the influence of different treatments of the model films have not been conducted yet. A lot of work had to be done in order to get usable experimental methods to characterize the model films with infrared spectroscopy, and to simulate the infrared spectra, in order to get a closer insight on the physical details.

There are no existing literature data, of infrared optical constants of cellulosec substances availabe. Therefore, a great deal of work as been invested into the development of an algorithm for the determination of optical constants from pm-IRRAS spectra (Sec. 7, Ref. (Gilli and Schennach 2010)). The method is based on a Kramers-Kronig method (Yamamoto 1994) and produces noise free data, by automated non-linear fitting, based on Lorentz-oszillators.

The optical constants obtained with this method could subsequently be used to measure the film thickness of cellulose model films by IRRAS and best match calculations (Sec. 8, (Djak et al. 2011)). With this work now the fundamentals are given to tackle the problem of fiber fiber bonding by the cellulose model films.

Another method that inevitably comes to mind when analyzing thin film systems is ellipsometry, because it is the only method to measure the real and imaginary part of a samples response to a light stimulus in the same measurement. Spectroscopic infrared ellipsometry, therefore, can fundamentally measure the optical constants of materials, without the need of Kramers-Kronig transformation and all the problems associated with it.

Due to monetary restrictions a commercial infrared spectroscopic ellipsometer was not available in the CD-Lab. Triggered by this situation, a new optical arrangement was invented, patented, and built in the course of the work. The system is an accessory unit to be placed into the sample compartment of a FTIR, in order to measure variable angle spectroscopic infrared ellipsometry (see Sec. 9, Ref. (Gilli et al. 2011c)). The system is still in a prototype stage, and therefore, could not be used for the CD-Lab yet.

All the above mentioned methods can be employed to tackle the problem of fiber-fiber bonding. As already mentioned above, the specific bond strength is only part of the picture, because paper strength is also dependent on the network parameters.

Here the situation becomes especially complicated, because of the high comlpexity of the system at multiple size scales. The fibers composing the network are by themselves a quite complex system of different sizes and shapes, on the larger scale, the network again is a complex statistical system. It is, therefore, not possible to define a standard network that could be implementet into a simulation, and verified by mechanical testing. To tackle the properties of the fiber network from the experimental and the theoretical point of view simultaniously a method is needed to measure the network properties and the network topology non-destructively. With this data finite element simulations of the micromechanics of the network could be carried out, and compared to macroscopic tensile tests on the same sheet of paper.

At the beginning of the research work within the CD-Lab, no such technique was available. With optical microscopy, the areas of unbonded, crossed fibers cannot be dis-

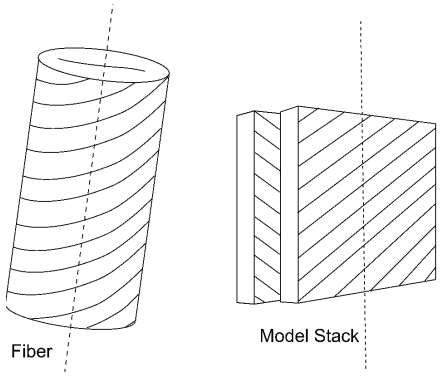

Figure 1.8.: Schematic drawing of the model approximation for simulating the optical behavior of pulp fibers.

tinguished from fiber-fiber bonds. The only other available technique to investigate the morphology of such a network is given by serial microtome sectioning in combination with optical microscopy and digital image analysis. This method is even capable of deciphering the tree-dimensional structure of the paper network, but is evidently destructive, and very time consuming.

As a first step to tackle this problem, the method of polarization microscopy of fiber networks was investigated. This method was published in 1960 (Page 1960), where it was claimed to be able to measure fiber-fiber bonds in a paper network. Unfortunately the contrast achieved with this method depends on the sample rotation in the microscope, and a distinction of fibe-fiber bonds from unbonded crossings is impossible. This was shown and proven by an optical model of the paper fibers and experiments (see Sec. 12, Ref. (Gilli et al. 2009c)), and was the first contribution of this dissertation to the problem of measuring fiber-fiber bonds by imaging optical methods.

The optical fiber model used, is built on the assumption, that the optical behaviour of fully collapsed pulp fibers can be well approximated by plan-parallel layer systems. This is shown in Fig. 1.8. Here, the fiber is not only approximated as a plan-parallel layered system, but also the cell wall is reduced to one layer. The optical behaviour of this layer is assumed to be determined by the s_2-layer of the cell wall, because this layer is the thickest, and has the highest degree of ordering of all the cell wall layers.

The model has shown to describe the behaviour of pulp fibers well. The indistinguishability of fiber bonds and unbonded crossings was first prognosed by the model and later found in the experiment. The model is not only able to reproduce the reflected intensity from the fiber systems, but also the color. It has brought deeper insigth into the optical proberties of pulp fibers and was used in further publications of the CD-Lab, that are not part of this dissertation (see Sec. A, Refs. (Kappel et al. 2010a; Kappel et al. 2010b)).

With the experience from ellipsometry (Sec. 9), and the simulation capabilities gained from the work with infrared spectra (Secs. 7,8), this measurement problem was revisited (see Sec. 13, Ref. (Gilli and Schennach 2011)). The basic idea was, to find a possibility to

distinguish crossed fibers from fiber bonds by the use of imaging ellipsometry. Therefore, the fiber model was employed with a much more powerful calculation method (Schubert 1996), and all the fibers' degrees of freedom were systematically searched for symmetries. By introducing changes to the beam path (an additional compensator after the samples position), finally a configuration could be found, where bonds and crossings indeed can be distinguished. It has to be emphasized that this discrimination works independent of geometric fiber properties and orientation.

Therefore, this method is capable of decrypting a fiber network, by means of a contact free optical measurement. It has to be stated, that the findings so far are only based on simulation. The concept would at first have to be proven with a prototype, before more distinct statements can be made. However, in combination with other already available microscopic techniques, such as infinite focus microscopy, this method has the potential to revolutionize the insight into the mechanical details of fiber networks.

1.4. Synopsis

The thesis at hand is divided into tree parts.

1. **Surface chemistry:** This part mainly deals with the problem of quantification of spectral features, measured by reflection spectroscopy (pm-IRRAS) of paper sheets. It could be shown in the two publications (Gilli et al. 2009a; Gilli et al. 2011b) constituting this part of the work, that chemical processes in the fibers and on the fiber surfaces can be measured by spectra from paper surfaces. This is at least not a straight forward statement, because there are many complex influences like e.g. scattering, that are neglected with this approach.

   The great advantage of this approach is the very much simplified sample preparation, the high reproducability and the high chemical sensitivity. Due to the size of the measurement spot, each spectrum is an average of a great number of single fibers. Therefore, the method is very tolerant against outliers. This is a very important feature, when dealing with biological systems.

   In both sections of this part an otherwise wet chemically measured parameter could be linearly corellated to spectral features, thus giving a possibility of contact-free measurement on the running paper machine.

Paper 1: E. Gilli et al. (2009a). *Analysis of CMC attatchment onto cellulosic fibers by infrared spectroscopy.* Cellulose, **16.**(5), pp. 825–832

This paper was in its main part written by myself. The experimental work and data analysis was carried out by me. The preparation of CMC coated pulp, and the forming of handsheets for spectroscopic analysis, as well as the writing of the corresponding experimental parts of the paper was carried out by A.T. and A.E. Horvath. The work was supervised by R. Schennach and U. Hirn.

Paper 2: E. Gilli et al. (2011b). *Analysis of lignin precipitates on ozone treated kraft pulp by FTIR and AFM.* Submitted to: Cellulose,

This paper is also written by myself in its majority. The spectroscopic measurement and data analysis, the discussion and interpretation have been done by me. The AFM measurements and corresponding data analysis was done by F. Schmied and C. Teichert, sample preparation was done by A.T. Horvath and S. Diebald. The literature review on ozonation in pulping in the introduction was written by S. Diebald. The work was supervised by R. Schennach.

2. **Spectroscopic methods:** This part is constituted by 3 publications, that are loosely related to each other by their motivation: The deeper understanding of the spectral features of cellulose model films, by measurement and simulation. The first paper describes a Kramers-Kronig based method to retrieve noise-free optical constants from pm-IRRAS measurements of materials, including an automated fitting procedure (Gilli and Schennach 2010). Data obtained with this method have been used in the second part to characterize cellulose model film systems by simulation of IRRAS measruements (Djak et al. 2011).

   The third publication of this part was also motivated by the cellulose model film systems. Here a setup for a variable angle spectroscopic mid infrared ellipsometer is described, that was built as a prototype (Gilli et al. 2011c). The performance of the prototype at its current stage did not allow to use it for the characterization of cellulose model films yet.

Paper 3: E. Gilli and R. Schennach (2010). *Determination of Noise-Free Optical Constants in the Infrared by Kramers-Kronig Troansformation of the Reflectance Ratio in s- and p-Polatization.* Applied Spectroscopy, **64**.(6), pp. 669–681

This paper has been completely written by myself. The theoretical work, simulations, sample preparations, and measuremetns have been carried out by myself. The work was supervisedd by R. Schennach.

Paper 4: M. Djak et al. (2011). *Thickness dependence of reflection absorption infrared spectra of supported thin Polymer films.* Macromolecules, **44**.(7), pp. 1775–1778

My part at this paper was the design of the experiment, data analysis, modeling of the optical system, and the writing of the infrared part, which makes the majority of the text. The infrared measurements were carried out by M. Djak under my supervision. The introduction and the experimental part concerning the preparation of the cellulose model films was written by E. Kontturi. The preparation of the cellulose model films was carried out by E. Kontturi.

Paper 5: E. Gilli et al. (2011c). *Optical arrangement and proof of concept prototype for mid infrared variable angle spectroscopic ellipsometry.* Submitted to: Infrared

Physics & Technology,

This paper is based on a joint patent (Gilli et al. 2011e) by the three authors. The paper was written by myself entirely, the corresponding prototype research project was fund raised and managed by myself under supervision of R. Schennach. The 3-D CAD modeling of the prototype and the mechanical construction was carried out by M. Kornschober in close collaboration with me. The experimental work, assembly, adjustment and optical layout of the system was done by myself.

3. **Optics of cellulosic fibers - Methods:** This last part deals with a completely different question. The measurement of bonded area between two fibers. This is needed to correlate measured bonding forces from tensile tests to specific bonding strength, which is the main target of the CD-Lab.

   The first paper of this part gives the theoretical background for an established, but inconclusive measurement technique (Gilli et al. 2009c), while the second publication introduces a new measurement technique, based on imaging ellipsometry, that is expected to yield conclusive results for bonded area in a paper network (Gilli and Schennach 2011).

Paper 6: E. Gilli et al. (2009c). *An optical model for polarization microscopy analysis of pulp fibre-to-fibre bonds*. Composite Interfaces, **16**.(5), pp. 901–922

This paper was fully written by myself with the exception of the introduction, which was written by U. Hirn, and the experimental part concerning microtome slicing, which was written by L. Kappel. The optical modeling, the simulation, and the microscope experiments were carried by me. Sample preparation was done by L. Kappel. The work was supervised by R. Schennach.

Paper 7: E. Gilli and R. Schennach (2011). *Imaging ellipsometry based method and algorithm for the analysis of fiber-fiber bonds in a paper network*. Submitted to: Applied Optics,

This paper has been completely written and carried out by myself. It is based on a patent application by the authors (see Sec. D of the Appendix) and was supervised by R. Schennach.

References

Djak, M. (2011). MA thesis. Graz University of Technology.

Djak, M., Gilli, E., Kontturi, E., and Schennach, R. (2011). *Thickness dependence of reflection absorption infrared spectra of supported thin Polymer films*. Macromolecules, **44**.(7), pp. 1775–1778.

Gilli, E., Horvath, A. E., Horvath, A. T., Hirn, U., and Schennach, R. (2009a). *Analysis of CMC attatchment onto cellulosic fibers by infrared spectroscopy.* Cellulose, **16**.(5), pp. 825–832.

Gilli, E. and Schennach, R. (2010). *Determination of Noise-Free Optical Constants in the Infrared by Kramers-Kronig Troansformation of the Reflectance Ratio in s- and p-Polatization.* Applied Spectroscopy, **64**.(6), pp. 669–681.

Gilli, E. and Schennach, R. (2011). *Imaging ellipsometry based method and algorithm for the analysis of fiber-fiber bonds in a paper network.* Submitted to: Applied Optics,

Gilli, E., Kappel, L., Hirn, U., and Schennach, R. (2009c). *An optical model for polarization microscopy analysis of pulp fibre-to-fibre bonds.* Composite Interfaces, **16**.(5), pp. 901–922.

Gilli, E., Schmied, F., Diebald, S., Horvath, A. T., Teichert, C., and Schennach, R. (2011b). *Analysis of lignin precipitates on ozone treated kraft pulp by FTIR and AFM.* Submitted to: Cellulose,

Gilli, E., Kornschober, M., and Schennach, R. (2011c). *Optical arrangement and proof of concept prototype for mid infrared variable angle spectroscopic ellipsometry.* Submitted to: Infrared Physics & Technology,

Gilli, E., Schennach, R., and Kornschober, M. (2011e). *Optische Anordnung für Ellipsometrie.* AT Patent Application. AT 508 690 A1.

Gullichsen, J. and Paulapuro, H. (1999). *Papermaking Science and Technology.* Helsinki: Fapet Oy.

Gullichsen, J. and Paulapuro, H. (2000). *Forest Products Chemistry.* Helsinki: Fapet Oy, pp. 24–26.

Kappel, L., Hirn, U., Gilli, E., Bauer, W., and Schennach, R. (2010a). *Revisiting Polarized Light microscopy for fiber-fiber bond area measurement - Part I: Theoretical fundamentals.* Nordic Pulp & Paper Research Journal, **25**, pp. 65–70.

Kappel, L., Hirn, U., Gilli, E., Bauer, W., and Schennach, R. (2010b). *Revisiting polarized Light microscopy for fiber-fiber bond area measurement - Part II: Poroving the applicability.* Nordic Pulp & Paper Research Journal, **25**, pp. 71–75.

Kontturi, E., Thüne, P. C., and Niemantsverdriet, J. W. (2003a). *Novel Method for preparing cellulose model surfaces by spin coating.* Polymer, **44**, pp. 3621–3625.

Kontturi, E., Thüne, P. C., and Niemantsverdriet, J. W. (2003b). *Cellulose Model Surfaces - Simplified Preparation by Spin Coating and Characterization by X-ray Photoelectron Spectroscopy, Infrared Spectroscopy, and Atomic Force Microscopy.* Langmuir, **19**, pp. 5735–5741.

Kontturi, E., Tammelin, T., and Österberg, M. (2006). *Cellulose-model flims and the fundamental approach.* Chemical Society Reviews, **35**, pp. 1287–1304.

Lindström, T., Wågberg, L., and Larsson, T. (2005). "On the Nature of Joint Strength in Paper- A Review of Dry and Wet Strength Resins used in Paper Manufacturing". In: *13th Fundamental Research Symposium.* Cambridge, pp. 457–562.

Page, D. H. (1960). *Fibre-to-fibre bonds, Part 1 - A method for their direct observation.* Paper technology, **1**.(4), pp. 407–411.

Persson, B. N. J. (1998). *Sliding Friction*. Nanoscience and technology. Berlin Heidelberg: Springer.

Schennach, R., Hirschmugl, C., Gilli, E., and Tysoe, W. T. (2009). *A New Method for Performing Polarization-Modulation Infrared Reflection-Absorption Spectroscopy of Surfaces.* Applied Spectroscopy, **63**.(3), pp. 369–372.

Schubert, M. (1996). *Polarization-dependent optical parameters of arbitrarily anisotropic homogeneous layered systems*. Physical Review B, **53**, pp. 4265–4274.

Sixta, H., ed. (2006a). *Handbook of Pulp*. Vol. 1. Wiley-VCH Weinheim.

Sixta, H., ed. (2006b). *Handbook of Pulp*. Vol. 2. Wiley-VCH Weinheim.

Wiltsche, M, Donoser, M, Kritzinger, J, and Bauer, W (2011). *Automated serial sectioning applied to 3D paper structure analysis*. Journal of Microscopy, **242**.(2), pp. 197–205.

Wiltsche, M. (2006). "Three Dimensional Analysis of Paper Structure Using Automated Microtomy". PhD thesis. Graz University of Technology.

Yamamoto, K. (1994). "Optical theory applied to thin films". PhD thesis. Case Western Reverse University.

Part I.

Surface Chemical Analysis of Paper Sheets by Infrared Reflection Spectroscopy

2. Introductory remarks

Infrared reflection spectroscopy, especially infrared reflection absorption (or sometimes adsorption) spectroscopy (IRRAS) is a spectroscopic method, normally used to perform measurements on thin layer systems, mostly on metallic substrates (Umemura 2002). Interpretation of such spectra is more or less straight forward, if the sample geometry is simple and the data does not have to be quantified.

Quantification of the spectral features of such systems is more complicated, because the light absorption of such thin layers does not simply follow the Beer Lambert law (Tolstoy et al. 2003). The effects of interfaces are often ignored (Yamamoto and Ishida 1994b), even though they do play a role even at liquid samples in transmission. The situation becomes more complicated if the substrates are nonmetallic. In this case the surface selection rules (Tolstoy et al. 2003), which state, that the absorption signal in the reflected light is only found in p-polarization, and therefore, the s-polarized reflectance can be used as a background, do not apply strictly anymore (Kattner and Hoffmann 2002).

If the layers under investigation have thicknesses which are not well below the wavelength of the light used, but rather in the same order of magnitude (which is often the case in infrared spectroscopy), another effect has to be taken into account, namely interference within the layer. Actually this has to be taken into account for every system employing more than one interface, which also applies for more or less every sample in transmission spectroscopy. Anyhow, in transmission the situation in most cases is treated as if the Lambert Beer law was sufficient to understand the phenomena, which is at least quantitatively incorrect.

In the case of paper sheets the situation is even more complex. The samples are elongated structures, which are statistically oriented, with diameters in the range of the wavelength, and consist of many layers. The scattering effects that also occur in this case, make it seem improbable, that a fundamental simulation of all the optical effects in such a sheet is possible today.

Therefore, usually other techniques than reflection spectroscopy are used at this kind of samples, e.g. Diffuse Reflectance Infrared Fourier Transform Spectroscopy (DRIFTS) (Tolstoy et al. 2003), or Atenuated Total Reflection FTIR (ATR) (Tolstoy et al. 2003). Both of these methods have apparent advantages over IRRAS, which at a first thought seems more suitable for thin films or adsorbates on metallic substrates.

DRIFTS was not used on paper sheets in the course of this work, simply because it was not available, and the quantitative interpretation is even more complicated due to a lot of reflection angles from the sample taken into account. ATR was done on paper sheets, and it also shows linear corellations to surface coatings. Here the great advantage of ATR is the independence from the sample form, and the well defined penetration depth

of the light into the sample surface. Interestingly though, ATR turned out to be inferior in surface sensitivity in comparison to the polarization modulated IRRAS, that was used in the following publications. Another problem of the ATR is, that the coatings are often destroyed in the course of the measurement, simply because they stick to the ATR crystal, and therefore, are removed from the surface of the measured pulp.

As it turned out in the course of the work, a semiquantitative analysis, with a high surface sensitivity is possible, with a second independent method available for calibration. The method that was used here is a rudimentary version of polarization modulation IRRAS (pm-IRRAS) as described in Ref. (Schennach et al. 2009) (see Sec. B). By chosing incidence angles slightly below the brewster angle, the polarization modulated signal,

$$S_{PM} = R_p/R_s = \tan^2 \Psi, \tag{2.1}$$

or

$$S_{PM} = \frac{R_p - R_s}{R_p + R_s} = \cos(2\Psi), \tag{2.2}$$

with R_p and R_s being the reflectance in $p-$ and in $s-$polarization, respectively, $S_{P/M}$, being two different but widely equivalent representations of the polarization modulated signal, and the ellipsometric angle Ψ, shows very surface sensitive features, that can be linked directly to different functional groups.

This part of the work on surface chemistry studies at paper sheets features two publications on this issue. The first of them deals with the semiquantitative detectability of carboxymethylcellulose (CMC) coatings on the fiber surfaces. CMC is attatched to te fibers in order to increase surface charges, and therefore, specific bond strength. On the one hand, the CMC on the surface can be measured by detecting the bands of the carboxylate ion, because native cellulose does not contain carboxylate. This approach yields a linear corellation of limited sensitivity as well in pm-IRRAS as in ATR. On the other hand a 3rd order corellation to the coating thickness could be found that possibly stems from a thin film phenomenon firstly described by D.W. Berreman (Berreman 1969) and therefore, known as the Berreman effect. The sensitivity of this band to difference in CMC attatchment is very high.

The second publication on pm-IRRAS at paper surfaces applies more straight forward surface chemistry. Here the same method was applied at paper sheets from ozone treated pulps. The ozon treatment is applied to the pulp in order to reduce the lignin content (delignification) and to produce carboxylate groups on the fiber surfaces (again to increase the surface charges). The lignin in the fiber can be detected rather easily and quite precise, because it is chemically not as similar to cellulose as the CMC.

The lignin is the only constituent of the fibers that has an aromatic structure, thus the araomatic bands can be linked directly to lignin-content.

In paper science the lignin content of pulps is measured by the Kappa number, a high Kappa corresponds to a high lignin content. This is a standardized wet chemical measurement method described by the ISO standard 302:2004. It is a measure of oxidizable structures in the pulp, and therefore, does not only measure lignin, but also other

structures. The Kappa number shows a proportionality to lignin content, that varies over different pulps (see (Sixta 2006a), pp.257).

Here it turned out, that not only the delignification can be observed in the IR, also the entire follow-up reactions could be observed and deciphered. Additionally the lignin on the fiber surface can be observed by atomic force microscopy (AFM) as hemisperical precipitates. Also with AFM, the amount and size of the precipitates could be linked to the lignin content.

As a conclusion from these results it may be said that - even though the very high geometric complexity of the fiber networks does not allow for fundamental interpretation of every given feature - very detailed surface chemical analysis is possible by applying pm-IRRAS to paper sheets, which at a first thought seems surprising, given the many different phenomena that determine the spectral behaviour.

The key to the surface chemical sensitivity seems to be, that scattering of the fiber networks is to a great extend isotropic in polarization for mid infrared light, and therefore, many of the disturbing effects are cancelled by polarization modulation.

References

Berreman, D. W. (1969). *Infrared Absorption at Longitudinal Optic Frequency in Cubic Crystal Films.* Physical Review, **130**, pp. 2193–2198.

Kattner, J. and Hoffmann, H. (2002). "External Reflection Spectroscopy of Thin Films on Dielectric Substrates". In: *Handbook of Vibrational Spectroscopy.* Ed. by J. M. Chalmers and P. R. Griffiths. Vol. 2. Chichester: John Wiley & Sons, pp. 1009–1027.

Schennach, R., Hirschmugl, C., Gilli, E., and Tysoe, W. T. (2009). *A New Method for Performing Polarization-Modulation Infrared Reflection-Absorption Spectroscopy of Surfaces.* Applied Spectroscopy, **63**.(3), pp. 369–372.

Sixta, H., ed. (2006a). *Handbook of Pulp.* Vol. 1. Wiley-VCH Weinheim.

Tolstoy, V. P., Chernyshova, I. V., and Skryshevsky, V. A. (2003). *Handbook of Infrared Spectroscopy of Ultrathin Films.* Hoboken, New Jersey: John Wiley and Sons, Inc.

Umemura, J. (2002). "Reflection-Absorption Spectroscopy of Thin Films on Metallic Substrates". In: *Handbook of Vibrational Spectroscopy.* Ed. by J. M. Chalmers and P. R. Griffiths. Vol. 2. Chichester: John Wiley & Sons, pp. 982–998.

Yamamoto, K. and Ishida, H. (1994b). *Optical theory applied to infrared spectroscopy.* Vibrational Spectroscopy, **8**, pp. 1–36.

3. Paper published in Cellulose 2009

The following publication (Gilli et al. 2009a) was written at an early stage of the work. The measurements with pm-IRRAS on the paper sheets had not been tried before, but showed very interesting results. The spectroscopic work was entirely carried out by myself, as well as most of the writing of the paper. The experimental details of sample preparation and CMC-attatchment onto the fiber surfaces was written by A. T. and A. E. Horvath. The interpretation and data analysis was done by myself.

The valuable and very fruitful discussuion about this paper with Prof. Peter Knoll from the University of Graz shall be acknowledged here.

References

Gilli, E., Horvath, A. E., Horvath, A. T., Hirn, U., and Schennach, R. (2009a). *Analysis of CMC attatchment onto cellulosic fibers by infrared spectroscopy.* Cellulose, **16**.(5), pp. 825–832.

Cellulose (2009) 16:825–832
DOI 10.1007/s10570-009-9289-x

Analysis of CMC attachment onto cellulosic fibers by infrared spectroscopy

E. Gilli · A. E. Horvath · A. T. Horvath · U. Hirn · R. Schennach

Received: 3 October 2008 / Accepted: 17 February 2009 / Published online: 3 March 2009

Abstract Infrared spectroscopy has been used to measure the amount of carboxymethyl cellulose (CMC) attached to cellulosic fibers. CMC was attached to an unbleached kraft pulp in aqueous conditions. Isotropic handsheets were then prepared and ATR spectroscopy was used to measure the intensity of the carboxyl vibration, which correlates to the amount of attached CMC that was determined using a wet chemical approach. The ATR method is rather time consuming as several measurement points on the sample have to be averaged, although it is still much faster than the wet chemical approach. Infrared reflection absorption spectroscopy (IRRAS) using polarized light was further used to measure the amount of attached CMC. In this method the intensity of an electromagnetic wave confined to the thin layer is used to correlate the spectroscopy to the amount of CMC on the fiber surface in the paper sample. The measurement time is shorter than with the ATR method. The proposed IRRAS method could be employed as a fast and reliable way to quantify adsorption of chemicals on pulp fibers.

Keywords FTIR · IRRAS · CMC · ATR · Paper fibers

E. Gilli · R. Schennach (✉)
Institute of Solid State Physics, Graz University of Technology, Petersgasse 16/2, 8010 Graz, Austria
e-mail: robert.schennach@tugraz.at
URL: http://www.staff.tugraz.at/robert.schennach/

E. Gilli · A. E. Horvath · U. Hirn · R. Schennach
CD-Laboratory for Surface Chemical and Physical Fundamentals of Paper Strength, Graz University of Technology, Graz, Austria

A. E. Horvath · A. T. Horvath
Mondi Frantschach GmbH, Frantschach, Sankt Gertraud, Austria

U. Hirn
Institute of Pulp and Paper Technology, Graz University of Technology, Graz, Austria

Introduction

Cellulosic fibers maintain an anionic charge under typical papermaking conditions due to the dissociation of weak acidic groups located in the fiber wall and on the fiber surface. These charged groups have been shown to be important for fiber swelling (Lindström 1980), the retention of cationic additives (Lindström 1989) and the final paper properties (Barzyk et al. 1997a, b; Laine et al. 2003). Recent research has focused on increasing the number of anionic charges on the fiber surface by attaching carboxymethyl cellulose (CMC) (Laine et al. 2000; Lindström et al. 2005; Duker and Lindström 2008).

The amount of CMC attached to the fiber surface can be related to the increase in the fiber surface charge (Horvath and Lindström 2007), which is most

commonly measured by indirect polyelectrolyte titration (Horvath et al. 2006; Wågberg et al. 1989; Winter et al. 1986). If the surface charge is measured before and after CMC attachment, the amount of CMC can be calculated from the difference in the surface charge if the charge density of the CMC is known. However, this is a time consuming method and can only be performed under laboratory conditions. Therefore, it is of interest to develop new methods for determining the amount of attached CMC.

This paper is aimed at presenting two methods using fourier transform infrared spectroscopy (FTIR), which can be used to measure the amount of CMC in a paper sample within minutes. As IR spectroscopy is very sensitive to different functional groups in molecules and polymers, it can be used to differentiate between cellulose and CMC.

The first method presented in this work is attenuated total reflection (ATR) FTIR, which is quite surface sensitive for this application. However, ATR cannot be automated as the samples need to be pressed against the ATR crystal. The second method highlighted here is infrared reflection absorption spectroscopy (IRRAS). When polarized light is used this method is also surface sensitive, and the reflection geometry could in principle be used in an online measuring device. Further development of these methods should lead to a fast and reliable routine method to control attachment of CMC or other chemical additives to improve paper strength in paper making.

Experimental

An unbleached softwood kraft pulp (Mondi Frantschach GmbH, Austria) was used in all experiments. The pulp had a κ number of 42 and was not refined. The total charge of the pulp was measured to be 87 μequiv/g by conductometric titration (Katz et al. 1984). The surface charge, measured by polyelectrolyte titration (Winter et al. 1986) using polydiallyldimethylammonium chloride (from Sigma–Aldrich, $Mw = 5.4 \times 10^5$ Da and $\varepsilon = 6.19$ mequiv/g), was measured to be 7.5 μequiv/g. The total and surface charges are generally attributed to dissociated carboxyl groups occurring in the fiber.

CMC was used to modify pulp suspensions through a method adapted from (Laine et al. 2000). The charge density of the CMC was measured to be 4.17 mequiv/g using polyelectrolyte titration (Terayama 1952). The amount of attached CMC to the fiber surface was determined from the surface charge of the treated pulp. As the charge density of the CMC is already known, the amount of CMC attached is calculated from the difference in the surface charge between the untreated and treated pulps. These values were used to calibrate the IR measurements. Isotropic handsheets having a basis weight of 80 g/m^2 were made using a Rapid-Köthen sheet former (PTI, Austria).

ATR measurements

IR measurements were made on 2 × 3 cm sections of the sheets using a Bruker ifs66/vS FTIR (Bruker Optics, Germany). Attenuated total reflection (ATR) measurements were made using a single reflection unit from Specac (MKII Golden Gate). The ATR crystal was a diamond and the incident angle was approximately 45°. A sampling rate of 100 kHz, and a recording time of 30 min was used unless otherwise stated.

IRRAS measurements

Infrared reflection absorption spectroscopy (IRRAS) measurements were performed using a reflection unit (specular reflection) with variable angle and a polarizer from Bruker Optics. The IRRAS spectra were measured with an incidence angle of $\Theta = 62°$. The Brewster angle of paper is approximately 60.5° and the Brewster angle of CMC is approximately 64.5° (Gilli 2008) and an angle between the two Brewster angles was therefore chosen for the incidence angle, Θ, as it is expected that the signal-to-noise ratio is best at angles close to the Brewster angle. The spectra were recorded for 5 min at a sampling rate of 100 kHz. The manipulation function for subtracting the background is given by

$$I = \left(I_s - I_p\right)/\left(I_s + I_p\right) \quad (1)$$

with I being the corrected signal, I_s, the intensity of the s-polarized spectrum and I_p, the intensity of the p-polarized spectrum. This correction function is commonly used for polarization modulation IRRAS and has the advantage of giving more significance to

differences between the polarization directions if the over all signal is small.

For the quantitative analysis of the CMC thin film peaks, the program package Quant1, which is part of the spectrometers software OPUS 4.2 from Bruker, was used. After the calculation of the difference in signal, the spectra were baseline corrected with the OPUS-software, using a polynomial method with two base points at 3,000 and at 1,820 cm^{-1}. The baseline corrected spectra were evaluated with integration within the interval of 1,144 and 1,319 cm^{-1}. The baseline of the integration was zero. These integration values were correlated with the attached amount of CMC measured with the polyelectrolyte titration technique in a cubic model. The cubic model was chosen because it is predicted by theory (Tolstoy et al. 2003).

All IR measurements were done under vacuum conditions with a base pressure of about 4 mbar.

Background

When analyzing thin layers on metallic substrates with IR spectroscopy, the method of choice is always an IRRAS, using linear polarized incident light. This is due to the surface selection rule, which states that a signal from the surface can only be measured with p-polarized incident light, making the s-component a perfect background spectrum. However, the situation is not as easy with dielectric substrates, but also in this case a lot of useful information can be gained from polarized IRRAS spectra. Comparing the s-polarized and the p-polarized components of IRRAS spectra of thin film structures (sample thickness is small compared to the wavelength of the light used) with non-normal incidence, additional bands can be found in the p-spectrum that are not visible in the s-spectrum. In an electromagnetic viewpoint, these bands appear due to surface charges on the thin layered structure, and become important due to the high aspect ratio and thus the high surface to volume ratio. The first theoretical explanation of this effect was given by (Berreman 1969), who gave the effect its name. The Berreman effect was later explained within the quantum mechanical regime of Polaritons (Tolstoy et al. 2003), where the thin film structure causes an additional oszillator, and thus an additional optical phonon band.

The additional peaks appear near the transverse optic (TO) or the longitudinal optic (LO) frequency (ν_{TO}, ν_{LO}). These frequencies are characterized by the maxima of the TO and the LO energy loss function of the optical phonons. The functions can be obtained from the complex refractive index of the material in the given geometric setup by the relations (Yamamoto and Ishida 1994):

$$\mathrm{TO} = \nu\,\mathrm{Im}[\varepsilon(\nu)] = \nu\varepsilon''(\nu) \quad (2)$$

$$\mathrm{LO} = \nu\,\mathrm{Im}[-1/\varepsilon(\nu)] = \nu\varepsilon''(\nu)/(\varepsilon'(\nu)^2 + \varepsilon''(\nu)^2) \quad (3)$$

where ν is the frequency or equivalently the wavenumber, ε is the complex dielectric function, Im gives the imaginary part, and ε' and ε'' are the real and the imaginary part of the dielectric function, respectively.

If the incident wave is now s-polarized, it oscillates parallel to the surface, independent of the angle of incidence Θ and therefore interacts with the film as if it was an infinite crystal. This leads to only one band from this oszillator in the s-spectrum near the TO frequency ν_{TO}. The p-polarized wave now oscillates in the angle of incidence Θ, and can excite LO as well as TO modes, depending on the angle of incidence. Because of the thin film structure the mode at the LO frequency is not purely longitudinal anymore. This gives for the p-spectrum a band at the TO frequency (as in the s-polarized case) and an additional band at the LO frequency ν_{LO}. Therefore, all the bands that only exist in the p-spectrum can be detected very well by subtracting the s-spectrum from the p-spectrum, which yields a very sensitive detection method for thin films on dielectric or metallic substrates (Tolstoy et al. 2003).

For the measurement and quantification it should be pointed out that the intensity of the modes is dependent on the film thickness, while the frequency is only slightly shifted (Harbecke et. al. 1985; Trasferetti et al. 2000). This opens up the possibility of quantitative measurements of CMC attached to cellulosic fibers. A Berreman minimum can be distinguished from chemical vibrations by its dependancy on the incidence angle in p-polarization. This can be demonstrated by a combination of numerical simulation and measurement (e.g. Hoffman et al. 1995; Mielczarski and Mielczarsky 1999, 2005), and it also is a well known effect of phononic surface polaritons (Berreman 1969; Hopfield 1965).

Results and discussion

ATR spectra of two samples (sample 1 and 2 from Table 1) with different amounts of attached CMC are shown in Fig. 1 together with a transmission spectrum of pure CMC. The carboxylate peaks around 1,593 and 1,430 cm^{-1} can be seen on both the pure CMC and the samples with CMC attached to the fibers. Two additional peaks are identified where the intensity changes with the attached amount of CMC. The first peak occurs at 1,740 cm^{-1} and can be assigned to the acid function. The second peak occurs at 1,434 cm^{-1} and is in the fingerprint region, and therefore cannot be assigned unambiguously. The penetration depth of the ATR method into the sample has been calculated according to (Gilli 2008) for all the peaks assigned in Fig. 1. The method is quite surface sensitive as the penetration depth is between 293 and 357 nm in this wavelength region. Therefore, this method primarily measures the CMC on the fiber surface, and the contribution of CMC that has diffused into the bulk of the fiber is rather low.

The amount of attached CMC can be estimated by integrating the IR spectra between about 1,760 cm^{-1} and 1,500 cm^{-1}. For a quantitative measurement the IR data was calibrated against the polyelectrolyte titration technique for measurements of the attached amount of CMC. The five samples from Table 1 with 1.90, 4.21, 7.76, 9.70 and 14.50 mg CMC/g fiber were compared with the integration values from the IR measurements. Measurements were taken at nine different places per sample, as it was clear that the CMC is not distributed evenly on the samples. The size of the ATR spot is about 1 mm^2. An average of the nine measurements of each paper sample was calculated and subsequently the average spectrum was integrated. The result of this procedure is shown in Fig. 2, where it can be seen that the amount of CMC correlates well to the peak area. However, the error bars are still quite large, which is probably due to the limited amount of samples that were measured and due to the high lateral variation of the CMC attachment on the surface. Nevertheless, the correlation is significant, showing that ATR can be used to determine the amount of attached CMC.

Table 1 List of the paper samples used and the corresponding surface charge and the amount of attached CMC

Sample no.	Surface charge (μequiv/g)	Attached CMC (mg/g)
Ref.	7.5	–
1	47.9	9.7
2	68.0	14.5
3	15.4	1.9
4	25.1	4.21
5	39.9	7.76

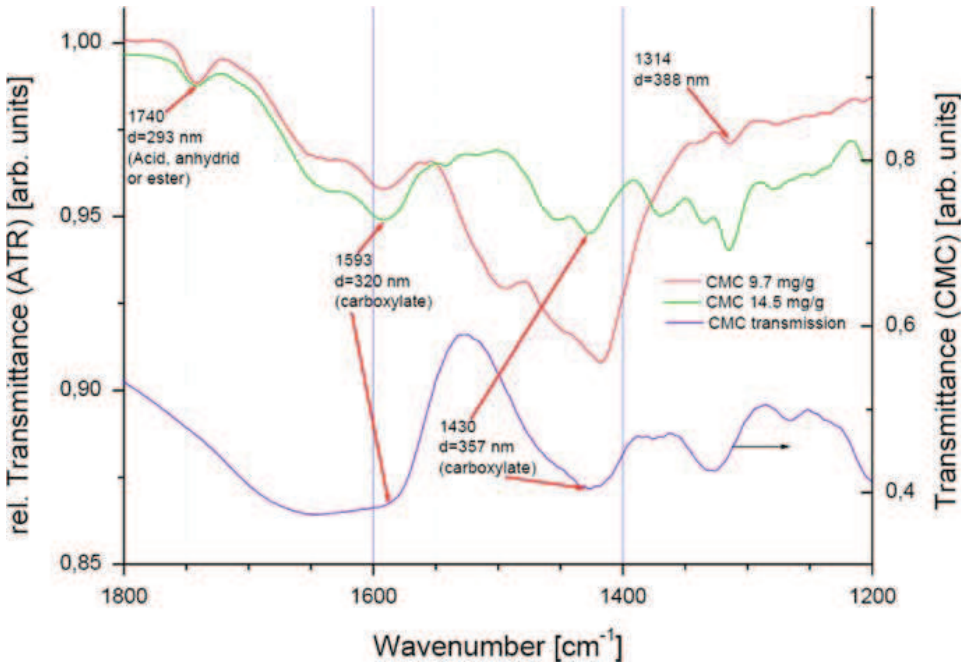

Fig. 1 ATR spectra of two samples with attached CMC and transmission IR spectrum of pure CMC. Note that the right axis belongs to the pure CMC spectrum

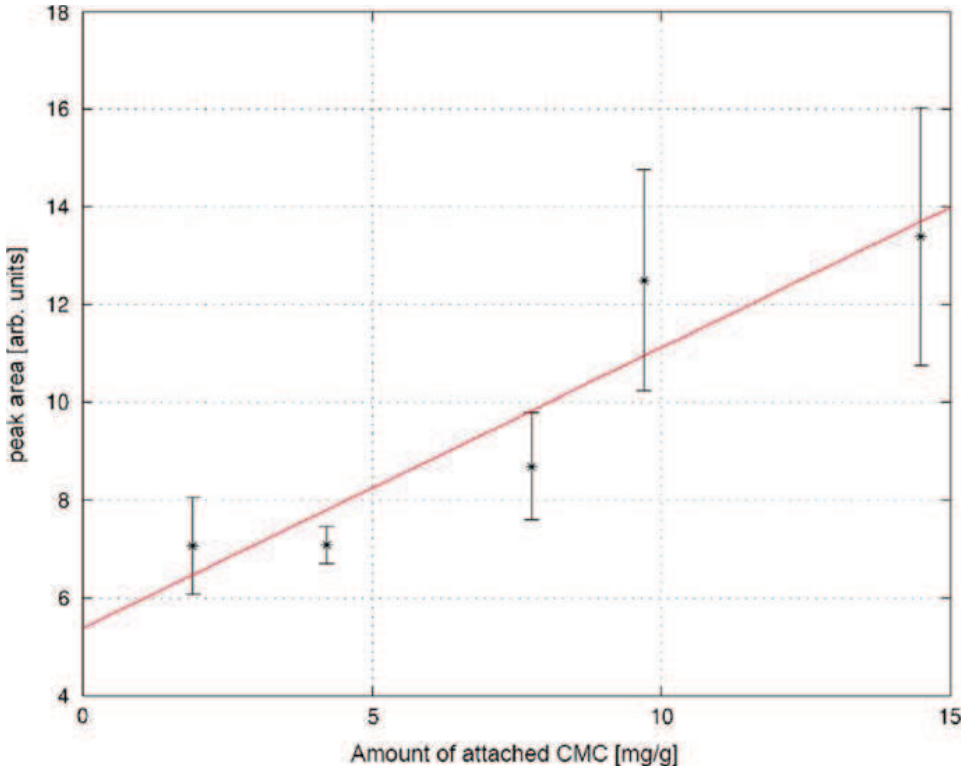

Fig. 2 Integrated peak area from ATR–IR measurements as a function of the attached amount CMC measured by the polyelectrolyte titration technique. The error bars give the standard deviation of the ATR measurements and the line is the linear regression

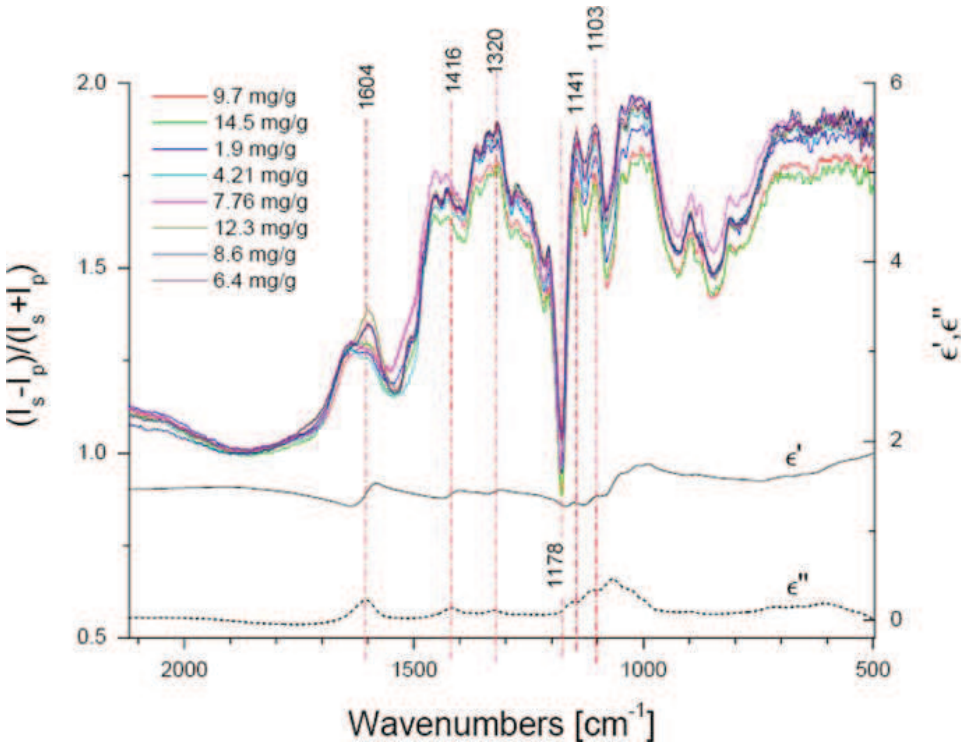

Fig. 3 IR spectra of samples with CMC in reflection geometry with s- and p-polarized light. The *solid black line* and the *dotted line* are the real ε' and the imaginary ε'' part of the dielectric function of a pure CMC sample, respectively

Figure 3 shows a series of polarized IRRAS spectra of the samples described in Table 1 together with the real ε' (*solid black line*) and the imaginary ε'' (*dotted line*) part of the dielectric function of a pure CMC sample.

A way to test whether a peak in a spectrum is due to the Berreman effect is to examine the dielectric function of the material that makes the thin film. The dielectric function can be obtained through Kramers Kronig Transformation (KKT) of an IRRAS

spectrum of pure material. This measurement was made with a pellet made from pure CMC, to find the TO and LO frequencies. The real part of the dielectric function, ε', has an inflection point at the TO frequency, while the imaginary part ε'' has a maximum (Tolstoy et al. 2003). However, the problem of the measurement is the grain size of the CMC particles. The grains are elongated agglomerates that are both flexible and ductile. This can be problematic, because the KKT measurement has to be performed with pellets made from samples with a grain size below the wavelength used, in order to minimize diffuse scattering. Nevertheless, the calculated dielectric functions shown in Fig. 3 appear to be usable. The fact that ε' never crosses the zero-line (see Fig. 3) can be due to the strongly damped oscillators in the material (Borstel and Falge 1977). At 1,604 cm^{-1} (see Fig. 3) the dielectric functions behave as they do at a TO frequency (maximum in the imaginary part, while the real part has a deflection point). The same can be stated for the point at 1,103 cm^{-1}. Here the signal is disturbed by a lot of noise, which could be a consequence of diffuse reflection on the pure CMC sample. The band at 1,604 cm^{-1} again represents the carboxylate peak. The frequency of the maximum of ε'' and the inflection point of ε' at 1,103 cm^{-1} corresponds more or less exactly to an absorption peak of the samples. Close to this peak, at 1,141 cm^{-1}, another absorption peak is visible, which is in the fingerprint region of the CMC (and also of the

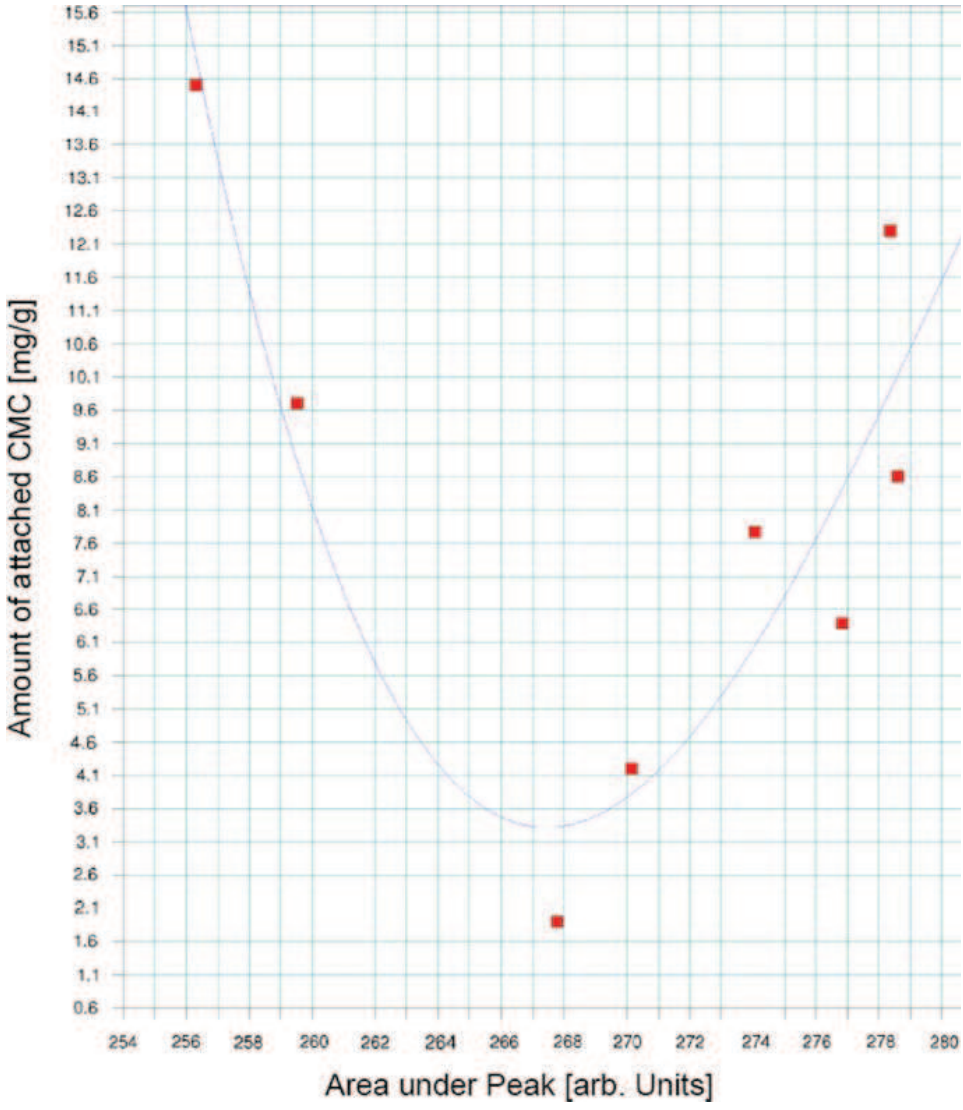

Fig. 4 The measured integration values of the 1,178 cm^{-1} peak from Fig. 3 are plotted against the attached amount of CMC measured by the polyelectrolyte titration technique as *squares*, the optimized correlation function is plotted as a *line*

cellulose). The very distinctive negative peak in Fig. 3 at 1,178 cm^{-1} does not correspond to a maximum in the dielectric function of CMC, and therefore it cannot be caused by the chemistry of the CMC. This peak is partly caused by the thin CMC film, and to some extent it is also caused by the primary wall of the fibers, as the primary wall is a thin film too. Therefore the measured Berreman peak is a combination effect of the two thin films. As long as the primary wall does not differ too much between the different samples the main change in the peak observed can be attributed to the CMC.

In summary one only needs to measure two IR spectra in reflection near the Brewster angle, one with s- and one with p-polarized light and subsequently calculate the resulting spectra according to Eq. 1 explained in the experimental section, in order to take advantage of the Berreman effect.

The cubic correlation function, which is expected from the Polariton model (Tolstoy et al. 2003) and the measured peak areas of the Berreman peak at 1,178 cm^{-1} from Fig. 3 is presented in Fig. 4. The integration method gives a correlation coefficient 0.9195 and a standard deviation of 2.13 mg/g. This means that the method is highly correlated to the true amount of attached CMC, but the measurement error is still quite high. This could probably be improved by taking more spectra of one sample and using the mean value of the integrations, as was done in the ATR measurements.

Even though the correlation exists, the noise in the data is still rather high for a quantitative measurement method. This can be due to different reasons. One has to bear in mind that both the primary wall of the fiber as well as the CMC will contribute to the Berreman peak. Therefore, different fibers and different fiber treatments (both of which will change the primary wall) will also influence the result. In this study only untreated soft wood fibers were used. The given CMC concentrations are measured via the difference in the surface charge density of the fibers with and without CMC. Here an influence of near surface charges cannot be ruled out completely. The IRRAS method on the other hand yields pure surface information. The lateral distribution of the CMC also remains unknown. ATR measurements on the same samples showed that the attached amount is not constant over the entire sample. This fact also contributes to the noise in the IRRAS data.

Conclusions

It has been shown that it is possible to measure the amount of attached CMC to cellulosic fibers from a paper sample using infrared spectroscopy. This can be achieved unambiguously with ATR spectroscopy, where the intensity of a carboxyl vibration is correlated to the amount of CMC. The ATR method is rather time consuming as several measurement points on the sample have to be averaged. However, it is still much faster than the wet chemical approach. The second method is IRRAS using polarized light. In this method the intensity of an electromagnetic wave confined to the thin layer is used to correlate the spectroscopy to the amount of CMC on the fiber surface in the paper sample. However, here contributions of the primary wall to the overall signal have to be taken into account. In principle the proposed IRRAS method could be applied in pulping and papermaking science and technology as a fast and reliable way to quantify the adsorption of chemicals on pulp fibers. Possible applications are in papermaking wet end chemistry. As it is a contact—free method one might even consider applying it to an online sensor.

Acknowledgments Funding by the Christian Doppler Society is greatly appreciated. E. Gilli and R. Schennach are indebted to P. Knoll for helpful discussions.

References

Barzyk D, Page DH, Ragauskas A (1997a) Acidic group topochemistry and fibre-to-fibre specific bond strength. J Pulp Pap Sci 23(2):J59–J61

Barzyk D, Page DH, Ragauskas A (1997b) Carboxylic acids groups and fibre bonding. In: The fundamentals in papermaking materials: the transaction of the 11th fundamental research symposium, vol 2. Cambridge, UK, pp 893–907

Berreman DW (1969) Infrared absorption at longitudinal optic frequency in cubic crystal films. Phys Rev 130:2193–2198. doi:10.1103/PhysRev.130.2193

Borstel G, Falge HJ (1977) Surface phonon—polaritons at semi infinite crystals. Phys Status Solidi B 83(11):11–45

Duker E, Lindström T (2008) On the mechanisms behind the ability of CMC to enhance paper strength. Nordic Pulp Pap Res J 23(1):57–64. doi:10.3183/NPPRJ-2008-23-01-p057-064

Gilli E (2008) IR spectroscopic investigations on the chemical surface properties of cellulose fibers. Diploma thesis, Graz University of Technology, Graz

Harbecke B, Heinz B, Grosse P (1985) Optical properties of thin films and the Berreman effect. Appl Phys A 38:263–267. doi:10.1007/BF00616061

Hoffman H, Mayer U, Krischanitz A (1995) Structure of alkylsiloxane monolayers on silicon surfaces investigated by external reaction infrared spectroscopy. Langmuir 11: 1304–1312. doi:10.1021/la00004a043

Hopfield JJ (1965) Polariton absorption lines. Phys Rev Lett 15(1):22–25. doi:10.1103/PhysRevLett.15.22

Horvath AE, Lindström T (2007) Indirect polyelectrolyte titration of cellulosic fibers—surface and bulk charges of cellulosic fibers. Nordic Pulp Pap Res J 22(1):87–92. doi: 10.3183/NPPRJ-2007-22-01-p087-092

Horvath AE, Lindström T, Laine J (2006) On the indirect polyelectrolyte titration of cellulosic fibers. Conditions for charge stoichiometry and comparison with ESCA. Langmuir 22(2):824–830. doi:10.1021/la052217i

Katz S, Beatson RP, Scallan AM (1984) The determination of strong and weak acidic groups in sulfite pulps. Svensk Papperstidning 87(6):48–53

Laine J, Lindström T, Glad-Nordmark G, Risinger G (2000) Studies on topochemical modification of cellulosic fibres. Part 1. Chemical conditions for the attachment of carboxymethyl cellulose onto fibres. Nordic Pulp Pap Res J 15(5): 520–526. doi:10.3183/NPPRJ-2000-15-05-p520-526

Laine J, Lindström T, Bremberg C, Glad-Nordmark G (2003) Studies on topochemical modification of cellulosic fibres. Part 5. Comparison of the effects of surface and bulk chemical modification and beating of pulps on paper properties. Nordic Pulp Pap Res J 18(3):326–333

Lindström T (1980) Influence of chemical factors on fiber swelling and paper strength. Papier 34(12):561–568

Lindström T (1989) Some fundamental chemical aspects on paper forming. In: Fundamentals of papermaking: transaction of the 9th fundamental research symposium, vol 1. Cambridge, UK, pp 311–412

Lindström T, Wagberg L, Larssson T (2005) On the nature of joint strength in paper—a review of dry and wet strength resins used in paper manufacturing. In: Proceedings of the 13th fundamental research symposium, vol 1. Cambridge, FRC, pp 457–562

Mielczarski JA, Mielczarsky E (1999) Infrared external reection spectroscopy of adsorbed monolayers in a region of strong absorption of substrate. J Phys Chem B 103:5852–5859. doi:10.1021/jp990529m

Mielczarski JA, Mielczarsky E (2005) Monitoring mineral surface phenomena by infrared reaction spectroscopy. Physicochem Probl Miner Process 39:33–46

Terayama H (1952) Method of colloid titration (a new titration between polymer ions). J Polymer Sci 8(2):243–253. doi: 10.1002/pol.1952.120080209

Tolstoy VP, Chernyshova IV, Skryshevsky VA (2003) Handbook of infrared spectroscopy of ultrathin films. Wiley, Hoboken

Trasferetti BC, Davanzo CU, Da Cruz NC, De Moraes MAB (2000) Observation of the Berreman effect in infrared reflection-absorption spectra of amorphous titanium oxide thin films deposited on aluminum. Appl Spectrosc 54(5): 687–691. doi:10.1366/0003702001949933

Wågberg L, Ödberg L, Glad-Nordmark G (1989) Charge determination of porous substrates by polyelectrolyte adsorption. Nordic Pulp Pap Res J 4(2):71–76. doi: 10.3183/NPPRJ-1989-04-02-p071-076

Winter L, Wågberg L, Ödberg L, Lindström T (1986) Polyelectrolytes adsorbed on the surface on cellulosic materials. J Colloid Interface Sci 111(2):537–543. doi:10.1016/0021-9797(86)90057-3

Yamamoto K, Ishida H (1994) Optical theory applied to infrared spectroscopy. Vib Spectrosc 8:1–36. doi:10.1016/0924-2031(94)00022-9

4. Paper submitted to Cellulose 2011

This paper treats the delignification process of fibers by ozone treatment. The aromatic vibrations of the lignin can be observed very well in polarized IRRAS, and the entire chemical process of decrease of lignin and build up of following products can be watched. On the other hand hemispherical lignin precipitates have been investigated on single fiber samples in AFM. Their size and number can also be correlated to the delignification which was independently determined wet-chemically.

The spectroscopic measurement and data analysis, the discussion and interpretation, as well as the major part of writing have been done by me.

Cellulose manuscript No.
(will be inserted by the editor)

Analysis of lignin precipitates on ozone treated kraft pulp by FTIR and AFM

Eduard Gilli · Franz Schmied · Stefan Diebald · Andrew T. Horvath · Christian Teichert · Robert Schennach

Received: date / Accepted: date

Abstract By the use of polarization modulated Fourier transform infrared spectroscopy and atomic force microscopy the process of ozone bleaching of kraft pulp is studied. The complementary information from the two methods allows for a detailed analysis of reaction sites on the fibers, and give a detailed view of the reaction mechanisms of delignification by ozone treatment. Furthermore we describe a simple method to measure the κ number of paper sheets by infrared spectroscopy.

Keywords Kappa Number · AFM · pm-IRRAS · FTIR · Lignin · Ozonation · Ozone delignification

1 Introduction

The use of ozone as a bleaching agent in elementary chlorine free (ECF) and totally chlorine free (TCF) bleaching plants has been established in several industrial pulp and paper mills over the past 20 years [2]. Further investigations on ozone as a pulping agent in kraft pulp mills have been made. Gas phase ozonation of mechanical pulp performed by Liebergott [8] showed improved mechanical properties of the pulp after treatment with a small amount of ozone. It has further been shown that gas phase ozonation of high Kappa kraft pulp at high consistency results in an increased fiber bonding potential while the fiber length is preserved [13]. Due to high selectivity, ozone treatment primarily leads to degradation of lignin whereas the cellulose structure remains mostly unchanged [10,9]. Ozone attacks aromatic and olefinic units of lignin and lignin is degraded to water-soluble products containing carboxyl and carbonyl functionalities [10,11]. Fourier Transform infrared (FTIR) spectroscopy has been shown to be an applicable tool in chemical pulp analysis by McKelvey et.al. [10] and since then it has been successfully used in several studies concerning the chemical composition of pulp [9,11]. Atomic force microscopy (AFM) has been used to obtain information on the morphology of fiber surfaces [11,6,5]. AFM images of ozonated mechanical pulp have shown that oxidation and reduction of lignin mainly take place on the fiber surface [6]. The formation of loose lignin degradation products on the fiber surface due to ozone oxidation of thermomechanical pulp has also been shown using AFM [11].

The reaction mechanisms on the fibers, however, remain unclear to some extend. In this paper the mechanisms of ozone bleaching of kraft pulp are studied. For understanding the changes in chemistry caused by ozonation, Fourier Transform infrared (FTIR) spectroscopy has been applied as a bulk sensitive measurement. Atomic force microscopy (AFM) has been performed to show changes on the structure of lignin precipitates on the fiber surface during ozone exposure. The combination of the two methods gives valuable insight into the surface

E. Gilli · S. Diebald · R. Schennach
Institute of Solid State Physics, Graz University of Technology, 8010 Graz, Austria
Tel.: +43-316-873-8130
Fax: +43-316-873-8466
E-mail: gilli@tugraz.at

F. Schmied · C. Teichert
Institute of Physics, University of Leoben, 8700 Leoben, Austria

E. Gilli · F. Schmied · S. Diebald · C. Teichert · R. Schennach
CD-Laboratory for Surface Chemical and Physical Fundamentals of Paper Strength, Graz University of Technology, Graz, Austria

A.T. Horvath
Tetra Pak Packaging Solutions, Ruben Rausings gata, 22186 Lund, Sweden

and bulk reaction scheme of ozone bleaching of kraft pulp. The good bulk sensitivity of FTIR in terms of the penetration depth of the infrared radiation into the fibers allows for a quantifyable measurement method of κ number in paper sheets.

2 Materials and Methods

2.1 Pulp Sample Preparation

Pulp treatment and κ-number measurement A never-dried unrefined kraft pulp was supplied by Mondi Frantschach GmbH. The pulp was an unbleached softwood that had a Kappa number of 45. As it was an industrial pulp, the fibers were rinsed thoroughly with deionized water to remove any residual alkali. The pulp was ozonated at low consistency in a 1L pressurized vessel fitted with a medium-shear mixer. Delignification of the pulp was done at 60°C and at pH 6. To ensure proper mixing, experiments were performed at a consistency of 5% by sparging a 4 wt% flow of ozone continuously through the suspension. The concentration of the ozone was measured using a Model GL-1 from PCI Ozone & Control Systems, Inc., West Caldwell, NJ, USA. An overpressure of 1.5 bar was maintained throughout the delignification process to dissolve more ozone in the suspension. Pulp suspensions were delignified for various times to prepare pulps having a range in Kappa number. The pulps were then rinsed and the Kappa number was determined chemically by titrating with a standard potassium permanganate solution using ISO 302:2004.

2.2 Atomic Force Microscopy

A Nanoscope IIIa Multimode AFM with an Extender Box and an AS-130 (J) Piezo Scanner (Digital Instruments/ Veeco, Santa Barbara, CA, USA, Software: V6.13R1) was employed. This AFM is equipped with an optical microscope (OM) from Nikon with a 10 times magnification, which helps to locate the fiber position in the AFM. For storing the optical information, a CCD camera incorporated in the OM is used. The measurements were carried out under ambient conditions (temperature: 22°C ± 0.5°C, relative humidity: 40% ± 10%). We used silicon cantilevers (PPP-NCHR from Nanosensors^{TM}) with a resonance frequency around (300 ± 10) kHz driven with 3% offset, which offered stable measurement conditions. The half cone angle of the tip apex is 10° and the typical tip radius is less than 7 nm, which leads to an enlargement of protruding surface features by about 2 nm [3].

All samples were measured in tapping mode, allowing to capture simultaneously topography and phase images [1,18]. In tapping mode more details of the nanostructure have been revealed and were thus analyzed as it is common practice in AFM investigation of pulp fiber surfaces [17,4]. In order to record the phase lag (ϕ) as adhesive interaction, a light-moderate tapping was performed using a damping ratio r_s (=A_{sp}/A_0) of approximately 0.7 [1]. Trace and retrace signals of the phase were compared to exclude morphology artifacts in the phase image and to verify a true phase signal. Initially, 5 μm x 5 μm images have been recorded to obtain an overview on the fiber morphology. The quantitative analysis based on a watershed algorithm is in detail described in Schmied et al. [16] and was employed on 2 μm x 2 μm phase images (512x512 pixels). The fast scan direction was perpendicular to the main fiber axis and the scan speed was 2.4 $\frac{\mu m}{s}$.

2.3 FTIR

For the infrared measuerments the pulp samples were prepared as Rapid Köten hand sheets. Samples of 1.5 by 1.5 cm were cut from the center of the sheets.

A Bruker ifs66v/s vacuum Fourier Transform Infrared (FTIR) spectrometer with a variable angle reflection unit (A513) from Bruker Optics (Ettlingen, Germany) was used at an incidence angle of 62°. The samples were measured under vacuum with a base pressure of 5 mbar. The polarization modulation measurements were carried out using a manual substrate free gold wire grid polarizer from infraspecs (Filderstadt, Germany), and a motorized wire grid on KRS-5 polarizer from Bruker Optics, with a polarization modulation method described elsewere [15].

The data were plotted in stokes vector representation, a representation frequently used in polarization modulation infrared reflection absorption spectroscopy (pm-IRRAS), where the signal is represented as

$$I_{pm} = \frac{R_p - R_s}{R_p + R_s}, \tag{1}$$

with the reflectance in p- and s-polarization R_p and R_s.

For each spectrum five single channel spectra of each polarization were recorded for 1 minute at a mirror velocity of 100 kHz and averaged. The quantification of the peaks was carried out by integration for the carbonyl and the aromatic ring bands and by depth measurement for the carboxylate bands, with the spectrometer software OPUS 4.2.

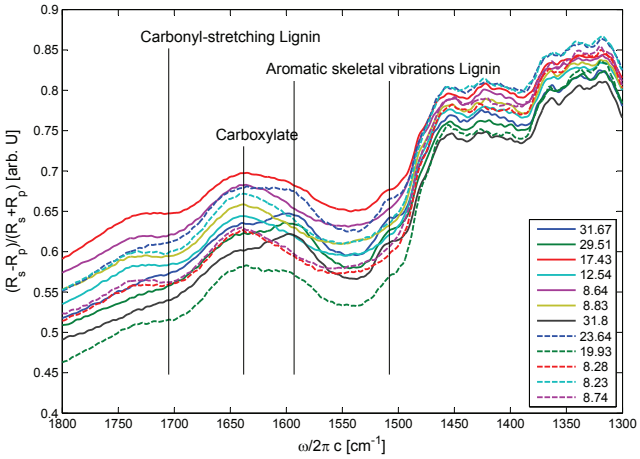

Fig. 1 The polarization modulated spectra of sheets prepared from ozonated and cooked pulps and the four characteristic bands, used for quantification of the process. The legend indicates the κ values of the different samples.

3 Results and Discussion

The polarization modulated infrared spectra in the relevant range are depicted in Fig. 1. From the spectra four relevant bands can be identified. The carbonyl-stretching of unconjugated ketone and carboxyl groups in guaiacyl-syringyl-lignin [7] at 1710 cm^{-1}, the carboxylate band [14] at 1638 cm^{-1}, and two bands from aromatic skeletal vibrations in guaiacyl-syringyl-lignin [7] at 1505 cm^{-1} and 1595 cm^{-1}. At a closer inspection of the spectra, it is apparent that the amplitude of these 4 peaks is different at the respective samples. This is especially well visible at the two aromatic skeletal vibration bands of lignin at 1505 cm^{-1} and 1595 cm^{-1}, which grow with growing κ number, and vanish for the highly ozonated samples.

The carbonyl-stretching band at 1710 cm^{-1} and the aromatic skeletal vibration band at 1593 cm^{-1} have been integrated for each spectrum. For the carboxylate band, the peak depth (or height) has been measured with respect to a local baseline. The data of this analysis as a function of the κ number are depicted in Fig. 2. The top frame of Fig. 2 represents the depth of the carboxylate band at 1638 cm^{-1}, the middle frame represents the area of the carbonyl stretching band at 1710 cm^{-1}, and the bottom frame represents the area of the aromatic skeleton band of lignin at 1593 cm^{-1}. All three values are plotted over the κ number of the pulp samples.

The integration of the aromatic skeletal vibration of lignin in the bottom frame of Fig. 2 clearly shows a linear behaviour with the κ number. This, however, fits well to the fact, that the signal of the aromatic skeletal

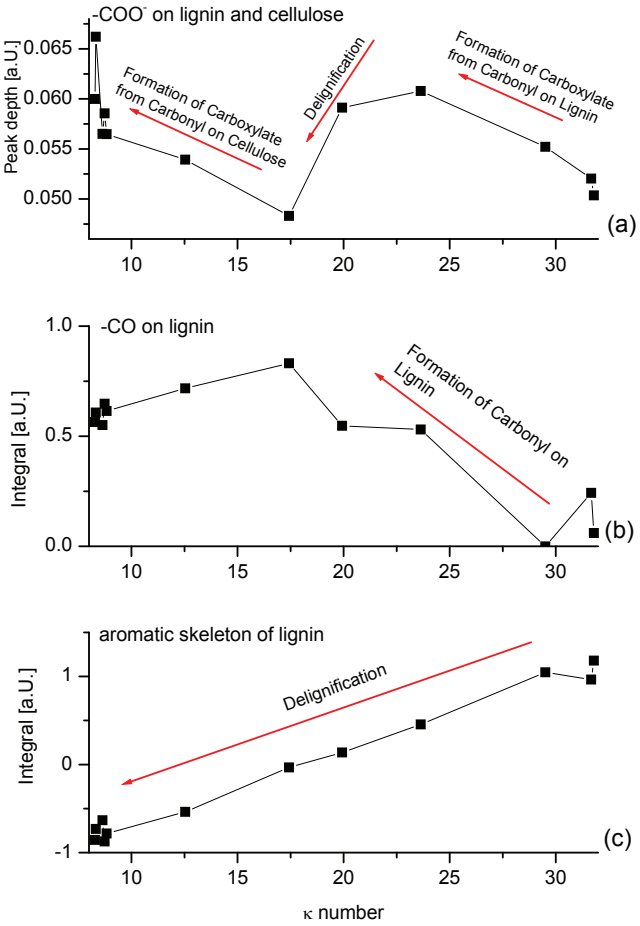

Fig. 2 FTIR analysis of the chemical process by the quantification of three bands: The carboxylate band at 1638 cm^{-1} (a), the carbonyl stretch band at 1710 cm^{-1} (b), and the aromatic skeletal vibration band at 1593 cm^{-1} (c).

vibration can only be caused by lignin, because no other substance in the fibers shows such a structure.

The delignification process can also be observed by the build up of carbonyl groups on lignin, which is depicted in the middle frame of Fig. 2. These carbonyl groups are formed from the oxidation of aromatic rings of lignin by ozone. With decreasing amount of lignin on the fibers ($\kappa = 18$) the carbonyl vibration reverses its trend and the corresponding band bekomes weaker. This can be attributed to the increased loss of carbonyl groups on the lignin which is removed, and the small amount of remaining lignin.

In the top frame of Fig. 2 the signal of the carboxylate band and its trends can be studied. The carboxylate is formed from the oxidation of carbonyl groups. At the beginning of the delignification process this primarily takes place with the carbonyl groups of lignin, simply because of the great amount of carbonyl groups on lignin formed in the early stages of ozonation. With increasing delignification the amount of carboxylate groups

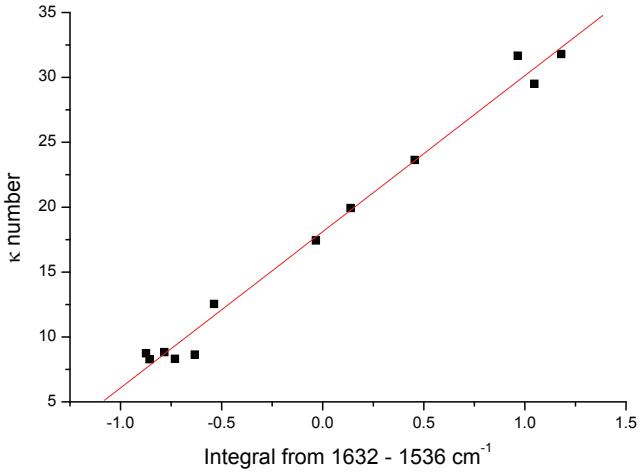

Fig. 3 The process of delignification observed by κ number as a function of the integral of the aromatic band at 1593 cm^{-1}. Linear fitting yields a correlation coefficient of 0.994 and a P-value of $P < 0.0001$.

which are removed together with the lignin increases. Therefore, the further increase of carboxylate groups becomes smaller and leads to a decrease for $\kappa < 23$. At about $\kappa = 18$ the amount of carboxylate groups in the fiber reaches a minimum, exactly at the position, where the amount of carbonyl groups on lignin starts to decrease (see Fig. 2, middle frame).

This is the point where the oxidation of $-OH$ groups in cellulose and hemicelluloses starts to overrule the oxidation of aromatic rings in lignin, due to the small amount of residual lignin. The inrease of carboxylate groups for $\kappa < 18$ nicely corresponds to a decrease of carbonyl groups, indicating that the build up of carbonyl now has slower reaction kinetics than the oxidation of carbonyl to carboxylate.

This is a clear sign that at κ numbers below 18 a different species with slower reaction kinetics ($-OH$) is oxidized to carbonyl than at higher κ numbers (oxidation of aromatic rings), which substantiates the above made interpretation, that the ozone primarily attacks lignin, and, to a much smaller degree celluloses and hemiceluloses.

The high linearity of the aromatic skeletal vibration at 1593 cm^{-1} calls for a quantification, which would allow to use the here used infrared measurement as a calibrated measurement of the κ number. The calibration line is depicted in Fig. 3. Here, the κ number of the pulps is plotted as a function of the peak area of the aromatic skeletal vibration band. Linear fitting yields a very high corellation (P-Value < 0.0001, correlation coefficient: 0.994) and a link from polarization modulated mid infra red spectra to κ number. The peak area is determined by a linear local baseline between the integration limits (1536 cm^{-1}-1632 cm^{-1}), and the κ number is determined by

$$\kappa = 18.11 + 12.03 * A \pm 1.1, \tag{2}$$

with A the peak area between 1536 cm^{-1} and 1632 cm^{-1}, and the uncertainity determined by the standard deviation of the linear fit.

The penetration depth of the infrared radiation onto the pulp fibers consequently yields bulk data of the lignin content in the fibers. Therefore, the κ number can be measured correctly, and the entire chemical process can be elucidated, while no information about the location of the lignin on or in the fiber can be obtained. This question can much better be studied by AFM measurements of the fiber surfaces, where reprecipitated lignin can be observed.

Figure 4 summarizes the findings based on high-resolution AFM phase imaging. Here, 2x2 μm^2 AFM phase images for differently treated pulps with a κ-number ranging from 8-45 are presented in figure 4a-d. According to the microfibrilar angle, which is more or less perpendicular to the direction of the main fiber axis, the revealed surface layer is the secondary wall 1. Figure 4e illustrates the evaluation of the precipitation diameter for the different κ-numbers. Here, the precipitation diameter is mainly influenced by the kinetics of the lignin precipitation onto the fiber surface or the kinectics of the oxidation process. Therefore, the precipitation diameter is only a measure for the process parameters and not directly correlated with the κ-number. The standard deviation of the lignin precipitation diameter (figure 4f) is a measure for the uniformity of the investigated lignin precipitates and thus related to the process conditions. Due to the fact that the surface treatments are starting with an industrial pulp (κ-number = 32), a higher uniformity is expected for a harsher surface treatment of the pulp. The smaller standard deviation of the precipitation diameter for the κ-number 8 is representing a higher uniformity for the lignin precipitation diameter than for the pulp fibers closer to the standard pulp. Assuming circular footprints of the lignin precipitates, the surface coverage Θ_{surf} can be estimated as

$$\Theta_{surf} = \frac{d^2 * \pi}{4} * N * \frac{1}{A} \tag{3}$$

where d, N, A are the diameter of the lignin precipitation, the number of identified particles and the scanned area. This evaluation is represented in figure 4g for each κ-number and describes a non-linear increase of the surface coverage with the κ-number. the scatter from the trendline is attributed to the inhomogenous distribution of the lignin precipitates on the fiber sur-

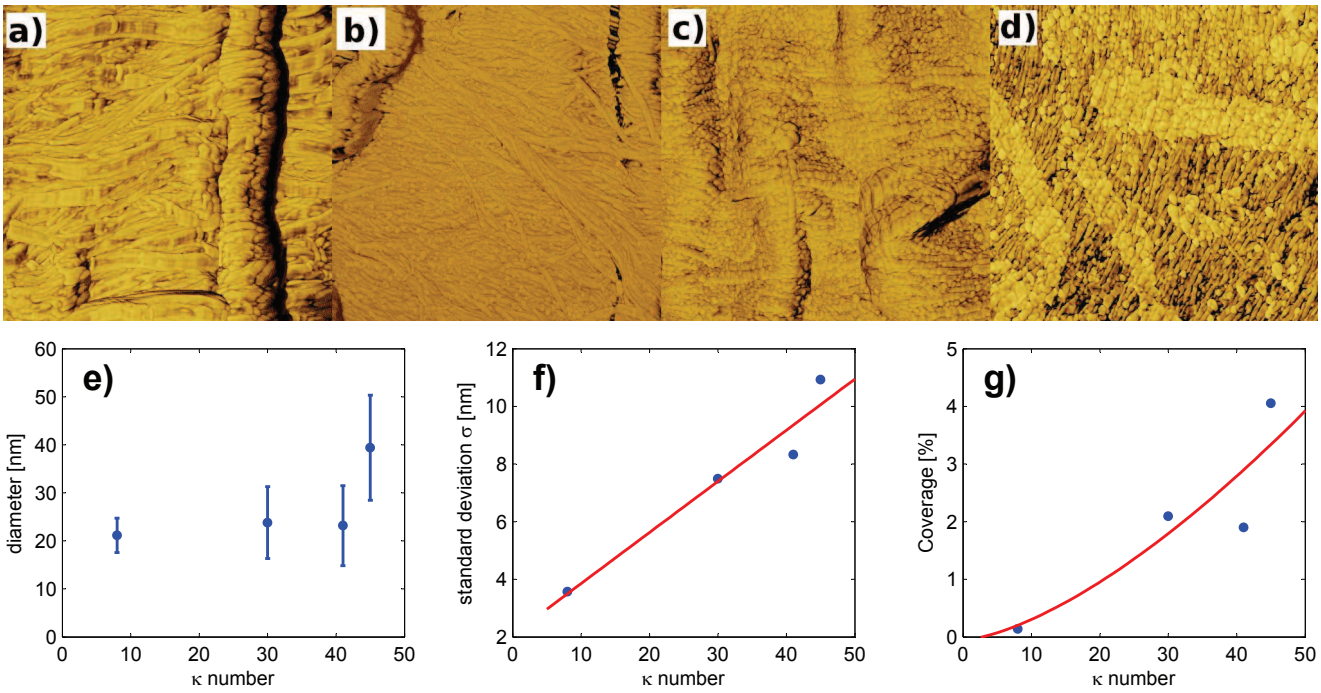

Fig. 4 Summary of precipitation analysis of differently treated pulps with a κ-number ranging from 8-45 of 2x2 μm^2 AFM phase images, ϕ-scale = 50°. a) κ = 8, b) κ = 30, c) κ = 41, d) κ = 45, e) Diameter of precipitation versus κ-number, f) Standard deviation of precipitation diameter versus κ-number, and g) lignin coverage versus κ-number together with a $\kappa^{3/2}$ non-linear fit.

face and an incomplete detection of all lignin precipitates perhaps present on the pulp fiber surface [16].

With the infrared data a linear increase of lignin content with κ number was observed. Together with the AFM data, the kinetics of the delignification of native and reprecipitated lignin can be elucidated.

Taking into acount, that the surface coverage measured with AFM represents a planar projection of the precipitates, a non-linear increase of the coverage with the amount of precipitated lignin is expected for hemispherical precipitates. By assuming hemispherical precipitates the amount of precipitated lignin is proportional to the third power of the precipitate radius. The coverage being a two dimensional projection of the precipitate footprint consequently is proportional to the square of the precipitate radius. Therefore the proportionality between coverage and κ number is expected to be close to

$$\theta_{surf} \propto \kappa^{\frac{3}{2}}, \tag{4}$$

which fits well to the observed behavior (see Fig. 4g).

The reduced scatter of the precipitate diameters with increasing ozone treatment also can be attributed to the geometry of the precipitates and yield further insite into the reaction sites. Histograms of the precipitate diameters for the different samples are given in Fig. 5.

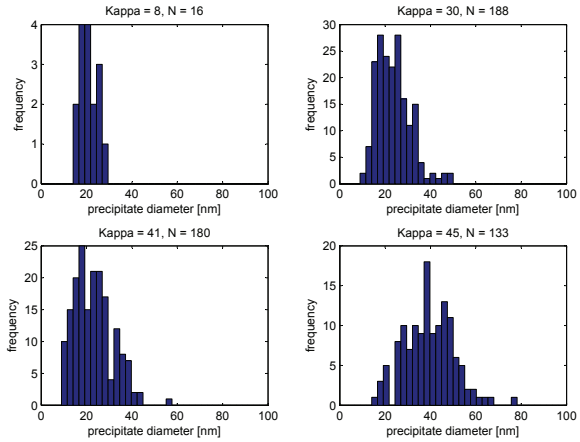

Fig. 5 Histograms of the precipitate radii for κ=8 (top left hand frame), κ=30 (top right hand frame), κ=41 (bottom left hand frame), and κ=45 (bottom right hand frame).

Comparing the histograms in Fig. 5 shows a strong narrowing of the distribution of precipitate diameters for increasing ozone treatment. This is a clear sign for a dependency of the reaction kinetics on the precipitate radius. By this dependence, the reaction sites on the lignin precipitates can be identified. There are two possibilities: First, the ozone attacks the lignin at preferred sites, such as the interface between lignin and cellulose, and second, the lignin is uniformly attacked by ozonation on its entire surface.

The number of active reaction sites, a, is proprtional to the removed volume of lignin, dV, thus

$$\frac{dr}{dV} \propto \frac{r}{a}, \tag{5}$$

with the precipitate radius r.

For the case of a localized ozone attack at the lignin cellulose interface, the number of active reaction sites is proportional to the precipitate radius, while for the case of a uniform attack, the number of active sites is proportional to the precipitate surface and thus to the square of the precipitate radius, which gives a linear behavior of the precipitate radius for the first case

$$\frac{dr}{dV} \propto 1, \tag{6}$$

and an indirect r-proportionality for the second case

$$\frac{dr}{dV} \propto \frac{1}{r}. \tag{7}$$

Therefore, by assuming the oxidation reaction to uniformly take place on the precipitate surface, it can be explained that the radii of smaller precipitates are reduced faster than for the larger precipitates. This asumption fits well to recent studies of the structure of lignin aggregates by molecular dynamics and neutron scattering [12], where the aggregate surfaces show a very high roughness, that offers many evenly distributed reaction sites troughout the entire aggregate surface. For the distribution of precipitate diameters this means, that the small precipitates vanish quickly while the diameters of the larger ones are reduced more slowly, causing a reduction of scatter, while the mean value is comparatively stable.

4 Conclusions

By the combination of the chemical bulk sensitivity of infrared spectroscopy and the surface information from AFM, it was possible to elucidate the reaction kinetics of fiber delignification. It has been demonstrated that the ozone reaction is proprtional to the exposed lignin surface and that the delignification reaction can be observed quantitatively in the mid infrared by polarization modulated reflection spectroscopy. It has further been shown, that cellulose and hemicelluloses are not oxidized by the ozone treatment as long as a sufficient amount of lignin is available in or on the fiber, because the oxidation of aromatic rings in lignin needs less activation energy than the oxidation of $-OH$-groups on cellulose and hemicelluloses.

Acknowledgements The financial support by the Austrian Federal Ministry of Economy, Family and Youth and the national Foundation for Research, Technology and Development is gratefully acknowledged.

References

1. Bar, G., Thomann, Y., Brandsch, R., Cantow, H.J., Whangbo, M.H.: Factors affecting the height and phase images in tapping mode atomic force microscopy. study of phase-separated polymer blends of poly(ethene-co-styrene) and poly(2,6-dimethyl-1,4-phenylene oxide). Langmuir **13**(14), 3807–3812 (1997)
2. Dence, C.W., Reeve, D.W.: Pulp bleaching - principles and practice. Tech. rep., TAPPI PRESS, Atlanta, Georgia (1996)
3. Fahlen, J., Salmen, L.: Pore and matrix distribution in the fiber wall revealed by atomic force microscopy and image analysis. Biomacromolecules **6**, 433–438 (2005)
4. Gustafsson, J., Ciovica, L., Peltonen, J.: The ultrastructure of spruce kraft pulps studied by atomic force microscopy (afm) and x-ray photoelectron spectroscopy (xps). Polymer **44**(3), 661–670 (2003)
5. Karlsson, J.O., Andersson, M., Berntsson, P., Chihani, T., Gatenholm, P.: Swelling behaviour of stimuli-responsive cellulose fibers. Polymer **39**(16), 3589–3595 (1998)
6. Koljonen, K., Österberg, M., Johansson, L.S., Stenius, P.: Surface chemistry and morphology of different mechanical pulps determined by esca and afm. Colloids and Surfaces A: Physiochem. Eng. Aspects **228**, 143–158 (2003)
7. Levlin, J.E., Sderhjelm, L.: Pulp and Paper testing. Fapet Oy, Helsinki (1999)
8. Liebergott, N.: Sequential treatment of mechanical pulps at high consistency with H_2O_2 and O_3 - the paprizone process - effect on pulp brightness and strength. Pulp Paper Mag. Can. **73**(9), T214–T217 (1972)
9. Mamleeva, N.A., Autlov, S.A., Bazarnova, N.G., Lunin, V.V.: Delignification of softwood by ozonation. Pure Appl. Chem. **81**(11), 2081–2091 (2009)
10. McKelvey, R.D., Thompson, N.S., Lyse, T.E.: The ozone oxidation of alkali-fiberized loblolly pine wood. Cellulose Chem. Technol. **17**, 355–361 (1983)
11. Östenson, M., Gatenholm, P.: Improvement of the wetting and absorption properties of lignocellulosic fibers by means of gas phase ozonation. Langmuir **21**(1), 160–165 (2005)
12. Petridis, L., Pingali, S.V., Urban, V., Heller, W.T., O'Neill, H.M., Foston, M., Ragauskas, A., Smith, J.C.: Self-similar multiscale structure of lignin revealed by neutron scattering and molecular dynamics simulation. Physical Review E **83**, 061,911 (2011)
13. Procter, A.R.: Ozone gas treatments of high kappa kraft pulps. Pulp Paper Mag. Can. **75**(6), T210–T214 (1974)
14. Schantl, J.: Charakteristische gruppenschwingungen organischer moleküle im infrarot-spektrum. Script for the lecture "Einführung in die Molekülspektroskopie", Institut für organische Chemie, Universität Innsbruck (1971)
15. Schennach, R., Hirschmugl, C., Gilli, E., Tysoe, W.T.: A new method for performing polarization-modulation infrared reflection-absorption spectroscopy of surfaces. Applied Spectroscopy **63**(3), 369–372 (2009)
16. Schmied, F.J., Teichert, C., Kappel, L., Hirn, U., Schennach, R.: Quantitative analysis of precipitated lignin on kraft pulp fibers using atomic force microscopy. submitted to Cellulose (2011)
17. Simola, J., Malkavaara, P., Aln, R., Peltonen, J.: Scanning probe microscopy of pine and birch kraft pulp fibres. Polymer **41**(6), 2121–2126 (2000)
18. Whangbo, M., Bar, G., Brandsch, R.: Qualitative relationships describing height and phase images of tapping mode atomic force microscopy. an application to

micro-contact-printed patterned self-assembled monolayers. Appl. Phys. A: Mater. Sci. Process. **66**, 1267–1270 (1998)

5. Subsumption Surface Chemistry

In the former two publications a simple self-made pm-IRRAS method (Schennach et al. 2009) has been sucessfully applied to paper sheet systems. The results show that, firstly the pm-IRRAS method gives good results and yields very reproducable data, and secondly, that it is indeed feasible to use polarization modulated specular reflection in the infrared at such complicated systems as paper sheets.

With the method, very thin surface layers on the individual fibers were measurable and together with calibration quantifyable. The combination with AFM data shows, that this method is a reliable measurement setup for fiber surface chemistry analysis. The data shows a good agreement and the lignin content can be measured with this method on the full range.

Especially the high surface sensitivity of the method together with the robustnes against scattering effets shall be pointed out here, because it can be realized by simple equipment without the need of employing a step scanner and a photoelastic modulator.

The results that can be obtained this way on paper sheets, have a high relevance for the applied research, especially the possibility of online measurement on the paper machine seems very interesting in this context. Anyhow, for the fundamental question of the molecular mechanisms of fiber bonding other means have to be taken into account. This question can only be addressed in an unambiguous way with systems that can be simulated on a fundamental level. One possibility of such systems will be discussed in the second part of this dissertation, which deals with cellulose model film systems, their simulation and spectroscopic measurement, especially the measurement of the optical properties of the involved biomacromolecules, and spectroscopic methods.

References

Schennach, R., Hirschmugl, C., Gilli, E., and Tysoe, W. T. (2009). *A New Method for Performing Polarization-Modulation Infrared Reflection-Absorption Spectroscopy of Surfaces.* Applied Spectroscopy, **63**.(3), pp. 369–372.

Part II.

Spectroscopic methods

6. Introductory remarks

In the following chapters, work is discussed that was motivated by the research on cellulose model films, or directly deals with these model systems. The model films were used to mimic the fiber-fiber bond in a controllable and simulateable macroscopically accessible system as discussed in the introduction (Sec. 1).

For a systematic research of the fundamentals of fiber-fiber bonding, these model systems represent an ideal system. The surfaces show only little scattering in the infrared, the geometry is simple, and the only bonding mechanisms that take place here, are surface physical and surface chemical effects. The geometric effects of mechanical interlocking or interdiffusion do not occur with these systems, the bonding due to surface charges can be controlled by introducing charged species to the surfaces. Initialy the cellulose surfaces do not contain any charged species.

These simplified systems yield the possibility of a more fundamental understanding of the spectroscopic features. As with any thin film system, especially with planparallel interfaces, optical effects due to thin film interference have to be taken into account. This can be done in a quantitative way by optical simulation.

There is one necessary prerequisite for optical simulation: the optical properties of all the substances present in the sample have to be known. The accuracy of this data is a very crucial point in order to get the right answers from the simulations.

As it turned out in the course of the work, the optical constants of cellulosic materials have not been measured yet in the mid infrared. There is no literature data available. Yet the entire approach of the thin film cellulose systems is completely dependent on optical simulation and therefore, on the knowledge of the necessary optical data.

For these reasons a possibility was searched to measure these data. The approach chosen in this work is described in the first paper of this part of this dissertation (Sec. 7, Ref. (Gilli and Schennach 2010)). A Kramers-Kronig approach from polarization modulated reflectance data was chosen, that is quite robust against scattering problems, which is necessary, because the cellulosic materials cannot be produced in a crystalline form, but rather as powders, which is a fundamental problem with Kramers-Kronig transformation.

The second paper of this part is more on the applied side. Here, systematic measurements on cellulose model films were carried out, and is was shown that it is possible to determine the film thickness from reflectance data by optical simulation (Sec. 8, Ref. (Djak et al. 2011)).

The difficulty with the Kramers-Kronig measurements which can never be exact, but rather more or less erroneous, could be overcome by measuring the samples with spectroscopic ellipsometry. Here the problem of scattering still remains, but the necessary data is fully measured instead of calculated by a non-exact numeric transformation.

The scattering can be ruled out by measurng the optical data on prepared thin films of the cellulosic substances. This approach with spectroscopic infrared ellipsometry would be ideal for the measurement of optical constants of cellulosic materials. A difficulty in this case is the necessity to have exact knowledge of the film thickness. The fact that cellulosic films swell in moist environments is a great problem in this case. Therefore, a spectroscopic infrared ellipsometer with a fully controlable atmosphere is necessary.

This is the motivation for the work that led to the third publication of the current part of this dissertation (Sec. 9, Ref. (Gilli et al. 2011c)). An optical unit for spectroscopic infrared ellipsometry with variable angle of incidence was developed. This unit fits into the evacuated sample compartment of the Bruker ifs66v/s vacuum spectrometer used in the course of this work.

The unit is still in a prototype stage, but a working proof of concept exists.

References

Djak, M., Gilli, E., Kontturi, E., and Schennach, R. (2011). *Thickness dependence of reflection absorption infrared spectra of supported thin Polymer films.* Macromolecules, **44**.(7), pp. 1775–1778.

Gilli, E. and Schennach, R. (2010). *Determination of Noise-Free Optical Constants in the Infrared by Kramers-Kronig Troansformation of the Reflectance Ratio in s- and p-Polatization.* Applied Spectroscopy, **64**.(6), pp. 669–681.

Gilli, E., Kornschober, M., and Schennach, R. (2011c). *Optical arrangement and proof of concept prototype for mid infrared variable angle spectroscopic ellipsometry.* Submitted to: Infrared Physics & Technology,

7. Paper published in Applied Spectroscopy 2010

The following publication (Gilli and Schennach 2010) was motivated by the need for optical constants data of the cellulosic materials involved in the model film systems, as discussed in Sec. 8 and Ref. (Djak et al. 2011). These data cannot be obtained from literature, because first, the complex cellulosic biomacromolecules, as it seems, have not been measured yet, and second, the exact optical behaviour of these materials is strongly influenced by the production processes, due to purity issues.

The only feasible solution was to measure the necessary material constants. This is a highly untrivial problem. The possibility of measuring the optical constants by spectroscopic infrared ellipsometry could be ruled out in the beginning, simply because the CD-Lab did not have access to such a system.

Therefore, the way of Kramers-Kronig transormation was chosen. Here, as well as with the spectroscopic ellipsometry, the fact that the substances can only be prepared from powders is a huge problem. The grain sizes of the powders were chosen as small as possible, in order to be under the diffraction limit of the used infrared radiation, still the measurement on pellets prepared from powders is strictly speaking incorrect.

A lot of analytic work on the errors, made with this method was carried out in the following publication.

It should also be noted that - besides the actual Kramers-Kronig part - the method can as well be used to obtain noise-free data from spectroscopic ellipsometry measurements, and is not just limited to Kramers-Kronig transformation.

I want to acknowledge the fruitful discussions with Prof. Ewald Schachinger from the Institute of Theoretical and Computational Physics at the Graz University of Technology.

References

Djak, M., Gilli, E., Kontturi, E., and Schennach, R. (2011). *Thickness dependence of reflection absorption infrared spectra of supported thin Polymer films.* Macromolecules, **44**.(7), pp. 1775–1778.

Gilli, E. and Schennach, R. (2010). *Determination of Noise-Free Optical Constants in the Infrared by Kramers-Kronig Troansformation of the Reflectance Ratio in s- and p-Polatization.* Applied Spectroscopy, **64**.(6), pp. 669–681.

Determination of Noise-Free Optical Constants in the Infrared by Kramers–Kronig Transformation of the Reflectance Ratio in *s*- and *p*-Polarization

EDUARD GILLI* and ROBERT SCHENNACH

Institute for Solid State Physics, Graz University of Technology, Graz, Austria (E.G., R.S.); and Christian Doppler Laboratory for Surface Chemical and Physical Fundamentals of Paper Strength, Graz, Austria (E.G., R.S.)

A method for Kramers–Kronig transformation of the reflectance ratio of *s*- and *p*-polarized light is discussed. The method is well suited for the determination of the optical constants of isotropic samples such as pellets prepared from powders. An algorithm is given that performs the transformation, including extrapolation at the data margins and an automated data fitting routine, that can handle very complex spectra of, e.g., biomacromolecules such as cellulose to obtain noise free spectra. Criteria for evaluation of the quality of the obtained data are given, and experimental data for cellulose II and xylane are presented.

Index Headings: **Kramers–Kronig transformation; Complex refractive index; Automated peak detection; Noise-free optical constants; Polarization modulation; Biomacromolecules; Cellulose; Xylane.**

INTRODUCTION

It is an often occurring task in spectroscopy and especially in spectroscopic simulation to obtain data of optical constants (complex refractive index $\hat{n} = n = ik$, with the refractive index n and the extinction coefficient k or dielectric function $\hat{\varepsilon} = \varepsilon' + i\varepsilon''$). This can be done by different means, the most prominent of them probably being the Kramers–Kronig transformation (KKT) methods. These are used in transmission as well as in reflection measurements. The reflection measurements are preferred due to the fact that only one interface has to be considered in the data analysis.

There exist commercial solutions to perform KKT of reflectance data. They often have shortcomings, especially when dealing with non-standard samples, e.g., for samples prepared from powders, the grain size of the powder must be taken into account. Another problem is the noise reduction of the measured data. Noisy optical constants cannot be used for optical simulation due to error propagation. The only means of removing the noise without altering the shapes of the spectra is nonlinear fitting of the optical constants. For complex molecules, e.g., biomacromolecules such as cellulose, it can be very tedious to perform the fitting manually.

The original work on the Kramers–Kronig relations was given by Hendrik A. Kramers[1] in 1927 and Ralph de L. Kronig[2] in 1926. In 1928 a joint paper was published.[3] The method of deriving the optical constants from reflection measurements was introduced by Tousey[4] in 1939. He derived the constants at a single wavelength by at least two measurements of the reflection at different incidence angles using the generalized Fresnel equations to obtain a system of two equations, which he solved graphically.

Received 3 February 2009; accepted 2 March 2010.
* Author to whom correspondence should be sent. E-mail: gilli@tugraz.at.

The Tousey method was improved by Avery in 1952. Instead of the reflectance Avery[5] introduced the possibility of measuring the ratio of reflectance in *s*- and *p*-polarization, which yields a background-independent measurement, similar to ellipsometry, as long as the light source is isotropic in polarization. Robinson[6,7] introduced a method to derive the phase difference from the reflectance measurement in a graphical way, which basically is a KKT.

An important part of the theoretical background of the Kramers–Kronig transformations was given by Toll in 1956. He derived a proof that the Kramers–Kronig transformations hold for any causal complex function, especially for dispersion relations.[8] His paper gives the theoretical justification of using the Kramers–Kronig transformations for optical constants. First applications can be found at the end of the 1950s.[9,10]

The method of Robinson and Price was generalized by Plaskett and Schatz in 1963 for reflection measurements through a transparent window; in addition, they introduced improvements to the Kramers–Kronig integral.[11] Roesseler derived improvements of the numerical analysis for better stability of the integral at finite integration intervals for normal incidence[12] and for oblique incidence.[13] The form of the Kramers–Kronig integral used in the present paper was given by Berreman in 1967.[14]

In 1972 Hensler showed that scattering effects on surfaces with spherical scatterers are independent of the state of polarization.[15] Stagg and Charalampopoluos[16] generalized this statement and showed that the ratio of reflectance in *s*- and *p*-polarization is not altered by scattering from spherical scatterers. This is a very important result for the measurement of reflectance ratios on pellets prepared from powders, which is an easily accessible technique in spectroscopy. Building on the results of Stagg et al.,[16] Yamamoto[17] developed a KKT method to derive the optical constants of a material from the reflectance ratio of the *s*- and *p*-polarized reflectance that is quite robust regarding grain size and surface roughness, as long as the scatterers are spherical.

In this paper we will analyze the possible shortcomings and measurement errors that can occur with Yamamoto's[17] approach. The analysis is done by comparison of model dielectric functions and simulated measurement data. Furthermore, an algorithm is given that can perform automated peak detection, extrapolation of the measurement data, and fitting of the resulting optical constants by a Lorentz oscillator model to obtain noise-free data needed for optical simulation.

THEORETICAL FOUNDATIONS

Reflection. The reflectivities of a single surface of an arbitrary material are given by the generalized Fresnel

0003-7028/10/6406-0669$2.00/0

equations for reflection:[18]

$$\hat{r}_s = \frac{n_0 \cos\theta_0 - \hat{n}_1 \cos\hat{\theta}_1}{n_0 \cos\theta_0 + \hat{n}_1 \cos\hat{\theta}_1} \tag{1a}$$

$$\hat{r}_p = \frac{\hat{n}_1 \cos\theta_0 - n_0 \cos\hat{\theta}_1}{\hat{n}_1 \cos\theta_0 + n_0 \cos\hat{\theta}_1} \tag{1b}$$

with the coefficients of reflection $\hat{r}$ (Fresnel coefficients), the refractive index of the surrounding medium n_0, the complex refractive index of the material $\hat{n}_1$, and the refraction angles θ or $\hat{\theta}$ for complex angles. The complex refractive index is defined by

$$\hat{n} = n + ik \tag{2}$$

The reflectance $R_{s/p}$, which is proportional to the reflected intensity, is given by the squared absolute values of the Fresnel coefficients. Therefore, the Fresnel coefficients can be written as

$$\hat{r}_s = \sqrt{R_s} e^{i\delta_s} \tag{3}$$

and

$$\hat{r}_p = \sqrt{R_p} e^{i\delta_p} \tag{4}$$

with the phase shifts in *s*- and *p*-orientation δ_s and δ_p. These phase shifts are defined in the interval $(-\pi < \delta_{s/p} < \pi)$ in the following. This relation gives the connection between the Fresnel coefficients and the measured data.

The ratio of the Fresnel coefficients is given by the fundamental equation of ellipsometry as[19,20]

$$\hat{\rho} = \frac{\hat{r}_p}{\hat{r}_s} = \sqrt{\frac{R_p}{R_s}} e^{i\delta_p - \delta_s} = \tan\Psi e^{i\Delta} \tag{5}$$

with the ellipsometric angles $\Psi = \arctan\left[\sqrt{(R_p/R_s)}\right]$ and $\Delta = \delta_p - \delta_s$.

Kramers–Kronig Relations. The Kramers–Kronig relations (KKR) are Hilbert transforms between the real and the imaginary part of an arbitrary causal function. A complex function is causal if and only if it is analytic in the upper half plane,[8] which is the prerequisite for the KKR to hold.

The Kramers–Kronig relations are given as[21]

$$\mathrm{Re}[\chi(\omega)] = \frac{2}{\pi} P \int_0^\infty \mathrm{d}\omega' \frac{\omega' \mathrm{Im}[\chi(\omega')]}{\omega'^2 - \omega^2} \tag{6}$$

$$\mathrm{Im}[\chi(\omega)] = -\frac{2\omega}{\pi} P \int_0^\infty \mathrm{d}\omega' \frac{\mathrm{Re}[\chi(\omega')]}{\omega'^2 - \omega^2} \tag{7}$$

with a susceptibility function χ, the frequency ω, and the principal value integral P.

The reflection ratio $\hat{\rho}$ Eq. 5 can be split into a real and an imaginary part by applying a logarithm:

$$\ln(\hat{\rho}) = \ln\left(\sqrt{\frac{R_p}{R_s}}\right) + i\Delta = \frac{1}{2} \ln\frac{R_p}{R_s} + i\Delta \tag{8}$$

The reflectance ratio R_p/R_s can be measured with standard spectroscopic techniques, and the phase factor Δ, which can only be measured experimentally by ellipsometry, can be determined by KKT. We substitute from frequency ω to wavenumbers $\nu = (\omega/2\pi c)$:

$$\mathrm{Im}[\ln\hat{\rho}] = \Delta_{\mathrm{kk}}(\nu) = -\frac{\nu}{\pi} P \int_0^\infty \mathrm{d}\nu' \frac{\ln\dfrac{R_p(\nu')}{R_s(\nu')}}{\nu'^2 - \nu^2} \tag{9}$$

This integral diverges at $\nu' = \nu$, which leads to well-known problems in solving principal value integrals numerically. This can be improved by introducing an additional constant in the numerator of the integrand.[14,22] The proof that such a factor does not alter the integral is given by Yamamoto.[17] This means that the enumerator of the integrand in Eq. 9 can be changed by an arbitrary constant without altering the integral. Choosing a factor $\ln[R_p(\nu')/R_s(\nu')]$, the integral can be written in a form without a singularity at $\nu = \nu'$ and the principal value integral becomes a standard Riemann integral:[22]

$$\Delta_{\mathrm{kk}}(\nu) = -\frac{\nu}{\pi} \int_0^\infty \mathrm{d}\nu' \frac{\ln\dfrac{R_p(\nu')}{R_s(\nu')} - \ln\dfrac{R_p(\nu)}{R_s(\nu)}}{\nu'^2 - \nu^2} \tag{10}$$

More importantly, this form minimizes errors due to finite integration intervals, as discussed more closely in the Extrapolation of the Reflectance Data subsection of the Uncertainty Analysis section below.

The calculation rule given by Eq. 10 only holds for external reflections at incidence angles above the Brewster angle θ_B. For every other case the phase shift must be corrected by an additional factor Δ_{corr}. According to Eq. 5, this factor is given as the difference of the two phase-correction factors in *s*- and *p*-polarization, $\Delta_{\mathrm{corr}} = \delta_{p,\mathrm{corr}} - \delta_{s,\mathrm{corr}}$. These two factors are given by Yamamoto.[23,24] The factor Δ for the different cases is given in Table I.

Calculating the Optical Constants. As known from ellipsometry,[17] the optical constants can be determined from the Fresnel equations (Eqs. 1a and 1b), and Snell's law ($n_0 \sin\theta_0 = \hat{n}_1 \sin\hat{\theta}_1$):[17]

$$\hat{n}_1(\nu) = n_0 \sin\theta_0 \left\{1 + \left[\frac{1 - \hat{\rho}(\nu)}{1 + \hat{\rho}(\nu)}\right]^2 \tan^2\theta_0\right\}^{1/2} \tag{11}$$

Taking into account the correction factor for the phase shift, it must be stated that it is important to choose incidence angles that are far away from the Brewster angle. The Brewster angle depends on the involved wavenumbers and therefore shifts at the position of optical oscillations. This causes shifts of the correction factor at the positions of optical oscillations and therefore the result can be wrong if the incidence angle is too close to the Brewster angle. This will be discussed in detail in the Angle of Incidence subsection of the Uncertainty Analysis section below.

UNCERTAINTY ANALYSIS

In the following, different experimental uncertainty influences will be discussed. Where feasible, they will be analyzed by optical simulation.

Some distinct statements can be given about influencing parameters. One of the influences is given by the quality of the polarization filter. This influence can be quantified by the

TABLE I. Phase correction factors for the different experimental conditions. n_0: refractive index of the surrounding (non-absorbing) medium, $\hat{n}_1$: complex refractive index of the sample, θ_0: incidence angle, θ_b: Brewster angle, θ_c: critical angle of total internal reflection. Adapted from Yamamoto.[17]

Condition	Δ_{corr}
$n_0 < \hat{n}_1$, $\theta_0 < \theta_b$	π
$n_0 < \hat{n}_1$, $\theta_b < \theta_0$	0
$n_0 > \hat{n}_1$, θ_0, $< \theta_b$	$-\pi$
$n_0 > \hat{n}_1$, $\theta_b < \theta_0 < \theta_c$	0
$n_0 > \hat{n}_1$, $\theta_c < \theta_0$	$2\left\{\arctan\left[\frac{n_0\left(\frac{n_0^2}{\hat{n}_2^1}\sin^2\theta_0 - 1\right)^{1/2}}{\hat{n}_1\cos\theta_0}\right] - \arctan\left[\frac{(n_0^2\sin^2\theta_0 - \hat{n}_1^2)^{1/2}}{n_0\cos\theta_0}\right]\right\}$

contrast ratio of the polarizer and will be discussed in the Measurements on Cellulose II and Xylane section below. Another influence is the angle of incidence, which affects the parameters in two different ways. First, a commercial reflection measurement unit focuses the beam onto the sample. Therefore, there is no distinct incidence angle but a range of incidence angles. This influence is more dominant at large incidence angles (oblique incidence) and is smaller at near normal incidence because the Fresnel coefficients have a smaller slope for small angles.

Yamamoto, therefore, states[17] that due to this reason a near normal incidence angle is the better choice for a good measurement. This statement, however, is overruled by a second influence, given by the incidence angle, because the difference between *s*- and *p*-polarized reflectance increases with the incidence angle and vanishes for normal incidence. Therefore, small incidence angles have the shortcoming of a small signal-to-noise ratio. This will be discussed closely in the Angle of Incidence subsection below.

More distinct statements can be made about the numerical behavior of the method. This can be achieved by simulating reflectance spectra from dielectric functions of fictitious model substances and subsequently obtaining the dielectric function or refractive index by KKT. The dielectric function $\hat{\varepsilon}(\nu)$ of a metallic or isolating material with multiple oscillators can be described by the Lorentz model:[25]

$$\hat{\varepsilon}(\nu) = \varepsilon_\infty - \sum_j \frac{4\pi\rho_j\nu_{0,j}^2}{\nu^2 + i\gamma_j\nu - \nu_{0,j}^2} \qquad (12)$$

with the dielectric constant for very high frequencies without absorption ε_∞, the oscillator strength ρ_j, the central frequency of the oscillators $\nu_{0,j}$, and the damping constant γ_j. The parameters chosen for the following analysis are listed in Table II.

TABLE II. Model parameters for a fictitious substance to test the experimental parameters.

ε_∞	j	$4\pi\rho_j$	$\nu_{0,j}$	γ_j
2.25				
	1	0.005	2400	20
	2	0.005	2410	30
	3	0.002	2415	45
	4	0.01	2420	30
	5	0.015	2425	20
	6	0.005	2460	32
	7	0.02	2600	35
	8	0.01	2120	30

The complex refractive index is given by $\hat{n} = \sqrt{\hat{\varepsilon}}$ for non-magnetic materials with $\mu = 0$. The refractive index, obtained by Eq. 12 with the parameters of Table II, is given in Fig. 1, where n is represented by the solid line and k is represented by the dash-dotted line.

Angle of Incidence. The influence of the angle of incidence on the quality of the data can be analyzed by simulating the reflectances of a fictitious substance for different incidence angles and subsequently re-obtaining the optical data by KKT. In the following, the simulated reflectances will be referred to as simulated experimental data in order to prevent confusion with the simulations based on the data obtained by KKT. Figure 2 represents the simulated reflectance and transmittance spectra of a single surface of the fictitious substance at different angles of incidence. The simulation was carried out by a transfer matrix algorithm described by Hansen[26] and generalized by Yamamoto and Ishida.[27] The black solid line in Fig. 2 represents the reflectances and transmittances for an incidence angle of 12° and the gray solid line represents the data for an incidence angle of 85°. The other lines represent intermediate angles.

The optical constants were subsequently obtained by KKT of the reflectance ratio of the data given in Fig. 2. They are

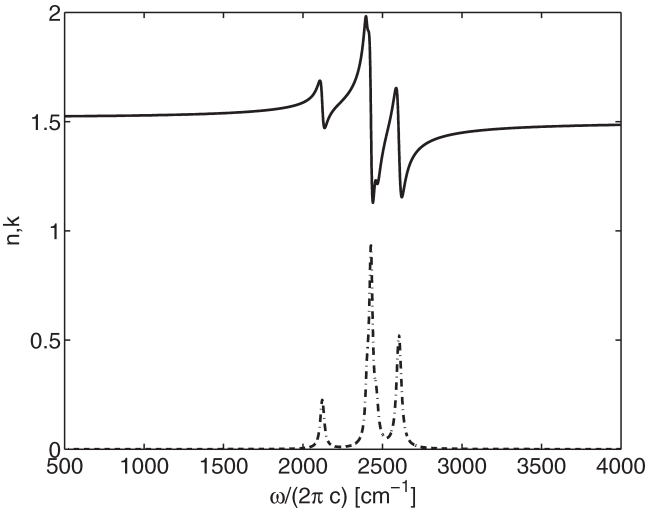

FIG. 1. Complex refractive index of a fictitious substance, calculated using Eq. 12. The corresponding oscillator parameters are given in Table II. Solid line (*n*), dash dotted line (*k*).

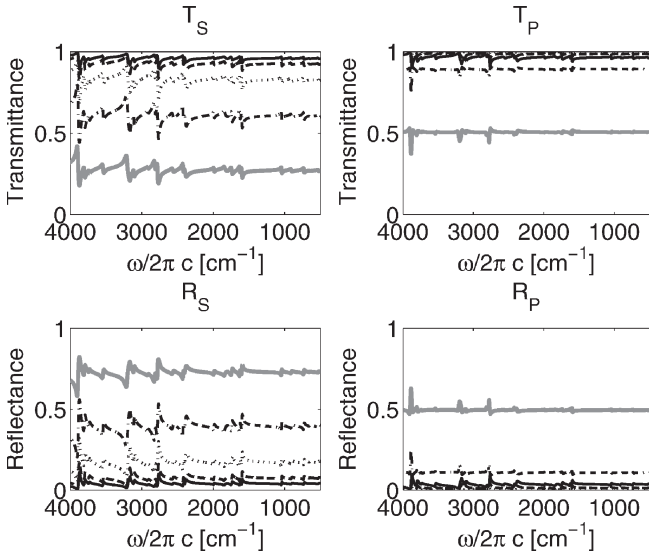

FIG. 2. (**Top**) Simulated transmittance and (**bottom**) reflectance for the fictitious substance given in Fig. 1 for (**left**) *s*- and (**right**) *p*-polarization, at different incidence angles. Black solid line: 12°, dashed line: 40°, dotted line: 60°, dash-dotted line: 75°, and gray solid line: 85°.

presented in Fig. 3, top panel, together with the deviation from the original model data (Fig. 3, bottom panel). The black solid line in Fig. 3 represents the optical constants for an incidence angle of 12° and the gray solid line represents the data for an incidence angle of 85°. The other lines represent intermediate angles. When looking at the differences between the original model data and the Kramers–Kronig obtained data it is immediately apparent that the greatest errors occur at the oscillator frequencies, where the Brewster angle of the material shifts due to changes in the refractive index. Another tendency that is visible in the bottom frame of Fig. 3 is to big errors for intermediate angles. The error becomes smaller farther away from the Brewster angle.

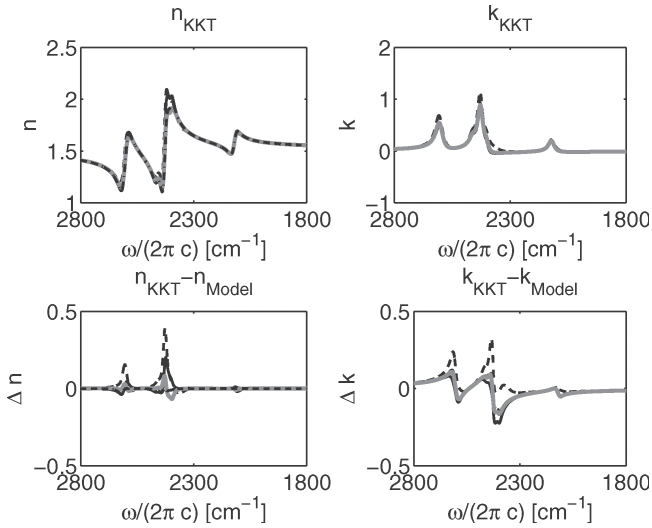

FIG. 3. (**Top**) Optical data obtained by KKT of the reflectance ratio from Fig. 2, and (**bottom**) difference between the calculated optical data and the original data given in Fig. 1. Black solid line: 12°, dashed line: 60°, dash-dotted line: 75°, and gray solid line: 85°.

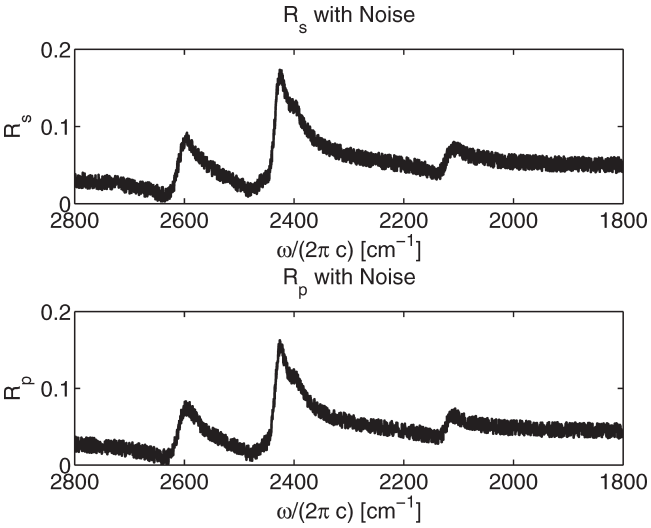

FIG. 4. Simulated reflectance of the fictitious substance from Fig. 1 with white noise for an incidence angle of 12°.

In the following, the influence of the incidence angle on the signal-to-noise ratio will be investigated. Therefore, a white noise of constant magnitude (1% of the maximum intensity of the spectrum with the greatest reflectance) is added to the simulated reflectance spectra. Subsequently, the optical constants are obtained by KKT.

For small angles (12°) the noisy spectra are given in Fig. 4, and the subsequently calculated optical constants are given in Fig. 5. The signal-to-noise ratio of the reflectance data is already problematic, as can clearly be seen in the obtained refractive indices in Fig. 5. After the KKT, most of the signal is lost and the amplitude of the noise is orders of magnitude bigger than the signal at some frequencies. Therefore, it can clearly be stated that the better choice is a large incidence angle.

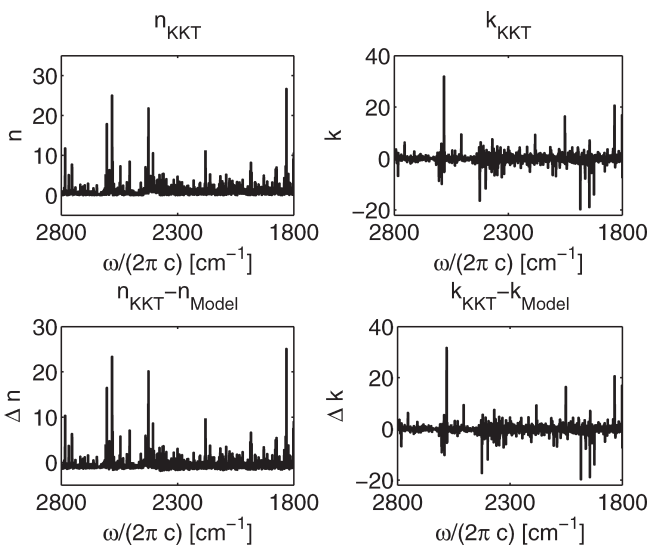

FIG. 5. (**Top**) Optical data obtained by KKT of noisy simulated reflectance data given in Fig. 4, and (**bottom**) difference between the calculated optical data and the original data given in Fig. 1, for an incidence angle of 12°.

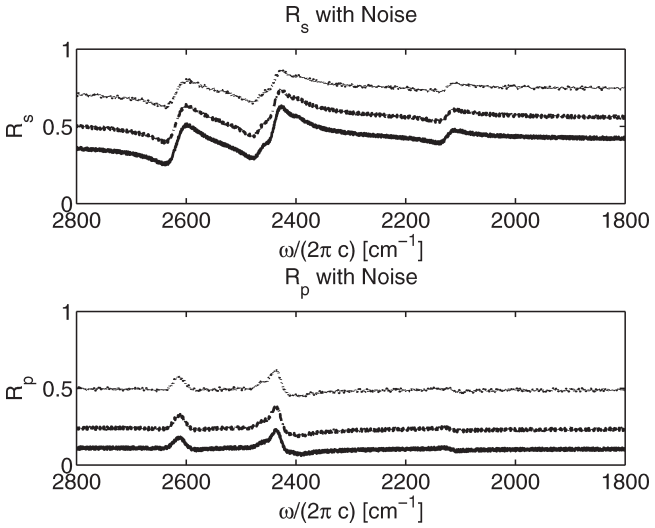

FIG. 6. Simulated reflectance of the fictitious substance from Fig. 1 with white noise for the angles 75° (solid line), 80° (dash-dotted line), and 85° (dotted line).

This situation is simulated in Fig. 6 for angles between 70° and 85°. Due to the higher reflectance and the bigger difference between *s*- and *p*-polarization, the signal-to-noise ratio is much bigger than at small angles. The optical constants obtained from this data are presented in Fig. 7. The signal-to-noise ratio of the data improves with the angle of incidence. While for 75° (solid line) the signal-to-noise ratio is still problematic, it becomes very good at 85° (dotted line). For further improvement of the quality, the data can be fitted with Eq. 12 as a model function in order to obtain noise free data, necessary for numerical simulation of spectra.

Extrapolation of the Reflectance Data. Kramers–Kronig transformation is a mathematically exact method. However, the integration must be carried out over all frequencies from 0 to ∞,

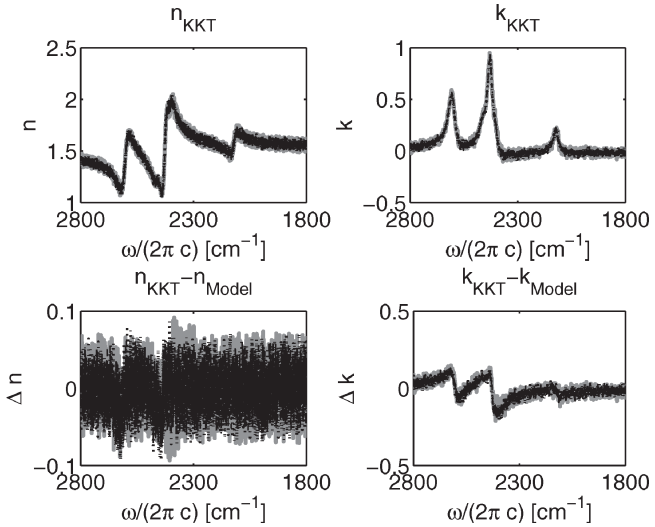

FIG. 7. (**Top**) Optical data obtained by KKT of noisy simulated reflectance data given in Fig. 6, and (**bottom**) difference between the calculated optical data and the original data given in Fig. 1 (bottom), for the angles 75° (solid line), 80° (dashed line), and 85° (dash-dotted line).

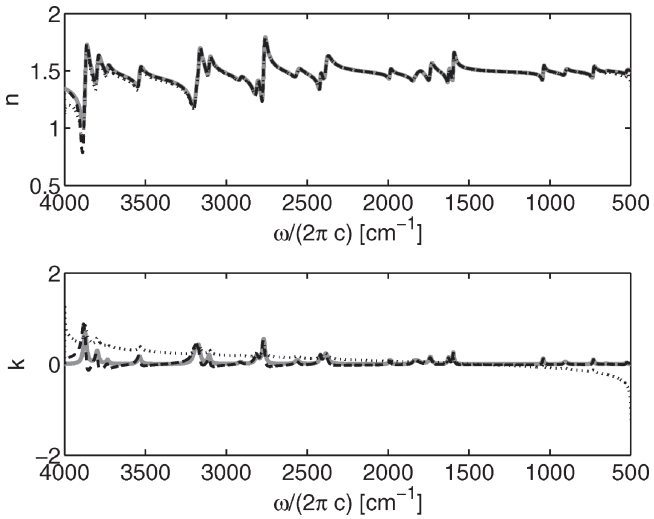

FIG. 8. Randomly generated optical model data (gray solid line) and corresponding calculated data by KKT of simulated reflectance at 82° incidence, for the Kramers–Kronig integral by Berreman,[14] given in Eq. 10 (dashed line) and by Lucarini et al.[21] given in Eq. 7 (dotted line).

according to Eq. 10. This, of course, is not feasible in experiment. Therefore, the integration will always be carried out over a finite interval, and, therefore, will cause numerical errors. The integral that is calculated at KKT is of the following form:

$$\Delta_{kk}(\nu) = -\frac{\nu}{\pi}\int_{\nu_{min}}^{\nu_{max}} d\nu' \frac{\ln\dfrac{R_p(\nu')}{R_s(\nu')} - \ln\dfrac{R_p(\nu)}{R_s(\nu)}}{\nu'^2-\nu^2} \qquad (13)$$

with the lower and the upper boundary of the measurement region ν_{min} and ν_{max}. Figure 8 presents a randomly generated refractive index, together with the refractive indices that were obtained by KKT of simulated reflectance data using two different integrals (the corresponding oscillator parameters are presented in Table III). The gray solid line represents the original model function, the dotted line represents the optical data obtained by KKT with the integral according to Lucarini,[21] and the dashed line represents the data obtained by KKT with the integral according to Berreman.[14] Here the difference between the standard Kramers–Kronig integral given in Eq. 7 and the integral introduced by Berreman in Eq. 10 becomes obvious.

It is clearly observable, that the error is bigger in the imaginary part for both integrals (Fig. 8, bottom frame) and that the integral of the form of Eq. 10 yields better results, especially at the margins of the data. Also, it can be observed that the errors are bigger at the high frequency limit. Still, the results obtained using the integral according to Berreman are erroneous and have to be improved by proper extrapolation of the data.

A simple approach to extrapolate reflectivity data is given by Jerzierski.[28] His extrapolation strategy presumes an ω^{-4}-proportionality of the intensity at the margins of reflectance peaks towards infinity. This extrapolation can be done by least squares fitting of the margins of the measured data. For the small frequency limit, a ω^4-proportionality towards 0 is

TABLE III. Randomly generated model parameters for a fictitious substance to test the extrapolation and the peak detection algorithm.

ε_∞	j	$4\pi\rho_j$	$\nu_{0,j}$	γ_j
2.10				
	1	0.0018	1806.4	33.1765
	2	0.0018	1988.2	13.9206
	3	0.0040	3181.9	28.4090
	4	0.0054	3868.2	19.1795
	5	0.0031	2561.5	32.4847
	6	0.0012	2912.5	27.7026
	7	0.0042	2383.0	29.9929
	8	0.0011	652.9	17.7965
	9	0.0035	527.0	18.5305
	10	0.0024	2418.6	12.9885
	11	0.0057	2770.0	16.9797
	12	0.0042	2810.4	24.3822
	13	0.0040	1041.4	10.9460
	14	0.0034	3536.7	23.3587
	15	0.0059	2764.5	17.8009
	16	0.0050	3190.5	36.0441
	17	0.0056	3168.2	19.9137
	18	0.0055	730.8	13.4823
	19	0.0048	3871.2	24.8922
	20	0.0051	3797.1	22.5772
	21	0.0035	3105.7	18.6952
	22	0.0029	1825.2	31.0976
	23	0.0011	1840.3	18.6127
	24	0.0042	905.0	22.9582
	25	0.0013	3733.6	18.5538
	26	0.0059	2384.7	37.4826
	27	0.0012	3875.3	18.0098
	28	0.0057	1596.3	11.5089
	29	0.0059	1738.5	21.6886
	30	0.0035	1625.5	13.7845

assumed. The only prerequisite for these nonlinear fits are estimates of the parameters of the two outermost peaks. This problem will be discussed in the Peak Detection subsection of the Nonlinear Fitting of Optical Data for Noise Suppression and Error Detection section below.

The model function for the extrapolation is given by

$$f(\nu) = a(\nu - \nu_0)^{-4} + f_0 \tag{14}$$

with the central wavenumber of the outermost peak ν_0, the wavenumber ν, the value of the reflectance function at infinity or at zero f_0, and the parameter a, which controls the slope.

An extrapolation of simulated reflectance ratio data is presented in Fig. 9, which was carried out by a nonlinear fit. The initial values for the fitting routine, as well as parameters for a robust estimation, are given by simple considerations. The central wavenumber ν_0 can be estimated from the shape of the peak (this is discussed in the Peak Detection subsection of the Nonlinear Fitting of Optical Data for Noise Suppression and Error Detection section below). For the other two parameters, the following equations are easily derived:

$$a = \frac{df(\nu)}{d\nu} \cdot \frac{(\nu - \nu_0)^5}{4} \tag{15a}$$

$$f_0 = f(\nu) - a(\nu - \nu_0)^{-4} \tag{15b}$$

The parameters for the fitting routine can therefore be estimated from Eqs. 15a and 15b. The shortcoming of this estimate is that the first derivative of the data is not robust

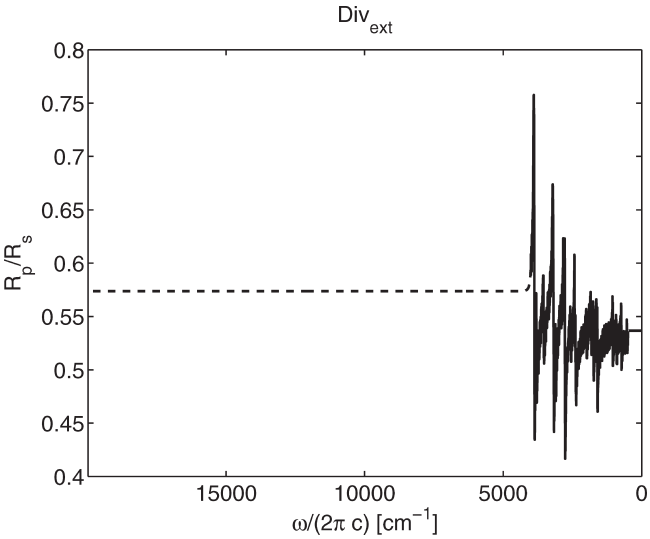

FIG. 9. Extrapolation (dashed line) of the reflectance ratio data (solid line) by nonlinear fitting.

towards noise. If the fit is not usable for this reason, a robust estimate of the values is given by the assumption that $f(\nu)$ can be estimated by the mean value of the reflectance ratio for the cases $\nu \to \infty$ and $\nu \to 0$. Thus, we obtain

$$f_0 \approx \overline{\rho} + \frac{a}{\nu_0^4} \tag{16}$$

This results in

$$a = [f(\nu) - \overline{\rho}] \cdot \frac{\nu_0^4}{1 + \dfrac{\nu_0^4}{(\nu - \nu_0)^4}} \tag{17}$$

for an estimate of the parameter a.

The detection of errors from false extrapolation remains difficult. Erroneous optical data is not easily recognized using a simulation of the experiment with KKT obtained data (see the Checking the Fit Parameters by Simulation of the Measurement Data subsection of the Nonlinear Fitting of Optical Data for Noise Suppression and Error Detection section below). In many cases, the errors become big when simulating multilayered systems with the obtained data. In these cases, wrong absorption data can lead to wrong resonant behavior of the multilayered systems (see the same subsection referenced above).

Figure 10 shows the already used randomly generated optical data (Table III) together with optical data obtained by KKT of simulated reflectance data, with different extrapolation ranges. It can be stated, that extrapolation improves the situation a lot in the imaginary part of the dielectric function. An optimum is reached at an extrapolation range of ten times the original data range (black dashed line in Fig. 10). With further extrapolation, the result becomes worse due to extrapolation errors.

This problem could be improved by using an independently measured value for ε_∞ to obtain the parameter f_0.

NONLINEAR FITTING OF OPTICAL DATA FOR NOISE SUPPRESSION AND ERROR DETECTION

Simulating optical spectra on the basis of measured optical constants can be very problematic if the optical constants used are noisy. Therefore, noise-free optical data are needed as input parameters for simulation. This can be achieved by fitting the obtained measured data with the Lorentz oscillator model. The fitting also carries the advantage of the possibility of checking the obtained fit parameters on their physical consistency. The parameters for the standard Lorentz oscillators have to be real values, which gives a good indicator for the quality of the data. Numerical errors of the KKT cause distortions of the peaks (see Fig. 10), and these distortions often yield complex values for the fit parameters (see the Fit subsection below).

The general model function for the fitting routine is given in Eq. 12. To carry out a fit, knowledge of the number of oscillators and their positions is necessary, as well as a good estimate of the remaining parameters.

For the complex spectra of biomacromolecules such as cellulose, this is a tedious task if carried out manually. In the following, an automated routine will be described that can detect the oscillators and the needed initial values from measured data.

Noise Reduction by Apodization. A first prerequisite for automated peak detection of experimental data is the suppression of noise. This noise reduction needs to conserve the shape of the peaks in a qualitative way. The noise-reduced spectrum is only needed to estimate initial values for a fitting routine; therefore, it is not necessary to keep the size and the quantitative behavior of the peaks unaltered.

The dielectric function has turned out to be the most useful representation of the data for peak detection. This is the best representation of the experimental data also with respect to the fitting routine, because on the one hand there is a simple model function available that is based on a physical model (Lorentz model), and on the other hand they are the data in which we are interested.

Therefore, the first step in peak detection is a preliminary KKT of the raw experimental data to obtain the dielectric function. A widely used method for noise reduction is the technique of apodization. The spectral data is Fourier transformed and multiplied with an apodization function, which serves as a weight. Subsequently, the data is transformed back to the frequency space by inverse Fourier transform. The apodization function can be shaped such that it strongly suppresses the high frequency components of the data. Depending on the resolution of the data, the function has to be tuned to yield optimal results.

Usually spectral data are apodized with a triangular function. This ensures that the peak shapes are not altered too much. In our case this is not a matter of concern; the effective reduction of noise is more important. The function

$$f(x) = \cos^{2k}\left(\frac{2\pi x}{n}\right) \tag{18}$$

with n the number of data points, x the coordinate in position space, and k the exponent, which controls the slope of the function and the width of the bandpass, has proven to be very useful for this matter. By adjusting the parameter k, the apodization can be tuned in sensitivity. A higher k yields a narrower apodization and therefore a cutoff at lower frequencies. Figure 11 shows the normalized Fourier transform of the dielectric function given in Fig. 10 and the apodization function given by Eq. 18 with the parameter $k = 60$.

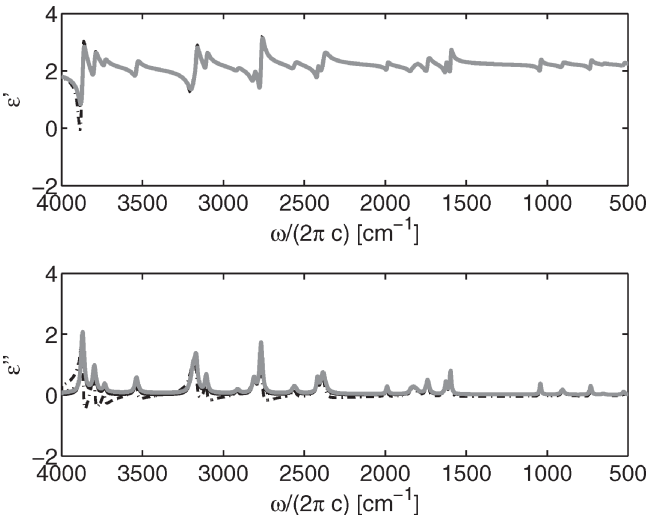

FIG. 10. Randomly generated optical model data given in Fig. 8, and optical data obtained by KKT of the simulated reflectance data given in Fig. 9 for different extrapolation regions. Model data: black solid line; KKT without extrapolation: black dash-dotted line; extrapolation: 3 times: black dotted line, 10 times: black dashed line, and 40 times: gray solid line.

An estimate for the width of the bandpass given by the apodization can be obtained from the inflection points of the apodization function (represented by the crosses in Fig. 11), which are a good estimation for the full width at half-maximum:

$$x_0 = \pm\frac{n}{2\pi}\arctan\left[\left(\frac{1}{2k-1}\right)^{1/2}\right] \tag{19}$$

The behavior of the positive inflection point x_0 as a function of k is given in Fig. 12. The graph can be interpreted as the bandwidth of the filter as a function of the exponent k.

The effect of the apodization is presented in Fig. 13. The dielectric model function is depicted as a solid line, together with the raw noisy data as the dash-dotted line. The noise-reduced data (gray solid line in Fig. 13) clearly has an altered shape, baseline, and smaller peaks, but it is also effectively noise reduced and good enough for a peak detection.

Peak Detection. The peak detection is a multi-step procedure. The first step is the detection of regions that are likely to contain peaks (see Fig. 14, gray dots). These regions can contain one or more peaks and are more closely analyzed in a subsequent step. The regions are detected by a comparison of the real and the imaginary part of the first derivative of the dielectric function. This is motivated by the fact that the dielectric function contains an inflection point at an oscillator in its real part and a maximum in the imaginary part. Therefore, we define the difference between the real part and the imaginary part of the first derivative of the dielectric function as

$$\xi = \mathrm{Im}\left[\frac{\mathrm{d}\hat{\varepsilon}(\nu)}{\mathrm{d}\nu}\right] - \mathrm{Re}\left[\frac{\mathrm{d}\hat{\varepsilon}(\nu)}{\mathrm{d}\nu}\right] \tag{20}$$

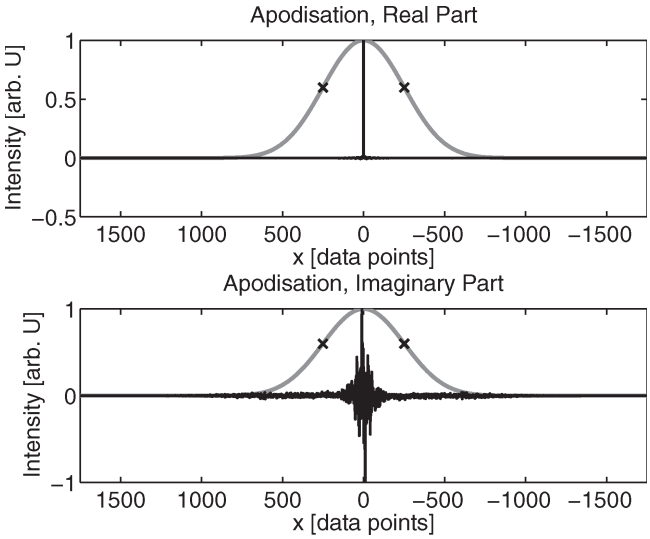

FIG. 11. Fourier transform of the dielectric model function (black solid line) and the apodization function used to suppress noise (gray solid line). The Inflection points x_0 at both sides of the peak, which are used as an estimate for the bandwidth of the apodization filter, are indicated by crosses (×).

The algorithm is searching for the set of wavenumbers ν_{Range} where the parameter ξ is greater than a parameter m:

$$\nu_{\mathrm{Range}} = \nu(\xi > m) \tag{21}$$

The parameter m is set to a default value and has to be adjusted to the actual data by the user in order to yield good results.

In a subsequent step the detected regions with a width smaller than the minimal width b_{min} are discarded. This parameter also has to be adjusted by user interaction. The remaining regions are now analyzed for peaks by finding the roots of the second derivative of the imaginary part of the dielectric function, thus by the inflection points (circles and crosses in Fig. 14). Inflection points with descending curvature

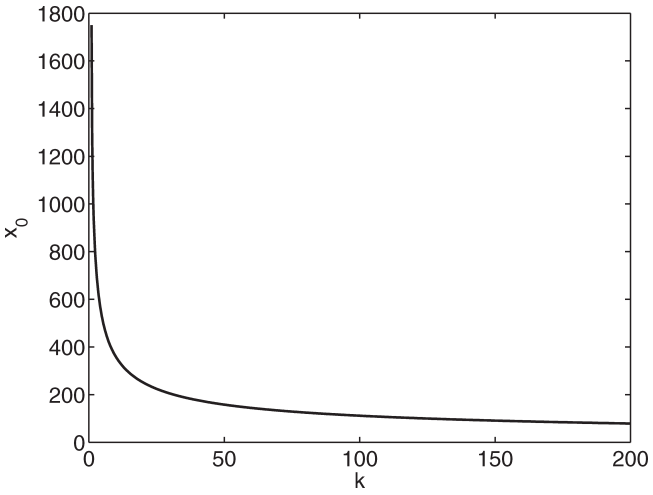

FIG. 12. Behavior of the inflection points x_0 ($\approx$ bandwidth) of the apodization function given in Eq. 18 with respect to the exponent k. Signal within the interval defined by the inflection points is merely altered.

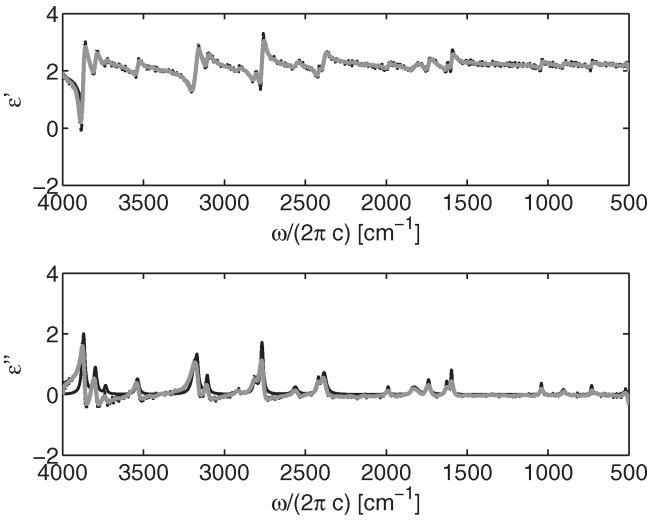

FIG. 13. Noise reduction algorithm. Black solid line: model data; dash-dotted line: data obtained by KKT of noisy reflectance data; gray solid line: noise-reduced KKT data by application of the apodization in Eq. 18 with an exponent of $k = 60$.

(circles in Fig. 14) are discarded.

$$\text{Peak at } \nu \text{ if: } \frac{\mathrm{d}^2\varepsilon''(\nu)}{\mathrm{d}\nu^2} = 0 \wedge \frac{\mathrm{d}^3\varepsilon''(\nu)}{\mathrm{d}\nu^3} < 0 \tag{22}$$

The number of points detected by this procedure yields the number of oscillators in the analyzed region. The wavenumbers ν_0 that are found by the local maximum of the imaginary part of the dielectric function $\varepsilon''(\nu)$ serve as initial values of the central wavenumbers of the oscillators (see Fig. 14, black stars).

After this three-step procedure, the user can interact, by setting all the relevant parameters (apodization k, sensitivity m,

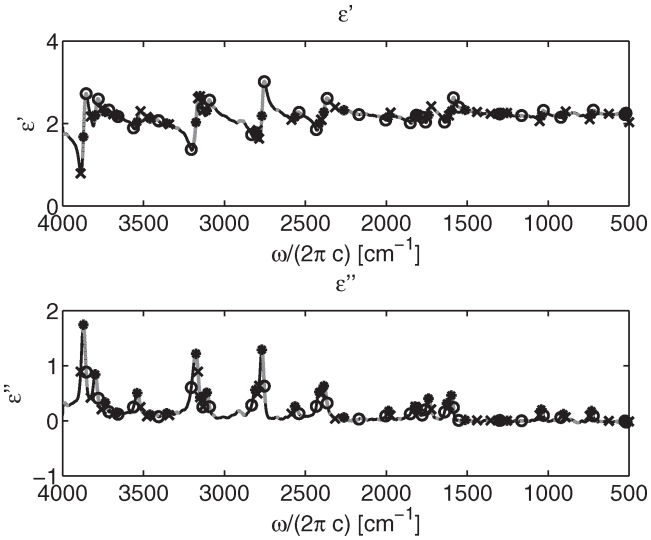

FIG. 14. Peaks, detected by the algorithm from the KKT of simulated reflectance data from Fig. 10. Peak positions are indicated by black stars, estimates for the full width at half-maximum are indicated by crosses (lower wavenumber than oscillator) or circles (higher wavenumber than oscillator), and detected regions (ν_{Range}) are indicated by gray dots.

and minimal width $b_{\min}$). If peaks are missed by the algorithm, they can be added manually by user interaction.

The detected parameters can now be used for the extrapolation of the measured reflectance data and for the initial values of the fitting routine because the number of oscillators and their positions are known.

Initial Values. In the following, an effective method to estimate initial values for a nonlinear fit with a Lorentz oscillator model will be presented. Finding good estimates for initial conditions of fits is often problematic. Poorly estimated initial conditions lead to long iteration times and bad or false convergence. Particularly, model functions consisting of many parameters ($3n + 1$ parameters for n oscillators) need good initial conditions because the iteration needs a lot of computing power.

According to Eq. 12 the model function needs one global parameter (ε_∞) and another set of three parameters for each peak (ρ_j, γ_j, and $\nu_{0,j}$). The initial value of ε_∞ is chosen as the value of the dielectric function at maximum wavenumber. The initial values for the central frequencies ($\nu_{0,j}$) are given by the peak detection routine as the maxima of the imaginary part of the dielectric function (stars in Fig. 14).

The estimation of initial conditions for the oscillator strength ρ_j and the damping γ_j is more complicated for this purpose. It is useful to analyze each peak in a one oscillator approximation:

$$\varepsilon(\nu) = \varepsilon_\infty - \sum_j \frac{4\pi\rho_j\nu_{0,j}}{\nu^2 - i\gamma_j\nu - \nu_{0,j}^2} \approx \varepsilon_\infty - \frac{4\pi\rho_k\nu_{0,k}}{\nu^2 - i\gamma_k\nu - \nu_{0,k}^2} \tag{23}$$

Splitting this therm into a real and an imaginary part yields two equations:

$$\varepsilon_\infty - \varepsilon'(\nu) = \frac{4\pi\rho_k\nu_{0,k}^2(\nu^2 - \nu_{0,k}^2)}{(\nu^2 - \nu_{0,k}^2) + \gamma_k^2\nu^2} \tag{24}$$

$$\varepsilon''(\nu) = -\frac{4\pi\rho_k\nu_{0,k}^2\nu\gamma_k}{(\nu^2 - \nu_{0,k}^2) + \gamma_k^2\nu^2} \tag{25}$$

The second equation (Eq. 25, imaginary part of the dielectric function) gives at $\nu = \nu_{0,k}$:

$$\rho_k = -\frac{\gamma_k}{4\pi\nu_{0,k}}[\varepsilon''(\nu_{0,k})] \tag{26}$$

Together with Eq. 24 this yields

$$\gamma_k = \frac{\Delta}{2}\nu_{0,k}\alpha \pm \left(\frac{\Delta^2}{4}\nu_{0,k}^2\alpha^2 + \alpha\right)^{1/2} \tag{27}$$

with

$$\Delta =: -\frac{\varepsilon''(\nu_{0,k})}{\varepsilon_\infty - \varepsilon'(\nu_{0,k})} \tag{28a}$$

$$\alpha =: 1 - \frac{\nu_{0,k}^2}{\nu^2} \tag{28b}$$

The remaining problem is the choice of ν for the estimation of γ_k. The central frequency of the peak $\nu_{0,k}$ cannot be used. Firstly, the use of $\nu_{0,k}$ is not physically meaningful because the damping and the oscillator strength are more correlated to the full width at half-maximum, and secondly $\nu = \nu_{0,k}$ yields $\alpha = 0$ and thus $\gamma_k = 0\ \forall\ k$. The wavenumber at the points of full width at half-maximum is a good choice, but at peaks that are close to each other (or even worse at shoulders) this is not feasible. It has turned out to be useful in practice to choose $\gamma_k = 20\ \forall\ k$. With these initial values of γ_k the initial values of ρ_k can be calculated by Eq. 26.

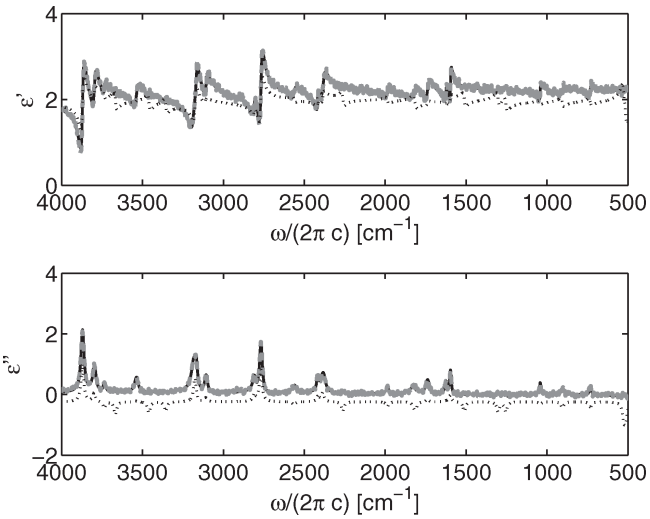

FIG. 15. Initial conditions of the fitting routine. Gray solid line: dielectric model function given in Table III; dashed line: data obtained by KKT of noisy simulated reflectance data (i.e., simulated measurement data); dotted line: generated model function with initial parameters before the optimization by a least square routine.

Figure 15 presents the initial condition of the fitting routine. The dielectric model function is represented by the gray solid line, while the dielectric function, determined by KKT from the simulated reflectance data, is represented by the black dashed line, and the initial conditions of the fitting model function are given by the dotted line. The estimated initial conditions resemble the original function quite well.

Fit. With the obtained initial values and the model function a nonlinear, least squares fit can be performed without any further prerequisites. There are two possibilities for the model function. The fit can be performed with the complex function or only on the real or the imaginary part. This is feasible because the real and imaginary parts are dependent on each other. They are determined by KKT and therefore contain mostly redundant information. The determination of which possibility is the best choice depends on the experimental data used. For the fitting of only one of the parts of the function, the Lorentz model function has to be separated into the real and imaginary part:

$$\hat{\varepsilon}(\nu) = \varepsilon_\infty - \sum_j \frac{4\pi\rho_j\nu_{0,j}^2}{\nu^2 - i\gamma_j\nu - \nu_{0,j}^2} \tag{29a}$$

$$\varepsilon'(\nu) = \varepsilon_\infty - \sum_j \frac{4\pi\rho_j\nu_{0,j}^2(\nu^2 - \nu_{0,j}^2)}{(\nu^2 - \nu_{0,j}^2)^2 + \gamma_j\nu^2} \tag{29b}$$

$$\varepsilon''(\nu) = -\sum_j \frac{4\pi\rho_j\nu_{0,j}^2\gamma_j\nu}{(\nu^2 - \nu_{0,j}^2)^2 + \gamma_j\nu^2} \tag{29c}$$

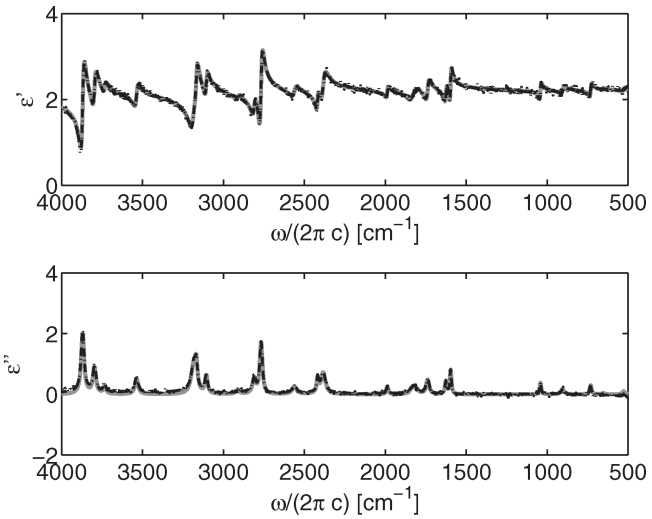

FIG. 16. Least squares fit of the dielectric function (dashed line) in comparison to the simulated noisy experimental data (dotted line) and the original model data (gray solid line).

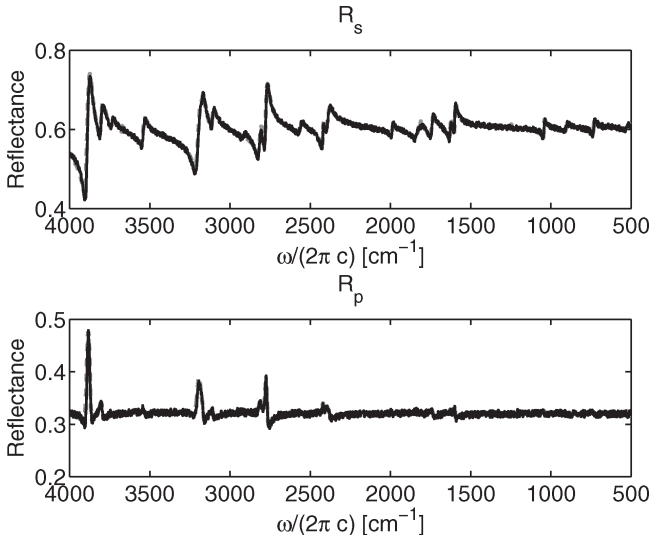

FIG. 17. Simulated noisy measurement data (black solid line) and simulated measurement with the optical data given in Fig. 16, obtained by the fitting routine (gray dotted line).

The result of the fitting of the previously described dielectric function is presented in Fig. 16. The fit was carried out with the Levenberg–Marquardt algorithm. A close look at the data shows that the fit nicely resembles the dielectric function in the real part. The two curves in the real part (gray solid line: model function; black dashed line: fit) look almost identical. The picture is similar for the imaginary part, but in the high frequency limit the fit has a constant shift towards higher values. This is a numerical error from the KKT, caused by erroneous extrapolation of the data.

One criterion that can distinguish such numerical errors is the fact that the imaginary part of the dielectric function has to be positive definite. With poorly extrapolated data, sometimes the imaginary part of the dielectric function has points below zero. This of course is unphysical, and it can be overcome by optimizing the extrapolation range and method.

Another criterion for the overall quality of the obtained dielectric function is given by the resulting fit parameters. By definition, these parameters are all positive and real. If the shapes of the peaks are altered by some reason (this can be caused by incorrect extrapolation, by measurement errors, or by incorrect peak detection), the optimized fit parameters will have a non-zero imaginary part.

This can be quantitatively evaluated for each fit. We introduce the parameter

$$\zeta = \left| \frac{\sum_i \mathrm{Im}(p_i)}{\sum_i \mathrm{Re}(p_i)} \right| = |\tan\bar{\phi}| \tag{30}$$

with the mean phase angle of the parameters in the complex plane $\bar{\phi}$ and with the parameters p_i, defined as:

$$p_1 = \varepsilon_\infty \tag{31a}$$

$$p_{3i-1} = \rho_i \tag{31b}$$

$$p_{3i} = \nu_{0,i} \tag{31c}$$

$$p_{3i+1} = \gamma_i \tag{31d}$$

This parameter ζ is a very useful quality criterion for the fitting routine and the KKT. If the fit is well behaved, ζ will be very small, while if ζ is greater than 0.1, the fits were found not to be applicable.

The fit in Fig. 16 yields a ζ of 0.0235, thus indicating an acceptable fit quality, which can be confirmed by comparing the result of the fit in Fig. 16 with the original model dielectric function. The solid line represents the original model data, the dotted line represents the simulated experimental data, and the dashed line represents the fit.

Checking the Fit Parameters by Simulation of the Measurement Data. In addition to the test of the fit parameters concerning physical consistency, the resulting dielectric function can be checked for consistency with measured data. This is done by simulating the measured reflectance spectrum with the obtained dielectric function. Unfortunately, this approach is not very sensitive: poorly fitted dielectric functions yield quite good results for single interface systems. This is presented in Fig. 17. The deviation of the imaginary part of the dielectric function in the limit of high frequencies is only barely visible. The simulated reflectance (dotted line in Fig. 17) almost perfectly resembles the measured data (solid line in Fig. 17).

The fact that such deviations do not lead to errors in simulating the single interface system does not imply that these deviations are negligible. These deviations do play an important role in the simulation of multilayered systems because in these systems interference effects occur, and thus the light passes through the medium many times, adding up the error. Particularly, deviations in the imaginary part cause problems in such cases, because the absorbance of the media is a false estimate. On one hand, if the imaginary part becomes negative at some points, the intensity at these points will be highly exaggerated, because a negative imaginary part of the dielectric function implies the unphysical behavior of negative absorbance. If it is overestimated on the other hand, the intensities will be underestimated.

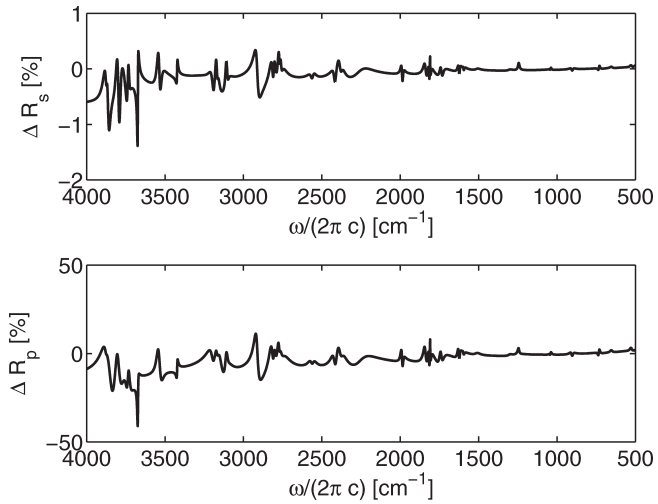

FIG. 18. Testing the dielectric function obtained by the fitting routine on a multilayer system (model substance on a silicon wafer). Difference between the reflectance spectra simulated with the original model dielectric function and with the dielectric function obtained by the fitting routine. (**Top**) *s*-polarization, (**bottom**) *p*-polarization. Thickness of the model layer: 300 nm.

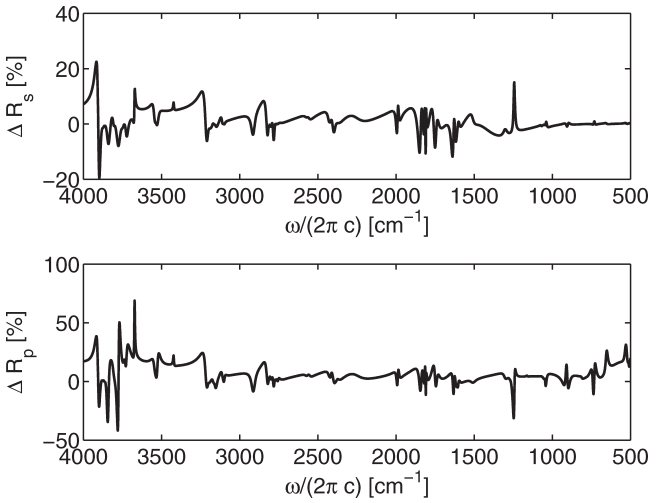

FIG. 19. Testing the dielectric function obtained by the fitting routine on a multilayer system (model substance on a silicon wafer). Difference between the reflectance spectra simulated with the original model dielectric function and with the dielectric function obtained by the fitting routine. (**Top**) *s*-polarization, (**bottom**) *p*-polarization. Thickness of the model layer: 1.5 μm.

This is shown in Fig. 18. A multilayer system consisting of a thin film of the fictitious material with a thickness of 300 nm on a silicon substrate with a 3 nm oxide layer is simulated. For the optical constants of SiO_2 and Si, literature data was used.[29] The system is calculated with the original model dielectric function and again with the fitted dielectric function. The ratio of the two is shown in Fig. 18. As expected, the highest deviations (up to $\pm 1.5\%$ in *s*-polarization and—due to the much smaller reflectance in *p*-polarization—up to $\pm 20\%$ at some points in *p*-polarization where the reflectance is close to zero) occur in the high frequency limit. The picture becomes even worse when the layer thickness is increased to 1.5 μm. The result of this calculation is presented in Fig. 19. The deviations occur at similar wavenumbers as for the thinner layer, but in this case the deviations go up to $\pm 20\%$ for *s*-polarization and $\pm 75\%$ for *p*-polarization. It must be stated that these very high deviations only occur at wavenumbers where the reflectivity is close to zero; considering this, the absolute value of the deviations is not as devastating as in the relative picture. This can be shown by analyzing the median deviation,

$$\Delta_\mu R_{s/p} = \mu_{(1/2)}(|\Delta R_{s/p}|) \tag{32}$$

with the median $\mu_{(1/2)}$. This gives a median deviation for the 300 nm layer system of $\Delta_\mu R_s = 0.06\%$ and $\Delta_\mu R_p = 2.5\%$. For the thicker layer of 1.5 μm we get $\Delta_\mu R_s = 2.0\%$ and $\Delta_\mu R_p = 8.3\%$.

The fact that the errors occur at the high frequency limit implies that the extrapolation before the KKT did not give correct results. This can be improved by better estimation values for ε_∞ or by an independent measurement of ε in a high frequency transparent region.

MEASUREMENTS ON CELLULOSE II AND XYLANE

The experiments were carried out on a Bruker ifs 66v/s vacuum Fourier Transform Infrared (FT-IR) Spectrometer with a Bruker A 513 variable angle specular reflection accessory. For a constant background in the *s*- and *p*-directions, a two polarizer method[30] was chosen, where the first polarizer is set to a polarization angle of 45° between the *s*- and *p*-directions. To get rid of time-dependent drifts of the spectrometer (especially in the region of water absorption), the measurement was carried out with an automatization macro that switches the angle of the second polarizer between the *s*- and *p*-direction repeatedly and yields the averaged *s*- and *p*-spectra.[30] For a single measurement, 200 scans were recorded at a mirror velocity of 100 kHz. The measurements were repeated 80 times and the resulting mean spectra were used as reflectance data. An incidence angle of 82° was chosen at a circular aperture of 5 mm.

As the first polarizer, a substrate-free P03 gold wire grid polarizer from Infraspecs (Infraspecs, Filderstadt, Germany) was used. The second polarizer was a Bruker Wire Grid Polarizer on a KRS-5 substrate in a motorized unit (Bruker A 121).

The cellulose II sample was prepared from Lenzing Tencel powder with an average grain size of 7 μm, and the xylane sample was prepared from xylane powder with a narrow molecular weight range from Lenzing (Lenzing AG, Lenzing, Austria). A pellet of the materials was prepared from 1 g of pure powder. These samples have a thickness of approximately 6 mm, which is sufficiently thick to exclude any reflections from the back surface.

Great care must be taken in sample mounting. Any reflection from the sample mount that reaches the detector will alter the result dramatically. It is especially important to avoid reflections at structured rough surfaces, because these can cause depolarization that is anisotropic in polarization angle, therefore giving rise to a strong error in the ratio of reflectance. This will cause baseline slopes, due to the dependence of scattering on the wavelength. If such an error occurs, the data cannot be used for KKT. On one hand, it yields incorrect results, while on the other hand, the peak detection algorithm

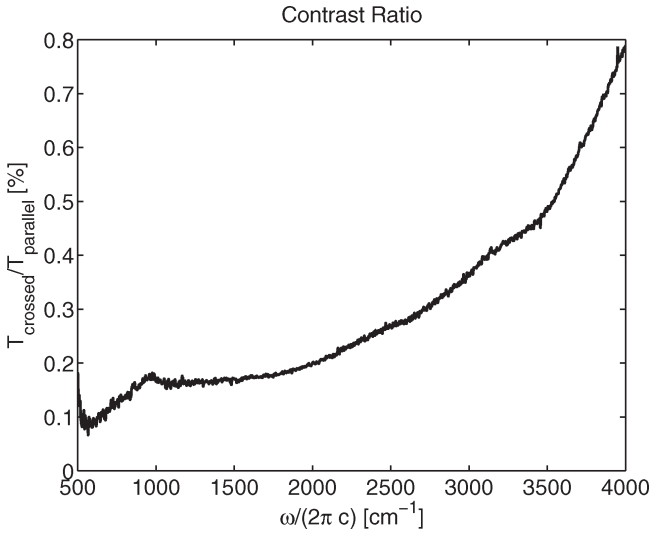

FIG. 20. Contrast ratio of the two used polarizers.

will fail (the slope of the baseline will be interpreted as many closely positioned peaks).

Another source of error is given by the polarizing filters. The contrast ratio of a wire grid polarizer depends on the wavelength, and therefore the polarizers also introduce a slightly ascending baseline. The contrast ratio is given by

$$k = \frac{T_s}{T_p} \tag{33}$$

with T_s and T_p the transmission through the two polarizers for normal or parallel adjustment, respectively. For the two polarizers used, the contrast ratio is presented in Fig. 20.

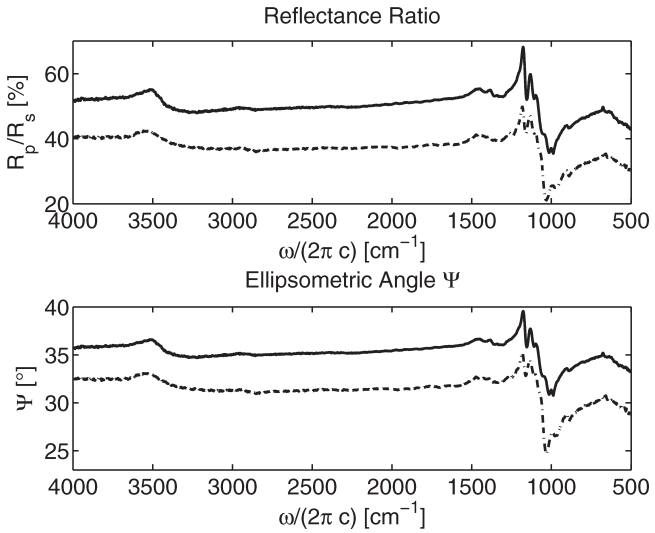

FIG. 21. (**Top**) Reflectance ratio R_s/R_p, and (**bottom**) ellipsometric angle Ψ, for cellulose II (solid line) and xylane (dashed line).

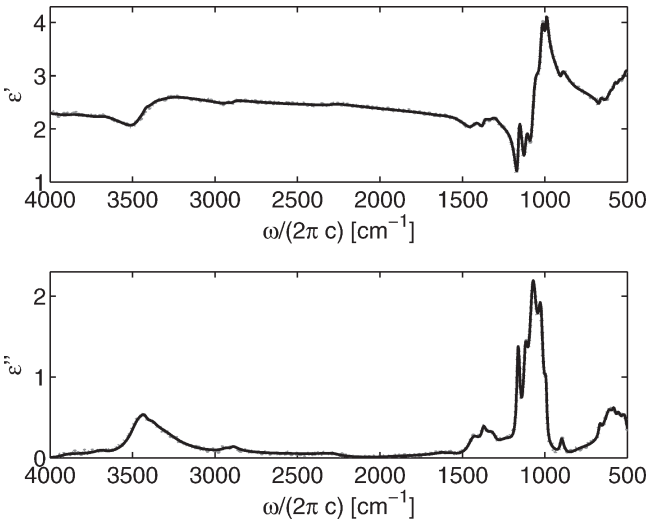

FIG. 22. Results of the least squares fit of the model function obtained by the peak detection routine for cellulose II. Solid line: fitted dielectric function; gray dotted line: KKT of the measured reflectance ratio.

To get rid of this error we define the experimental ratio of reflectance

$$\rho_{\text{exp}} := \frac{R_{p,\text{exp}}}{R_{s,\text{exp}}} = \frac{R_p - kR_s}{R_s - kR_p} \tag{34}$$

With $\rho = R_p/R_s$, this gives

$$\rho_{\text{exp}} = \frac{\rho - k}{1 - k\rho} \tag{35}$$

Isolating ρ yields

$$\rho = \frac{\rho_{\text{exp}} - k}{1 - \rho_{\text{exp}} k} \tag{36}$$

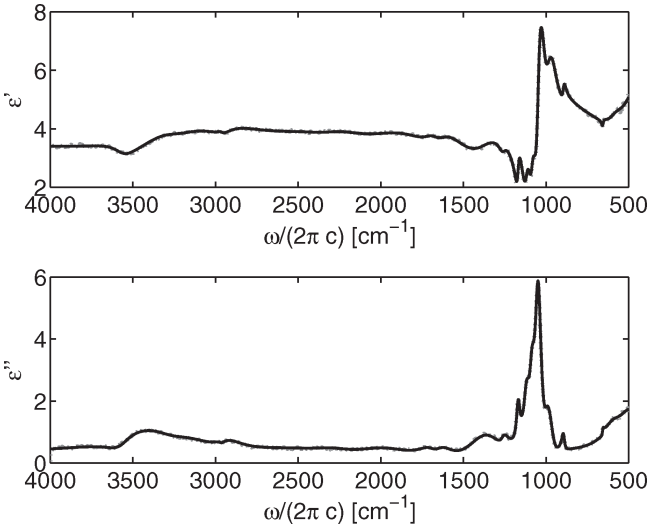

FIG. 23. Results of the least squares fit of the model function obtained by the peak detection routine for xylane. Solid line: fitted dielectric function; gray dotted line: KKT of the measured reflectance ratio.

Thus, we can correct the error that is made by the contrast ratio of the polarizers. The corrected reflectance ratios for cellulose II (solid line) and for xylane (dashed line) are presented in Fig. 21 (top frame) together with the ellipsometric angle Ψ (bottom frame). Due to the absence of anisotropic scattering effects, the baseline of the reflectance ratio is almost completely flat. This is a good indicator of the quality of the measured data.

For the spectra given in Fig. 21, the peak detection algorithm was able to detect the oscillations fairly well; some of the peaks (namely in the OH region 2800 cm^{-1}-3800 cm^{-1}), where cellulose and also hemicelluloses such as xylane have a lot of oscillations, had to be added manually. The extrapolation of the experimental data was carried out by nonlinear fitting of the margins of the data according to Eq. 14.

The results of fitting the dielectric functions are presented in Fig. 22 for cellulose II and in Fig. 23 for xylane. Both fits resemble the measured data accurately. To check the quality of the obtained functions one can use the previously introduced parameter ζ (see the Fit subsection above). Here it has to be considered that the peaks in the OH region cannot be resolved by the measurement. Therefore, it is impossible to find the correct number of oscillators in this region. If there are enough oscillators in the model function, the fit will resemble the data correctly, but this has no physical meaning. Therefore, it is to be expected that the parameters in the OH region do have a higher ζ value than all the other oscillators, without introducing an additional error to the dielectric function.

Without the correction of the contrast ratio of the polarizers, one ends up with an overall ζ of 0.027 for the cellulose II. The overall ζ for the fit in Fig. 22 (corrected) is $\zeta = 0.017$. Taking a look at the ζ value for the region 2400 cm^{-1} to 3400 cm^{-1}, we find $\zeta_{2400–3400} = 0.028$, which is a lot more than the average ζ, indicating, that most of the complex values of the fit parameters are caused by the lower OH region, as expected. The ζ value for the rest of the spectrum yields $\zeta_{500\text{-}1600} = 0.015$. The xylane fit gives an overall ζ of 0.037.

This means that the fits have some difficulties in the intermediate frequency range, namely, the broad and very weak peaks in the intermediate region. As an attempt to improve the physical consistency of the fit parameters, one could increase the number of oscillators in this region, but this would result in very long iterations rather than in better results.

CONCLUSION

A method for the determination of optical constants by Kramers–Kronig transformation of the reflectance ratio (R_p/R_s) was used to obtain optical constants of isotropic materials. The method was analyzed for experimental and numeric errors and a setup with grazing incidence was shown to be the best choice in experiment. An algorithm was presented to perform extrapolation of the reflectance data, KKT, determination of the oscillators, and nonlinear fitting of the obtained dielectric function.

The fitting algorithm is not limited to use with the KKT of reflectance ratios. It can be used to fit any dielectric function no matter whether it was determined by spectroscopic ellipsometry or other KKT techniques.

The feasibility of the reflectance ratio method has been shown by optical simulation of measurement data and redetermining the dielectric function. It has been demonstrated that the optimal experimental choice is grazing incidence, combined with repeated switching of the polarization filter between *s*- and *p*-polarization[30] to minimize experimental errors.

Optical constants for two biomacromolecules, cellulose II and the hemicellulose xylane, were measured, and the fitted dielectric functions (see Fig. 22 for cellulose II and Fig. 23 for xylane) were discussed. The main results are that the presented peak-detection algorithm was able to find most of the peaks and that the obtained dielectric functions are of good quality, as far as this can be judged by analysis of the fit parameters and the physical consistency of the dielectric functions.

ACKNOWLEDGMENTS

The financial support by the Federal Ministry of Economy, Family and Youth and the National Foundation for Research, Technology and Development is gratefully acknowledged. This work was also supported by the industrial partner Lenzing AG.

1. H. A. Kramers, "La diffusion de la lumiere par les atomes", in *Atti Cong. Intern. Fiscia, Como* (1927), **vol. 2,** pp. 545–557.
2. R. de L. Kronig, J. Opt. Soc. Am. **12,** 547 (1926).
3. H. A. Kramers and H. A. de L. Kronig, Zeitschrift für Physik **48,** 174 (1928).
4. R. Tousey, J. Opt. Soc. Am. **29,** 235 (1939).
5. D. G. Avery, Proc. Phys. Soc. Sect. B **65,** 425 (1952).
6. T. S. Robinson, Proc. Phys. Soc. Sect. B **65,** 910 (1952).
7. T. S. Robinson and W. C. Price, Proc. Phys. Soc. Sect. B **66,** 969 (1953).
8. J. S. Toll, Phys. Rev. **104,** 6 (1956).
9. F. C. Jahoda, Phys. Rev. **107,** 1261 (1957).
10. H. R. Philipp and E. A. Taft, Phys. Rev. **113,** 1002 (1959).
11. J. S. Plaskett and P. N. Schatz, J. Chem. Phys. **38,** 612 (1963).
12. D. M. Roesseler, Brit. J. Appl. Phys. **16,** 1119 (1965).
13. D. M. Roesseler, Brit. J. Appl. Phys. **16,** 1359 (1965).
14. D. W. Berreman, Appl. Opt. **6,** 1519 (1967).
15. D. H. Hensler, Appl. Opt. **11,** 2522 (1972).
16. B. J. Stagg and T. T. Charalampopoulos, Appl. Opt. **30,** 4113 (1991).
17. K. Yamamoto, Ph.D. Thesis Case Western Reverse University, Cleveland, OH (1994).
18. V. P. Tolstoy, I. V. Chernyshova, and V. A. Skryshevsky, *Handbook of Infrared Spectroscopy of Ultrathin Films* (John Wiley and Sons, Hoboken, NJ, 2003).
19. H. G. Tompkins and W. A. McGahan, *Spectroscopic Ellipsometry and Reflectometry* (John Wiley and Sons, New York, 1999).
20. A. Röseler and E. H. Korte, *Handbook of Vibrational Spectroscopy* (John Wiley and Sons, Chichester, 2002), vol. 2, Chap. Infrared Spectroscopic Ellipsometry, pp. 1065–1090.
21. V. Lucarini, J. J. Saarinen, K.-E. Peiponen, and E. M. Vartianen, *Kramers-Kronig Relations in Optical Materials Research* (Springer, Berlin, Heidelberg, New York, 2005).
22. K. Yamamoto and A. Masui, Appl. Spectrosc. **49,** 639 (1995).
23. K. Yamamoto and H. Ishida, Spectrochim. Acta, Part A **50,** 2079 (1994).
24. K. Yamamoto, A. Masui, and H. Ishida, Appl. Opt. **33,** 6285 (1994).
25. H. A. Lorentz, *The Theory of Electrons and its Application to the Phenomena of Light and Radiant Heat* (Teubner, Leipzig, 1916).
26. W. N. Hansen, J. Opt. Soc. Am. **58,** 380 (1968).
27. K. Yamamoto and H. Ishida, Vib. Spectrosc. **8,** 1 (1994).
28. K. Jezierski, J. Phys. C-Solid State Phys. **19,** 2103 (1986).
29. E. D. Palik, Ed., *Handbook of Optical Constants of Solids* (Academic Press, Orlando, FL, 1985).
30. R. Schennach, C. Hirschmugl, E. Gilli, and W. T. Tysoe, Appl. Spectrosc. **63,** 369 (2009).

8. Paper published in Macromolecules 2011

For the following publication the placement in the spectroscopic methods section is somewhat ambiguous. The paper could as well have been placed in the Surface chemistry section, because it is much further on the applied side than the two other publications in this section. However, the focus of this paper mainly is on the simulation of thin film systems of cellulose, and therefore, the publication is a direct consequence of the previous section 7 (Ref. (Gilli and Schennach 2010)), using the dielectric functions measuered there.

The paper deals with the simulation and measurement of polarized infrared spectra of cellulose model films, for different film thicknesses, and shows the possibility to measure the thickness of these films by best match calculations, without the need of a calibration scheme.

The modeling and simulation of this work was done by myself, as well as the writing part on infrared spectroscopy and simulation (Results & Discussion, Conclusions). The measured data were obtained by M. Djak under my supervision (Djak 2011).

References

Djak, M. (2011). MA thesis. Graz University of Technology.

Gilli, E. and Schennach, R. (2010). *Determination of Noise-Free Optical Constants in the Infrared by Kramers-Kronig Troansformation of the Reflectance Ratio in s- and p-Polatization*. Applied Spectroscopy, **64**.(6), pp. 669–681.

Macromolecules

COMMUNICATION TO THE EDITOR

pubs.acs.org/Macromolecules

Thickness Dependence of Reflection−Absorption Infrared Spectra of Supported Thin Polymer Films

M. Djak,[†,‡] E. Gilli,[†,‡] Eero Kontturi,[*,§] and R. Schennach[*,†,‡]

[†]Institute of Solid State Physics, Graz University of Technology, Graz, Austria

[‡]CD-Laboratory for Surface Chemical and Physical Fundamentals of Paper Strength, Graz University of Technology, Graz, Austria

[§]Department of Forest Products Technology, School of Chemical Technology, Aalto University, Helsinki, Finland

Supporting Information

INTRODUCTION

At present, supported thin and ultrathin films of various synthetic and native polymers are used for multiple purposes, including sensors,[1] transistors,[2] and model systems[3] among many others. In addition, the fundamental properties of ultrathin polymer films can be intriguing as witnessed by, for example, deviations observed in crystallization[4,5] or glass transition temperature.[6−8] Chemical characterization of such films is important when one wants to know about, e.g., film composition, its purity, chemical modifications performed after the initial preparation of the film, aging effects, or film's performance as a model substrate. Reflection−absorption infrared spectroscopy (RAIRS) is an indispensable tool for analysis of polymer thin films because of its surface sensitivity coupled with the analytical fingerprint detail on organic compounds in contrast to many other popular techniques like X-ray photoelectron spectroscopy which yields data mainly on the elemental composition of the film surface. As RAIRS on metallic substrates is based on the excitation caused by the p-component (perpendicular to the surface) of the infrared radiation reflecting at a grazing angle on the sample, a number of film properties, such as roughness and thickness, affect the spectrum.[9,10] The effect of film thickness on the spectrum is usually omitted, but it is potentially important when characterizing films over a wide thickness range. In the current study, we have performed RAIRS analysis of polymer films with thickness values ranging from 1 to >500 nm, and we go on to show that film thickness has a systematic influence on the spectral band intensities, a factor that must be considered when quantifying chemical changes in films characterized by RAIRS. The chosen film material was amorphous cellulose on a silicon substrate due to its well-characterized properties and reliable preparation in various thickness regimes by consecutive spin-coating steps.[11,12] To corroborate the interpretation arising from the influence of thickness on the spectra, we have also performed spectral simulations.

EXPERIMENTAL SECTION

Amorphous cellulose films were prepared by regenerating spin-coated films of trimethylsilyl cellulose (TMSC) on silicon wafers into cellulose by exposing the films to the vapor of aqueous 2 M HCl solution for 2 min as described in ref 11. The IRRAS spectra were measured under vacuum by using a reflection unit with variable angle and a polarizer from Bruker Optics with an incidence angle of 74°. The spectral simulations were carried out with the simulation tool SCOUT 3.1701. Film thickness was experimentally determined by spectroscopic ellipsometry (picometer ellipsometer, Beaglehole Instruments, Wellington, New Zealand) that was performed within 380−725 nm wavelength range at 75° measurement angle. Full experimental details are available in the Supporting Information.

RESULTS AND DISCUSSION

Cellulose films with thicknesses between 1 and 539 nm have been prepared on single side polished silicon wafers. The p-polarized IRRAS spectra of the clean substrate as a reference and four cellulose films with different thickness in the fingerprint region (1500−500 cm^{-1}) and in the OH region (4000−2500 cm^{-1}) are shown in Figure 1 together with the structure of cellulose. The reference spectrum from a plain silicon wafer shows that there are seven bands that stem from the substrate in the fingerprint region (Figure 1). With increasing film thickness, seven new bands arise at 670 cm^{-1} (OH out-of-plane bending), 1024 cm^{-1} (CO stretching), 1064 cm^{-1} (CO stretching), 1153 cm^{-1} (antisymmetric bridge COC stretching), 1199 cm^{-1} (OH in-plane bending), 1257 cm^{-1} (OH in-plane bending), and 1369 cm^{-1} (CH bending), all corresponding to the reported IR spectra of cellulose,[13] including amorphous cellulose.[14] Similarly, the bands in 3600−3000 cm^{-1} (OH stretching) and 2900 cm^{-1} region (CH and CH_2 stretching) in Figure 1 are characteristic of cellulose.[13,14] All of these bands increase in intensity, but there is no shift and no change in the band shape as a function of cellulose film thickness. These films have been shown to be amorphous in the ultrathin regime (few tens of nanometers).[12] Since crystallinity induces distinct patterns to the IR spectra of cellulose,[15] the lack of band shift in Figure 1 is a clear indication that the films stay amorphous to as thick as 539 nm.

Figure 2 shows the integrated bands from Figure 1 as a function of film thickness. It is apparent that the IR intensities are not a function of film thickness up to 50 nm, which can be ascribed simply to the IR signal noise being too large to see clear distinctions due to thickness. As the film thickness increases further, the intensities of the bands increase with different slopes depending on the vibration. However, the intensity of the

Received: December 20, 2010
Revised: March 14, 2011
Published: March 18, 2011

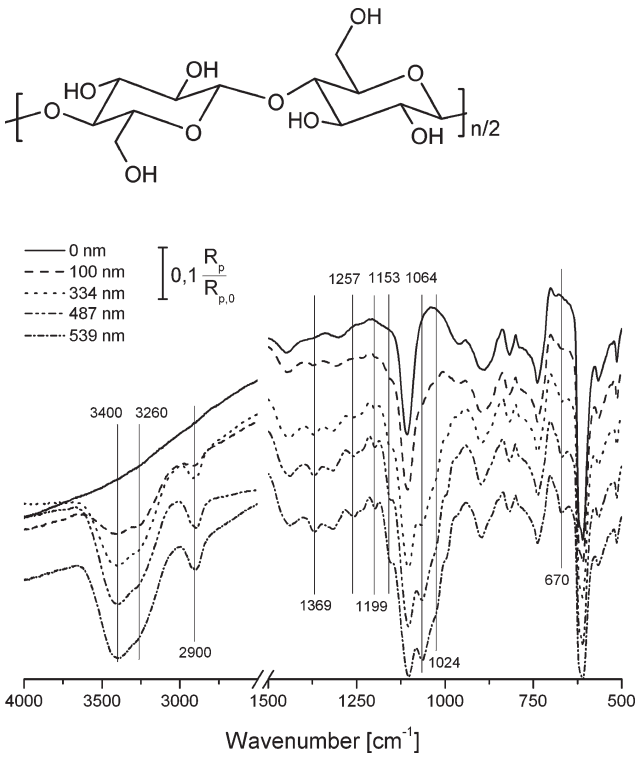

Figure 1. Top: structure of the repeating unit of cellulose. Bottom: p-polarized IR reflectance spectra of silicon-supported cellulose films of different thickness values. 0 nm thickness denotes the reference spectrum for a plain, uncoated silicon wafer.

infrared spectra measured in reflection depends not only on the amount of absorbing material but also on the reflectivity of the surface.[16] The latter is not the same for s- and p-polarized light, and it changes with surface roughness. Because of these facts, a steady increase of the intensity of any given vibration is not necessarily related to an increase in film thickness. Therefore, simulations of the spectra have been made to clarify if the increase found in Figure 2 is due to film thickness or reflectivity changes.

Measured s-polarized spectra have been juxtaposed with their simulated counterparts in Figure 3. The increase in the band intensities as a function of growing cellulose film thickness is clearly a trend which is reproduced both in measured and in simulated spectra in all regions. The biggest difference between experiment and simulation can be found in the OH region. This is due to the slow accumulation of water on the liquid nitrogen cooled detector during the experiments (see below).

It is immediately visible from Figure 3 that the simulation is capable of reproducing the dramatic baseline drop of the measured data, which is not featured in, for example, conventional transmission IR spectra of cellulose.[13,14] The strong drop of the baseline for thick cellulose films at high wavenumbers is caused by Fabry−Pérot resonances between the cellulose surface and the cellulose silicon interface.[17] Thicker films yield a lower central wavenumber (corresponding to a greater wavelength) of this absorption resonance. Therefore, this drop of the baseline arises at the high wavenumber limit for thin films, moving more toward the center of the spectral range for thick films, leading to the observed drop in the baseline (Figure 3). The systematic baseline drop, however, is not the reason for increased band

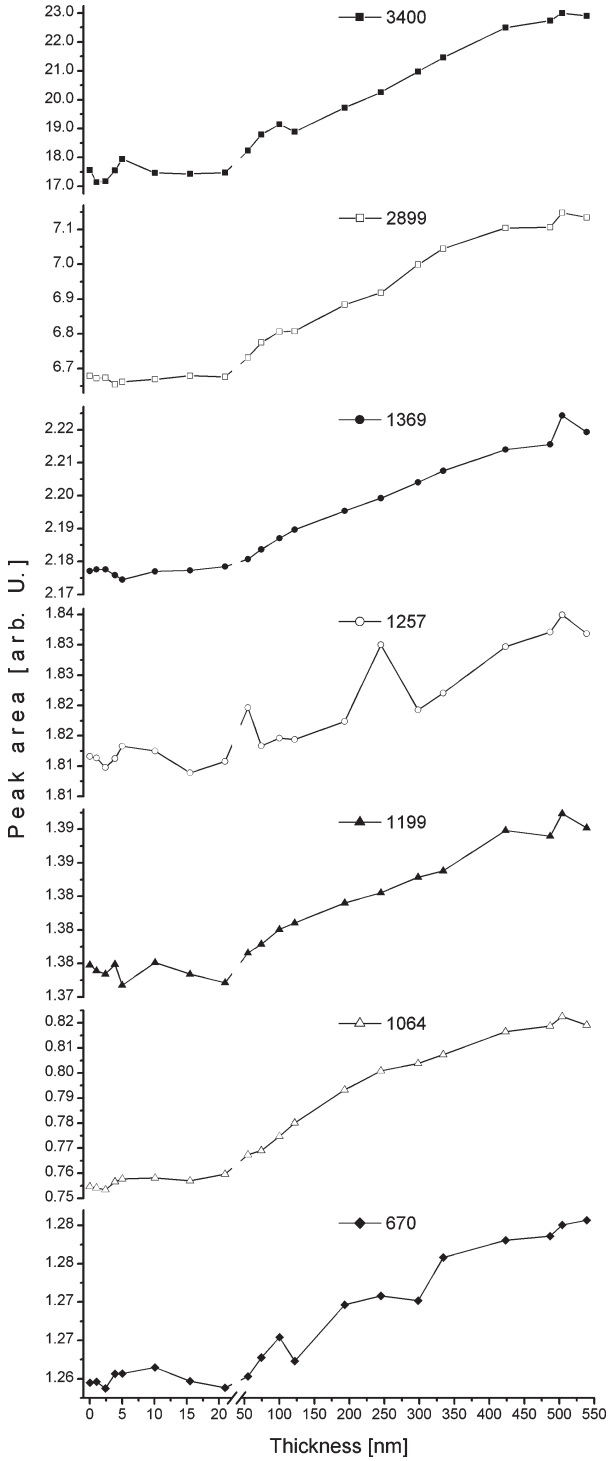

Figure 2. Integrated areas from the bands from Figure 1 as a function of cellulose film thickness obtained from ellipsometry. Note that all the curves have a different scale in the intensity. Upon integration, a common baseline for all spectra was used, which was made by normalizing the spectra to the lowest value of the peak (see Supporting Information for details).

intensities upon growing film thickness (Figure 2) because of the normalization procedure (see Supporting Information).

The only adjustable parameter used to simulate the spectra is the film thickness which can therefore be evaluated and then

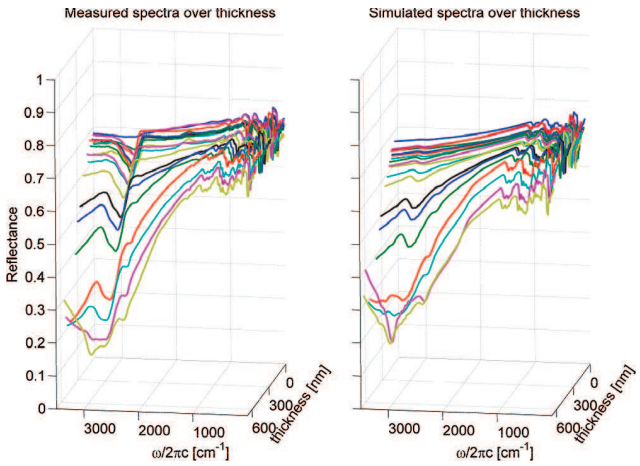

Figure 3. The s-polarized IR spectra as a function of cellulose film thickness: (left) measured spectra, (right) spectral simulations.

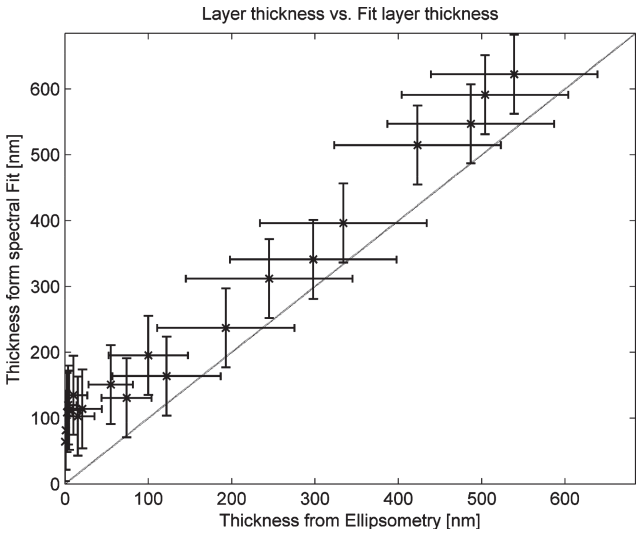

Figure 4. Thickness obtained from the simulated spectra versus the film thickness measured via spectroscopic ellipsometry in the visible range.

plotted against the film thickness (Figure 4), as measured by spectroscopic ellipsometry. This is a more direct approach to illuminating the systematic influence of cellulose film thickness on the RAIRS data than merely calibrating the measured band intensities (compare to Figure 2).

In fact, RAIRS data can be applied to estimate the thickness of the measured films. Figure 4 reveals that the thickness values are in good agreement within their confidence intervals for values over 100 nm. Below 100 nm the spectroscopic approach does not seem to be sufficiently sensitive for thickness determination. This is due partly to the aforementioned noise and partly to unknown optical constants of the cellulose film in the infrared region, which are approximated from a Kramers−Kroning transformation[18] of a cellulose sample. There is a constant overestimation of the film thickness by the spectral fit. However, the correlation is linear with the correct slope, and the deviation is within the confidence intervals (see line in Figure 4).

Here, one has to note two factors that influence the data. First, the liquid nitrogen cooled detector has a tendency to adsorb water on its window, which cannot be avoided completely, leading to an increase in the OH intensity over time, which cannot be distinguished from the increase due to cellulose. Second, there is an influence on the signal due to the surface roughness which increases with increasing cellulose film thickness.[11] This also leads to a change in the background of the IR signals, which cannot be accounted for in the simulation.

A way to get rid of the water signal on the MCT detector is to look at the ratio of p-polarized to s-polarized spectra. Here the signal of the ultrathin water layer on the detector will cancel itself out because the layer is isotropic in the lateral directions and measured under vertical illumination.[10] This leads to the same signal for s- and for p-polarization. However, the problem with the different roughness of the films still plays a role, and in the simulation of the ratio of p- to s-polarization one would have to take into account the effect of depolarization on the rough surface.

In our simulation approach, the roughness can only be simulated by an energy loss function, which is sufficient for normalized single spectra but does not account for depolarization. This causes a large difference in the baselines between simulation and experiment for the ratio of p- to s-polarized light, and fitting the ratio of p- and s-polarized spectra becomes impossible. Therefore, only the s-polarized spectra were used for fitting within the scope of this paper.

The experimental results (Figures 1 and 2) together with spectral simulations (Figures 3 and 4) demonstrate that the band intensities in a RAIR spectrum are quantitatively influenced by the thickness of a supported polymer film. Because RAIRS is one of the few ways to gain information about organic functional groups in supported films, this finding has implications in characterization of thin polymer films. For example, if aging has resulted in chemical alterations and thickness loss in a thin polymer film, the thickness change must be taken into account when quantifying the extent of chemical changes by RAIRS.

CONCLUSIONS

With thin supported polymer films, the spectral data from RAIRS were systematically influenced by the film thickness. This effect must be considered when RAIRS is applied to characterize the impact of treatments that may affect the film thickness, such as solvent-induced swelling, aging effects, or chemical reactions within the film. In addition, when an optical simulation of the obtained spectra was carried out, it was actually possible to quantify the film thickness from the RAIRS spectra if the thickness values were above 100 nm.

ASSOCIATED CONTENT

Supporting Information. Experimental details, specific information on the simulation of the IR spectra, and detailed description on the integration of the IR bands. This material is available free of charge via the Internet at http://pubs.acs.org.

AUTHOR INFORMATION

Corresponding Author

*E-mail: robert.schennach@tugraz.at, phone +43 316 873 8462, fax +43 316 873 8466 (R.S.); e-mail eero.kontturi@aalto.fi, phone +358 947024250, fax +358 947024259 (E.K.).

■ ACKNOWLEDGMENT

The financial support by the Austrian Federal Ministry of Economy, Family and Youth and the National Foundation for Research, Technology and Development is gratefully acknowledged. The support of the industrial partner Lenzing AG is greatly appreciated. E.K. acknowledges the Academy of Finland (Project No. 129068) for financial support.

■ REFERENCES

(1) Grate, J. W. *Chem. Rev.* **2008**, *108*, 726.
(2) Roberts, M. E.; Sokolov, A. N.; Bao, Z. *J. Mater. Chem.* **2009**, *19*, 3351.
(3) Kontturi, E.; Tammelin, T.; Österberg, M. *Chem. Soc. Rev.* **2006**, *35*, 1287.
(4) Capitan, M. J.; Rueda, D. R.; Ezquerra, T. A. *Macromolecules* **2004**, *37*, 5653.
(5) Napolitano, S.; Wübbenhorst, M. *Macromolecules* **2006**, *39*, 5967.
(6) Kawana, S.; Jones, R. A. L. *Phys. Rev. E* **2001**, *63*, 021501.
(7) Sharp, J.; Forrest, J. A. *Phys. Rev. Lett.* **2003**, *91*, 235701.
(8) Serghei, A.; Huth, H.; Schick, C.; Kremer, F. *Macromolecules* **2008**, *41*, 3636.
(9) Chabal, Y. J. *Surf. Sci. Rep*. **1988**, *8*, 211.
(10) Schennach, R.; Hirschmugl, C.; Gilli, E.; Tysoe, W. T. *Appl. Spectrosc.* **2009**, *63*, 369 and references therein.
(11) Kontturi, E.; Thüne, P. C.; Niemantsverdriet, J. W. *Langmuir* **2003**, *19*, 5735.
(12) Kontturi, E.; Suchy, M.; Penttilä, P.; Jean, B.; Pirkkalainen, K.; Torkkeli, M.; Serimaa, R. *Biomacromolecules* **2011**, *12*, 770.
(13) Klemm, D.; Philipp, B.; Heinze, T.; Heinze, U.; Wagenknecht, W. *Comprehensive Cellulose Chemistry*; Wiley-VCH: Weinheim, 1998; Vol. 1, Chapter 3.
(14) Kondo, T.; Sawatari, C. *Polymer* **1996**, *37*, 393.
(15) Barsberg, S. *J. Phys. Chem. B* **2010**, *114*, 11703.
(16) Yamamoto, K.; Ishida, H. *Vib. Spectrosc.* **1994**, *8*, 1.
(17) Bernazzani, P.; Sanchez, R. F.; Woodward, M.; Williams, S. *Thin Solid Films* **2008**, *516*, 7947.
(18) Gilli, E.; Schennach, R. *Appl. Spectrosc.* **2010**, *64*, 669.

Supporting Information

for

Thickness dependence of reflection absorption infrared spectra of supported thin polymer films

M. Djak, E. Gilli, Eero Kontturi*, R. Schennach*

This supporting Information contains three sections: Experimental details, description on the normalization procedure for integration of the IR bands, and elaboration on the spectral simulations.

Experimental details

Amorphous cellulose films were prepared by regenerating spin coated films of trimethylsilyl cellulose (TMSC) into cellulose by exposing the films to the vapor of aqueous 2M HCl solution for 2 minutes. The TMSC was prepared from Cellulose powder from spruce (Fluka) as described elsewhere.[S1] Toluene solutions of TMSC were deposited on a static silicon substrate with native oxide layer on top (Okmetic, Espoo, Finland) and spin coated at 4000 rpm with 2200 rpm/s acceleration for ca. 40 seconds. Prior to spin coating the substrates were cleaned in a UV/ozonator (Bioforce Nanosciences, Ames, Iowa) for 15 min. Cellulose film thickness values from 1-60 nm were obtained by varying the solution concentration (1-20 g dm^{-3}). Thicker films were obtained by consequent spin coating steps of 20 g dm^{-3} TMSC solutions. Between the deposition steps, the most recent TMSC layer was always regenerated into cellulose by acid vapor to prevent its subsequent dissolution in the following spin coating step. (Cellulose is insoluble in common solvents.)

Reflection absorption infrared spectroscopy (RAIRS) measurements were performed using a reflection unit (specular reflection) with variable angle, a manual polarizer from Infraspecs and a motorized polarizer from Bruker Optics. The IRRAS spectra were measured with an incidence angle of Θ = 74° with a polarization modulation technique.[S2] In short, the Infraspecs polarizer is mounted at the entrance to the sample chamber and positioned at 45° between p- and s- polarization. The second polarizer is placed before the reflection unit and alternating set to either s- or p- polarization adding 200 scans at a sampling rate of 100 kHz. For a total measurement polarizer positions are changed to add up a total of 6 measurements in s- and p-polarization, i.e. a total of 1200 scans at 100 kHz for each single polarized spectrum. This technique has the advantage of background independence and independence from time dependent drifts, when the ratios of p- and s-polarized reflectance are analyzed. All IR measurements were done under vacuum conditions with a base pressure of about 4 mbar.

Spectroscopic ellipsometry (Picometer Ellipsometer, Beaglehole Instruments, Wellington, New Zealand) was performed within 380-725 nm wavelength range at 75° measurement angle. The data were fitted with a Cauchy K model (parameters: N_0=1.59492, N_2=0.00113, N_4= 3.8×10^{-7}).

Normalization of IR bands and integration of the area

The IR band areas were determined in the following way. In order to avoid baseline corrections the band maxima were normalized to the highest value for each band. The area under the normalized curve was subsequently determined by integrating between two fixed wavenumbers as indicated below:

Band at 3400 cm^{-1} between 3005 and 3663 cm^{-1}

Band at 2900 cm^{-1} between 2805 and 2986 cm^{-1}

Band at 1369 cm^{-1} between 1349 and 1393 cm^{-1}

Band at 1257 cm^{-1} between 1242 and 1277 cm^{-1}

Band at 1199 cm^{-1} between 1187 and 1213 cm^{-1}

Band at 1064 cm^{-1} between 1050 and 1082 cm^{-1}

Band at 670 cm^{-1} between 654 and 678 cm^{-1}

Simulations

Simulations were carried out with the simulation tool SCOUT version 3.1701. The single side polished wafer substrates were simulated as an incoherently coupled silicon layer with a coherently coupled thin SiO_2 layer on top. The dielectric functions of both materials were obtained from literature.[S3,S4] The additional cellulose layer was simulated as a coherent thin film, the dielectric function of the cellulose material was obtained by a polarization modulated Kramers-Kronig technique.[S5] The scattering losses on rough interfaces were simulated by a fitted loss function. The only adjustable parameter used to fit the simulated spectra to the experiment was the film thickness of the cellulose films, in order to get this information directly out of the IR spectra without a need to calibrate band intensities.

REFERENCES

(S1) Kontturi, E.; Thüne, P. C.; Niemantsverdriet, J. W. *Langmuir* **2003**, *19*, 5735.

(S2) Schennach, R.; Hirschmugl, C.; Gilli, E.; Tysoe, W. T. *Appl. Spectrosc.* **2009**, *63*, 369.

(S3) Edwards, D. F. In *Handbook of optical constants of solids*, Palik, E. D., Ed.; Academic Press: Orlando, 1985, p 547.

(S4) Philipp, H. R. In *Handbook of optical constants of solids*, Palik, E. D., Ed.; Academic Press: Orlando, 1985, p 749.

(S5) Gilli, E; Schennach, R. *Appl. Spectrosc.* **2010**, *64*, 669.

9. Paper submitted to Infrared Physics & Technology

The work with optical constants of complex macromolecules had triggered the idea to build an accessory unit for spectroscopic infrared ellipsometry (Gilli et al. 2011c). Spectroscopic ellipsometry has the geat advantage over Kramers-Kronig based methods, that the phase difference between s- and p-polarized reflectance is actually measured, as well as the p/s reflectance ratio, thus this method provides both, the real and the imaginary part of the samples response to a light stimulus, which enables direct measurement of the complex refractive index or the dielectric function of the sample. Therefore, no numerical transformation errors of unknown magnitude are introduced. These mentioned problems are discussed in detail in section 7 (Gilli and Schennach 2010).

The primary idea of an ellipsometry accessory unit for a Bruker ifs66v/s vacuum spectrometer found its way to an Austrian, and subsequently an international patent application (Sec. C, Refs. (Gilli et al. 2011e; Gilli et al. 2011d), and was awarded a budget to build a prototype, by the Austria Wirtschaftsservice (AWS). The details of the prototype and its performance are described in this following publication(Gilli et al. 2011c).

The publication was written by myself entirely. The prototype project was carried out under my administration, and all the measurement, and data analysis was done by me.

References

Gilli, E. and Schennach, R. (2010). *Determination of Noise-Free Optical Constants in the Infrared by Kramers-Kronig Troansformation of the Reflectance Ratio in s- and p-Polatization*. Applied Spectroscopy, **64**.(6), pp. 669–681.

Gilli, E., Kornschober, M., and Schennach, R. (2011c). *Optical arrangement and proof of concept prototype for mid infrared variable angle spectroscopic ellipsometry*. Submitted to: Infrared Physics & Technology,

Gilli, E., Schennach, R., and Kornschober, M. (2011d). *Optical arrangement for ellipsometry*. PCT Patent Application. WO 2011/022745 A1.

Gilli, E., Schennach, R., and Kornschober, M. (2011e). *Optische Anordnung für Ellipsometrie*. AT Patent Application. AT 508 690 A1.

Optical arrangement and proof of concept prototype for mid infrared variable angle spectroscopic ellipsometry

Eduard Gilli[a,b,*], Martin Kornschober[b], Robert Schennach[a,b]

[a] *CD-Laboratory for Surface Chemical and Physical Fundamentals of Paper Strength, Austria*
[b] *Institute of Solid State Physics, Graz University of Technology, Austria*

Abstract

We present an optical setup for variable angle mid infra red spectroscopic ellipsometry. The arrangement can be placed into the sample compartment of a Bruker ifs66v/s vacuum fourier transform infrared spectrometer. A first prototype of the setup has been tested in the spectral range from 650cm^{-1} to 4000cm^{-1} and can measure incidence angles between 8° and 87°. We compare the measured data to reference measurements with a commercial variable angle infrared spectroscopic ellipsometer. The comparison gives a proof of concept for the discussed optical arrangement.

Keywords: variable angle spectroscopic infra red ellipsometry, spectroscopic ellipsometry, infra red ellipsometry

1. Introduction

Infrared spectroscopic ellipsometry is an already well established and very powerful spectroscopic technique, that combines the chemical sensitivity of infrared spectroscopy with the unique ability of ellipsometry to simultaneously determine the real and the imaginary part of the samples response to the incident irradiance. This makes spectroscopic infrared ellipsometry an ideal tool for the investigation of layered systems[1, 2, 3, 4, 5], because structural sizes well below the used wavelength can still be measured by the phase [6]. The long wavelenghts in the infrared ensure that quite rough surfaces can still be studied[7, 3]. Furthermore spectroscopic infrared ellipsometry is ideal to investigate excitation processes and charge carriers in solids[8, 9, 10, 11, 1, 12, 13, 14, 15], and it can be used to characterise optically anisotropic materials[16, 17].

The determination of both, the real and the imaginary part of the response of a sample to a light stimulus is also a very important feature for the measurement of optical properties of materials[18, 19, 20, 16, 21].

Spectroscopic ellipsometry in the infrared suffers from the lack of powerful lightsources[1]. This leads to laterally rather big sources with diameters of 10mm and more, instead of point like sources. Such a large lightsource causes quite a strong beam divergence and a relatively big measurement spot at the sample surface. Therefore, the angle of incidence is not a single well defined value but a range of angles, which has to be taken into account in data analysis.

Variable angle spectroscopic ellipsometers for the mid infrared region in most cases employ a goniometric setup with 2 arms, where one arm holds the source and the other arm holds the detector [6, 22, 23, 13, 7]. This implies a sample that is kept at ambient conditions, if not the entire goniometric setup is purged with inert gas.

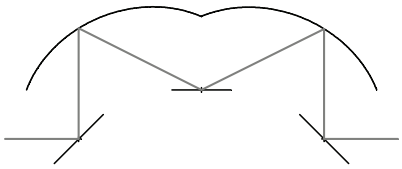

Figure 1: Schematic drawing of the optical path of the ellipsometer described by Dittmar et.al.[27]

High quality optical constants of cellulose and hemicelluloses in the mid infra-red are necessary to investigate the fundamental mechanisms of the bonding of paper-fibres[24, 25]. Cellulosic substances swell when in contact with moisture[26]. Therefore, the sample itself must be kept under a controlled surrounding in order to keep the film thickness constant. This can be best achieved with an ellipsometer that can be placed into the sample compartment of a spectrometer.

An ellipsometer to be placed into a sample compartment of a spectrometer has been described by Dittmar et.al.[27], following a setup by Milosevic et.al.[28, 29]. In this ellipsometer the incident light is focussed onto a mirror, that can be tilted around a hoizontal axis normal to the light propagation. The tiltable mirror describes the first focal point of an elliptical mirror, while the sample is positioned at the second focal point of the elliptical mirror. The optical path behind the sample position is analogous. A rough sketch of this setup is given in Fig. 1.

The optical arrangement, described in the current paper[30, 31] has two advantages over the ellipsometer described by Dittmar et.al. First, in the present arrangement it is possible, to place the polarizing elements immediately in front of and behind the sample position. This is an advantage insofar, as every

*Corresponding Author
Email address: gilli@tugraz.at (Eduard Gilli)

signal that occurs between the polarizer and the analyzer disturbs the measurement. In the setup by Dittmar et. al. there are 2 reflections between the polarizer and the sample and two more reflections between the sample and the analyzer. The incidence angles of these reflections vary with the chosen angle of incidence onto the sample. This causes slight alterations of the chosen state of polarization between polarizer and sample, and therfore introduces an additional source of possible error.

The second advantage is the relation between the angle of incidence and the tilt angle of the tiltable mirror. Dittmar et. al. report a non-linear relation between tilt angle and angle of incidence at the sample. In the present arrangement, there is a one to one relation between the angle of incidence at the sample surface, and the rotation angle of a rotatable mirror.

In the following, we will describe the experimental methods and materials used, followed by a detailed discussion of the optical path of our setup. Subsequently details about the built prototype will be given, and test measurement data will be shown in comparison to a commercial mid infrared variable angle spectroscopic ellipsometer.

2. Experimental details

The prototype of the optical arrangement is used in a Bruker ifs66v/s vacuum spectrometer comprising a liquid nitrogen cooled mercury cadmium telluride (MCT) detector. Measurements were carried out at an aperture of 4mm. A resolution of 32 cm^{-1} was used with a mirror velocity of 100kHz. For each analyzer position 100000 single scans were obtained if not otherwise indicated.

The measurement of the ellipsometric parameters was carried out by a 4 point rotating analyzer method, where the resulting intensities I_A, are measured at the analyzer positions A=0°, A=45°, A=90° and A=135°, while the polarizer is set to 45°. From these intensities the ellipsometric parameters in stokes vector representation can be determined[22, 27]. This yields

$$\cos 2\Psi = -\frac{I_0 - I_{90}}{I_0 + I_{90}} \tag{1}$$

and

$$\sin 2\Psi cos\Delta = \frac{I_{45} - I_{135}}{I_{45} + I_{135}}. \tag{2}$$

Two samples were used in order to obtain proof of concept data for the prototype, a polished aluminium surface and a silicon wafer with a defined oxide thickness. The silicon wafer was obtained from Siegert Consulting, Aachen, Germany. The wafer is single side polished with a nominal thickness of 675±20μm cut at < 100 >-orientation. It is Boron doped to a nominal resistivity of 1-20Ωcm, and comprises a thermal silica layer of 300nm±5%.

Reference measurements have been carried out on a commercial rotating compensator variable angle infrared spectroscopic ellipsometer(IR-VASE®, J. A. Woolam Co., Inc., Lincoln, NE, USA), at a resolution of 32cm^{-1}, with 20 scans per spectrum and 15 spectra per revolution. An aperture of 1.5cm was used, and the polarizer was set to 45°.

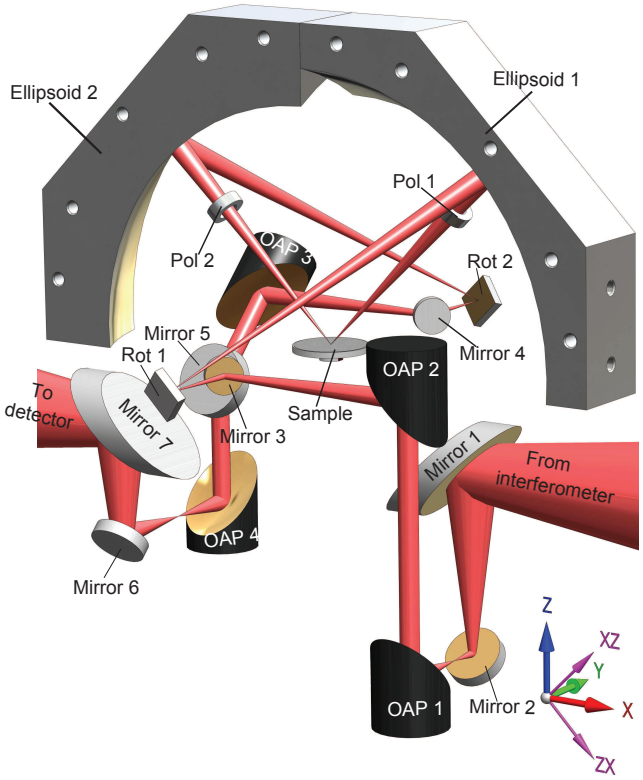

Figure 2: Three-dimensional image of the optical components of the arrangement. Plane mirrors are labeled with 'Mirror', with consecutive numbering in the order along the optical path, off axis parabolic mirrors are labeled with 'OAP' and consecutive numbering. The two rotatable plane mirrors to set the angle of incidence are labeled with 'Rot 1' and 'Rot 2' and the two polarizing filters (polarizer and analyzer) are labeled with 'Pol 1' and 'Pol 2'. The principal mirrors comprisied of an ellipse of revolution (spheroid) are labeled with 'Ellipsoid 1' and 'Ellipsoid 2'.

3. Optical path

The optical arrangement is depicted in the Figs. 2 and 3. Figure 2 gives a three dimensional representation of the optical arrangement, in order to get an overview of the geometric orientation of the different components. Detailed two dimensional technical drawings of the different planes along the optical path are given in Fig. 3. The unit is placed into the sample compartment of a Bruker ifs66v/s fourier transform infra red spectrometer (FTIR). Therefore, the incident light onto the first mirror is focussed towards the center of the sample compartment. Note that this is not the same position as the sample position of the ellipsometer unit. The incident light is reflected at two plane mirrors ('Mirror 1' and 'Mirror 2'; 'Plane 1' in Fig. 3) in order to pass the focus. Subsequently the now divergent beam is collimated by the off axis parabolic mirror (OAP) 'OAP 1', given in 'Plane 1' and 'Plane 2' in Fig. 3. The 'OAP 2' now focusses the beam via 'Mirror 3' onto the center point of the first rotatable mirror 'Rot 1', depicted in 'Plane 3' in Fig. 3. The effective focal length of 'OAP 2' is longer than the effective focal length of 'OAP 1' by a factor of 4. This yields a magnification of the image of the light source on the rotating mirror 'Rot 1' of 4 : 1.

This rotatable mirror can be rotated around an axis parallel to the y-axis of the coordinate system. The rotation axis is the cen-

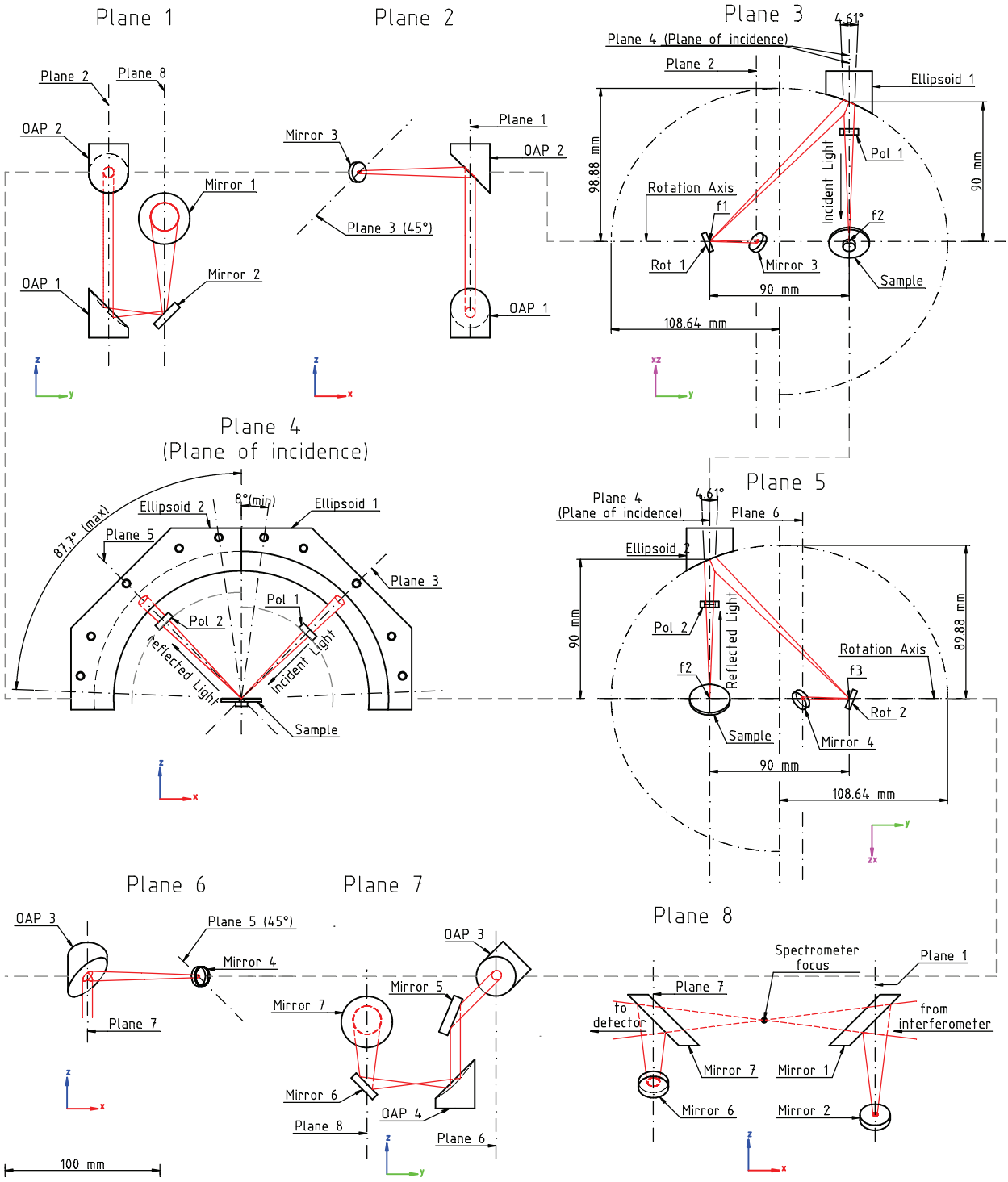

Figure 3: Detailed drawings of 8 planes along the optical path. The axes of the planes depict the orientation of the planes in respect to the coordinate system, defined in the 3-dimensional representation in Fig. 2. Plane mirrors are labeled with 'Mirror', with consecutive numbering in the order of their position along the optical path, off axis parabolic mirrors are labeled with 'OAP' and consecutive numbering. The two rotatable plane mirrors to set the angle of incidence are labeled with 'Rot 1' and 'Rot 2' and the two polarizing filters (polarizer and analyzer) are labeled with 'Pol 1' and 'Pol 2'. The principal mirrors comprising of an ellipse of revolution (spheroid) are labeled with 'Ellipsoid 1' and 'Ellipsoid 2'. Note that the planes 3 and 5 are not orthogonally oriented, but tilted around the y-axis by 45° and -45°, respectively, indicated by the 'xz' and the 'zx' axis in the coordinate system. The gray dashed line between the different planes indicates equal positions at the corresponding planes.

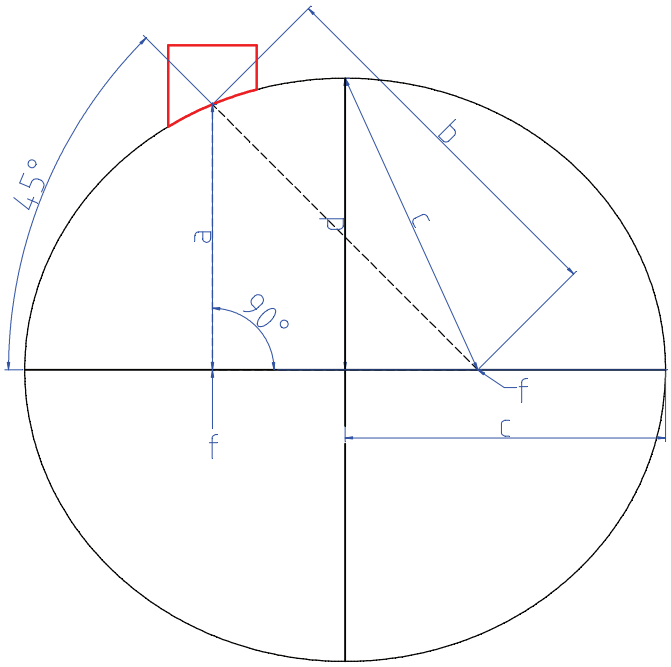

Figure 4: Drawing of the geometry of the ellipsoidal main mirrors.

tral symmetry element of the optical arrangement. The plane of the rotatable mirror is tilted with respect to the rotation axis by an angle of 22.5°. The light is irradiated onto the mirror from the direction of the rotation axis, thus the rotateable mirror reflects the light into a direction tilted by 45° with respect to the rotation axis onto the first elliptical mirror 'Ellipsoid 1'.

The elliptical mirror has the shape of an ellipse of revolution with its rotation symmetry axis collinear to the rotation axis of the rotatable mirror 'Rot 1'. The two foci of the ellipse are at the center of the rotatable mirror ('f1' in 'Plane 3' in Fig. 3) and the center of the sample ('f2' in 'Plane 3' in Fig. 3), respectively. The ellipse is constructed in a way that the distance between the foci is equal to the vertical distance from the center of the sample to the curve of the ellipse (90 mm in both cases), see 'Plane 3' in Fig. 3. Therefore, the light that is reflected from the rotatable mirror 'Rot 1' in an angle of 45° with respect to the rotation symmetry axis is focused onto the center of the sample in a right angle in respect to the rotation symmetry axis (see 'Plane 3' in Fig. 3).

Figure 4 shows the detailed geometry of the ellipse. The semi axes of the ellipse are chosen such, that the two focal points (f in Fig. 4) and the point on the perimeter where the light is reflected, describe an equal sided, right angled triangle, with a cathetus length of a and hypotenuse length of $b = a\sqrt{2}$. Therefore, the distance c between one focal point and the ends of the minor semi-axis, which is also identical to the length of the major semi-axis, is given by $(a + b)/2$ (see Fig. 4), and the minor semi axis is defined by the major cathetus of a right angled triangle, comprising a minor cathetus of the length $a/2$ (half the distance between the two foci), and a hypotenuse of the length $c = (a + b)/2$. The major semi-axis is, therefore, given by

$$c = \frac{a}{2}(1 + \sqrt{2}), \tag{3}$$

and the minor semi-axis is given by

$$d = a\sqrt{\frac{1}{2}(1 + \sqrt{2})}. \tag{4}$$

The distance between the two foci is 90mm, which, yields a minor semi-axis of 98.88mm and a major semi-axis of 108.64mm. This ensures, that the vertical distance from the sample surface to the perimeter of the ellipse is 90mm, as well as the distance between the foci, which is the distance between the center of the sample and the center of the corresponding rotating mirror (see Fig. 3). Therefore, the beam coming from the rotating mirror ('Rot 1' in Figs. 2 and 3) is set to an angle of 45° with respect to the axis of rotational symmetry.

The distance from the rotating mirror to the perimeter of the ellipse (to the mirror surface) is longer than the distance from the perimeter to the sample surface by a factor of $\sqrt{2}$, thus yielding a magnification of the image by the elliptic main mirror of $1 : \sqrt{2}$. Together with the magnification of the off axis parabolic mirrors 'OAP 1' and 'OAP 2', the arrangement gives a magnification of the lightsource by a factor of $2^{3/2} : 1$.

The angle of incidence onto the sample surface can be set by the rotation of the rotatable mirror 'Rot 1'. The rotational symmetry of the system 'Rot 1' and 'Ellipsoid 1' allows for an identical beam path onto the sample, where only the angle of incidence is varied, for any position of the rotatable mirror as long as the light meets the elliptic mirror. This is one of the most important features of this optical arrangement.

A polarizing filter, 'Pol 1', is placed between the first elliptic mirror 'Ellipsoid 1' and the sample (see 'Plane 3' in Fig. 3). This polarizer can be mounted on a goniometric arm that is placed on the side opposite to the rotatable mirror 'Rot 1', which ensures that the arm does not interfere with the optical path.

After passing the polarizing filter 'Pol 1', the incident light is reflected at the sample surface. This is depicted in 'Plane 4' in Fig. 3. The range of accessible incidence angles is limited by the beam divergence at the grazing incidence limit, and by the size of the polarizing filters in the near normal incidence limit, giving a range of incidence angles from 8° to 87.7°. The further optical path is very similar to the optical path before the sample, rotated by 180° around a vertical rotation axis through the center of the sample.

The light that is reflected at the sample passes through a second polarizing filter ('Plane 4' and 'Plane 5' in Fig. 3) and is reflected at the second elliptic mirror 'Ellipsoid 2'. This second elliopsoid has the same shape as the first one, but is rotated around a vertical axes through the center of the sample by 180° or rather through the focus 'f2' (see 'Plane 3' and 'Plane 5' in Fig. 3). The rotational symmetry axes of the second elliptic mirror 'Ellipsoid 2' is collinear to the rotation axis of the first elliptic mirror 'Ellipsoid 1'. One of the foci again, is positioned in the center of the sample ('f2' in Fig. 3, 'Plane 5'), the other focus ('f3' in Fig. 3, 'Plane 5') defines the center of a second rotatable mirror 'Rot 2' (see 'Plane 5' in Fig. 3). Thus the light that is reflected at the sample, passes throug a second polarizing filter 'Pol 2', and is focussed by the second elliptic mirror 'Elliposoid 2' onto the second rotatable mirror 'Rot 2'. As long

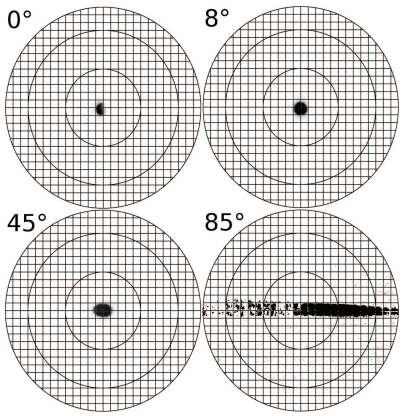

Figure 5: Photographs of the measurement spot at sample surface with a 1mm x 1mm grid, for different incidence angles. The entrance optics were focussed onto a circular aperture with a diameter of 0.6mm. Note that the contrast of the 85° picture was increased, to enhance the visibility.

as 'Rot 2' is rotated in the same way than 'Rot 1' (in the opposite direction). The light again is reflected at 'Rot 2' into the direction of the rotational symmetry axis (see 'Plane 5' in Fig. 3). Via the plane mirror 'Mirror 4' ('Plane 5' and 'Plane 6' in Fig. 3) the now divergent beam is collimated at the third OAP ('OAP 3' in 'Plane 6' and 'Plane 7' of Fig. 3).

Via the plane mirror 'Mirror 5' the parallel beam is focussed at a fourth OAP, 'OAP 4', in order to restore the beam geometry of the surrounding spectrometer. Subsequently the beam is reflected into the direction of the detector by the last two plane mirrors 'Mirror 6' and 'Mirror 7' (see Fig. 3, 'Plane 7').

Figure 3, 'Plane 8' depicts the plane of the incident light of the spectrometers sample compartment and the first and last two plane mirrors of the optical arrangement. The drawing of 'Plane 8' shows the optical path of the spectrometer within the sample compartment in a dotted line. 'Plane 8' is not placed at the center of the sample compartment of the used Bruker spectrometer. For space optimization reasons the plane of incidence ('Plane 4' in Fig.3), which is parallel to 'Plane 8', was shifted to the center of the sample compartment. Therefore, the optical paths in 'Plane 1' and 'Plane 7' (Fig. 3) are not the same.

By principles of geometrical optics, the optical arrangement is free of spherical and chromatic abberation errors. The optics are purely reflective, and all focusing elements are either elliptic or parabolic. Ray tracing simulations were not available within this project. However, the imaging properties of the arrangement can be studied by photographs of the sample surface as given in the Figs. 5 and 6. The photographs were all taken at identical aperture and shutter speed settings of the camera from a near normal view-angle. A 1mm by 1mm grid, printed on a piece of paper, was placed on the sample surface and used for rectification of the images. The polarization filters were removed. The intensity signal was isolated by digital color correction (identically for all images, except for the 85° incidence angle, where the contrast had to be increased for visibility) and, therefore, can give a qualitative estimate of the imaging properties of the arrangement. For the photographs, the arrangement was placed in an adjusting stage with a focused light source, comprising the same focal length as the incident light in the spectrometer. Therefore, by moving the light source, different elements can be focussed onto the measurement spot in the arrangement. This was fist carried out with a circular aperture (diameter: 0.6±0.1mm) in focus (Fig. 5), and second with the filament of the halogen lamp of the light source in focus (Fig. 6).

Figure 5 shows the image of the circular aperture at the sample surface, taken at different incidence angle settings of the optical arrangement, as indicated at the single frames. Dark spots indicate higher intensity. In the top left frame of Fig. 5 (incidence angle: 0°), only a half-disk at the surface is irradiated. This is caused by the fact that, due to beam divergence, only half of the incident light is irradiated onto the correct elliptic mirror at normal incidence (see 'Plane 4' in Fig. 3). As depicted in 'Plane 4' of fig. 3 the minimal angle of incidence is 8°. Here the full beam is reflected onto the sample. The sample spot at this minimal incidence is depicted in the top right frame of Fig. 5. It is of almost completely circular shape with a diameter of 1.7mm±0.2mm. This fits well to the aperture diameter of 0.6±0.1mm, taking into account the optical magnification of the arrangement ($2^{3/2} = 2.83$), which yields an expected diameter of the image of 1.7±0.3mm. At an incidence angle of 45° (see Fig. 5 bottom left frame), the shape becomes clearly elliptical with a long semi-axis of 2.6mm±0.2mm and a short semi-axis (corresponding to the beam diameter) of 1.8mm±0.2mm. By geometric considerations, the length of the long semi axis is expected to be the length of the short axis divided by the cosine of the incidence angle, which yields 2.55mm±0.4mm. The image is slightly out of focus at the boundaries close to the longer semi-axis, due to the tilt of the image plane with respect to the sample surface. At 85°, close to the maximum angle of incidence, the spot is highly elongated, with a width of 1.7mm±0.3mm (see Fig. 5, bottom right frame). It appears shifted away from the center of the sample surface to the right. This is caused by slight deviations of the sample surface from the horizontal alignment, due to the grid, printed on a piece of paper, that was placed onto the sample holder. For these reasons the length of the spot cannot be measured from the images accurately, it can only be estimated to be about 20mm. At a beam diameter of 1.7mm±0.3mm at 85° incidence a length of 20mm±7mm is expected.

The same situation as in Fig. 5 but with the filament of the lightsource in focus is depicted in Fig. 6, for the incidence angles 0°, 8°, 45°, and 85°. As already discussed above, only half of the image can be projected onto the sample surface at an incidence angle of 0°. For the minimum incidence angle of 8°, (Fig. 6 top left frame) the image of the filament is fully visible, and slightly rotated. The rotation angle of the image at the sample surface is equal to the angle of incidence, which can be seen much clearer in Fig. 6, bottom left frame. At an incidence angle of 85° the image appears very broad (about 4mm x 10mm) and with a small intensity (Note that the contrast of the 85° picture was increased, to enhance the visibility).

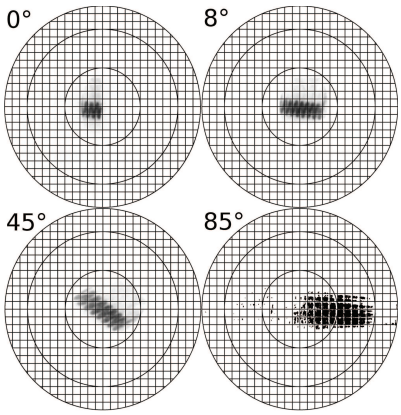

Figure 6: Photographs of the measurement spot at sample surface with a 1mm x 1mm grid, for different incidence angles. The entrance optics were focussed onto the filament of a halogen lamp. Note that the contrast of the 85° picture was increased, to enhance the visibility.

4. Setup of the prototype

The optical path and the imaging properties of the built prototype have already been descibed in the previus section. In the following, the mechanical setup, the optical components, and motorization concept of the prototype shall be discussed in more detail.

All mirrors are gold coated for maximum reflectivity in the mid-infrared. The plane mirrors (labeled with 'Mirror 1-7' in Fig. 2) are gold coated Pyrex glass mirrors obtained from Newport (Newport Spectra-Physics GmbH, Darmstadt, Germany). The off axis parabolic focussing mirrors ('OAP 1' - 'OAP 4' in Fig. 2) have effective focal lengths of 101.60mm ('OAP 2' and 'OAP 3' in Fig. 2), and 25.40mm ('OAP 1' and 'OAP 4' in Fig. 2) at a reflection angle of 90°, and were obtained from Edmund Optics GmbH, Karlsruhe, Germany. The ellipsoidal main mirrors ('Ellipsoid 1' and 'Ellipsoid 2' in Fig. 2) were custom made by Feldmann GmbH, Wetzlar, Germany. The detailed geometry of the mirrors can be seen in Fig. 3 in 'Plane 3', 'Plane 4', and 'Plane 5'. The two ellipsoidal mirrors are identical and rotated with respect to each other by 180° around the vertical axis. The ellipsoidal shape describes an ellipse of revolution (spheroid) with a horizontal axis of rotational symmetry ('y-axis' in the Figs. 2 and 3).

As polarization filters, substrate free gold wire grid polarizers were chosen (Infraspecs P03, infraSpecs, Filderstadt, Germany) with a free aperture of 6 mm. The choice of the free standing wire grids ensures no interference in the polarizer substrates, while it yields maximum intensity throughput.

The motorization concept is shown in Fig. 7. The drawing shows the arrangement of reflective optics with the most important mechanical components, namely the motors for the rotatable mirrors ('MRot1' and 'MRot2'), the motors for the goniometric arms ('MGon1' and 'MGon2'), the motors for the polarizing filters ('MPol1' and 'MPol2'). The six corresponding tooth belts with the corresponding tooth wheels and the goniometric arms are shown too. Two additional motors for height adjustment and rotation of the sample platform are not shown

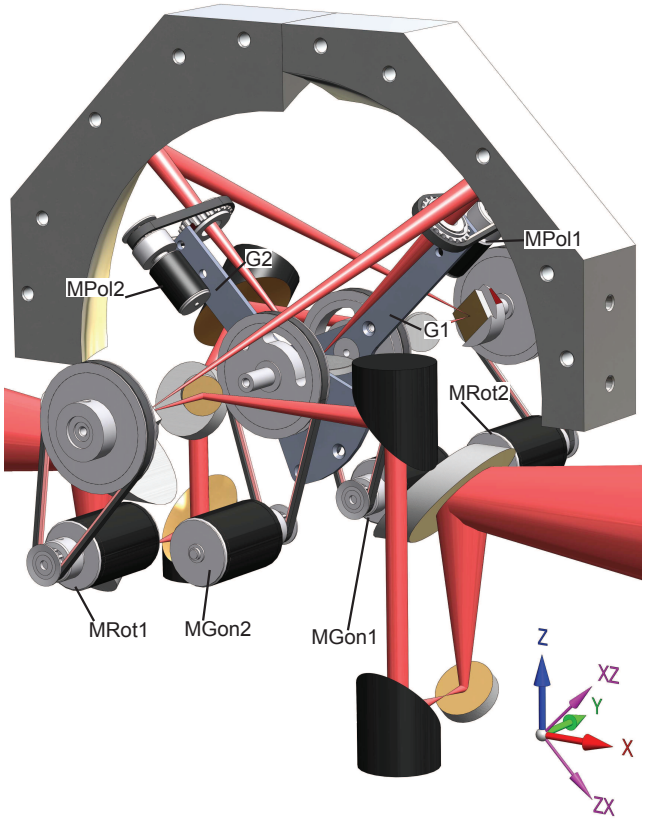

Figure 7: The motorization concept of the prototype. G1 and G2 denote the goniometric arms for the mounting of the polarization filters, Labels starting with M denote the different stepper motors (two motors for adjustment of the sample holder are not shown in the image).

in Fig. 7.

The rotation is transmitted from the stepper motors (Faulhaber PreciStep® AM 1524 ['MPol1' and 'MPol2'], and AM 2224 ['MRot1', 'MRot2', 'MGon1', and 'MGon2'], Faulhaber GmbH & Co. KG, Schönaich, Germany) to the moving components by tooth belts (Optibelt OMEGA 3M, Arntz Optibelt GmbH, Höxter, Germany). The mirrors, except for the elliptic main-mirrors are all mounted on adjustable mirror holder stages (Newport P100-AI38 ['OAP 1' - 'OAP 4', bearings for the rotation axes of 'Rot 1' and 'Rot 2'], Newport M-P100-P ['Mirror 1', 'Mirror 5', and 'Mirror 7'], Newport MM-075-HEX-M ['Mirror 2' and 'Mirror 6'], and Newport MM-050-HEX-M ['Mirror 3' and 'Mirror 4'], Newport Spectra-Physics GmbH, Darmstadt, Germany; for the nomenclature of the mirrors see Fig. 2). The custom made mountings and components were delivered by Anton Paar Shapetech GmbH, Graz, Austria.

The polarizers are mounted in tooth disks, as shown in Fig. 7 which themselves are held by a friction bearing in a housing that also holds the corresponding stepper motor (see Fig. 7, the housing itself is not shown). This arrangement is mounted on a goniometric arm ('G1' and 'G2' in Fig. 7), which is also driven by a stepper motor via tooth belt drive. The rotating mirrors ('Rot 1' and 'Rot 2' in Fig. 2) are mounted on an axis with a tilt angle between the surface normal and the rotation axis of 22.5°. This rotation axis is mounted via steel ball bearings in an adjustable optical mirror holder.

The ellipsometer within the infrared spectrometer is depicted in a block-diagram in Fig. 8. The motorization and electronic controls have been developed by technosert electronic GmbH, Wartberg ob der Aist, Austria. The drive system consists of the stepper motors with micro-stepping mode, near infrared light barriers for initialization of a zero position, and microprocessor controled driving electronics. The ellipsometer control unit recieves commands from a commmand-line controlable software interface.

The angle of incidence and the polarizer angles are controlable at a nominal precision of 0.02°. However, the torque introduced by the bending of the tooth belts and the bearings turned out to be at the limit of the stepper motors. This is a problem insofar, as the micro-stepping mode becomes very imprecise. The uncertainity in positioning is in the order of a full motorstep (± one halve step in the worst case), because the torque introduced by a stepper in microsteps is far below its nominal torque at full steps. This yields an uncertainity of ±2° for the angle of incidence, and ±4° for the polarization filters. Due to the strict limitation of space it is also not an option to introduce stronger stepper motors, because they need more space. A solution to this issue could be, to change the entire driving concept, and use brushless direct current (BLDC) motors with postioning sensors, because of their higher power density. This, however would imply a full redevelopment of the control electronics, which is out of the scope in the current project.

Therefore, this prototype can only be considered a proof of concept. The deficience in reproducability of the positions of movable parts renders calibration schemes as descibed for example in [32, 33, 34] pointless.

The measurements presented below were carried out as follows: The arrangement is initialized by rotating the components to their initialization points, which are detected by a light barrier. Starting from these points the components are rotated to their initial position. With the computer interface the user sets the incidence angle and the angles of transmission for the polarizer and the analyzer. Usually the polarizer is set to 45°. The analyzer is set by the user to the positions 0°, 45°, 90°, and 135°, and at each position a spectrum is recorded by the spectrometer software (for specifications refer to Sec. 2). Subsequently the ellipsometric parameters are determined by a Matlab routine (Matlab 7.1, The MathWorks, Inc., Natick, Mass., USA).

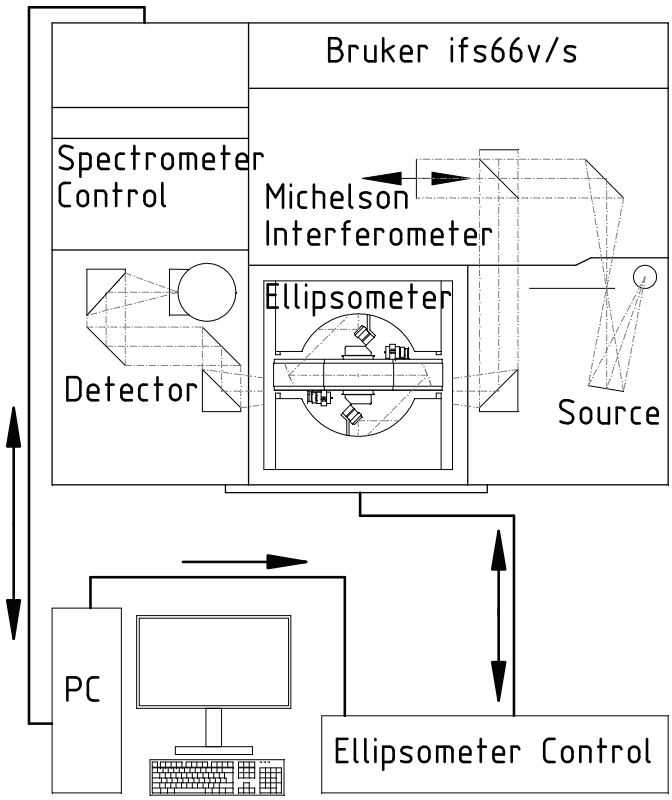

Figure 8: Block-diagram of the control system for the ellipsometer prototype.

5. Results and discussion

Test measurements have been carried out on a polished aluminium surface at 75° and 80° nominal incidence angle, and on a silicon wafer with a 300 nm thermal oxide layer at nominal incidence angles of 60° and 70°. Detailed descriptions of the samples can be obtained from Sec. 2. The measured data is compared to measurements obtained by a commercial mid infra red spectroscopic ellipsometer. Details can be obtained from Sec. 2.

Data of the measurement on aluminium are given in Fig. 9. The left frames depict a measurement of the polished aluminium surface at a nominal incidence angle of 75° (top: $\sin(2\Psi)\cos(\Delta)$, bottom: $-\cos(2\Psi)$), the right frames depict the same measurement at a nominal incidence angle of 80° (top: $\sin(2\Psi)\cos(\Delta)$, bottom: $-\cos(2\Psi)$). The solid, red lines in

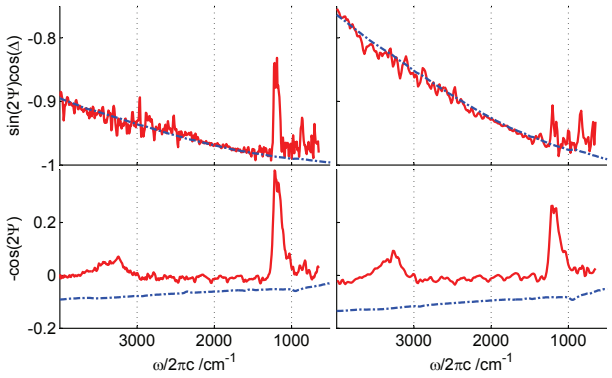

Figure 9: Measured ellipsometric parameters of a polished aluminium sample, obtained with the prototype (solid line) and with a commercial infrared spectroscopic ellipsometer (dash-dotted line), at an incicende angle of 75° (left frames) and 80° (right frames). The offset in the $-\cos(2\Psi)$-signal is due to imprecise rotating elements in the prototype.

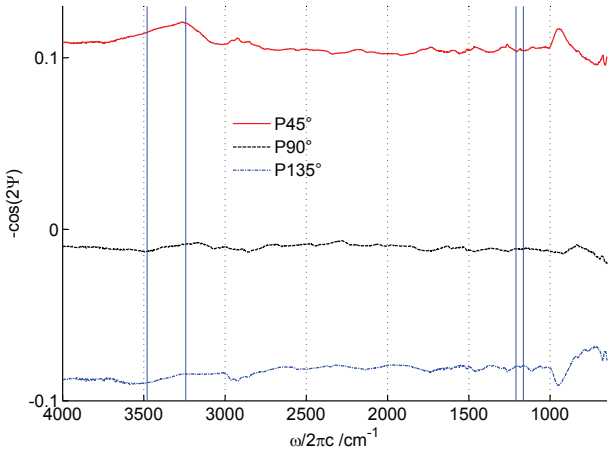

Figure 10: Measurement of the parameter $-\cos(2\Psi)$ of the empty spectrometer background in the regions of the two artefacts, measured with a 4 point rotating analyzer setup without the prototype for three different polarizer angles. Left: OH-stretching region, right: CH_2/CH_3 region. The deviation of the $-\cos(\Psi)$-data in the individual measurements is due to the imprecisions of a manual setup. Vertical solid lines indicate the artefact bands as identified with the aluminium sample.

Fig. 9 resemble the measurement with the prototype, the dash-dotted, blue lines were obtained with a commercial infrared spectroscopic ellipsometer.

Looking at the data of $-\cos(2\Psi)$ (bottom frames in Fig. 9) two differences between the prototype and the commercial instrument are immediately visible. The first is a strong chemical signal between 1000 cm^{-1} and 1400 cm^{-1}, that appears in the prototype data but not in the reference, namely two bands at 1165cm^{-1} and 1210cm^{-1}. In this spectral region vibrations of CH_2 and CH_3 can be found. The measured signal is clearly not caused by the aluminium or aluminium oxide but rather caused by a fatty contamination of a surface between the sample position and the detector.

The second clear difference between the prototype data and the reference data is a signal at wavenumbers above 3000 cm^{-1}. This is the region of OH-vibrations, suggesting moisture on the surface of the sample. However, in an evacuated spectrometer, there should not be a lot of moisture on the sample. The water signal is rather caused by accumulation of moisture on the window of the liquid nitrogen cooled MCT-detector. Due to the very small intensity throughput of our prototype, the measurement times have to be quite large (see the details in Sec. 2). This causes shifts in the background signal while the 4 analyzer positions are measured and therefore, the water artefact appears in the $-\cos(2\Psi)$-signal. This, of course, is a problem for an ellipsometer, but it could easily be overcome by a continous rotation of the analyzer, or by rotating compensator setups.

The offset of the $-\cos(2\Psi)$ lines, especially at 80° incidence (Fig. 9 bottom right frame) is due to imprecise rotation angles of the polarizing filters, and therefore, an inacurate polarizer angle, as discussed in the previous section.

To get a closer insight on the origin of the CH_2/CH_3-artefact the following things have to be kept in mind: First, signal from before the polariser cannot appear in the data, because the polarizer angle is kept constant. Second, the signal does not stem from the sample surface, as shown by the test measurements of Fig. 9. That means that the signal can only be caused by some polarization sensitivity of the optics behind the analyzer or by the detector. The detector and the optics of the spectrometer have been checked for this artefact, by measuring a background ellipsometry spectrum of the empty spectrometer, empolying two polarizers. This measurement has been repeated at different angles of the polarizer transmission axis, because the intensity of the artefact seems to depend on the chosen angle of incidence at the prototype, i.e. with the polarization direction of the intensity behind the ellipsometry unit.

The results of these background measurements are shown in Fig. 10. The OH-Band can slightly be seen, but it appears much smaller than in the ellipsometry measurement. This is due to a higher intensity throughput without the prototype and thus much smaller measurement times (The single intensity measurements for the data in Fig. 10 were carried out at a sampling rate of 100kHz and a resolution of 4cm^{-1}, averaging over a set of 3100 scans for about 5 minutes). Therefore the accumulation of moisture on the detector is smaller. The CH_2/CH_3-artefact does not appear at all in the data. This clearly shows that the CH_2/CH_3 signal is caused inside the prototype, making a fat-contaminated mirror surface at oblique incidence between the analyser and the exit of the unit the most probable explanation.

The resulting data from the test measurement on silicon/silicon oxide are depicted in Fig. 11. Solid, red lines resemble data measured with the prototype, dash-dotted, blue lines resemble reference data, measured with a commercial infrared spectroscopic ellipsometer. It has to be taken into account, that due to the imprecision of the motorized goniometer, the real incidence angle and the nominal incidence angle can diverge, especially at the region of grazing incidence, where the stepper motors are under asymetric mechanical load from the polarizer mounting. This issue has been discussed in Sec. 4. Therefore, different incidence angles were measured with the reference instrument, and the best matches are shown in Fig. 11.

The shape of the data is quite similar, however, at the re-

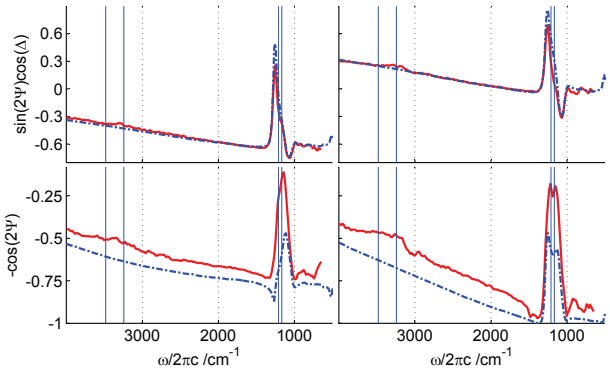

Figure 11: Measured ellipsometric parameters of a Si/SiO_2 wafer, obtained with the prototype (solid line) at a nominal incidence angle of 60° (left frames) and 70° (right frames), and with a commercial infrared spectroscopic ellipsometer (dash-dotted line) at an incidence angle of 62° (left frames) and 73° (right frames). The offset in the $-\cos(2\Psi)$-signal is due to imprecise rotating elements in the prototype. Vertical solid lines indicate the artefact bands as identified with the aluminium sample.

gions, where artefacts have been identified at the aluminium sample the prototype again shows differences to the reference (the positions of the artefact bands are indicated by vertical solid lines in Fig. 11). As it has already been shown with the aluminium sample, the prototype again shows a constant offset of the $-\cos(2\Psi)$-data towards the positive. The reason for this offset again is an inacurately rotated polarization filter.

Sumarizing the test measurements it can be stated, that the system yields results that show a proof of concept, considering the fact that the prototype could not be calibrated, due to the bad reproducability of the positioning elements.

6. Summary and outlook

We have introduced an optical arrangement for variable angle spectroscopic infrared ellipsometry, that can be placed into the sample compartment of an infrared spectrometer. The arrangement shows good imaging properties. With test measurements obtained with a first prototype, we have demonstrated, that ellipsometry measurements can be carried out with this setup. In contrast to a previous setup[27] the current setup has the polarizing elements immediately before and after the sample with no additional reflections in between. The relation between the rotation angle of the rotatable mirrors and the angle of incidence onto the sample is 1:1.

The comparison to a commercial spectroscopic infrared ellipsometer reveals an offset of the measured data, caused by a lack of precision of movable components, which also makes calibration pointless in the current state of development. It has to be stressed that this is not a shortcoming of the optical arrangement in principle, but a problem of the motorization concept.

Further development should concentrate on an accurate motorization system and an increase in intensity throughput. This could be achieved by a reduction of mirros employed for focussing the light onto the rotatable mirrors.

Having two polarization filters in the beam also opens the possibility to another measurement technique that can be regarded as a partial ellipsometry: Polarization modulation infrared reflection absorption spectroscopy (pm-IRRAS). It has been shown that this technique can be carried out using two polarizers without the need for a photoelastic modulator[35]. One of the polarizers is used to normalize the polarization of the incident light, the other one is repeatedly switched between p- and s-polraization (0° and 90°). The resulting signal in pm-IRRAS is represented as

$$\frac{R_p - R_s}{R_p + R_s}, \tag{5}$$

which is nothing else than $-\cos(2\Psi)$ as immediately visible from a comparison to Eq. 1. The Δ-information cannot be obtained by pm-IRRAS. This method is widely used due to its independence from atmospheric deviations. However, using a photoelastic modulator, the spectrum allways has a blind spot. This is not the case with the two polarizer setup.

7. Acknowledgments

The financial support by the Federal Ministry of Economy, Family and Youth and the national Foundation for Research, Technology and Development is gratefully acknowledged. Funding of the prototype by the Austria Wirtschaftsservice (AWS) is gratefully acknowledged.

The autors are indepted to Babak Dastmalchi and Kurt Hingerl from the CD-Laboratory for Surface Optics at the Center for surface and nanoanalytics at the University of Linz, Austria for carrying out the benchmark test measurements.

[1] M. Schubert, Infrared Ellipsometry on Semiconductor Layer Structures. Phonons, Plasmons and Polaritons, Springer, Berlin, Heidelberg, New York, 2004.

[2] H. Arwin, A. Askendahl, P. Tengvall, D. W. Thompson, J. A. Woolam, Infrared ellipsometry studies of thermal stability of protein monolayers and multilayers, Physica Status Solidi C 5 (2008) 1438–1441.

[3] W. Henrion, A. Röseler, H. Angermann, M. Rebien, Application of uv-vis and ftir spectroscopic ellipsometry to the characterization of wet-chemically treated si surfaces, Physica Status Solidi A 175 (1999) 121–128.

[4] K. Hinrichs, A. Röseler, K. Roodenko, J. Rappich, Surface-enhanced infrared absorption: Infrared ellipsometry of au evaporated ultrathin organic films, Applied Spectroscopy 62 (2008) 121–124.

[5] D. Tsankov, K. Hinrichs, A. Röseler, E. H. Korte, FTIR ellipsometry as a tool for studying organic layers: From langmuir-blodgett films to can coatings, Physica Status Solidi A 188 (2001) 1319–1329.

[6] A. Röseler, E. H. Korte, Infrared spectroscopic ellipsometry, in: J. M. Chalmers, P. R. Griffiths (Eds.), Handbook of Vibrational Spectroscopy, volume 2, John Wiley & Sons, Chichester, 2002, pp. 1065–1090.

[7] A. Röseler, Ir spectroscopic ellipsometry: instrumentation and results, Thin Solid Films 234 (1993) 307–313.

[8] C. Bernhard, J. Humlicek, B. Kreimer, Far-infrared ellipsometry using a synchrotron light source - the dielectric response of the cuprate high t_c superconductors, Thin Solid Films 455-456 (2004) 143–149.

[9] A. Kasic, M. Schubert, S. Einfeld, D. Hommel, T. E. Tiwald, Free-carrier and phonon properties of n- and p-type hexagonal GaN films maeasured by infrared ellipsometry, Physical Review B 62 (2000) 7365–7377.

[10] M. M. Qazilbash, K. S. Burch, D. Whisler, D. Shrekenhamer, B. C. Chae, H. T. Kim, D. N. Basov, Correlated metallic state of vanadium dioxide, Physical Review B 74 (2006) 205118.

[11] J. Rappich, K. Hinrichs, In situ study of nitrobenzene grafting on si(111)-h surfaces by infrared spectroscopic ellipsometry, Electrochemistry Communications 11 (2009) 2316 – 2319.
[12] M. Schubert, C. Bundesmann, H. v. Weckstern, G. Jakopic, A. Haase, N.-K. Persson, F. Zhang, H. Arwin, O. Ingans, Carrier redistribution in organic/inorganic (poly(3,4-ethylendioxy thiophene/poly(styrenesulfonate)polymer)-si) heterojunction determined from infrared ellipsometry)), Applied Physics Letters 84 (2004) 1311–1313.
[13] T. E. Tiwald, D. W. Thompson, J. A. Woolam, Optical determination of shallow carrier profiles using fourier transform infrared ellipsometry, Journal of Vacuum Science & Technology B 16 (1998) 312–315.
[14] T. E. Tiwald, D. W. Thompson, J. A. Woolam, W. Paulson, R. Hance, Application of ir variable angle spectroscopic ellipsometry to the determination of free carrier concentration depth profiles, Thin Solid Films 313-314 (1998) 661–666.
[15] T. E. Tiwald, J. A. Woolam, S. Zollner, J. Christiansen, R. B. Gregory, T. Wetteroth, S. R. Wilson, A. R. Powell, Carrier concentration and lattice absorption in bulk and epitaxial silicon carbide determined using infrared ellipsometry, Physical Review B 60 (1999) 11464–11474.
[16] P. Boher, J. P. Piel, B. Sacepe, Generalized ellipsometry for the characterization of anisotropic materials: influecne of the sample adjustment on the extracted optical incidices, Thin Solid Films 455-456 (2004) 581–585.
[17] M. Dressel, B. Gompf, D. Faltermeier, A. K. Tripathi, J. Pflaum, M. Schubert, Kramers-kronig-consistent optical functions of anisotropic crystals: generalized spectroscopic ellipsometry on pentacene, Optics Express 16 (2008) 19770–19778.
[18] J. H. W. G. den Boer, G. M. W. Kroessen, F. J. de Hoog, Measurenemt of the complex refractive index of liquids in the infrared using spectroscopic attenuated total reflection ellipsometry: correction for depolarization by scattering, Applied Optics 34 (1995) 5708–5714.
[19] E. T. Arakawa, T. Inagaki, M. W. Williams, Optical poroperties of metals by spectroscopic ellipsometry, Surface Science 96 (1980) 248–274.
[20] J. W. P. Bakker, G. Bryntse, H. Arwin, Determination of refractive index of printed and unprinted paper using spectroscopic ellipsometry, Thin Solid Films 455-456 (2004) 361–365.
[21] T. E. Tiwald, D. W. Thompson, J. A. Woolam, S. W. Pepper, Determination of the mid-ir optical constants of water and lubricants using ir ellipsometry combined with an atr cell, Thin Solid Films 313-314 (1998) 718–721.
[22] H. Fujiwara, Spectroscopic Ellipsometry - Principles and Applications, John Wiley & Sons, Hoboken, NJ, USA, 2007.
[23] A. Gombert, M. Khl, U. Weimar, Broadband spectroscopic ellipsometry based on a fourier transform spectrometer, Thin Solid Films 234 (1993) 352–355.
[24] E. Gilli, R. Schennach, Determination of noise-free optical constants in the infrared by kramers-kronig troansformation of the reflectance ratio in s- and p-polatization, Applied Spectroscopy 64 (2010) 669–681.
[25] M. Djak, E. Gilli, E. Kontturi, R. Schennach, Thickness dependence of reflection absorption infrared spectra of supported thin polymer films, Macromolecules 44 (2011) 1775–1778.
[26] H. Sixta (Ed.), Handbook of Pulp, volume 2, Wiley-VCH Weinheim, 2006.
[27] G. Dittmar, V. Offermann, M. Pohlen, P. Grosse, Extension of spectroscopic ellipsometry to the far infrared, Thin Solid Films 234 (1993) 346–351.
[28] M. Milosevic, N. J. Harrick, S. L. Berets, The seagull: A multifunctional variable-angle reflection attatchment, Applied Spectroscopy 45 (1991) 126–131.
[29] M. Milosevic, N. J. Harric, US Patent No. 5,048,970, 1991.
[30] E. Gilli, M. Kornschober, R. Schennach, AT Patent Application No. AT 508 690 A1, 2009.
[31] E. Gilli, M. Kornschober, R. Schennach, PCT Patent Application No. PCT/AT2010/000306, 2011.
[32] B. Johs, Regression calibration method for rotating element ellipsometers, Thin Solid Films 234 (1993) 095–398.
[33] J. H. G. W. den Boer, G. M. W. Kroesen, M. Haverlag, F. J. de Hoog, Spectroscopic ir ellipsometry with imperfect components, Thin Solid Films 234 (1993) 323–326.
[34] J. H. W. G. den Boer, Spectroscopic Infrared Ellipsometry: Components, Calibration, and Application, Ph.D. thesis, Eindhoven University of Technology, 1995.
[35] R. Schennach, C. Hirschmugl, E. Gilli, W. T. Tysoe, A new method for performing polarization-modulation infrared reflection-absorption spectroscopy of surfaces., Applied Spectroscopy 63 (2009) 369–372.

10. Subsumption

The outcome of this spectroscopic methods section is quite inhomogenious, due to the different fucuses of the three papers presented here. The red line that links all three papers is the optical data of complex materials. This data can be measured by the method described in the first paper of this part (Gilli and Schennach 2010) (Sec. 7), they are employed for simulation of thin film systems in the second publication of this part (Djak et al. 2011) (Sec. 8), and they could also be measured with the instrument described in the third publication of this part (Gilli et al. 2011c) (Sec. 9) of the dissertation at hand.

This part has now dealt with spectroscopic methods develloped or employed in the course of the work. The following part will cover a methodology topic that does not seem related to the spectroscopic methods part at a first glance, namely the optical behaviour of cellulose fibers in the visible range in a microscope. However, the theory behind both methodology parts are highly related. In both cases we deal with multi-layered optical systems.

References

Djak, M., Gilli, E., Kontturi, E., and Schennach, R. (2011). *Thickness dependence of reflection absorption infrared spectra of supported thin Polymer films.* Macromolecules, **44**.(7), pp. 1775–1778.

Gilli, E. and Schennach, R. (2010). *Determination of Noise-Free Optical Constants in the Infrared by Kramers-Kronig Troansformation of the Reflectance Ratio in s- and p-Polatization.* Applied Spectroscopy, **64**.(6), pp. 669–681.

Gilli, E., Kornschober, M., and Schennach, R. (2011c). *Optical arrangement and proof of concept prototype for mid infrared variable angle spectroscopic ellipsometry.* Submitted to: Infrared Physics & Technology,

Part III.

Optics of cellulosic fibers - Methods

11. Introductory remarks

One of the main influences on paper strength is the fiber network and its morphological properties, such as interwoven fibers, and bonded area. The connection between fiber network and mechanical properties of the paper is very complex and not fully understood today. One of the main limitations of a closer analysis of the influence of the network on the mechanical properties is the insufficient availability of acurate and non-destructive measurement methods for fiber network morphology.

Given a method to non-destructively measure the morphology of such a network it would be possible to perform mechanical simulations of the network and correlate the results to mechanical testing experiments, which could further elucidate the interplay between network properties and paper strength, and thus show new strategies to improve paper strenght.

The following part of this dissertation, consisting of two publications deals with this measurement problem. The first publication (Sec. 12, (Gilli et al. 2009c)) originates from a very early stage of the work. Here, an optical model for paper fibers in a polarization microscope was developed. This was motivated by the problem of measuring specific bond strength of single fiber-fiber bonds, where a non-destructive measurement of bonded area is necessary. As such a method polarization microscopy has been proposed (Page 1960). However, the physical interpretation of this method was unclear, and the results were ambiguous. By my findings in the first publication of this part of the dissertation at hand it was possible to physically interpret the optical behaviour of the fibers in the polarization microscope, and to use the method under close restrictions for the measurement of bonded area.

The validation as a measurement method was carried out by L. Kappel in her dissertation within the CD-Laboratory (Kappel 2010), and led to two publications given in the appendix (Sec. A).

After a lot of work on the spectroscopy side (see Secs.I,8, and 9) the problem of fiber-fiber bonded area measurement resurfaced with the background of ellipsometry. This led to a new idea of optical network analysis and is pointed out in the second paper (Gilli and Schennach 2011) of this part of the dissertation at hand. In this case the same fiber model was used, but a much more powerful, calculation method was employed, to get a hold on the ellipsometric parameters of pulp fibers in a microscope. The results of this work suggest, that it is possible to perform a full microscopic network analysis of a paper, by the exploitation of fundamental symmetries that can be found in the ellipsometric parameters of pulp fibers.

References

Gilli, E. and Schennach, R. (2011). *Imaging ellipsometry based method and algorithm for the analysis of fiber-fiber bonds in a paper network*. Submitted to: Applied Optics,

Gilli, E., Kappel, L., Hirn, U., and Schennach, R. (2009c). *An optical model for polarization microscopy analysis of pulp fibre-to-fibre bonds*. Composite Interfaces, **16**.(5), pp. 901–922.

Kappel, L. (2010). "Development and application of a method for fiber-fiber bonded area measurement". PhD thesis. Graz University of Technology.

Page, D. H. (1960). *Fibre-to-fibre bonds, Part 1 - A method for their direct observation*. Paper technology, **1**.(4), pp. 407–411.

12. Paper published in Composite Interfaces 2009

This paper establishes an optical pulp fiber model, based on a set of plane parallel anisotropic transparent slabs. Similar models for pulp fibers have been used before in different contexts, e.g. measurement of fibrillar angle (Bestsense and Ye 1995). The model is calculated by Jones matrices, for the transmission through the individual layers and fresnel reflection coefficients for the reflections at the interfaces. This is a feasible way to calculate such a system, but it neglects interference by multiple reflections in the layers and can only be employed for rather small anisotropies, because the interfaces cannot be calculated in an anisotropic manner, as pointed out in the paper.

On top of all these shortcomings of the calculation method by Jones matrices, the calculation is very teadious and needs a lot of calculation power. Therefore, it is not feasible to perform large parametric studies in order to analyze symmetries of the system along the different degrees of freedom.

However, the results validate the fiber model employed, and they resemble the findings of the microscopic images nicely, including the apparent color of the fibers. Therefore, it can be said that the model itself is applicable, to simulate optical behaviour of pulp fibers. The obvious next step of improving the employed calculation method was taken in a subsequent publication that in its application possibilities goes far beyond the scope of the first publication.

The paper was written by myself except for the introduction. The model and calculation was also done by me, as well as the experiments in the polarization microscopes.

References

Bestsense, O. and Ye, C. (1995). *Method and device for determining the orientation angle of the optical axis and the relative phase retardation of a birefingent specimen.* PCT Patent. WO96/10168.

VSP

Composite Interfaces 16 (2009) 901–922

COMPOSITE INTERFACES
www.brill.nl/ci

An Optical Model for Polarization Microscopy Analysis of Pulp Fibre-to-Fibre Bonds

E. Gilli [a,c], **L. Kappel** [b,c], **U. Hirn** [b,c] **and R. Schennach** [a,c,*]

[a] Institute for Solid State Physics, Graz University of Technology, 8010 Graz, Austria
[b] Institute for Paper, Pulp and Fibre Technology, Graz University of Technology, Austria
[c] Christian Doppler Laboratory for Surface Chemical and Physical Fundamentals of Paper Strength, Austria

Received 28 May 2008; accepted 18 November 2008

Abstract
Pulp fibre-to-fibre bonds were studied using polarization microscopy and microtome cuts. The experiments showed considerable discrepancies between these two experimental methods. While microtome cuts clearly show if a bond between two fibres has formed, polarization microscopy cannot unambiguously discern between crossed unbonded fibres and bonded fibres; also certain bonds cannot be detected with this method. To examine these shortcomings, a physical model of polarization microscopy of bonded and unbonded pulp fibers was built. Experimental validation of the model gave good agreement between calculations and reflectance measurements. Calculations based on this model clearly demonstrate that only bonded fibres resembling a plane parallel plate show as bonds. However, crossings of unbonded fibers also appear as bonds if the two fibres are flat and plane parallel to each other. The model provides a consistent interpretation for polarization microscopy imaging of pulp fibre bonds, an important topic in research of mechanical and optical properties of fibrous composites like paper.

Keywords
Polarization microscopy, fibre bond, bonded area, optical model, optical fibre model, Jones algebra, Jones calculus, paper fibre

1. Introduction

The tensile strength of paper mainly depends on the strength of the individual pulp fibres and on the ability to form fibre-to-fibre bonds [1]. The strength of the bonds is controlled by the size of the bonded area and the specific bonding force, i.e., the bonding force per area [2]. Consequently an increase of paper strength is usually achieved by pulp fibre flexibilization, which increases bonding area, or im-

* To whom correspondence should be addressed. E-mail: robert.schennach@tugraz.at

 DOI:10.1163/092764409X12477474036798

provement of bond strength by means of fibre treatment, e.g., refining, or chemical additives [2].

Several methods for determining the bonded area of fibre-to-fibre bonds have been published. Yang *et al*. [3] determined the bonded area using images of samples that were cut with a microtome. Jayme and Hunger [4] used an electron microscope to analyze the previously bonded areas of fibre-to-fibre bonds that were torn apart. Torgnysdotter [5] investigated the contact zone between fibres using light microscopy and a staining technique. Thomson [6] used fluorescence resonance energy transfer to analyze fibre-to-fibre bonds. Already in the 1960s Page and Tydeman [7, 8] introduced a method where the bonded area of a fibre-to-fibre bond was determined with polarized light microscopy. Figure 1 shows a fibre-to-fibre bond in reflection polarization microscopy between crossed polarizers. Whenever the fibres and the transmission directions of the polarizing filters enclose an angle of about 45°, the fibres appear bright, while the bonded area appears almost completely dark (Fig. 1(a), left frame). If the fibres and the transmission directions are parallel or perpendicular, the fibres appear in a minimal intensity, while the bonded area appears brighter than the single fibres (Fig. 1(a), right frame). However, the physical explanation for the dark appearance of the fibre bond given in the original paper [7] does not hold. Furthermore the bond area cannot be observed with all fibre-to-fibre bonds, e.g., Fig. 1(b), left frame.

In this paper we will present an optical model that describes the imaging of fibre-to-fibre bonds in polarization microscopy as described by Page and Tydeman [7, 8].

Experimental results will be presented that further underline the validity of the proposed model. The presented model explains why some fibre-to-fibre bonds are visible under polarization microscopy while others are not.

2. Experimental and Computational Details

The optical experiments were carried out on a Leitz DM RX polarization microscope in reflection and transmission mode. An Olympus BX 51 microscope with rotatable polarizer and analyzer was used in transmission.

The samples were prepared from unbleached and unrefined spruce kraft pulp fibres. To get an insight into the structure of the analyzed fibre-to-fibre bonds, single bonds were embedded in epoxy resin and cut with a Leica RM 2155 microtome. The exact description of the method can be found in Ref. [9].

The analysis of the experimental data was carried out using Matlab 7.1 R14, and the theoretical computation was assisted with the algebra system Mathemetica 5.2.

3. Experimental Results

A cellulose fibre between two crossed polarizers appears in distinct colors in reflection microscopy. Its intensity depends on the angles that are enclosed by the principal axis of the fibre and the transmission directions of the polarizing filters.

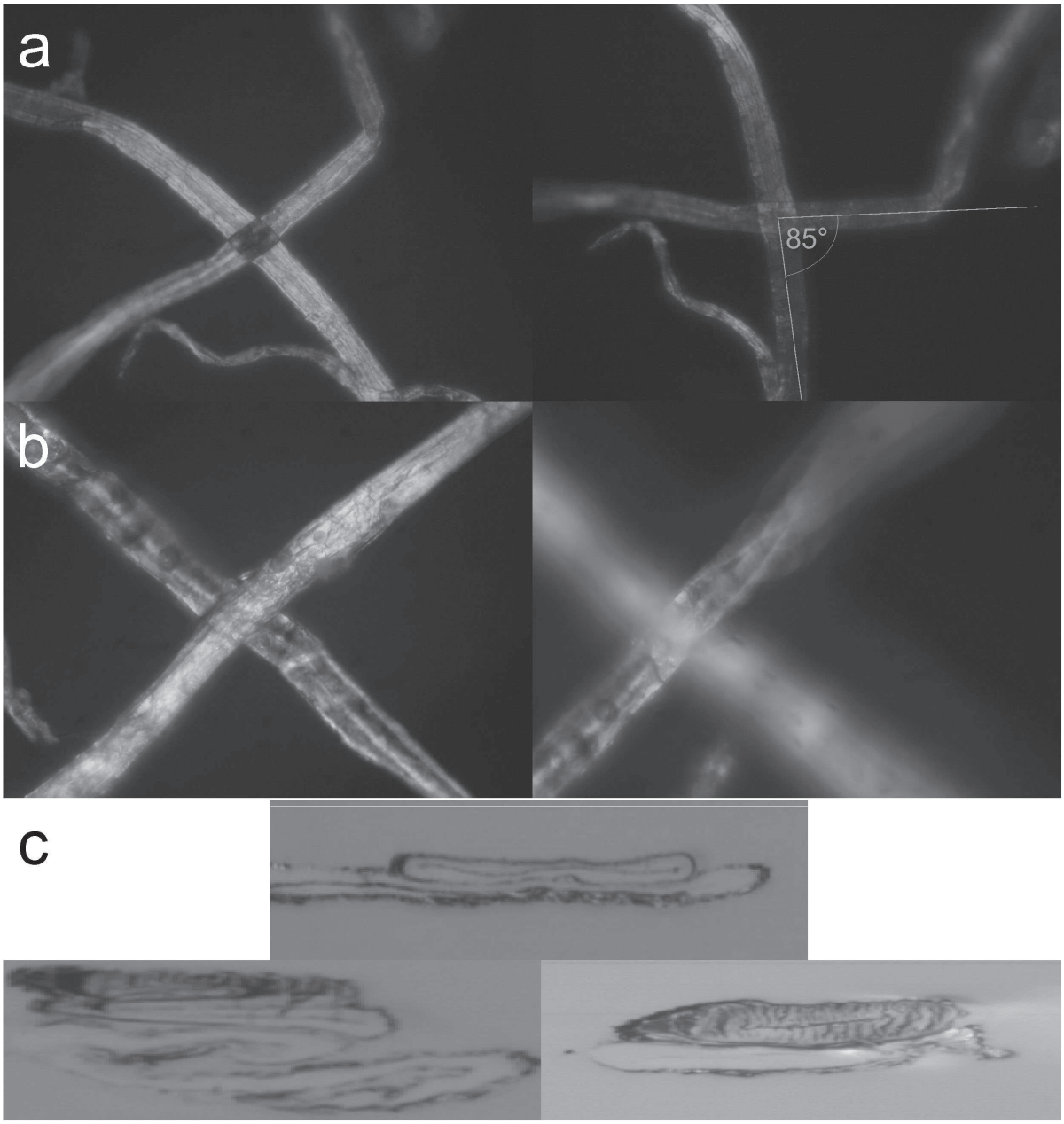

Figure 1. Fibre-to-fibre bond in reflection polarization microscopy with the polarizer vertical and the analyzer horizontal. (a) left: Fibres under a 45°-angle to the transmission direction of the polarizer, right: one fibre parallel to the transmission direction of the polarizer, the other orthogonal. The discussed effect is visible: The bond appears dark under a 45° angle between the transmission axis of the polarizing filters and the fibres. (b) Fibres under a 45°-angle to the transmission direction of the polarizer, left: before tearing apart, right: after tearing apart. The discussed effect is not visible: Bonded area and single fibre are of similar intensity. (c) Photos of microtome cuts of fibre-to-fibre bonds. Top: cut of the bond shown in (a), the effect of a dark bonding area is visible, the fibre is fully collapsed and approximately of the shape of a plane parallel plate, bottom: two bonds which did not show the effect of dark bond areas: left: not well collapsed fibres with multiple reflecting surfaces, right: fully collapsed fibres with an elliptic shape, not similar to a plane parallel plate.

Let ψ_p be the angle enclosed by the principal axis of a fibre and the transmission axis of the polarizer and let ψ_a be the angle enclosed by the principal axis of a fibre and the transmission axis of the analyzer. If the angles are close to 45°, the fibre

appears in its maximum intensity (see Fig. 1(a), left frame). If one of the angles is ≈0° and the other ≈90°, the fibre appears under a minimal intensity (see Fig. 1(a), right frame). The situation is quite different with fibre-to-fibre bonds. The bonded region appears dark when the principal axis of one fibre encloses an angle close to 45° with the transmission axes of the polarizing filters (Fig. 1(a), left frame), and it appears brighter than the single fibres when the fibres are parallel or orthogonal to the transmission axes (Fig. 1(a), right frame).

Crossings between two unbonded fibres almost always appear brighter than the single fibre, and there are fibre-to-fibre bonds that behave like unbonded crossings (see Fig. 1(b)). The fibre-to-fibre bond shown in Fig. 1(b), left frame, appears like a crossing of two unbonded fibres under crossed polarizers in reflection. This is a bond that cannot be observed in the polarization microscope, but its existence could be shown by tearing it apart after observation in the microscope (Fig. 1(b), right frame). Therefore polarization microscopy cannot observe all fibre-to-fibre bonds.

All bonds that were observed in the polarization microscope were cut with a microtome to understand their morphology. A microtome was used to cut the fibre-to-fibre bond shown in Fig. 1(a), and microscope images of a section are presented in Fig. 1(c). In this case the effect of the dark bonded area was visible. Both fibres of the bond are fully collapsed and flat springwood fibres. Two examples of bonds that could not be observed by polarization microscopy are shown in Fig. 1(c), bottom left and bottom right frame.

The left image shows a bond of not fully collapsed and folded fibres, resulting in an irregular geometry. The right image shows a bond consisting of fully collapsed fibres, with an elliptical shape.

As will be shown later, a fibre-to-fibre bond can only be seen in reflection polarization microscopy if both fibres are fully collapsed and lie flat, one upon the other (see Section 4). In the following, we will discuss these conditions and build an optical model for a cellulose fibre that can provide the required accuracy to describe the optical behaviour of fibre-to-fibre bonds.

4. Optical Model

In this section a model for the optical behavior of pulp fibres will be developed [10]. The behaviour of a fibre in polarization microscopy can be accurately modeled as an anisotropic plane parallel plate. To show that the assumption of plane parallel plates is feasible, a numerical simulation of the optical path length of collapsed fibres, as they can be seen in cutting areas of microtome cuts, was carried out for the collapsed fibre shown in Fig. 1(a) (the corresponding image of the cutting area is shown in Fig. 1(c), top frame).

A simulation of the optical path length difference between the beam that is refracted at the front surface to the back surface and the beam that is reflected at the back surface to the front surface, over the width of the fibre, is shown in Fig. 2. The difference between the two lengths stays well below 70 nm for a wide interval

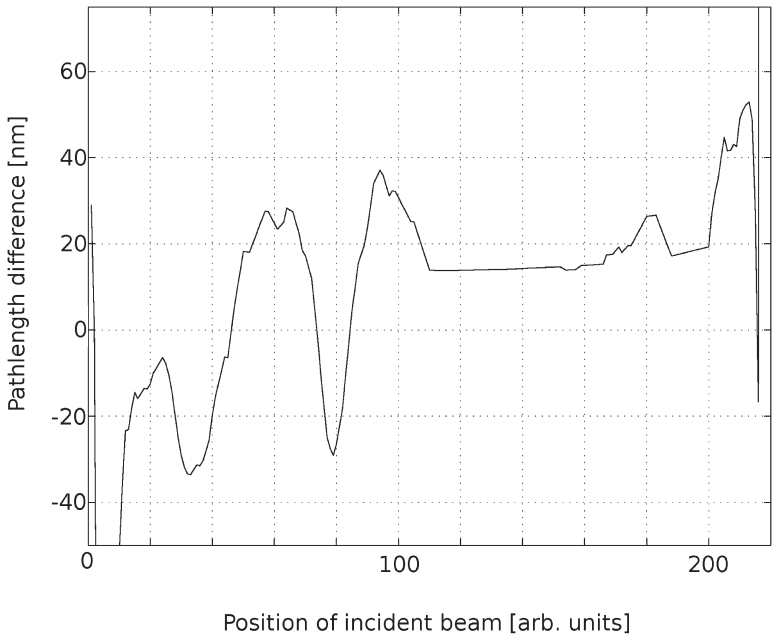

Figure 2. Numerically calculated optical path length difference between the incident and the reflected beam within the fibre shown in Fig. 1(a). The small difference is indicating the possibility of approximating the fibre as a plane parallel plate (see text).

(for a plane parallel plate it would be exactly zero). The points where the values go below -30 nm or over $+40$ nm are numerical artifacts due to the position close to the edge of the fibre, which causes errors in the automated edge detection. The difference moves towards $\pm\infty$ at the edges of the fibre where the beam is refracted at great angles. That means that the differences in the optical path length are smaller than the wavelength of visible light by an order of magnitude, justifying the approximation of the fibre as a plane parallel plate.

Taking this into account and considering the fact that cellulose fibres are optically anisotropic [11] leads to a suitable theory. An optical model will therefore be outlined to describe all of the observable phenomena very accurately.

The following premises have been used:

(1) Fibres showing an effect of dark bonded area can be approximated as birefringent plane parallel plates (fully collapsed fibres that lie upon each other). As shown above, the effect of a dark bonded region only shows if this assumption is fulfilled.

(2) The optical axes of the fibres correspond to the median angle of the microfibrils in the thickest layer of the fibre, the s_2 layer (see [12]). This leads to opposite directions of the fibrils in the two layers separated by the collapsed lumen.

Both of these premises have been used successfully with cellulose fibres before [13].

(3) Neglect of the interference effects within the fibres. The fibres are thick enough for sizeable internal reflections. However, multiple reflections and, therefore,

any interference effects within the fibre do not play an important role for the intensity in comparison to the intensity caused by birefringence within the first reflex. This is due to the low reflectivity of the fibre–air interface, of about 0.22 (see equation (18) with the parameters given in Section 5, equation (48)). For multiple reflexes the beam would have to reflect at least three times, i.e., there would be two additional reflections with a reflectivity of 0.22 each. This makes the second reflection by more than an order of magnitude ($\approx$0.05) smaller than the first one. The intensity being the norm square of the Jones vectors (see later) thus would be altered by about $\pm 0.25\%$ from interference effects by multiple reflections within the fibre.

The model does not show an effect without birefringence, which is also shown in the experiment. If interference would play a role in the transmission or reflection intensity of fibers, these fibers would have to appear in different colors, depending on their thickness, without the usage of polarization filters, and this clearly is not the case in the experiments.

With these three premises, the system can be calculated using the Jones formalism [14], which yields mean intensities over time for plane parallel layer systems. The great advantage of the Jones formalism is the possibility to combine different layers by multiplying their corresponding Jones matrices. Figure 3(a) shows the most important parameters for the model. The Jones matrix for a birefringent plane parallel plate (see Fig. 3(b)) with its fast axis parallel to the normal polarization direction (s) is given by:

$$\mathcal{P}_{\mathrm{pc}} = \begin{pmatrix} e^{\mathrm{i}\varepsilon_p} & 0 \\ 0 & e^{\mathrm{i}\varepsilon_s} \end{pmatrix}, \tag{1}$$

with ε_p and ε_s the phase retardation in parallel and normal directions (see, for example, Ref. [14]). The phase difference between s- (normal) and p-direction (parallel polarization) is given by $\Delta\phi = |\varepsilon_p - \varepsilon_s|$. For $\varepsilon_s = \Delta\phi/2$ and $\varepsilon_p = -\Delta\phi/2$ this gives:

$$\mathcal{P}_{\mathrm{pc}}(\Delta\phi) = \begin{pmatrix} e^{-\mathrm{i}(\Delta\phi/2)} & 0 \\ 0 & e^{\mathrm{i}(\Delta\phi/2)} \end{pmatrix}. \tag{2}$$

For an arbitrary angle, α, between the fast axis and the s-direction, the Jones matrix can be written as (see Fig. 3(b)):

$$\begin{aligned} \mathcal{P}_{\mathrm{pc}}(\Delta\phi, \alpha) &= \mathbb{R}(\alpha)\mathcal{P}_{\mathrm{pc}}(\Delta\phi)\mathbb{R}(-\alpha) \\ &= e^{\mathrm{i}(\Delta\phi/2)} \begin{pmatrix} e^{-\mathrm{i}\Delta\phi}\cos^2\alpha + \sin^2\alpha & (e^{-\mathrm{i}\Delta\phi} - 1)\cos\alpha\sin\alpha \\ (e^{-\mathrm{i}\Delta\phi} - 1)\cos\alpha\sin\alpha & \cos^2\alpha + e^{-\mathrm{i}\Delta\phi}\sin^2\alpha \end{pmatrix}, \end{aligned} \tag{3}$$

with the rotation matrix, $\mathbb{R}(\alpha)$, defined by:

$$\mathbb{R}(\alpha) = \begin{pmatrix} \cos(\alpha) & -\sin(\alpha) \\ \sin(\alpha) & \cos(\alpha) \end{pmatrix}. \tag{4}$$

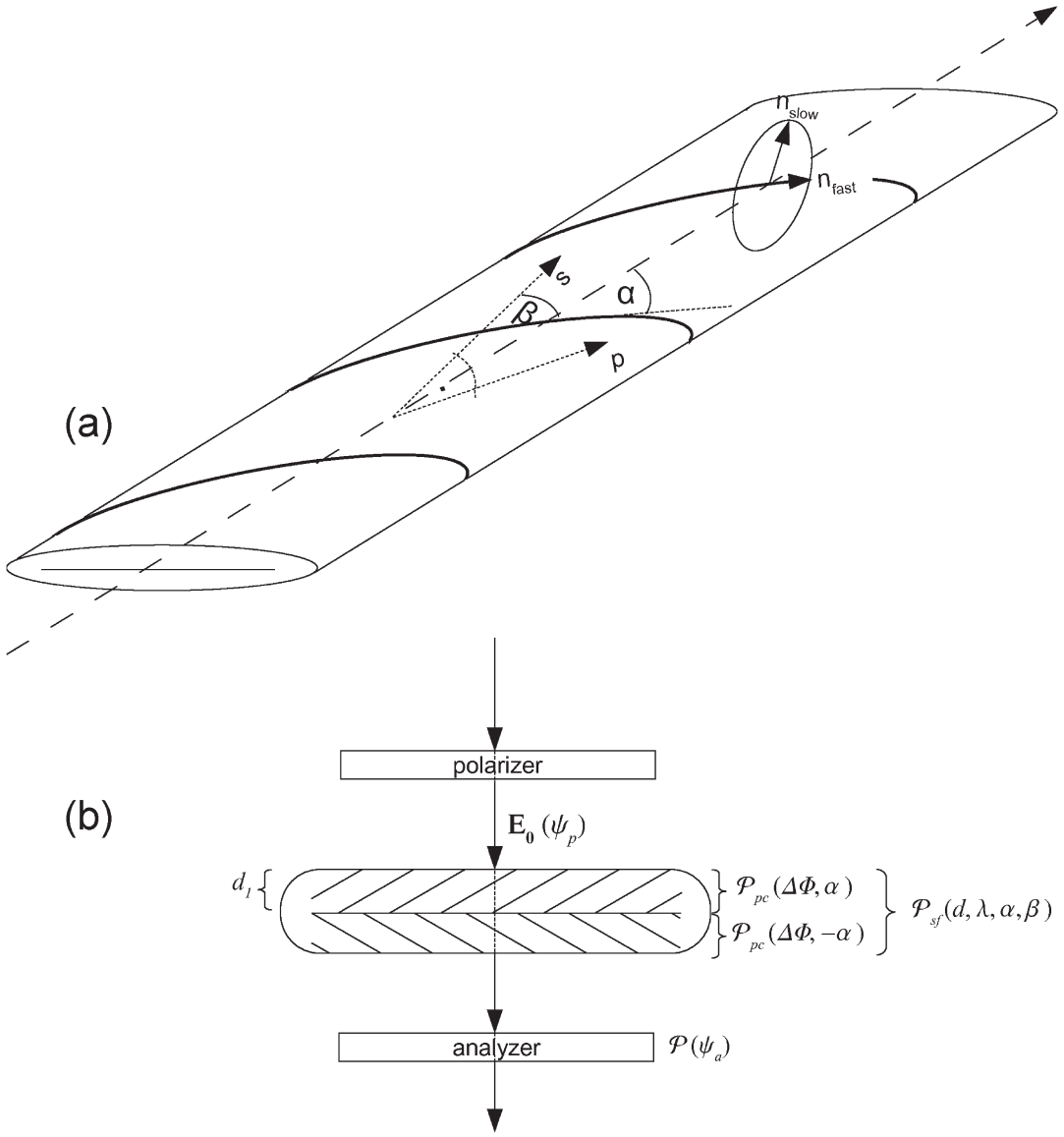

Figure 3. Important parameters and operators (Jones matrices) used by the model: (a) a fully collapsed fibre with its microfibrillar angle α, the ellipse of refraction with the two refractive indices n_{slow} and n_{fast}, the total rotation angle of the fibre, and the normal (s)- and parallel (p)-direction of polarization. (b) Single fibre with the wall thickness d_1 in transmission polarization microscopy, and the used Jones matrices for this case: The linearly polarized incident Jones vector $E_0(\psi_{\text{p}})$, with ψ_{p} the angle enclosed by the transmission direction of the polarizer and the s-direction, the Jones matrices of the two birefringent plates $\mathcal{P}_{\text{pc}}(\Delta\phi, \pm\alpha)$ and the combined Jones matrix of the entire fibre $\mathcal{P}_{\text{sf}}(d, \lambda, \alpha, \beta)$, and the Jones matrix of the analyzer $\mathcal{P}(\psi_{\text{a}})$.

The phase difference, $\Delta\phi$, of a wave traveling through an anisotropic plate can be described by the following [14]:

$$\Delta\phi(\lambda, d) = \frac{2\pi}{\lambda} \cdot d(n_{\text{slow}} - n_{\text{fast}}), \tag{5}$$

with λ being the wavelength, d the thickness of the plate, and n_{slow} and n_{fast} the ordinary and extraordinary refractive indices of the anisotropic plate, respectively (see Figs 3(a) and 4).

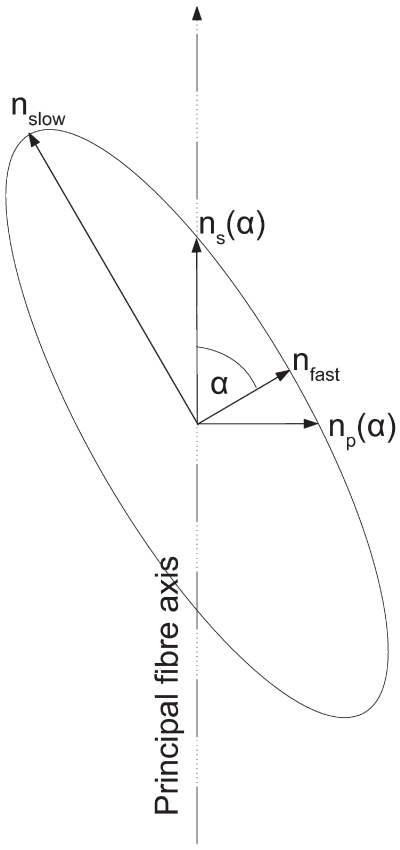

Figure 4. The ellipse of refractive indices of an anisotropic medium. α: angle between the fast optical axis and the normal (s)-direction of polarization, n_{slow} and n_{fast}: refractive indices in the directions of the optical axes of the medium, n_s and n_p: refractive indices in parallel (p)- and normal (s)-direction of polarization.

The Jones matrix for a linear polarizer with its transmission axis in the s-direction is given by

$$\mathcal{P}_v = \begin{pmatrix} 0 & 0 \\ 0 & 1 \end{pmatrix}, \tag{6}$$

which yields for an arbitrary angle between the transmission axis and the s-direction:

$$\mathcal{P}(\alpha) = \mathbb{R}(\alpha)\mathcal{P}_v\mathbb{R}(-\alpha) = \begin{pmatrix} \sin^2(\alpha) & -\cos(\alpha)\sin(\alpha) \\ -\cos(\alpha)\sin(\alpha) & \cos^2(\alpha) \end{pmatrix}. \tag{7}$$

Finally, the Jones vector of a linear polarized wave is represented by:

$$\mathbf{E} = \begin{pmatrix} p \\ s \end{pmatrix}, \quad \text{with } p, s \in \mathbb{R}, \tag{8}$$

with p and s being the amplitudes of the electric field in the p- and in the s-direction, respectively. For an arbitrary polarization angle, ψ_{p}, the Jones vector for the incident beam becomes:

$$\mathbf{E}_0(\psi_{\text{p}}) = \mathbb{R}(\psi_{\text{p}}) \begin{pmatrix} 0 \\ 1 \end{pmatrix} = \begin{pmatrix} -\sin(\psi_{\text{p}}) \\ \cos(\psi_{\text{p}}) \end{pmatrix}. \tag{9}$$

These are the operators needed for the calculation of the phase differences. For quantitative calculations of returned intensities, the well-known Fresnel formulas are required [14]:

$$\tau_s = \frac{2\sin\delta\cos\gamma}{\sin(\gamma+\delta)}, \tag{10}$$

$$\tau_p = \frac{2\sin\delta\cos\gamma}{\sin(\gamma+\delta)\cos(\gamma-\delta)}, \tag{11}$$

$$\rho_s = -\frac{\sin(\gamma-\delta)}{\sin(\gamma+\delta)}, \tag{12}$$

$$\rho_p = \frac{\tan(\gamma-\delta)}{\tan(\gamma+\delta)}, \tag{13}$$

where τ is the coefficient of transmittivity, ρ is the coefficient of reflectivity (indices s and p for normal and parallel polarization), γ is the angle between the incident beam and the optical plummet and δ is the angle between the optical plummet and the refracted beam.

Taking into account the projection of the beams onto the interface between the two media and the mean value of the amplitude over time yields an additional factor $\sqrt{n_2/n_1 \cdot \cos\delta/\cos\gamma}$ for transmission, which cancels to 1 for reflection (see, for example, Ref. [15]):

$$t_{s,p} = \sqrt{\frac{n_2\cos\delta}{n_1\cos\gamma}} \cdot \tau_{s,p}, \tag{14}$$

$$r_{s,p} = \rho_{s,p}, \tag{15}$$

where t is the coefficient of transmission, r is the coefficient of reflection (indices s and p for normal and parallel polarization), n_1 and n_2 are the refractive indices of the two media.

For the case of plane parallel plates only the limits for $\gamma \to 0$ and $\delta = \sin^{-1}(n_1/n_2 \cdot \sin(\gamma))$ (Snell's law) are required. This yields:

$$t_s(n_1,n_2) = 2\frac{\sqrt{n_1 n_2}}{n_1+n_2}, \tag{16}$$

$$t_p(n_1,n_2) = 2\frac{\sqrt{n_1 n_2}}{n_1+n_2}, \tag{17}$$

$$r_s(n_1,n_2) = \frac{n_1-n_2}{n_1+n_2}, \tag{18}$$

$$r_p(n_1,n_2) = -\frac{n_1-n_2}{n_1+n_2}, \tag{19}$$

where n_1 is the refractive index of the first medium and n_2 is the refractive index of the second medium.

These refractive indices depend on the angle α of the optical axis (anisotropic media), such that the actual refractive index is an elliptic 2-vector function of the angle between the principal axis of the fibre and the fast axis (see Figs 3(a) and 4). This cannot be described by the Jones formalism because an elliptically polarized wave rotates its incident polarization angle around 2π within one period with changing intensities. The Jones matrices already give the mean value over an entire period, therefore losing basis invariance at the reflections and the transmissions. An exact solution must be made by calculating the time dependent electromagnetic wave with all the interactions in the different layers and building the mean value over time at the end, which would go far beyond the scope of this paper. For the sake of simplicity, the surfaces of the fibres are approximated as being isotropic (with the mean value of the two refractive indices as a refractive index). This is feasible because the difference in the refractive indices of the fibres is very small (an estimate of the error, caused by this approximation is given in equation (50) in Section 5). The refractive index at the surface thus is defined by:

$$n_{\text{surf}} = \frac{n_{\text{fast}} + n_{\text{slow}}}{2}. \tag{20}$$

This gives the operators of transmission ($\mathcal{T}$) and reflection ($\mathcal{R}$):

$$\mathcal{R}(n_1, n_2) = \begin{pmatrix} r_p(n_1, n_2) & 0 \\ 0 & r_s(n_1, n_2) \end{pmatrix}, \tag{21}$$

$$\mathcal{T}(n_1, n_2) = \begin{pmatrix} t_p(n_1, n_2) & 0 \\ 0 & t_s(n_1, n_2) \end{pmatrix}. \tag{22}$$

The angle α can be interpreted physically. A cellulose fibre consists of multiple layers which consist of microfibrils [12]. The thickest layer, s_2, has a high degree of crystallinity and its microfibrils are arranged non-parallel to the principal axis of the fibre (see Fig. 3(a)).

The other layers are an order of magnitude thinner and show a less ordered structure. Uncollapsed fibres are hollow, and the microbrils form a helix around the principal axis at an angle of $\alpha \approx 20°$ to $30°$ for springwood. A fibre with a collapsed lumen can be approximated as consisting of two oriented layers. Seen from above, one fibre is rotated by α and the other fibre by $-\alpha$ (see Fig. 3(b)). It is inevitable that this orientation influences the optical properties of the fibre, and it is very plausible to assume that the angle α gives the orientation of the optical axes of the fibre (see also Ref. [13]).

The fibre can therefore be modeled as a set of two anisotropic plane parallel plates on top of each other, one with its fast optical axis oriented in $+\alpha$ and the other in $-\alpha$-direction, with a general rotation β of the principal fibre axis (see Fig. 3(a)). The Jones matrix for a single fibre therefore becomes:

$$\begin{aligned} &\mathcal{P}_{\text{sf}}(d, \lambda, \alpha, \beta) \\ &\quad = \mathcal{P}_{\text{pc}}(\Delta\phi(\lambda, d), -\alpha + \beta) \overbrace{\mathcal{T}(n_{\text{surf}}, n_{\text{surf}})}^{=\mathbb{1}} \mathcal{P}_{\text{pc}}(\Delta\phi(\lambda, d), \alpha + \beta) \\ &\quad = \mathcal{P}_{\text{pc}}(\Delta\phi(\lambda, d), -\alpha + \beta) \mathcal{P}_{\text{pc}}(\Delta\phi(\lambda, d), \alpha + \beta), \end{aligned} \tag{23}$$

with $\mathbb{1}$ being the unity matrix. In the case of $\alpha = \pi/4$, the two layers would be exactly inverse to each other and have no effect on the wave:

$$\mathcal{P}_{\mathrm{pc}}(\Delta\phi, \pi/4)\mathcal{P}_{\mathrm{pc}}(\Delta\phi, -\pi/4) = \begin{pmatrix} 1 & 0 \\ 0 & 1 \end{pmatrix} = \mathbb{1}. \tag{24}$$

With $\alpha = 0$ (or both layers in the same α) the layers form one layer with doubled phase shift:

$$\mathcal{P}_{\mathrm{pc}}(\Delta\phi, \alpha)\mathcal{P}_{\mathrm{pc}}(\Delta\phi, \alpha) = \mathcal{P}_{\mathrm{pc}}(2\Delta\phi, \alpha). \tag{25}$$

The two layers with an arbitrary angle behave similar to a linear combination of transmission and a phase retarder.

4.1. Transmission

The intensities for transmission polarization microscopy are modeled using all the previously defined operators (see Fig. 3(b)).

4.1.1. Single Fibre

The single fibre between two polarizers is modeled by:

$$\begin{aligned}&\mathbf{E}_{\mathrm{sf,trans}}(\psi_{\mathrm{p}}, \psi_{\mathrm{a}}, \lambda, \alpha) \\ &\quad = \mathcal{P}(\psi_{\mathrm{a}})\mathcal{T}(n_{\mathrm{surf}}, n_{\mathrm{air}})\mathcal{P}_{\mathrm{sf}}(d_1, \lambda, \alpha, 0)\mathcal{T}(n_{\mathrm{air}}, n_{\mathrm{surf}})\mathbf{E}_0(\psi_{\mathrm{p}}).\end{aligned} \tag{26}$$

4.1.2. Fibre-to-Fibre Bond

Here the wave travels through two fibres which enclose the angle β_{f}:

$$\begin{aligned}&\mathbf{E}_{\mathrm{bond,trans}}(\psi_{\mathrm{p}}, \psi_{\mathrm{a}}, \lambda, \alpha, \beta_{\mathrm{f}}) \\ &\quad = \mathcal{P}(\psi_{\mathrm{a}})\mathcal{T}(n_{\mathrm{surf}}, n_{\mathrm{air}})\mathcal{P}_{\mathrm{sf}}(d_2, \lambda, \alpha, \beta_{\mathrm{f}}) \\ &\qquad \times \underbrace{\mathcal{T}(n_{\mathrm{surf}}, n_{\mathrm{surf}})}_{=\mathbb{1}}\mathcal{P}_{\mathrm{sf}}(d_1, \lambda, \alpha, 0) \cdot \mathcal{T}(n_{\mathrm{air}}, n_{\mathrm{surf}})\mathbf{E}_0(\psi_{\mathrm{p}}) \\ &\quad = \mathcal{P}(\psi_{\mathrm{a}})\mathcal{T}(n_{\mathrm{surf}}, n_{\mathrm{air}})\mathcal{P}_{\mathrm{sf}}(d_2, \lambda, \alpha, \beta_{\mathrm{f}}) \\ &\qquad \times \mathcal{P}_{\mathrm{sf}}(d_1, \lambda, \alpha, 0)\mathcal{T}(n_{\mathrm{air}}, n_{\mathrm{surf}})\mathbf{E}_0(\psi_{\mathrm{p}}).\end{aligned} \tag{27}$$

4.1.3. Crossing of Two Unbonded Fibres

$$\begin{aligned}&\mathbf{E}_{\mathrm{cross,trans}}(\psi_{\mathrm{p}}, \psi_{\mathrm{a}}, \lambda, \alpha, \beta_{\mathrm{f}}) \\ &\quad = \mathcal{P}(\psi_{\mathrm{a}})\mathcal{T}(n_{\mathrm{surf}}, n_{\mathrm{air}})\mathcal{P}_{\mathrm{sf}}(d_2, \lambda, \alpha, \beta_{\mathrm{f}}) \\ &\qquad \times \mathcal{T}(n_{\mathrm{air}}, n_{\mathrm{surf}})\mathcal{T}(n_{\mathrm{surf}}, n_{\mathrm{air}})\mathcal{P}_{\mathrm{sf}}(d_1, \lambda, \alpha, 0)\mathcal{T}(n_{\mathrm{air}}, n_{\mathrm{surf}})\mathbf{E}_0(\psi_{\mathrm{p}}).\end{aligned} \tag{28}$$

The resulting intensities are obtained by the absolute square of the resulting E-vector:

$$I = |\mathbf{E}|^2. \tag{29}$$

For information on the reflected or transmitted color of a single fibre the intensity for a single fibre ($I_{\mathrm{ref,sf}}$) can be integrated over the visible spectrum, with a spectral sensitivity function as weight. For the spectral sensitivity, the CIE functions for the human eye (red, green and blue) were used [16], because these functions are the

basis of all RGB-coordinate systems.

$$I_{\text{total}} = \left| \int_{\lambda_{\min}}^{\lambda_{\max}} \mathrm{d}\lambda\, \mathbf{E}(\lambda) S(\lambda) \right|^2, \tag{30}$$

$$I_{\text{r,g,b}} = \left| \int_{\lambda_{\min}}^{\lambda_{\max}} \mathrm{d}\lambda\, \mathbf{E}(\lambda)[\text{r, g, b}](\lambda) \right|^2, \tag{31}$$

with $S(\lambda) = (\text{r}(\lambda) + \text{g}(\lambda) + \text{b}(\lambda))/3$, and $[\text{r, g, b}](\lambda)$ the spectral sensitivity functions as functions of the wavelength λ, for red green and blue [16].

4.2. Reflection

Reflection models are more complicated than transmission models due to multiple beams and reflections on different interfaces. This results in longer algebraic expressions, but is not qualitatively different from the transmission model. For the different situations (single fibre, fibre-to-fibre bond, crossed fibres), nine different reflected Jones vectors have to be defined. Their respective intensity vectors are shown in Fig. 5(a).

(1) All cases: reflection at the surface:

$$\mathbf{E}_1(\psi_{\text{p}}, \psi_{\text{a}}, \alpha) = \mathcal{P}(\psi_{\text{a}}) \mathcal{R}(n_{\text{air}}, n_{\text{surf}}) \mathbf{E}_0(\psi_{\text{p}}). \tag{32}$$

(2) All cases: reflection at the interface within the first fibre:

$$\begin{aligned} &\mathbf{E}_2(\psi_{\text{p}}, \psi_{\text{a}}, \lambda, \alpha) \\ &\quad = \mathcal{P}(\psi_{\text{a}}) \mathcal{T}(n_{\text{surf}}, n_{\text{air}}) \mathcal{P}_{\text{pc}}(\Delta\phi(\lambda, d_1), \alpha) \underbrace{\mathcal{R}(n_{\text{surf}}, n_{\text{surf}})}_{=0} \\ &\qquad \times \mathcal{P}_{\text{pc}}(\Delta\phi(\lambda, d_1), \alpha) \mathcal{T}(n_{\text{air}}, n_{\text{surf}}) \mathbf{E}_0(\psi_{\text{p}}) \\ &\quad = 0. \end{aligned} \tag{33}$$

(3) Fibre-to-fibre bond: reflection at the fibre-to-fibre interface:

$$\begin{aligned} &\mathbf{E}_3(\psi_{\text{p}}, \psi_{\text{a}}, \lambda, \alpha, 0) \\ &\quad = \mathcal{P}(\psi_{\text{a}}) \mathcal{T}(n_{\text{surf}}, n_{\text{air}}) \mathcal{P}_{\text{sf}}(d_1, \lambda, -\alpha, 0) \\ &\qquad \times \underbrace{\mathcal{R}(n_{\text{surf}}, n_{\text{surf}})}_{=0} \mathcal{P}_{\text{sf}}(d_1, \lambda, \alpha, 0) \mathcal{T}(n_{\text{air}}, n_{\text{surf}}) \mathbf{E}_0(\psi_{\text{p}}) \\ &\quad = 0. \end{aligned} \tag{34}$$

(4) Fibre-to-fibre-bond: reflection at the interface within the second fibre:

$$\begin{aligned} &\mathbf{E}_4(\psi_{\text{p}}, \psi_{\text{a}}, \lambda, \alpha, \beta_{\text{f}}) \\ &\quad = \mathcal{P}(\psi_{\text{a}}) \mathcal{T}(n_{\text{surf}}, n_{\text{air}}) \mathcal{P}_{\text{sf}}(d_1, \lambda, -\alpha, 0) \\ &\qquad \times \underbrace{\mathcal{T}(n_{\text{surf}}, n_{\text{surf}})}_{=\mathbb{1}} \mathcal{P}_{\text{pc}}(\Delta\phi(\lambda, d_2), \alpha + \beta_{\text{f}}) \\ &\qquad \times \underbrace{\mathcal{R}(n_{\text{surf}}, n_{\text{surf}})}_{=0} \mathcal{P}_{\text{pc}}(\Delta\phi(\lambda, d_2), \alpha + \beta_{\text{f}}) \underbrace{\mathcal{T}(n_{\text{surf}}, n_{\text{surf}})}_{=\mathbb{1}} \\ &\qquad \times \mathcal{P}_{\text{sf}}(d_1, \lambda, \alpha, 0) \mathcal{T}(n_{\text{air}}, n_{\text{surf}}) \mathbf{E}_0(\psi_{\text{p}}) \\ &\quad = 0. \end{aligned} \tag{35}$$

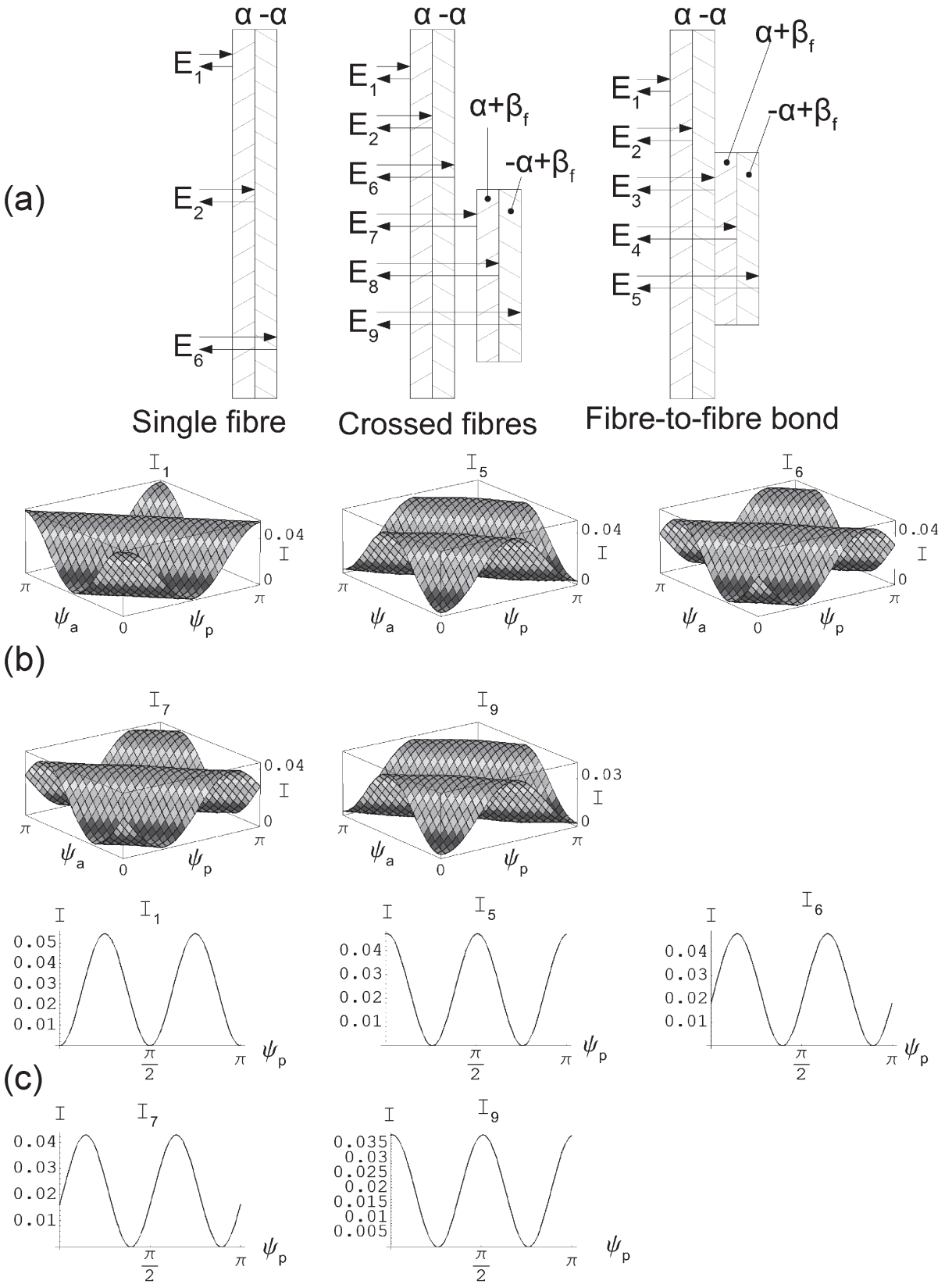

Figure 5. (a) Optical setup of the model, and reflections taken into account for single fibres, unbonded crossed fibres and fibre-to-fibre bonds. (b) The simulated non-zero intensities of the reflections shown in (a), as functions of polarizer (ψ_p) and analyzer (ψ_a) angle (see text). (c) Same as (b), but for crossed polarizers ($\psi_a = \psi_p + \pi/2$).

(5) Fibre-to-fibre bond: reflection at the back surface:

$$\begin{aligned}
&\mathbf{E}_5(\psi_\mathrm{p}, \psi_\mathrm{a}, \lambda, \alpha, \beta_\mathrm{f}) \\
&\quad = \mathcal{P}(\psi_\mathrm{a})\mathcal{T}(n_\mathrm{surf}, n_\mathrm{air})\mathcal{P}_\mathrm{sf}(d_1, \lambda, -\alpha, 0) \\
&\qquad \times \underbrace{\mathcal{T}(n_\mathrm{surf}, n_\mathrm{surf})}_{=\mathbb{1}} \mathcal{P}_\mathrm{sf}(d_2, \lambda, -\alpha, \beta_\mathrm{f})\mathcal{R}(n_\mathrm{surf}, n_\mathrm{air}) \\
&\qquad \times \mathcal{P}_\mathrm{sf}(d_2, \lambda, \alpha, \beta_\mathrm{f}) \underbrace{\mathcal{T}(n_\mathrm{surf}, n_\mathrm{surf})}_{=\mathbb{1}} \mathcal{P}_\mathrm{sf}(d_1, \lambda, \alpha, 0) \\
&\qquad \times \mathcal{T}(n_\mathrm{air}, n_\mathrm{surf})\mathbf{E}_0(\psi_\mathrm{p}) \\
&\quad = \mathcal{P}(\psi_\mathrm{a})\mathcal{T}(n_\mathrm{surf}, n_\mathrm{air})\mathcal{P}_\mathrm{sf}(d_1, \lambda, -\alpha, 0) \\
&\qquad \times \mathcal{P}_\mathrm{sf}(d_2, \lambda, -\alpha, \beta_\mathrm{f})\mathcal{R}(n_\mathrm{surf}, n_\mathrm{air})\mathcal{P}_\mathrm{sf}(d_2, \lambda, \alpha, \beta_\mathrm{f}) \\
&\qquad \times \mathcal{P}_\mathrm{sf}(d_1, \lambda, \alpha, 0)\mathcal{T}(n_\mathrm{air}, n_\mathrm{surf})\mathbf{E}_0(\psi_\mathrm{p}).
\end{aligned} \tag{36}$$

(6) Single fibre and unbonded crossed fibres: reflection at the back surface of the first fibre:

$$\begin{aligned}
&\mathbf{E}_6(\psi_\mathrm{p}, \psi_\mathrm{a}, \lambda, \alpha, \beta_\mathrm{f}) \\
&\quad = \mathcal{P}(\psi_\mathrm{a})\mathcal{T}(n_\mathrm{surf}, n_\mathrm{air})\mathcal{P}_\mathrm{sf}(d_1, \lambda, -\alpha, 0) \\
&\qquad \times \mathcal{R}(n_\mathrm{surf}, n_\mathrm{air})\mathcal{P}_\mathrm{sf}(d_1, \lambda, \alpha, 0)\mathcal{T}(n_\mathrm{air}, n_\mathrm{surf})\mathbf{E}_0(\psi_\mathrm{p}).
\end{aligned} \tag{37}$$

(7) Unbonded crossed fibres: reflection at the front surface of the second fibre:

$$\begin{aligned}
&\mathbf{E}_7(\psi_\mathrm{p}, \psi_\mathrm{a}, \lambda, \alpha, \beta_\mathrm{f}) \\
&\quad = \mathcal{P}(\psi_\mathrm{a})\mathcal{T}(n_\mathrm{surf}, n_\mathrm{air})\mathcal{P}_\mathrm{sf}(d_1, \lambda, -\alpha, 0) \\
&\qquad \times \mathcal{T}(n_\mathrm{air}, n_\mathrm{surf})\mathcal{R}(n_\mathrm{air}, n_\mathrm{surf})\mathcal{T}(n_\mathrm{surf}, n_\mathrm{air}) \\
&\qquad \times \mathcal{P}_\mathrm{sf}(d_1, \lambda, \alpha, 0)\mathcal{T}(n_\mathrm{air}, n_\mathrm{surf})\mathbf{E}_0(\psi_\mathrm{p}).
\end{aligned} \tag{38}$$

(8) Unbonded crossed fibres: reflection at the interface within the second fibre:

$$\begin{aligned}
&\mathbf{E}_8(\psi_\mathrm{p}, \psi_\mathrm{a}, \lambda, \alpha, \beta_\mathrm{f}) \\
&\quad = \mathcal{P}(\psi_\mathrm{a})\mathcal{T}(n_\mathrm{surf}, n_\mathrm{air})\mathcal{P}_\mathrm{sf}(d_1, \lambda, -\alpha, 0) \\
&\qquad \times \mathcal{T}(n_\mathrm{air}, n_\mathrm{surf})\mathcal{T}(n_\mathrm{surf}, n_\mathrm{air})\mathcal{P}_\mathrm{pc}(\Delta\phi(\lambda, d_2), \alpha + \beta_\mathrm{f}) \\
&\qquad \times \underbrace{\mathcal{R}(n_\mathrm{surf}, n_\mathrm{surf})}_{=0} \mathcal{P}_\mathrm{pc}(\Delta\phi(\lambda, d_2), \alpha + \beta_\mathrm{f})\mathcal{T}(n_\mathrm{air}, n_\mathrm{surf}) \\
&\qquad \times \mathcal{T}(n_\mathrm{surf}, n_\mathrm{air})\mathcal{P}_\mathrm{sf}(d_1, \lambda, \alpha, 0)\mathcal{T}(n_\mathrm{air}, n_\mathrm{surf})\mathbf{E}_0(\psi_\mathrm{p}) \\
&\quad = 0.
\end{aligned} \tag{39}$$

(9) Unbonded crossed fibres: reflection at the back surface of the second fibre:

$$\begin{aligned}
&\mathbf{E}_9(\psi_\mathrm{p}, \psi_\mathrm{a}, \lambda, \alpha, \beta_\mathrm{f}) \\
&\quad = \mathcal{P}(\psi_\mathrm{a})\mathcal{T}(n_\mathrm{surf}, n_\mathrm{air})\mathcal{P}_\mathrm{sf}(d_1, \lambda, -\alpha, 0) \\
&\qquad \times \mathcal{T}(n_\mathrm{air}, n_\mathrm{surf})\mathcal{T}(n_\mathrm{surf}, n_\mathrm{air})\mathcal{P}_\mathrm{sf}(d_2, \lambda, -\alpha, \beta_\mathrm{f})\mathcal{R}(n_\mathrm{surf}, n_\mathrm{air}) \\
&\qquad \times \mathcal{P}_\mathrm{sf}(d_2, \lambda, \alpha, \beta_\mathrm{f})\mathcal{T}(n_\mathrm{air}, n_\mathrm{surf})\mathcal{T}(n_\mathrm{surf}, n_\mathrm{air})\mathcal{P}_\mathrm{sf}(d_1, \lambda, \alpha, 0) \\
&\qquad \times \mathcal{T}(n_\mathrm{air}, n_\mathrm{surf})\mathbf{E}_0(\psi_\mathrm{p}).
\end{aligned} \tag{40}$$

The non-zero single intensities are shown in Fig. 5(b and c). (The chosen parameters will be discussed in Section 5.) The reflected Jones vectors $\mathbf{E}_1$ to $\mathbf{E}_9$ (see Fig. 5(a)) can be combined to total intensities by the absolute squares of their sums:

- Single fibre:

$$I_{\mathrm{ref,sf}} = |\mathbf{E}_1(\psi_\mathrm{p}, \psi_\mathrm{a}, \alpha) + \mathbf{E}_2(\psi_\mathrm{p}, \psi_\mathrm{a}, \lambda, \alpha) + \mathbf{E}_6(\psi_\mathrm{p}, \psi_\mathrm{a}, \lambda, \alpha, \beta_\mathrm{f})|^2. \quad (41)$$

- Fibre-to-fibre bond:

$$I_{\mathrm{ref,bond}} = |\mathbf{E}_1(\psi_\mathrm{p}, \psi_\mathrm{a}, \alpha) + \mathbf{E}_2(\psi_\mathrm{p}, \psi_\mathrm{a}, \lambda, \alpha) + \mathbf{E}_3(\psi_\mathrm{p}, \psi_\mathrm{a}, \lambda, \alpha, \beta_\mathrm{f}) + \mathbf{E}_4(\psi_\mathrm{p}, \psi_\mathrm{a}, \lambda, \alpha, \beta_\mathrm{f}) + \mathbf{E}_5(\psi_\mathrm{p}, \psi_\mathrm{a}, \lambda, \alpha, \beta_\mathrm{f})|^2. \quad (42)$$

- Crossing of two unbonded fibres:

$$I_{\mathrm{ref,cf}} = |\mathbf{E}_1(\psi_\mathrm{p}, \psi_\mathrm{a}, \alpha) + \mathbf{E}_2(\psi_\mathrm{p}, \psi_\mathrm{a}, \lambda, \alpha) + \mathbf{E}_6(\psi_\mathrm{p}, \psi_\mathrm{a}, \lambda, \alpha, \beta_\mathrm{f}) + \mathbf{E}_7(\psi_\mathrm{p}, \psi_\mathrm{a}, \lambda, \alpha, \beta_\mathrm{f}) + \mathbf{E}_8(\psi_\mathrm{p}, \psi_\mathrm{a}, \lambda, \alpha, \beta_\mathrm{f}) + \mathbf{E}_9(\psi_\mathrm{p}, \psi_\mathrm{a}, \lambda, \alpha, \beta_\mathrm{f})|^2. \quad (43)$$

5. Computational Results

With the intensities of the different geometries, given in Fig. 5(a), the system of plane-parallel plates, describing the fibres can be simulated, given the geometric parameters of the fibre. The refractive indices and the wavelength of the light used are known.

The angle of the bond, $\beta_\mathrm{f} = 85°$, can be obtained from Fig. 1(a). The microfibrilar angle, α, was chosen to be $\alpha = -27° = -0.471$ rad. Absolute values for the fibril angle of spruce pulp, the fibers used in our experiments, vary for individual fibers between 0° and 50° [17], an average angle of 27° is a reasonable choice. Cellulose fibrils in wood always form a right handed spiral along the fiber principal axes [18]. According to Fig. 4(a) the parameter of the microfibrillar angle, α, therefore has a negative sign. The refractive indices of a cellulose fibre in the longitudinal and transversal direction are $n_\mathrm{l} = 1.618$ and $n_\mathrm{t} = 1.554$, as given in [11].

The refractive indices in the fast and slow optical axes are given by the ellipse of refraction (see Fig. 4). For a given n_slow and n_fast, the transversal and longitudinal refractive indices are:

$$n_\mathrm{l} = \sqrt{n_\mathrm{fast}^2 \cos^2\alpha + n_\mathrm{slow}^2 \sin^2\alpha}, \quad (44)$$

$$n_\mathrm{t} = \sqrt{n_\mathrm{fast}^2 \sin^2\alpha + n_\mathrm{slow}^2 \cos^2\alpha}. \quad (45)$$

Solving the system for n_slow and n_fast yields:

$$n_\mathrm{slow} = \sqrt{\frac{n_\mathrm{t}^2 \cos^2\alpha - n_\mathrm{l}^2 \sin^2\alpha}{\cos^4\alpha - \sin^4\alpha}} \quad (46)$$

and

$$n_{\text{fast}} = \sqrt{\frac{n_{\text{t}}^2 \sin^2\alpha - n_{\text{l}}^2 \cos^2\alpha}{\sin^4\alpha - \cos^4\alpha}}. \tag{47}$$

It is to be expected that the refractive indices in the longitudinal and transversal direction are a function of the microfibrillar angle and that the refractive indices in the direction of the fast and slow optical axis stay rather constant. If the indices n_{slow} and n_{fast} were to be considered as a function of α, one would arrive at false answers for the intensity as a function of α (see Fig. 7). Equation (46) still gives a useful approximation of the refractive indices. With α chosen as above, this yields:

$$n_{\text{slow}}(\alpha = -0.471) = 1.63985, \tag{48}$$

$$n_{\text{fast}}(\alpha = -0.471) = 1.53092. \tag{49}$$

The thickness of the fibre can be measured from images taken from the microtome cuts. For the fibre-to-fibre bond shown in Fig. 1(a), the thickness of the first fibre is 3.054 μm and the thickness of the second fibre is 2.090 μm. The parameter d represents the thickness of only one s_2 layer (see Fig. 3(b)), while the thickness measured from the microtome images is the thickness of two s_2 layers. Thus the thickness has to be taken as half the measured thickness: 1.527 μm for the first fibre and 1.045 μm for the second fibre. The assumption that the fibre wall thickness equals the thickness of the s_2 layer is feasible, because this layer contains 80–95% of the fibre material [13]. The wavelength of the incident light was chosen in the visible range, $\lambda = 400$ nm for monochromatic calculations.

Figure 5(b) shows the calculated reflected, non-zero single intensities ($I_n = |E_n|^2$) as a function of the polarizer angle (ψ_{p}) and the analyzer angle (ψ_{a}). The different intensities show different periodic behavior. The reflected intensity on the top surface I_1, shows a phase shift of π resulting from the reflection on a medium with higher refractive index (equation (16)). The other intensities show a behavior similar to a $\lambda/2$ phase retarder plate (which also gives a phase shift of π) but with an additional shift in the maxima resulting from rotation of the polarization. Additionally, I_5 and I_9 (Fig. 5(b)) show a slight curve along the $\psi_{\text{a}} = -\psi_{\text{p}} + \pi/2$-direction, resulting from transmission-like behavior. The polarization rotation of the intensity maxima is higher at I_5 and I_9 than at I_6 and I_7 (Fig. 5(b)).

The case for crossed polarizers as a function of ψ_{p} is shown in Fig. 5(c). This represents a section through the intensities in Fig. 5(b) (along the line $\psi_{\text{a}} = \psi_{\text{p}} + \pi/2$). Here the shift of the maxima of intensity can be observed better. The intensities I_5 and I_9 (Fig. 5(c)) are shifted in respect to I_1 by $\pi/4$, while the intensities I_6 and I_7 (Fig. 5(c)) are shifted by about $\pi/6$. These shifts are the main reason for the effect of dark bonded areas, because the amplitude of the different intensity maxima is quite similar.

The intensities I_2, I_3, I_4 and I_8 are exactly zero (equations (33)–(35) and (39)). This is due to the fact that these are the intensities of reflection on the inner interface of a fibre, or on the bonded interface, where the index of refraction was set to

n_{surf} (equation (20)). This yields a reflectivity $\mathcal{R}(n_1 = n_2) = 0$ (equation (16)). The error arising from this approximation is not large. For a circular polarized wave, the difference in reflectivity cancels totally over a period: the biggest error is to be expected for a linear polarized wave, parallel to one of the optical axes of the two media (for example two s_2-layers of a pulp fibre), when these optical axes enclose an angle of 90°. The refractive index in the first medium would then be n_{slow} and in the second medium n_{fast} (or *vice versa*). This yields a reflectivity of:

$$\mathcal{R}(n_{\text{slow}}, n_{\text{fast}}) = \begin{pmatrix} -0.03 & 0 \\ 0 & 0.03 \end{pmatrix}, \tag{50}$$

with n_{slow} and n_{fast} chosen according to equation (46). This means a maximum error of 3% in every reflection or transmission, while most of these reflections and transmissions will take place with elliptically polarized light, making the error smaller.

The total intensities for reflection polarization microscopy are shown in the Figs 6 and 7. Figure 6(a) shows the resulting total intensity for a fibre-to-fibre bond, a single fibre, and crossed unbonded fibres as a function of the polarizer angle (ψ_{p}) enclosed by the principal axis of the fibre and the transmission axis of the polarizer, and the analyzer angle (ψ_{a}), enclosed by the transmission axis of the analyzer and the principal axis of the fibre. Fibre-to-fibre bond and an unbonded fibre crossing show the same shift of intensity maxima, resulting from the shift in the single intensities, while the behavior of the intensity of the single fibre is similar to a $\lambda/2$-phase retarder plate without a big shift (Fig. 6(a)). For a constant angle between the polarizer and the analyzer, it is always observed that the fibre-to-fibre bond has its maximum of intensity shifted in respect to the maximum of intensity of the single fibre by $\approx\pi/4$, such that it looks identical to the unbonded fibre crossing. This is due to the fact that the two reflections between the unbonded fibres (I_6 and I_7, Fig. 5(b)) interfere negatively while the reflection at the bonded surface (I_3) is zero because of the identical refractive indices on the two surfaces (equation (16)). The negative interference occurs because the reflection I_7 takes place at an interface from a medium with a lower refractive index to a medium with a higher index (specular reflection). This causes a phase shift of π at the reflection I_7, while the reflection I_6 (internal reflection) is not shifted (equation (16), Fig. 5(a)).

Experimentally the similarity between the bond and the crossing is a rather rare effect. This is not surprising because the probability of two fibres crossing each other exactly plane parallel is quite small. The difference in intensity between the fibre-to-fibre bond and the unbonded fibre crossing is only due to the relative alignment of the two fibres and, therefore, the correlation of dark bonded areas with the existence of fibre-to-fibre bonds is a purely statistical phenomenon.

The situation of Fig. 6(a) is plotted in Fig. 6(b) for crossed polarizers ($\psi_{\text{a}} = \psi_{\text{p}} + \pi/2$) for the case of a fibre-to-fibre bond, the two different single fibres (different thickness) and a crossing of the two unbonded fibres. The bond and the unbonded crossing yield an intensity that is smaller than the intensity of the single fibres by a factor 2. This is due to the fact that the single intensity I_6

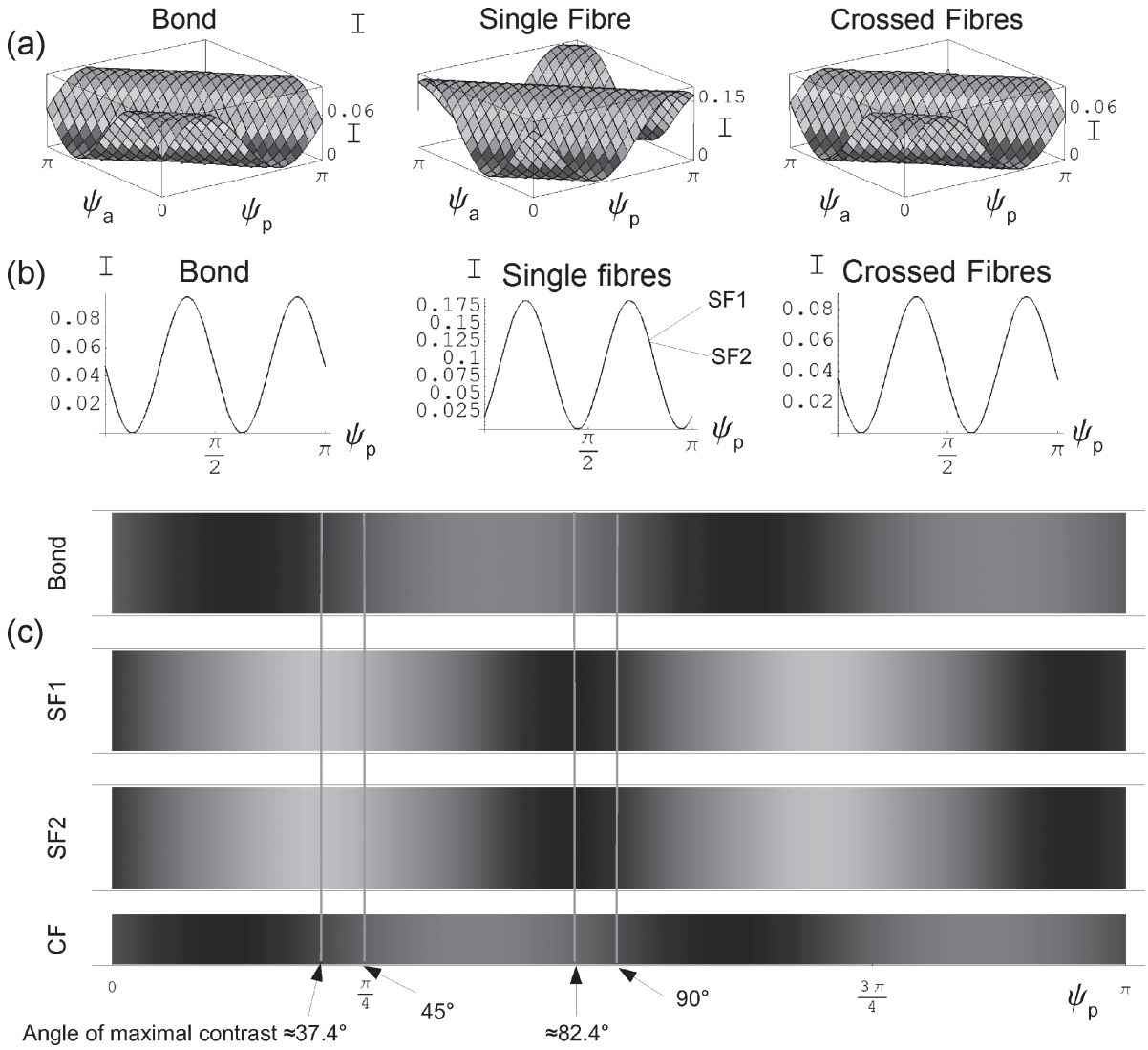

Figure 6. Reflected total intensities for two single fibres (SF1, SF2), their unbonded crossing (CF) and a fibre-to-fibre bond between them (bond). (a) As a function of polarizer (ψ_p) and analyzer angle (ψ_a), only one single fibre shown (SF1). (b) As a function of polarization angle (ψ_p) with crossed analyzer ($\psi_a = \psi_p + \pi/2$). (c) As a function of polarization angle (ψ_p) with crossed ($\psi_a = \psi_p + \pi/2$) analyzer and calculated reflection color. Compare the angles of high contrast to Fig. 1(a).

is preserved in the case of the single fibres, because it does not interfere negatively with I_7 (see Fig. 5(a)). A comparable illustration of the intensities and colors for $\alpha = -27°$ and crossed polarizers is given by Fig. 6(c). This result is in very good agreement to the microscope picture in Fig. 1(a), the bond area is clearly darker than the fibre (which can even be seen in the greyscale). Please note that two unbonded crossing fibres (Fig. 6(c), CF) would also form a crossing area that is darker than the fibers. The color functions were calculated from the spectra of the returned intensities weighed with the CIE-sensitivity functions for the human eye [16]. The colors should only be considered as a rough estimate.

Some conclusions can be drawn about the behavior of the system with different microfibrilar angles α: in reflection for $\alpha \to \pm\pi/4$, the effect of the dark bonds

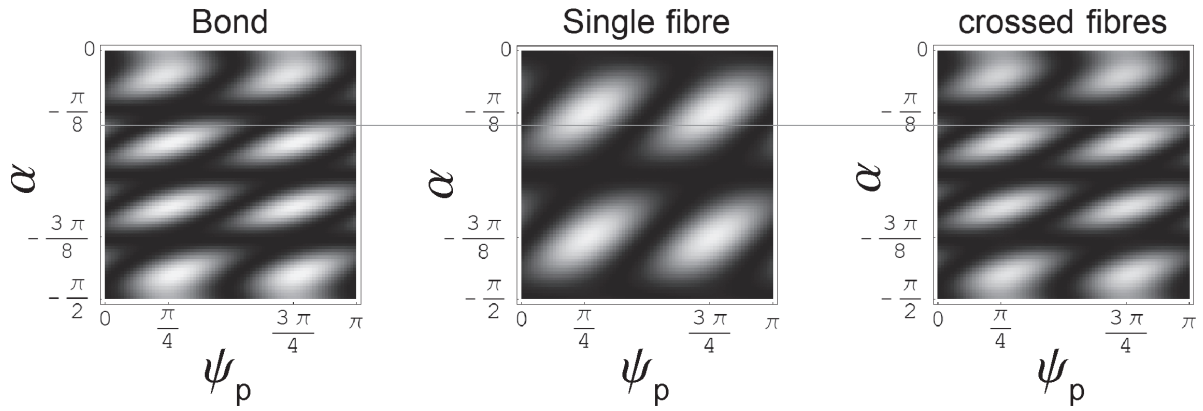

Figure 7. Reflection intensities for one single fibre (SF1), fibre-to-fibre bond and unbonded crossed fibres between crossed polarization filters, as a function of the angle of the polarizer (ψ_p) and the angle of the microfibrils (α). For $\alpha \to k \cdot \pi/4$ and $\alpha \to (2k+1) \cdot \pi/16$, with $k \in \mathbb{Z}$ the effect vanishes (see text). The line indicates the chosen parameter $\alpha = -27°$.

has to vanish due to the fact that the Jones matrices of a fibre for this case yield unity (see equation (24)). This fact is shown in Fig. 7 for crossed polarizers. The influence of the fibres vanishes at $\alpha = -\pi/4$, i.e., that the Jones matrices of the fibres at $\alpha = \pm\pi/4$ yield unity. With a microfibrillar angle $\alpha = \pm\pi/8, \pm 3\pi/8$, the bond would appear completely dark for all polarizer angles ψ_p. For a microfibrillar angle α of $\pm\pi/16, \pm 3\pi/16, \ldots$, the fibre-to-fibre bond and single fibres would have their intensity maxima at the same polarizer angle ψ_p (Fig. 7). Therefore it can be said that all the mentioned effects can only occur for microfibrillar angles $\alpha \neq k \cdot \pi/4$ and $\alpha \neq (2k+1) \cdot \pi/16$ with $k \in \mathbb{Z}$. The red line in Fig. 7 indicates the chosen angle $\alpha = -27°$.

To underline the validity of the model, further experiments regarding light dispersion of fibers under stress were carried out and simulated by the model. A comparison of experimental and computational results is shown in Fig. 8. Figure 8(a) presents a single fibre under longitudinally applied mechanical stress, in transmission microscopy. In this case the transmission axis of the analyzer was parallel to the principal axis of the fibre, while the polarizer was rotated (polarization angle, ψ_p indicated above the images). The fibre shows a dispersion that is depending on the polarization angle. The dispersion of this fibre under mechanical stress in longitudinal direction, was numerically analyzed. For the analysis, squares of 100×100 pixels from the middle of the fibre were extracted from the pictures and split into red, green and blue. Their mean values are shown in Fig. 8(b). A $\cos^2(\psi_p + \phi)$-dependency (with ψ_p being the angle enclosed by the principal axis of the fibre and the polarizer) with different phase-shifts ϕ for different colors can be observed. For fibres that were not under mechanical stress, the effect of phase-shifts between the different colors was not observable (see Fig. 8(d)).

Figure 8(c) shows the simulation of the same situation for the parameters $n_{slow} = 1.798$, $n_{fast} = 1.50$, $d = 2.46$ and $\alpha = -0.4$. The agreement between the calculated and the measured values is quite good, except for a total shift of the polarization angle by about 0.5 rad. It is impossible to make a distinct statement, as the geometric

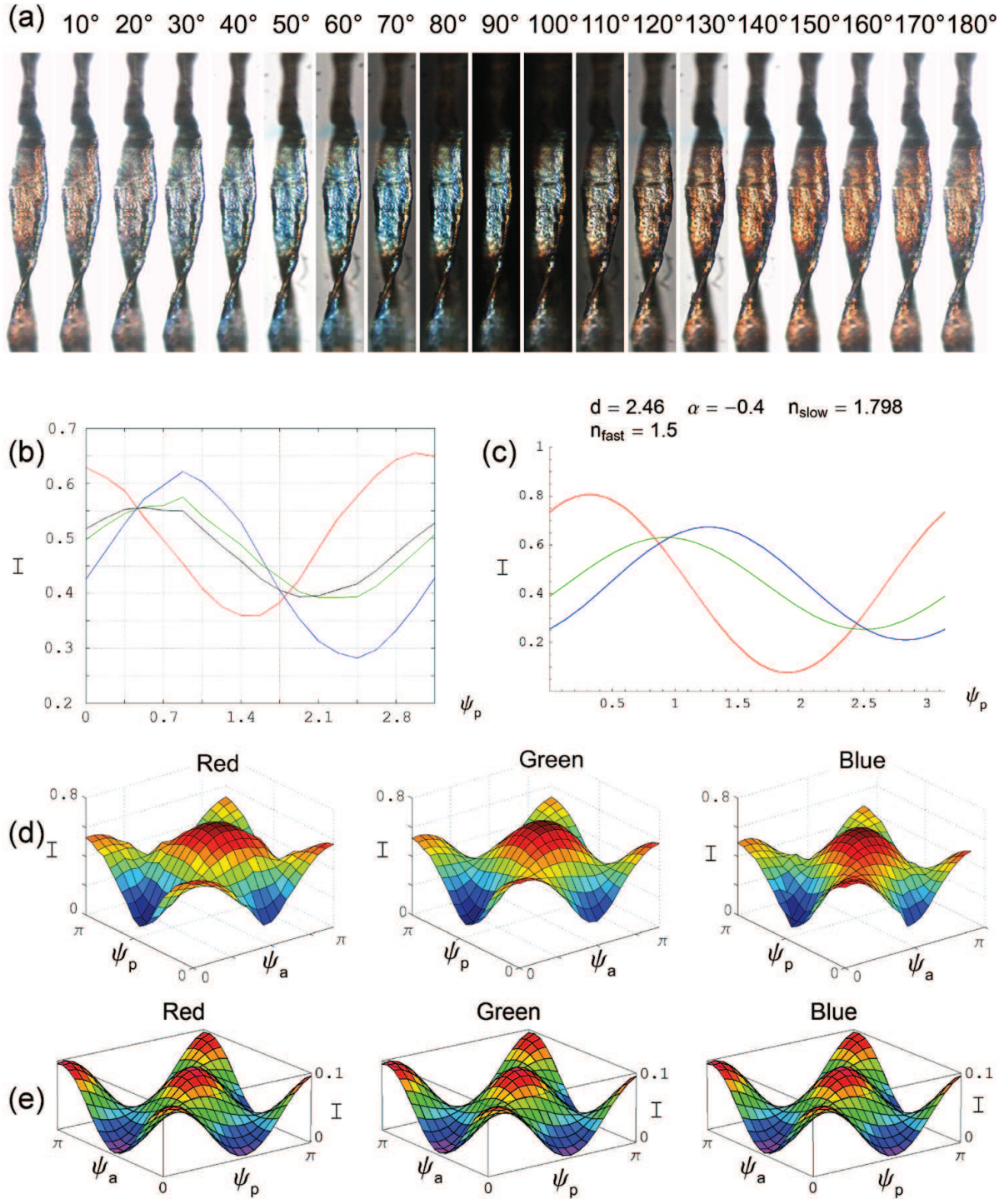

Figure 8. Comparison of measured data and calculation. (a) Single fibre under longitudinal mechanical stress in polarization transmission microscopy. The polarizer is rotated from $\psi_p = 0°$ to $\psi_p = 180°$, the analyzer stays parallel to the fibre. A dispersion, depending on the polarization angle can be observed. (b) Measured dispersion of a fibre in transmission under longitudinal mechanical stress, as a function of the polarization angle (shown in (a)), with the analyzer parallel to the fibre. (c) The effect of mechanical stress can be simulated with the model by reducing the absolute value of the angle of the microfibrils and increasing the anisotropy of refractive indices. (d) Measurement of transmission intensities for a single fibre as a function of polarizer and analyzer angle. Red, green and blue are separated numerically. (e) Simulation of (d) for polychromatic light (CIE color space R, G, B [16]).

parameters of the fibre investigated were not obtainable. A clear statement can be made: that the dispersion can indeed be described appropriately by the model, by increasing the optical anisotropy and by decreasing the microfibrillar angle.

The transmission intensity of a single fibre as a function of the angle between the transmission axis of the polarizer and the principal axis of the fibre (ψ_p) and the angle between the transmission axis of the analyzer and the principal axis of the fibre (ψ_a) was measured by a series of photographs. They were also analyzed for red, green and blue intensity. The results are shown in Fig. 8(d). The pictures show a behavior similar to a $\lambda/4$-phase retarder plate without noticeable dispersion, due to the absence of mechanical stress. Figure 8(e) shows the simulation of the same situation for a fibre with a thickness of $d = 1.85$ and with its microfibrillar angle $\alpha = -20°$. The calculation was carried out for polychromatic light, with the CIE red, green and blue functions [16] as weights (equation (30)). The experiment and the computation show a very high correlation. The broader peaks in the experimental data could be due to non-perfect polarization filters or ambient light.

6. Conclusions

A physical model is presented that describes reflection and transmission of pulp fibre surfaces under polarized vertical illumination. It employs the Jones formalism to model the optical appearance of pulp fibres and fibre-to-fibre bonds.

The model clearly shows that only for fibres that are fully collapsed and lie flat upon each other, thus resembling a system of plane parallel plates, the bonding areas appear as dark regions in polarization microscopy. If there are wrinkles or other irregularities in the fibre morphology no dark bonding region is visible under the microscope although the fibres are effectively bonded. Comparison of microscope images and microtome cuts of bonded fibres confirmed the model calculations. Not plane parallel fibre bonds, i.e., fibres with wrinkles in the bond or fibres with elliptic shape, did not show as bonds under polarization microscopy.

Furthermore it was found that fully collapsed, flat and parallel but unbonded fibres show a dark area in the crossing region, similar to the bonding region of bonded fibres. We know that paper has a highly layered structure where fibres are to a large extent aligned in the plane of the sheet, which makes it likely that a considerable amount of unbonded fibres in paper actually lie parallel to each other. Polarization microscopy on the one hand cannot identify all bonds between fibres and on the other hand some unbonded fibre crossings appear as bonds. Polarization microscopy cannot unambiguously discern between crossed unbonded fibres and bonded fibres, thus we find that this method is only to a limited extent suitable to determine bonded area of fibre-to-fibre bonds.

Calculations from the introduced model agreed very well with reflectance values measured from various bonded and unbonded chemical pulp fibres. It can be concluded that the presented model gives an accurate description of pulp fibre microscopy under polarized vertical illumination. Considering that the bonded area between fibres is a key factor for the mechanical and optical properties of paper,

a correct interpretation for polarized light microscopy images of pulp fibre-to-fibre bonds will contribute to a better understanding of paper network strength.

Acknowledgements

This work has been financed by Mondi Packaging Frantschach and the Christian Doppler Society of the Austrian Industrial Research Promotion Fund FFG. The authors are indebted to E. Schachinger for helpful discussion.

References

1. D. H. Page, A theory for the tensile strength of paper, *Tappi* **52**, 674–681 (1969).
2. T. Lindström, L. Wagberg and T. Larsson, On the nature of joint strength in paper — a review of dry and wet strength resins used in paper manufacturing, in: *13th Fundamental Research Symposium*, Cambridge, UK, pp. 457–562 (2005).
3. C. Yang, A. R. K. Eusufzai, R. Sankar, R. E. Mark and R. W. Perkins Jr., Measurements of geometrical parameters of fiber networks, Part 1. Bonded surfaces, aspect ratios, fiber moments of inertia, bonding state probabilities, *Svensk Papperstidning* **13**, 426–433 (1978).
4. G. Jayme and G. Hunger, Electron microscope 2- and 3-dimensional classification of fibre bonding, formation and structure of paper, in: *Transactions of the 2nd Fundamental Research Symposium*, Oxford, UK, pp. 135–170 (1961).
5. A. Torgnysdotter, The link between the fiber contact zone and the physical properties of paper: a way to control paper properties, *J. Compos. Mater*. **41**, 1619–1633 (2007).
6. C. I. Thomson, Probing the nature of cellulosic fibre interfaces with fluorescence resonance energy transfer, *PhD Thesis*, School of Chemistry and Biochemistry, Georgia Institute of Technology, USA (2007).
7. D. H. Page, Fibre-to-fibre bonds, Part 1. A method for their direct observation, *Paper Technol*. **1**, 407–411 (1960).
8. D. H. Page and P. A. Tydeman, Fibre-to-fibre bonds, Part 2. A preliminary study of their properties in paper sheets, *Paper Technol.* **1**, 519–530 (1960).
9. M. Donoser, M. Wiltsche and H. Bischof, A new automated microtomy concept of 3D paper structure analysis, in: *Proc. 9th IAPR Conference on Machine Vision Applications*, pp. 76–79 (2005).
10. E. Gilli, IR spectroscopic investigations on the chemical surface properties of cellulose fibres, *Master's Thesis*, Institute for Solid State Physics, Graz University of Technology, Austria (2008).
11. J. Brandrup and E. H. Immergut, *Polymer Handbook*. Wiley, New York, USA (1975).
12. J. Gullichsen and H. Paulapuro, Forest products chemistry, in: *Fapet Oy, Book 3*, pp. 24–26 (2000).
13. O. Bestsense and C. Ye, Method and device for determining the orientation angle of the optical axis and the relative phase retardation of a birefringent specimen, International Patent Number: WO 96/10168 (1995).
14. E. Hecht, *Optics*. Addison-Wesley Reading, MA, USA (1987).
15. W. Demtröoder, *Experimentalphysik 2*. Springer, Berlin, Germany (2006).
16. CIE Commission internationale de l'ecclairage, CIE 1964 Supplementary Standard Colorimetric Observer (1964), URL http://www.cie.co.at/publ/abst/datatables15_2004/x10.txt,/y10.txt,/z10.txt.
17. H. Jang, G. Weigel, R. Seth and C. Wu, The effect of fibril angle on the transverse collapse of papermaking fibers, *Paperi ja Puu* **84**, 112–115 (2002).
18. P. Viitaharju and K. Niskanen, Chiral curl in thin papers, *J. Pulp and Paper Soc*. **20**, J148–J152 (1994).

13. Paper submitted to Applied Optics

This publication can be regarded as the consequent continuation of the paper in the previous section (Sec. 12, (Gilli et al. 2009c)). The basic idea of this work was to find a distinguishing method for fiber-fiber bonds in an imaging method. After quite some work at the polarization microscopy, it seemed plausible, that imaging ellipsometry would yield by far better results, due to two reasons. First, in comparison to polarization microscopy, imaging ellipsometry is a quantitative method, where actual photometric parameters of the sample are measured, rather than the mere information of "brigth" or "dark". This first advantage could of course also be achieved with polarization microscopy, if implemented. The second, much more important reason is the availability of phase information in ellipsometric data. This results in two independent sets of data, and therefore, increases the chances of finding a possibility of distinguishing fiber-fiber bonds from other cases in a network.

With that idea in mind, the fiber model established in the previous publication on that topic (Gilli et al. 2009c) was used with a more powerful calculation method, namely a 4x4-transfer-matrix method (Berreman 1972), wich takes into account forward and backwards travelling waves, and therefore, also accounts for all interference effects that could take place in the different layers. For the case of arbitrarily oriented anisotropic multilayer systems the transfer matrices can be calculated by a solution given by Schubert (Schubert 1996), which reduces the problem to simple matrix inversion.

Many different apparatus approaches have been tried and simulated with this method. The one configuration that finally allowed a discrimination of fiber bonds from other cases is described and simulated in this following publication (Gilli and Schennach 2011).

This method has been filed for a german patent (E. Gilli, R. Schennach, "Vorrichtung und Verfahren zur Untersuchung von Faserkreuzungen und Faserbindungen in einem Fasernetzwerk", ref. no.: 10 2011 001 106.4, priority date: 4.3.2011). The paper was written by myself and all simulations were carried out by me.

References

Berreman, D. W. (1972). *Optics in Stratified and Anisotropic Media: 4x4-Matrix Formulation*. Journal of the Optical Society of America, **62**.(4), pp. 502–510.

Gilli, E. and Schennach, R. (2011). *Imaging ellipsometry based method and algorithm for the analysis of fiber-fiber bonds in a paper network*. Submitted to: Applied Optics,

Gilli, E., Kappel, L., Hirn, U., and Schennach, R. (2009c). *An optical model for polarization microscopy analysis of pulp fibre-to-fibre bonds*. Composite Interfaces, **16**.(5), pp. 901–922.

Schubert, M. (1996). *Polarization-dependent optical parameters of arbitrarily anisotropic homogeneous layered systems*. Physical Review B, **53**, pp. 4265–4274.

Imaging ellipsometry based method and algorithm for the analysis of fiber-fiber bonds in a paper network

Eduard Gilli[1, 2, *] and Robert Schennach[1, 2]

[1] *Institute of Solid State Physics, Graz University of Technology, Graz, Austria*

[2] *CD-Laboratory for Surface Chemical and Physical Fundamentals of Paper Strength, Austria*

The measurement of bonded ara of pulp fibers has been an unsolved issue in paper science for more than 40 years. By the use of an established pulp fiber model, and a 4x4-transfer matrix formalism we simulated the optical behaviour of pulp fibers in a modified imaging ellipsometer, and we demonstrate that there are rather strong symmetries in the ellipsometric angles Ψ and Δ when comparing single fibers, unbonded fiber crossings, and fiber-fiber bonds. Based on these symmetries we propose and test an algorithm which allows to distinguish the three cases single fibers, unbonded fiber crossings, and fiber-fiber bonds in the analysis of ellipsometric data.

OCIS codes: 100.3008, 110.5405, 120.2130, 160.1435.

*Corresponding author: gilli@tugraz.at

1. Introduction

Paper strength depends, roughly speaking, on the area of fiber-fiber bonds in the fiber network (relative bonded area) and the force of the bonds per unit area (specific bond strength). Relative bonded area, therefore, is one of the most important parameters of a paper network [1].

Several methods to measure the bonded area have been published, including microtome cutting [2–4], electron microscopy of formally bonded area [5], staining and light microscopy [6], fluorescence resonance energy transfer [7] and polarized light microscopy [8]. Despite a lot of work dedicated to the development of a measurement method to determine relative bonded area, no unambiguous non destructive method capable of paper network analysis is available thus far.

For the deeper understanding of the influence of network morphology onto the mechanical properties of paper it is necessary to link the morphological network parameters to mechanical testing. This cannot be done in a fundamental way without the availability of a nondestructive method, which is able to unambiguously decipher the complete fiber network. It is the objective of this paper to introduce such a method, based on an algorithm to analyze data from a modified imaging ellipsometer under normal incidence (also refered to as reflectance anisotropy). The method measures the area of fiber-fiber bonds in a paper network, i.e. independent of the alignment of the fibers. Simulation data show, that the method is able to distinguish single fibers, fiber-fiber bonds, and unbonded fiber crossings. Carried out in an imaging ellipsometric setup, the method can identify for each pixel of an image whether it shows an unbonded fiber crossing, a single fiber, a fiber-fiber bond or background.

It has to be emphasized, that this method is not limited to pulp fibers. The general idea of the proposed measurement system should be applicable to any kind of ansisotropic fiber material, such as regenerated cellulose fibers (viscose, etc.), or plastic fibers.

We will first describe the optical fiber model which has already been used sucessfully before [9–12]. Subsequently a detailed description of the simulation algorithm will be given, the optical setup will be described, and simulation data will be shown and discussed to demonstrate the feasibility of the described method.

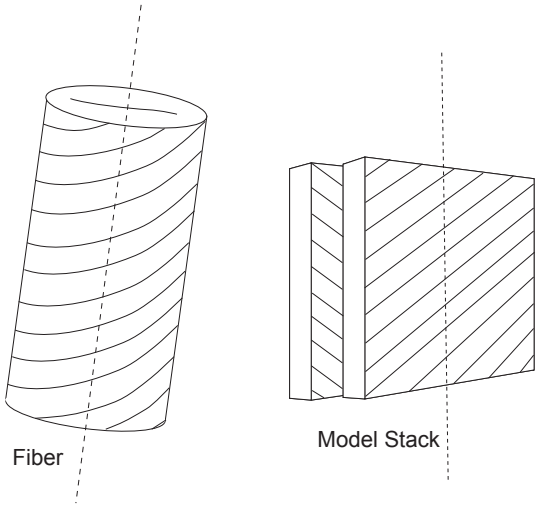

Fig. 1. Schematic drawing of the s_2-layer of a pulp fiber (left), and the layer stack used, to simulate the fiber. Hatching indicates the direction of the microfibrils, which can be identified with the slow optical axis. The dashed line indicates the principal fiber axis.

2. Simulation Methods

A. The Fiber model

A wood fiber consists of five layers of different order, thickness and crystallinity, which form a tube-like shape aroud the fiber lumen [13], which in a living wood cell is responsible for water transport. In refined pulp fibers the lumen is collapsed, and therefore, the fibers can be treated optically as a plane parallel layer stack. Only one of the layers of the fiber defines its optical behavior: The secondary fiber wall s_2, which makes up the major part of the fiber material (55%-70% of the wall thickness [13]) and has the highest order and crystallinity. The fiber wall s_2 consists of microfibrils (crystalline domains of cellulose polymers chains[13]), which form a helical shape around the lumen. The inclination angle of the helix (the microfibrillar angle) determines the optical axis of the layers. It strongly depends on the wood used for pulping, and can be found between 0° and 30° [14] in a right handed spiral [15]. This is depicted in the left hand frame of Fig. 1.

As an optical model, the fiber can be described as a two layer system of uniaxial anisotropic layers, whose optical axes are aligned to the microfibrillar angle. The right frame of Fig. 1 presents the layer stack model used to simulate the optical behaviour of pulp fibers. This model has already been used successfully for single fibers, fiber-fiber bonds and unbonded fiber crossings [9–12].

The unbonded fiber crossings and the fiber-fiber bonds can be modeled as a stack of two fibers with or without an air gap between them. Consequently a model of the single fiber, a fiber-fiber bond or a crossing of unbonded fibers can be built by a stack of plane parallel layers, where each layer has an individually rotated dielectric tensor.

The dielectric tensor of one s_2-layer of a fiber ϵ_{s_2}, without rotation is given by

$$\epsilon_{s_2}(0,0,0) = \begin{pmatrix} n_{fast}^2 & 0 & 0 \\ 0 & n_{slow}^2 & 0 \\ 0 & 0 & n_{fast}^2 \end{pmatrix}, \tag{1}$$

with the fast and slow refractive index of the fiber given by [10]

$$n_{fast} = 1.53092 \tag{2}$$

$$n_{slow} = 1.63985. \tag{3}$$

The rotation of the dielectric tensor can be carried out by a rotation, R_x, R_z, around the three Euler angles Ψ, Θ, Φ employing the rotation matrices

$$R_z(\alpha) = \begin{pmatrix} \cos\alpha & -\sin\alpha & 0 \\ \sin\alpha & \cos\alpha & 0 \\ 0 & 0 & 1 \end{pmatrix} \tag{4}$$

and

$$R_x(\alpha) = \begin{pmatrix} 1 & 0 & 0 \\ 0 & \cos\alpha & -\sin\alpha \\ 0 & \sin\alpha & \cos\alpha \end{pmatrix}, \tag{5}$$

and combining them to a full euler rotation

$$R_{Euler}(\Psi,\Theta,\Phi) = R_z(\Psi)R_x(\Theta)R_z(\Phi), \tag{6}$$

which gives for the dielectric tensor

$$\epsilon_{s_2}(\Psi,\Theta,\Phi) = R_{Euler}(\Psi,\Theta,\Phi)\epsilon_{s_2}(0,0,0)R_{Euler}^{-1}(\Psi,\Theta,\Phi). \tag{7}$$

The microfibrillar angle, or equivalently the optical axis can now be defined by a rotation by the Euler angle Ψ. The procedure is carried out in complete analogy for all the other layers. All adjustable parameters used in this model are depicted in Fig. 2.

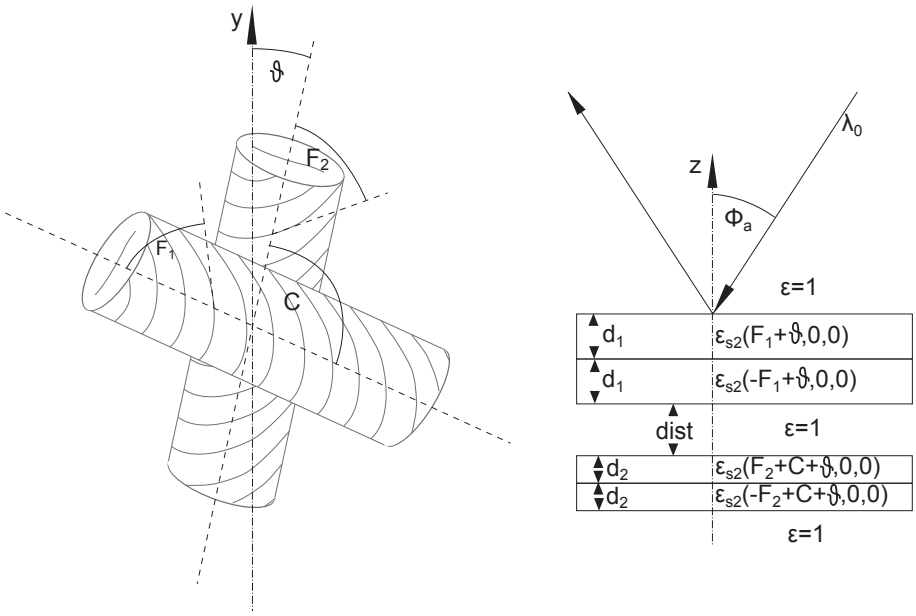

Fig. 2. Schematic drawing of the fiber crossing model, with all adjustable parameters of the simulation. ϑ: rotation of the system (both fibers) with respect to the coordinate system, F_1, F_2: microfibrillar angle of fiber 1 and 2, respectively, C: Crossing angle between the two fibers, d_1, d_2: Wall thickness of fiber 1 and 2, respectively, dist: Distance between the two fibers, Φ_a: angle of incidence, and λ_0: wavelength of the incident light.

A stack of arbitrarily many uniaxially or biaxially anisotropic layers of arbitrary orientation can be described by a 4x4 transfer matrix formalism introduced by Berreman [16]. A general solution to this formalism (for symmetric dielectric tensors) was given by Schubert [17]. For a detailed description of this algorithm, the reader is referred to [17, 18]. In the following we will discuss the compatibility of this formalism to Jones calculus, which will be used here, to simulate the apparatus surrounding the sample.

We start from the 4x4 transfer matrix T_{ij} following Schubert's nomenclature [17]

$$\begin{pmatrix} A_s \\ B_s \\ A_p \\ B_p \end{pmatrix} = \mathbf{T} \begin{pmatrix} C_s \\ D_s \\ C_p \\ D_p \end{pmatrix} = \begin{pmatrix} T_{11} & T_{12} & T_{13} & T_{14} \\ T_{21} & T_{22} & T_{23} & T_{24} \\ T_{31} & T_{32} & T_{33} & T_{34} \\ T_{41} & T_{42} & T_{43} & T_{44} \end{pmatrix} \begin{pmatrix} C_s \\ 0 \\ C_p \\ 0 \end{pmatrix}, \tag{8}$$

where $A_{s/p}$ is the incident wave, $B_{s/p}$ is the reflected wave, $C_{s/p}$ is the transmitted wave, and $D_{s/p}$ indicates a backwards travelling wave behind the sample and therefore is set to 0.

The sample in Jones matrix representation, $\mathbf{J}_{\mathrm{Pr}}$, reads

$$\mathbf{J}_{\mathrm{Pr}} = \begin{pmatrix} r_{pp} & r_{ps} \\ r_{sp} & r_{ss} \end{pmatrix}, \tag{9}$$

with the Jones reflection coefficients r_{ij}. These can be determined from the elements of T_{ij} (Eq. (8)) of the 4x4 transfer matrix [19]

$$r_{pp} = \frac{T_{11}T_{43} - T_{13}T_{41}}{T_{11}T_{33} - T_{13}T_{31}} \tag{10}$$

$$r_{sp} = \frac{T_{11}T_{23} - T_{13}T_{21}}{T_{11}T_{33} - T_{13}T_{31}} \tag{11}$$

$$r_{ps} = \frac{T_{33}T_{41} - T_{31}T_{43}}{T_{11}T_{33} - T_{13}T_{31}} \tag{12}$$

$$r_{ss} = \frac{T_{33}T_{21} - T_{31}T_{23}}{T_{11}T_{33} - T_{13}T_{31}}. \tag{13}$$

Therefore, the data from the simulation can be integrated into a surrounding optical setup by ordinary Jones calculus.

B. The Optical Setup

The measurement setup will be explained in the following. The setup is similar to a reflection microscope, employing some additional elements. Two equivalent versions of the setup are depicted in Fig. 3. The setup A consists of a monochromatic lightsource (not depicted in the figure), a polarizer with a fixed angle, a non-polarizing beamsplitter, a rotatable sample stage with a sample, a $\lambda/4$-retarder with its fast axis aligned to the polarizer, and an analyzer, which is depicted for the case of a 4 point rotating analyzer measurement. The analyzer, naturally, can also be realized by any other desired way, with additional retarders, or modulators. The setup B (Fig. 3) is equivalent to A. Here, the optical elements (polarizer, retarder and analyzer) are rotated, instead of the sample, which is an advantage for imaging data analysis, because the images are not rotated. Setup B employs an additional non-polarizing mirror, in order to compensate the phase shift that occurs at the beamsplitter.

In Jones formalism, the setups $\mathbf{J}_{\mathrm{A}}$ and $\mathbf{J}_{\mathrm{B}}$ can be represented as

$$\mathbf{J}_{\mathrm{A}} = \mathbf{J}_{\lambda/4}(0) \cdot \mathbf{J}_{\mathrm{BS}}(0) \cdot \mathbf{J}_{\mathrm{Pr}}(\vartheta) \cdot \mathbf{J}_{\mathrm{P}}(0), \tag{14}$$

$$\mathbf{J}_{\mathrm{B}} = \mathbf{J}_{\lambda/4}(-\vartheta) \cdot \mathbf{J}_{\mathrm{M}}(0) \cdot \mathbf{J}_{\mathrm{BS}}(0) \cdot \mathbf{J}_{\mathrm{Pr}}(0) \cdot \mathbf{J}_{\mathrm{P}}(-\vartheta), \tag{15}$$

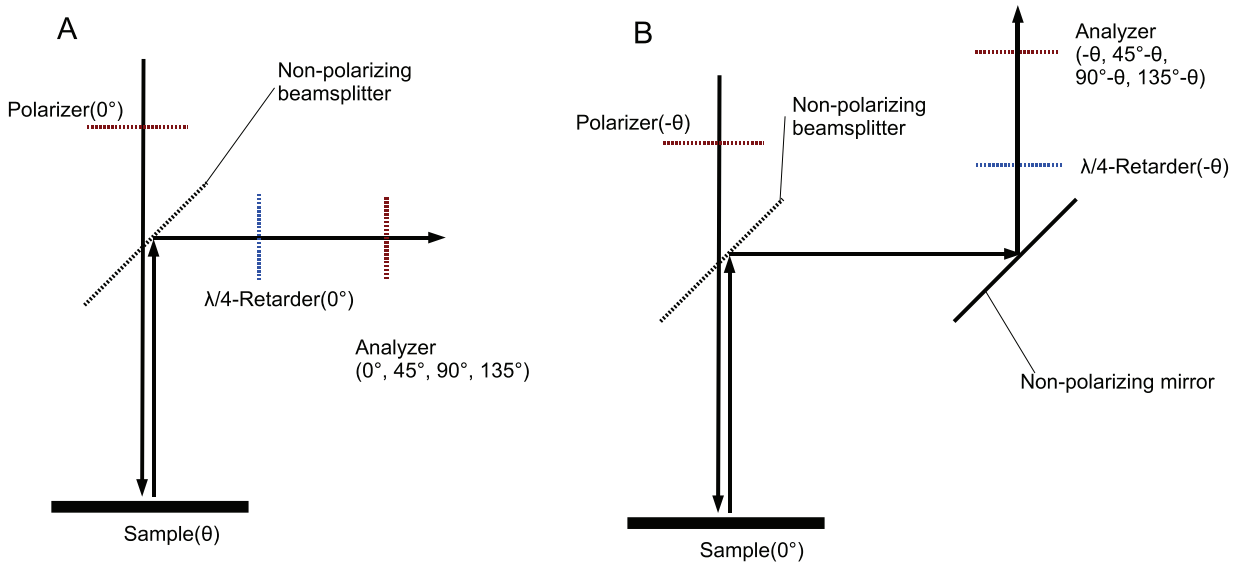

Fig. 3. Schematic image of the optical setup in two versions: A: The sample is rotated, B: The relevant optical components are rotated (see text).

with the Jones matrices of the optical elements:

$$\mathbf{J}_{\mathrm{P}} = \begin{pmatrix} 1 & 0 \\ 0 & 0 \end{pmatrix} \qquad \text{polarizer,} \tag{16}$$

$$\mathbf{J}_{\lambda/4} = \begin{pmatrix} -i & 0 \\ 0 & 1 \end{pmatrix} \qquad \lambda/4\text{-phase retarder,} \tag{17}$$

$$\mathbf{J}_{\mathrm{M}} = \begin{pmatrix} -1 & 0 \\ 0 & 1 \end{pmatrix} \qquad \text{non-polarizing mirror,} \tag{18}$$

$$\mathbf{J}_{\mathrm{BS}} = \begin{pmatrix} -0.5 & 0 \\ 0 & 0.5 \end{pmatrix} = 0.5 \cdot \mathbf{J}_{\mathrm{M}} \qquad \text{non-polarizing beamsplitter.} \tag{19}$$

Now the equivalence of the two setups (Eqns. (14)-(15)) can be shown. Setup A can be

reduced to

$$\begin{aligned}\mathbf{J}_{\mathrm{A}} =& \begin{pmatrix} -i & 0 \\ 0 & 1 \end{pmatrix} \begin{pmatrix} -0.5 & 0 \\ 0 & 0.5 \end{pmatrix} \begin{pmatrix} r_{pp} & r_{ps} \\ r_{sp} & r_{ss} \end{pmatrix} \begin{pmatrix} 1 & 0 \\ 0 & 0 \end{pmatrix} \\ =& 0.5 \begin{pmatrix} ir_{pp} & 0 \\ r_{sp} & 0 \end{pmatrix},\end{aligned} \tag{20}$$

and Setup B gives

$$\begin{aligned}\mathbf{J}_{\mathrm{B}} =& \mathbf{R}(-\vartheta)\mathbf{J}_{\lambda/4}(0)\,\mathbf{R}(\vartheta) \underbrace{\begin{pmatrix} -1 & 0 \\ 0 & 1 \end{pmatrix} \begin{pmatrix} -0.5 & 0 \\ 0 & 0.5 \end{pmatrix}}_{=0.5\cdot\mathbb{1}} \mathbf{J}_{\mathrm{Pr}}(0)\,\mathbf{R}(-\vartheta)\mathbf{J}_{\mathrm{P}}(0)\,\mathbf{R}(\vartheta) \\ =& 0.5\,\mathbf{R}(-\vartheta)\mathbf{J}_{\lambda/4}(0)\,\mathbf{R}(\vartheta)\mathbf{J}_{\mathrm{Pr}}(0)\,\mathbf{R}(-\vartheta)\mathbf{J}_{\mathrm{P}}(0)\,\mathbf{R}(\vartheta) \\ =& 0.5\,\mathbf{R}(-\vartheta)\mathbf{J}_{\lambda/4}(0)\mathbf{J}_{\mathrm{Pr}}(\vartheta)\mathbf{J}_{\mathrm{P}}(0)\,\mathbf{R}(\vartheta) \\ =& 0.5\,\mathbf{R}(-\vartheta) \begin{pmatrix} -ir_{pp} & 0 \\ r_{sp} & 0 \end{pmatrix} \mathbf{R}(\vartheta).\end{aligned} \tag{21}$$

with the rotation matrix $\mathbf{R}(\alpha)$

$$\mathbf{R}(\alpha) = \begin{pmatrix} \cos\alpha & -\sin\alpha \\ \sin\alpha & \cos\alpha \end{pmatrix}. \tag{22}$$

The difference between the two setups, therefore, consists of a change in sign and a rotated coordinate system. The rotated coordinate system has no effect, because the polarization state detector (consisting of a rotating analyzer in the drawing in Fig. 3) is rotated in setup B as well.

From the Jones matrix of the system we can obtain the ellipsometric angles Ψ and Δ, which are defined by

$$\hat{\rho} = \frac{r_p}{r_s} = \tan\Psi e^{-i\Delta}, \tag{23}$$

with the complex reflectivity $\hat{\rho}$. The complex reflectivity $\hat{\rho}$ can easily be obtained from the Jones matrix of the system as

$$\begin{aligned}\hat{\rho}_A &= i\frac{r_{pp}}{r_{sp}}, \\ \hat{\rho}_B(-\vartheta) &= -i\frac{r_{pp}}{r_{sp}},\end{aligned} \tag{24}$$

with the Jones reflection coefficients r_{pp} and r_{sp} obtained, according to Eqs. (10) and (11),

respectively. The ellipsometric angles follow straight forward as

$$\Psi = \arctan|\hat{\rho}|, \tag{25}$$

$$\Delta = -\arg\hat{\rho} = -\ln(\mathrm{Im}(\hat{\rho})). \tag{26}$$

The change in sign between setup A [Eq. (20)] and setup B [Eq. (21)] introduces a shift of the ellipsometric phase angle Δ by 180°. Therefore, the ellipsometric parameters for the two setups are given by

$$\begin{aligned} \hat{\rho}_B(-\vartheta) = -\hat{\rho}_A(0) = \hat{\rho}_A(0)e^{\pm i\pi} = \tan\Psi e^{i(\Delta\pm\pi)}, \\ \Psi_B = \Psi_A, \\ \Delta_B = \Delta_A \pm 180^\circ. \end{aligned} \tag{27}$$

This phase difference does not influence the algorithm, as will be shown in the following section.

3. Simulation Results

As discussed in the previous section it is equivalent to rotate the sample in a non rotating setup or to rotate the optical elements with a non rotating sample. The calculation of the sample rotation can easily be carried out by the azimut angle ϑ in the layer stack (rotation of all layers around the z-axis by the Euler angle Ψ). Therefore, the setup with the rotating sample was simulated, rather than the setup with the rotating elements.

To study the symmetries in the system, a simulation of a great number of different configurations of fibers, fiber-fiber bonds, and fiber crossings has been carried out, and the determined ellipsometric angles have been anlyzed in their dependency of the azimut angle ϑ of the sample. The applied simulation parameters are given in Tab. 1. The resulting ellipsometric angles as a function of the azimut of the sample are given as two-dimensional histograms in Fig. 4. The figure shows the frequency of the ocurrence of different values of the ellipsometric parameters over the saple's azimut in contour lines. Looking at the Ψ-histograms in Fig. 4, it is clearly visible that all 3 systems (single fibers, fiber crossings, fiber bonds) show distinct Ψ-minima close to an azimut of 45° and 135°. In the following, we will call these angles the critical angles. There are slight shifts in azimut between minima of the different systems, but over all the plots look quite similar. The minimum value at the minima however shows distinct differences for fiber-fiber bonds with respect to the two other systems. The Ψ-minima of the bonds are all smaller than 85.5°, whereas the Ψ-minima

Parameter	Minimum	Increment	Maximum
λ_0	658nm		
Φ_a	0°	0.5°	5°
ϑ	0°	1°	180°
C	0°	5°	90°
F_1	0.01°	5°	25.01°
F_2	0.01°	5°	25.01°
d_1	0.5μm	3.5μm	6.5μm
d_2	0.5μm	3.5μm	6.5μm
dist	0.1μm	0.5μm	2.6μm

Table 1. Simulation parameters used to study the symmetries of the system

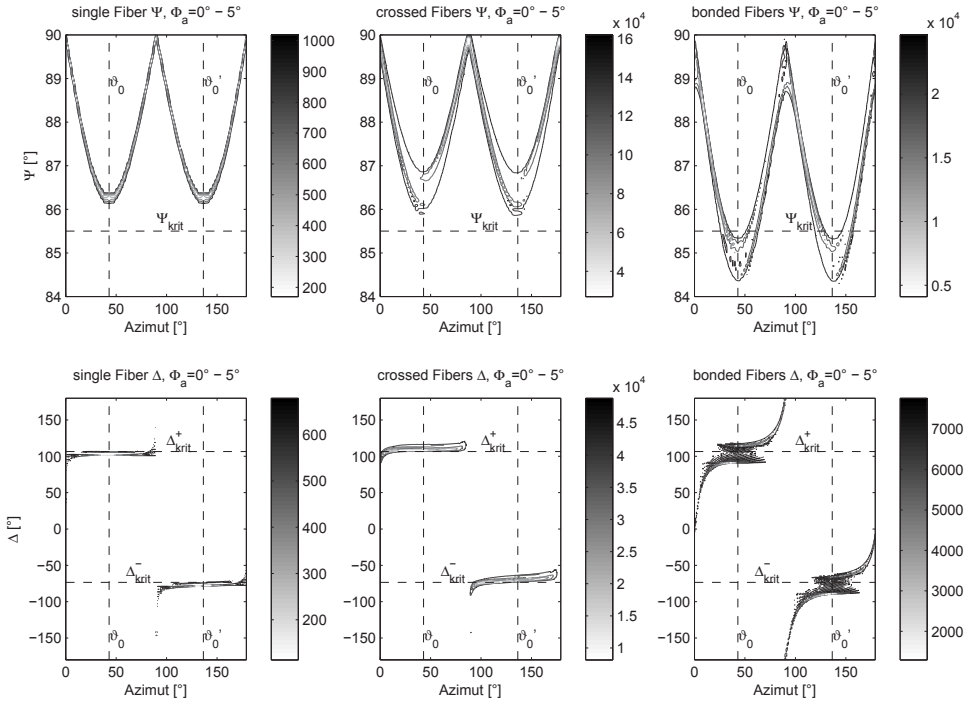

Fig. 4. Contour plot of a 2-dimensional histogramm of ellipsometric angles for single fibers (left hand frames), unbonded fiber crossings (center frames) and fiber bonds (right hand frames). Top frames: Ellipsometric angle Ψ, bottom frames: Ellipsometric angle Δ.

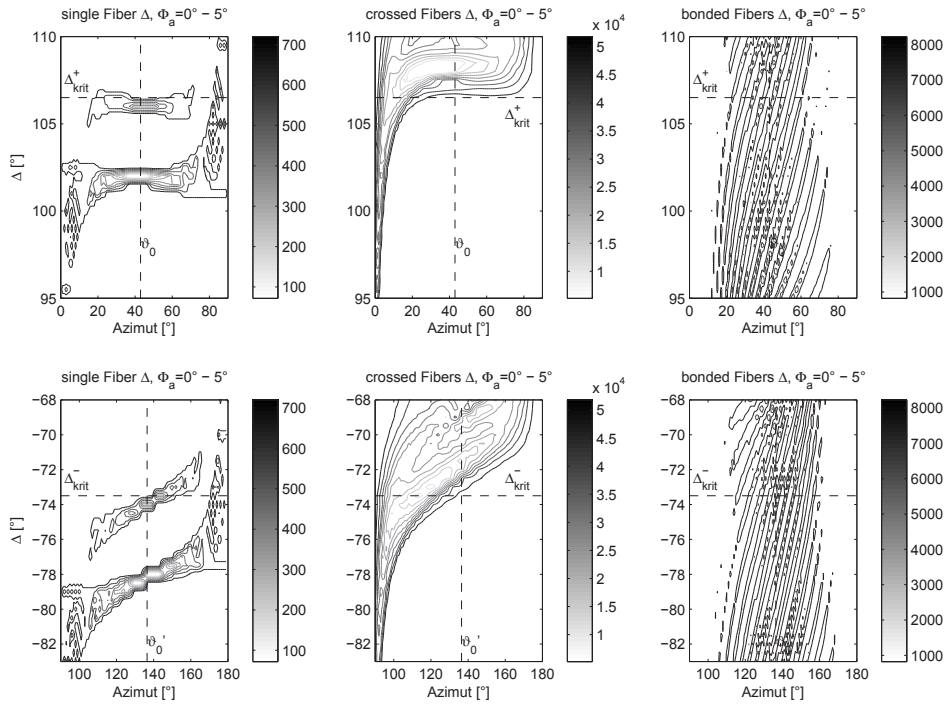

Fig. 5. Contour plot of a 2-dimensional histogramm of ellipsometric angles Δ for single fibers (left hand frames), unbonded fiber crossings (center frames) and fiber bonds (right hand frames).

of the other systems are all above this value. Therefore, by this difference an unambigous discrimination of fiber-fiber bonds from crossings or single fibers can be achieved, as long as the sample is measured from different azimut angles. We will, therefore, define the critical angle of Ψ

$$\Psi_{krit} = 85.5°. \tag{28}$$

The discrimination of single fibers and unbonded crossings is somewhat more subtle. It can be achieved analyzing the Δ-data at the critical angles. The single fibers show a smaller Δ-value at these angles than the crossed fibers. However, the ranges are quite close to each other, making the discrimination more sensible to noise. A detailed view of the relevant azimut- and Δ-ranges is given in Fig. 5. The figure shows Δ-histograms for azimut angles below 90° (top frames) and for azimut-angles above 90° (bottom frames), in the relevant Ψ-ranges, respectively. The two different ranges can be discriminated by the sign of Δ. By a comparison of the single fibers and the crossed fibers in Fig. 5 a discrimination of the two systems is possible, if the critical azimut angle ϑ_0 has already been detected and the fiber

bonds have already been sorted out.

Looking at the data in Fig. 5, it can be seen that at the critical azimut angle ϑ_0 the single fibers and the unbonded crossings are separable at a critical value. However there are two different critical values for azimut angles below, or above 90°. The two situations can be distinguished by the sign of Δ. We, therefore, define the critical angles of Δ:

$$\Delta^{+}_{krit} = 106.5° \tag{29}$$

$$\Delta^{-}_{krit} = -73.5°. \tag{30}$$

The Δ-values at the two critical angles differ by 180°. An algorithm to distinguish single fibers from unbonded fiber crossings needs to be independent from such shifts. Therefore, the shift in Δ between the two configurations discussed in the previous section has no influence on the detection algorithm.

4. Detection algorithm

With the symmetries, identified in the previous section, a simple and effective algorithm can be develloped to identify single fibers, fiber bonds, unbonded fiber crossings, and background. This algorithm, applied to data obtained with an imaging ellipsometer as described above, yields a non destructive and rapid analysis method for fiber networks.

Due to the azimut dependence, the data has to be obtained for a set of azimut angles within an interval of at least 90°, with an increment $\leq 20°$. Within this interval the critical azimut angle can be approximated by the minimum of Ψ. The following equations establish the analyzing algorithm:

$$\min[\Psi(\vartheta)] = \Psi(\vartheta_0) \tag{31}$$

$$\Psi(\vartheta_0) \begin{cases} < \mathbf{\Psi_{krit}} & \Rightarrow \textbf{fiber-fiber bond} \\ > \Psi_{krit} \rightarrow \begin{cases} \Delta(\vartheta_0) & \begin{cases} > 0 \;\; \Delta_{krit} = \Delta^{+}_{krit} \\ < 0 \;\; \Delta_{krit} = \Delta^{-}_{krit} \end{cases} \\ \Delta(\vartheta_0) & \begin{cases} > \mathbf{\Delta_{krit}} & \Rightarrow \textbf{single fiber} \\ < \mathbf{\Delta_{krit}} & \Rightarrow \textbf{unbonded crossing} \end{cases} \end{cases} \end{cases} \tag{32}$$

This detection algorithm has been tested with data produced by the simulation as follows. For a set of different fiber parameters, a randomly chosen starting azimut ϑ was applied. Starting from this azimut, a single fiber, an unbonded fiber crossing and a fiber-fiber bond

Parameter	Minimum	Increment	Maximum
λ_0	658nm		
Φ_a	0°	0.2°	3°
C	0°	5°	90°
F_1	0.01°	10°	30.01°
F_2	0.01°	10°	30.01°
d_1	0.5μm	1μm	8μm
d_2	0.5μm	1μm	8μm
dist	0.1μm	1μm	10μm

Table 2. Simulation parameters used to simulate the measurement with the algorithm, using noise-free data.

	case single	case bond	case crossing
detected as single	3 112 960	0	0
detected as bond	0	3 112 960	0
detected as crossing	0	0	3 112 960

Table 3. Detection rate for $n = 3112960$ simulated measurements, using noise-free simulation data.

were simulated for a set of azimut angles with an increment of 20° within a range of 180° (10 datapoints). Subsequently the detection algorithm was applied for each system and the results were saved in a 3x3 table.

Two results produced by simulated measurement will be discussed in the following. The first was carried out as described above. For the second test white noise was added to the data before the detection algorithm was applied.

The noise-free test was carried out for parameters given in Tab. 2, which represent about 3.1×10^6 simulated fiber measurements. The outcome of the detection algorithm is given in Tab. 3, showing a perfect detection rate. Obviously with a real measurement there will be noise, which will deteriorate the perfect outcome of the detection. But for a noise-free setup it can be said that the detection algorithm yields an unambigous and perfect discrimination of bonds, crossings and single fibers, as long as the distance between two unbonded fibers stays above 100 nm. It is noteworthy, that this 100nm limit is almost an order of magnitude

Parameter	Minimum	Increment	Maximum
λ_0	658nm		
ϑ	$0°$	$10°$	$120°$
Φ_a	$0°$	$1°$	$5°$
C	$0°$	$10°$	$90°$
F_1	$0.01°$	$2°$	$30.01°$
F_2	$0.01°$	$2°$	$30.01°$
d_1	0.5μm	1μm	7μm
d_2	0.5μm	1μm	7μm
dist	0.1μm	2μm	10.1μm

Table 4. Simulation parameters as used, to simulate the measurement with the algorithm, using noisy data with a noise level of 0.5% in Ψ and 3.5% in Δ.

smaller than the used wavelength. At such small distances the effect of optical tunneling starts to play a major role. Thus, we have a continuous transition from unbonded fiber crossings to fiber-fiber bonds at distances below 100nm.

For a realistic simulation of the measurement process, it is necessary to introduce noisy data. However, it cannot be assumed, that the noise level is the same in Ψ and Δ. Therefore, an estimate of the ratio of the noise levels is helpful. For the most simple of all methods to measure the ellipsometric parameters, the 4 point rotating analyzer method, we determined a noise level ratio in the given range of $\Psi \in [84°, 87°]$ and $\Delta \in [90°, 120°] \cap [-90°, -60°]$, of

$$\frac{\delta\Delta}{\delta\Psi} \leq 6.75, \tag{33}$$

with $\delta\Delta$ the noise level in Δ, and $\delta\Psi$ the noise level in Ψ.

For the simulation a noise level of 0.5% in Ψ was chosen. According to Eq. (33) this gives a noise level of about 3.5% in Δ. After simulating the ellipsometry parameters, white noise of the chosen level was added, and subsequently the detection algorithm was carried out. This was done for a set of fiber parameters given in Tab. 4

The results of this simulated measurement are given in Tab. 5, and show, that 99% of the bonds are still correctly identified. There is a a great amount of false interpretation between single fibers and crossings. In sum this makes 15% of false interpretations between unbonded fiber crossings and single fibers. However, crossings and single fibers can be distinguished

	case single	case bond	case crossing
detected as single	4 181 633	44 621	420 138
detected as bond	0	4 411 180	33 945
detected as crossing	274 208	40	4 001 758

Table 5. Detection rates for $n = 4515840$ simulated fiber configurations, using noisy simulation data.

from each other visually. The more improtant problem is the distinction between fiber-fiber bonds and unbonded crossings, which still shows a correct detection rate of 99% at this noise level. This, of course, is a consequence of the much lower noise level in Ψ, where the distinction between unbonded crossings and fiber-fiber bonds is carried out.

Using other polarization state analyzers instead of a rotating analyzer, would result in different noise level ratios. One could e.g. implement a phase modulating polarization state detector (see e.g. [20]) which comprises a much smaller noise level, and rapid measurement.

5. Summary

By the use of an established pulp fiber model, and a 4x4-transfer matrix formalism we have simulated the optical behaviour of pulp fibers in different configurations: As single fibers, as fiber-fiber bonds, and as unbonded fiber crossings. The discrimination of the latter two cases is an old measurement problem in fiber technology, not only in the case of a fiber network but also with individual fiber bonds. The simulation of these fiber systems in a modified imaging ellipsometer shows rather strong symmetries of the different cases, even over large ranges of different fiber wall thicknesses, different microfibrillar angles or fiber crossing angles. For each case the ellipsometric parameters can be found in well defined regions, which gives rise to a very simple algorithm which allows to distinguish the different cases from each other. We have shown by simulation of a large number of different fiber configurations that such an algorithm can unambiguously discern single fibers, unbonded fiber crossings, and fiber-fiber bonds from each other. Such a measurement, applied to a fiber network in an imaging ellipsometer is able to decipher the morphology of this network. This not only includes the detection of bonded and unbonded area; by use of the samples azimut angle ϑ, also the direction of the principal fiber axis can be determined.

References

1. T. Lindström, L. Wågberg, and T. Larsson, "On the nature of joint strength in paper-a review of dry and wet strength resins used in paper manufacturing," in "13th Fundamental Research Symposium," (Cambridge, 2005), pp. 457–562.
2. C. Yang, A. R. K. Eusufzai, R. Sankar, R. E. Mark, and R. W. Perkins Jr., "Measurements of geometrical parameters of fiber networks, part 1. bonded surfaces, aspect ratios, fiber moments of inertia, bonding state probabilities," Svensk Papperstidning **13**, 426–433 (1978).
3. M. Donoser, M. Wiltsche, and H. Bischof, "A new automated microtomy concept for 3d paper structure analysis," in "Proceedings of the 9th IAPR Conference on Machine Vision Applications," (2005), pp. 76–79.
4. M. Wiltsche, M. Donoser, J. Kritzinger, and W. Bauer, "Automated serial sectioning applied to 3D paper structure analysis," Journal of Microscopy **242**, 197–205 (2011).
5. G. Jayme and G. Hunger, "Electron microscope 2- and 3-dimensional classification of fibre bonding, formation and structure of paper," in "Transactions of the 2nd Fundamental Research Symposium Oxford," (1961), pp. 135–170.
6. A. Torgnysdotter, "The link between the fiber contact zone and the physical properties of paper: A way to control paper properties," Journal of Composite Materials **41**, 1619–1633 (2007).
7. C. I. Thomson, "Probing the nature of cellulosic fibre interfaces with fluorescence resonance energy transfer," Ph.D. thesis, School of Chemistry and Biochemistry, Georgia Institute of Technology (2007).
8. D. H. Page, "Fibre-to-fibre bonds, part 1 - a method for their direct observation," Paper technology **1**, 407–411 (1960).
9. O. Bestsense and C. Ye, "Method and device for determining the orientation angle of the optical axis and the relative phase retardation of a birefingent specimen," International Patent Number: WO 96/10168 (1995).
10. E. Gilli, L. Kappel, U. Hirn, and R. Schennach, "An optical model for polarization microscopy analysis of pulp fibre-to-fibre bonds," Composite Interfaces **16**, 901–922 (2009).
11. L. Kappel, U. Hirn, E. Gilli, W. Bauer, and R. Schennach, "Revisiting polarized light microscopy for fiber-fiber bond area measurement - part I: Theoretical fundamentals,"

Nordic Pulp & Paper Research Journal **25**, 65–70 (2010).

12. L. Kappel, U. Hirn, E. Gilli, W. Bauer, and R. Schennach, "Revisiting polarized light microscopy for fiber-fiber bond area measurement - part II: Poroving the applicability," Nordic Pulp & Paper Research Journal **25**, 71–75 (2010).
13. H. Sixta, ed., *Handbook of Pulp*, vol. 1 (Wiley-VCH Weinheim, 2006).
14. H. Jang, G. Weigel, R. Seth, and C. Wu, "The effect of fibril angle on the transverse collapse of papermakingfibers," Paperi ja Puu-Paper and Timber **84**, 112–115 (2002).
15. P. Viitaharju and K. Niskanen, "Chiral curl in thin papers," Journal of Pulp and Paper Science **20**, J148–J152 (1994).
16. D. W. Berreman, "Optics in stratified and anisotropic media: 4x4-matrix formulation," Journal of the Optical Society of America **62**, 502–510 (1972).
17. M. Schubert, "Polarization-dependent optical parameters of arbitrarily anisotropic homogeneous layered systems," Physical Review B **53**, 4265–4274 (1996).
18. M. Schubert, *Infrared Ellipsometry on Semiconductor Layer Structures. Phonons, Plasmons and Polaritons* (Springer, Berlin, Heidelberg, New York, 2004).
19. H. Fujiwara, *Spectroscopic Ellipsometry - Principles and Applications* (John Wiley & Sons, Hoboken, NJ, USA, 2007).
20. P. A. Letnes, I. S. Nerbø, L. M. S. Aas, P. G. Ellingsen, and M. Kildemo, "Fast and optimal broad-band stokes/mueller polarimeter design by the use of a genetic algorithm," Optics Express **18**, 23095–23103 (2010).

14. Subsumption

The necessity of a reliable method to determine bonded area in a paper fiber network has been discussed. Building up from these premises two substantial contibutions have been made. First the optical theory behind the phenomena of fibers in a polarization microscope could be elucidated, and it could be shown that the approach to detect fiber bonds in a polarization microscope does not yield clear statements in a straight forward way (Gilli et al. 2009c; Kappel et al. 2010a). This, however, can be improved by staining one of the fibers of a single fiber-fiber bond (Kappel et al. 2010b), that at least for single fiber bonds the optically bonded area can be detected. A shortcoming of this approach is the staining. It can not be completely ruled out, that the staining of one of the fibers influences the chemistry of the bond itself. Therefore, this approach has to be used with caution.

A clear improvement to this situation is given by the second contribution to this topic (Gilli and Schennach 2011). By the simulation of monochromatic imaging ellipsometric data of fibers, fiber crossings, and fiber bonds, and a systematic analysis of the phase spaces of all relevant degrees of freedom of this system, symmetries could be found that allow for a simple discrimination of fiber bonds, fiber crossings and single fibers.

This approach has several advantages, the most important of them being the invariance in fiber specific parameters (fiber wall thickness, microfibrilar angle, crossing angle, fiber distance), the independence from the sample rotation angle, the feasibility of measurement of networks, and the non-destructiveness. Therefore, this method can be employed in fiber networks, to give detailed laterally resolved information of the network, which would be perfectly suited for finite element network simulations in connection to mechanical testing.

References

Gilli, E. and Schennach, R. (2011). *Imaging ellipsometry based method and algorithm for the analysis of fiber-fiber bonds in a paper network*. Submitted to: Applied Optics,

Gilli, E., Kappel, L., Hirn, U., and Schennach, R. (2009c). *An optical model for polarization microscopy analysis of pulp fibre-to-fibre bonds*. Composite Interfaces, **16**.(5), pp. 901–922.

Kappel, L., Hirn, U., Gilli, E., Bauer, W., and Schennach, R. (2010a). *Revisiting Polarized Light microscopy for fiber-fiber bond area measurement - Part I: Theoretical fundamentals*. Nordic Pulp & Paper Research Journal, **25**, pp. 65–70.

Kappel, L., Hirn, U., Gilli, E., Bauer, W., and Schennach, R. (2010b). *Revisiting polarized Light microscopy for fiber-fiber bond area measurement - Part II: Poroving the applicability.* Nordic Pulp & Paper Research Journal, **25**, pp. 71–75.

Part IV.

Summary and Outlook

15. Summary

The work of this dissertation started off from a point where it was virtually impossible to quantify spectral features of reflectance spectra of paper sheets. For this issue, an elegant solution could be found in employing polarization modulated spectra, obtained by a method described in (Schennach et al. 2009), empolying two polarizers in a standard spectrometer. The former is used to normalize the intensity in s- an p-polarization, while the latter is repeatedly switched between the two directions. This method was extensively used for different systems, because it turned out not only to be quite nicely useable for the quantitative interpretation of spectral features of paper sheets, as e.g. used in the publications (Gilli et al. 2009a) and (Gilli et al. 2011b), but also for the determination of optical constants of powdered samples as published in Applied Spectroscopy (Gilli and Schennach 2010).

The new aspects here are mainly the adoption of a method typically used in surface science for the analysis of smooth surfaces and thin layers to the very irregular surfaces of paper sheets. However complex the implicated effects of such an unordered system of multi-layered fibers with fiber diamerers in the range of the used radiation may be, the experiments show a very good contrast and make a semiquantitative chemical analysis of the pulps possible. The optimal incidence angle for this measurement on paper was found to be 62°.

The very complex scattering behaviour of a paper network - comprising of unordered multi-layered elongated structures - does not allow for quantitative analysis of spectral features witout calibration. Therefore, the possibility of employing cellulosic model films was chosen, in order to get a more fundamental hold of the surface processes, and the interaction of cellulose and hemicelluloses.

This approach has the additional advantage to yield the necessary link between the mechanical behaviour of fiber-fiber bonds and the chemical and geometrical analysis by infrared spectroscopy, simply by the possibility of macroscopic mechanical testing of these films, or bonds built from such films. On the other hand, there is little scattering on flat parallel model film systems which very much easens the spectral analysis. Furthermore, it opens the possibility of spectral simulation, and therefore, yields a possibility of quantification of spectral features without a calibration, as shown in the paper (Djak et al. 2011). Being able to simulate these spectra, depending on adjustable parameters can yield - if correctly done - additional valuable information about the geometry, the uniformity, crystallinity and isotropy.

A necessary preriquisite for spectral simulation is the knowledge about the optical constants of the materials involved, namely of the complex dielectric functions. To measure these functions on solid powdered samples, and to bring them into a form suitable for simulation was a major part of the dissertation (Gilli and Schennach 2010).

Building up on these new possibilities the model films could be quantified geometrically by optical simulation of the measured spectra (Djak et al. 2011).

During the work with the polarization modulated spectroscopy it turned out that the method of choice for the thin cellulose films, and the measurement of the optical constants of the cellulosic materials would be spectroscopic infrared ellipsometry. This led to the idea of devellopping an ellipsometer unit, for use in the Bruker spectrometer used at the institute (Gilli et al. 2011c; Gilli et al. 2011e; Gilli et al. 2011d).

A proof of concept for this ellipsometer unit was made by a prototype built within the framework of this dissertation at the institute of Solid State Physics. With this working prototype, financed by the prototoype prize (PRIZE 2009) of the Austria Wirtschaftsservice (AWS), it was possible to find an industrial partner, who is interested in further developing the system and will possibly build a commercial ellipsometer based on this system.

A topic which at a first glance seems quite remote to the above mentioned research is the microscopic optical behaviour of pulp fibers and pulp fiber networks. However, this is a question of high interest for paper research, and is the missing link between bonding strength and paper strength, because a thorough understanding of the paper network is one of the main issues to fully understand the mechanical behaviour of paper.

Here two contributions were made which for themselves constitute a self-contained part of this dissertation. Starting off from a polarization microscopy method from the 1960ies (Page 1960) an optical model for pulp fibers and bonds was developed and simulated. With the simulations it could be shown that this method did not work the way described and generally accepted. The proposed model can explain the phenomena of pulp fibers in the polarization microscope to a very accurate degree (Gilli et al. 2009c). This model was later used again with a much more powerful and general 4x4 transfer matrix formalism by D.W. Berreman (Berreman 1972) and the general numerical solution to the same by M. Schubert (Schubert 1996). Here the fiber bond was simulated for a modified imaging ellipsometer (Gilli and Schennach 2011). In the course of these simulations a method was be found that could finally solve the old measurement problem in paper science of fiber-fiber bonded area, and yield a contact free, rapid and accurate method to decrypt pulp fiber networks, in a very general way. A proof of concept in terms of a working prototype does not exist yet, but due to the quite simple setup needed it is probably only a question of time.

The accomplishments of this work can be summarized as follows:

- Application of pm-IRRAS on paper sheets and proof of feasibility by quantitative characterization of two different chemical processes on the fiber surfaces.
- Application of Cellulose model films.
- Application of the pm-IRRAS method for the measurement of dielectric functions of cellulosic materials.
- Modelling infrared spectra of cellulose model films and measuring film thickness by best match calculation.

- Development and construction of a prototype of a mid infrared variable angle spectroscopic ellipsometry unit for a Bruker ifs66v/s Fourier transform infrared spectrometer (Austrian patent, international patent pending).
- Model for the optical behaviour of cellulose fibers in the visible range.
- Application of that model to explain the problems of a polarization microscopy based method to measure bonded area.
- Application of the same model to find symmetries in the phase spaces of all degrees of freedom of a cellulose fiber-fiber bond in an imaging ellipsometer.
- Employing these symmetries into a detection algorithm to distinguish fiber bonds from fiber crossings (German patent pending).

References

Berreman, D. W. (1972). *Optics in Stratified and Anisotropic Media: 4x4-Matrix Formulation*. Journal of the Optical Society of America, **62**.(4), pp. 502–510.

Djak, M., Gilli, E., Kontturi, E., and Schennach, R. (2011). *Thickness dependence of reflection absorption infrared spectra of supported thin Polymer films*. Macromolecules, **44**.(7), pp. 1775–1778.

Gilli, E., Horvath, A. E., Horvath, A. T., Hirn, U., and Schennach, R. (2009a). *Analysis of CMC attatchment onto cellulosic fibers by infrared spectroscopy*. Cellulose, **16**.(5), pp. 825–832.

Gilli, E. and Schennach, R. (2010). *Determination of Noise-Free Optical Constants in the Infrared by Kramers-Kronig Troansformation of the Reflectance Ratio in s- and p-Polatization*. Applied Spectroscopy, **64**.(6), pp. 669–681.

Gilli, E. and Schennach, R. (2011). *Imaging ellipsometry based method and algorithm for the analysis of fiber-fiber bonds in a paper network*. Submitted to: Applied Optics,

Gilli, E., Kappel, L., Hirn, U., and Schennach, R. (2009c). *An optical model for polarization microscopy analysis of pulp fibre-to-fibre bonds*. Composite Interfaces, **16**.(5), pp. 901–922.

Gilli, E., Schmied, F., Diebald, S., Horvath, A. T., Teichert, C., and Schennach, R. (2011b). *Analysis of lignin precipitates on ozone treated kraft pulp by FTIR and AFM*. Submitted to: Cellulose,

Gilli, E., Kornschober, M., and Schennach, R. (2011c). *Optical arrangement and proof of concept prototype for mid infrared variable angle spectroscopic ellipsometry*. Submitted to: Infrared Physics & Technology,

Gilli, E., Schennach, R., and Kornschober, M. (2011d). *Optical arrangement for ellipsometry*. PCT Patent Application. WO 2011/022745 A1.

Gilli, E., Schennach, R., and Kornschober, M. (2011e). *Optische Anordnung für Ellipsometrie*. AT Patent Application. AT 508 690 A1.

Page, D. H. (1960). *Fibre-to-fibre bonds, Part 1 - A method for their direct observation*. Paper technology, **1**.(4), pp. 407–411.

Schennach, R., Hirschmugl, C., Gilli, E., and Tysoe, W. T. (2009). *A New Method for Performing Polarization-Modulation Infrared Reflection-Absorption Spectroscopy of Surfaces.* Applied Spectroscopy, **63**.(3), pp. 369–372.

Schubert, M. (1996). *Polarization-dependent optical parameters of arbitrarily anisotropic homogeneous layered systems.* Physical Review B, **53**, pp. 4265–4274.

16. Outlook

This thesis ends at a point were many different methods have been developed to be usable with cellulose systems and paper. The quantitative and systematic results are yet to be produced. This will be the main direction of future work.

Especially the method of polarization modulated IRRAS on model films should be employed for systematic studies. Some effort also still has to be put into the simulation of more layers on the cellulose model films, which inevitably means measuring the dielectric functions of more materials. As we now have a method available to do so, this is not a principle problem.

The main focus of the remaining work to do until the end of the CD-Lab will be harvesting results in paper science from the methods which are now implemented. The cellulosic model film systems have a high potential of yielding more insight into the fundamental bonding processes, and therefore, studies of well chosen different surface treatments and their effect on bonding force and energy will be a major part of future work.

The combination of infrared spectroscopy and scanning probe methods should also be intensified in the follow up work, especially in the direction of kelvin probe force microscopy where, as first tests imply, celluloses and hemicelluloses can possibly be distinguished. The interaction of cellulose and hemicelluloses is one of the key questions in the fiber-fiber bond, not only for pulp, but also for synthetic cellulose fibers, such as viscose.

17. Acknowledgements

Many people should be acknowledged here, as it is with interdisciplinary research. Therefore, I start this by appologizing by all those people who I did not mention here.

I want to thank my family for their patience, and encouragement. I thank my supervisor Robert Schennach for the kind, encouraging and helpful mentoring of my work. The many inspiring and helpful discussions with Ewald Schachinger and his attendance to proof-read many of my manuscripts also shall be mentioned here. I thank my colleagues from the CD-Lab (alphabetical): Wolfgang Bauer, Robert Schnenach, Stefan Diebald, Mario Djak, Rene Eckhart, Wolfgang Fischer, Christian Ganser, Ulrich Hirn, Barbara Hummer, Lisbeth Kappel, Franz Schmied, Christian Teichert, Frederic Weber, and all the others I did forget.

This work was financially supported by the Christian Doppler Research Society (Christian Doppler Gesellschaft) and the industrial partner of the Christian Doppler Laboratory for Surface Chemical and Physical fundamentals of Paper Strength, Lenzing AG.

Bibliography

Arakawa, E. T., Inagaki, T., and Williams, M. W. (1980). *Optical Poroperties of Metals by Spectroscopic Ellipsometry*. Surface Science, **96**, pp. 248–274.

Arwin, H., Askendahl, A., Tengvall, P., Thompson, D. W., and Woolam, J. A. (2008). *Infrared ellipsometry studies of thermal stability of protein monolayers and multilayers*. Physica Status Solidi C, **5**, pp. 1438–1441.

Avery, D. G. (1952). *An Improved Method for Measurements of Optical Constants by Reflection*. Proceedings of the Physical Society. Section B, **65**.(6), pp. 425–428.

Bakker, J. W. P., Bryntse, G., and Arwin, H. (2004). *Determination of refractive index of printed and unprinted paper using spectroscopic ellipsometry*. Thin Solid Films, **455-456**, pp. 361–365.

Bar, G, Thomann, Y, Brandsch, R, Cantow, H. J., and Whangbo, M. H. (1997). *Factors affecting the height and phase images in tapping mode atomic force microscopy. study of phase-separated polymer blends of poly(ethene-co-styrene) and poly(2,6-dimethyl-1,4-phenylene oxide)*. Langmuir, **13**.(14), pp. 3807–3812.

Barsberg, S. (2010). *Prediction of Vibrational Spectra of Polysaccharides - Simulated IR Spectrum of Cellulose Based on Density Functional Theory*. J Phys Chem, **114**.(36), pp. 11703–11708.

Barzyk, D, Page, D. H., and Ragauskas, A (1997a). *Acidic group topochemistry and fibre-to-fibre specific bond strength*. J Pulp Pap Sci, **23**.(2), J59–J61.

Barzyk, D, Page, D. H., and Ragauskas, A (1997b). "Carboxylic acids groups and fibre bonding". In: *The fundamentals in papermaking materials: the transaction of the 11th fundamental research symposium*. Vol. 2. Cambridge, UK, pp. 893–907.

Bernazzani, P., Sanches, R. F., Woodward, M., and Williams, S. (2008). *Determination of the glass transition temperature of thin unsupported polystyrene films using interference fringes*. thin Solid Films, **516**, pp. 7947–7951.

Bernhard, C., Humlicek, J., and Kreimer, B. (2004). *Far-infrared ellipsometry using a synchrotron light source - the dielectric response of the cuprate high T_c superconductors*. Thin Solid Films, **455-456**, pp. 143–149.

Berreman, D. W. (1969). *Infrared Absorption at Longitudinal Optic Frequency in Cubic Crystal Films*. Physical Review, **130**, pp. 2193–2198.

Berreman, D. W. (1967). *Kramers-Kronig Analysis of Reflectance Measured at Oblique Incidence*. Applied Optics, **6**.(9), pp. 1519–1521.

Berreman, D. W. (1972). *Optics in Stratified and Anisotropic Media: 4x4-Matrix Formulation*. Journal of the Optical Society of America, **62**.(4), pp. 502–510.

Bestsense, O. and Ye, C. (1995). *Method and device for determining the orientation angle of the optical axis and the relative phase retardation of a birefingent specimen*. PCT Patent. WO96/10168.

Boher, P., Piel, J. P., and Sacepe, B. (2004). *Generalized ellipsometry for the characterization of anisotropic materials: influecne of the sample adjustment on the extracted optical incidices*. Thin Solid Films, **455-456**, pp. 581–585.

Borstel, G. and Falge, H. J. (1977). *Surphace Phonon-Polaritons at Semi-Infinite Crystals*. Physica Status Solidi B, **83**.(11), pp. 11–45.

Brandrup, J. and Immergut, E. H. (1975). *Polymer Handbook*. New York: Wiley.

Capitàn, M. J., Rueda, D. R., and Ezquerra, T. A. (2004). *Inhibition of the Crystallization in Nanofilms of Poly(3-hydroxybutyrate)*. Macromolecules, **37**.(15), pp. 5653–5659.

Chabal, Y. J. (1988). *Surface Infrared Spectroscopy*. Surface Science Reports, **8**.(5-7), pp. 211–357.

CIE Commission internationale de l'ecclairage (1964). *CIE 1964 Supplementary Standard Colorimetric Observer*.

de L. Kronig, R. (1926). *On the theory of the dispersion of X-Rays*. Journal of the Optical Society of America, **12**, pp. 547–557.

Demtröder, W. (2006). *Experimentalphysik 2*. Berlin, Heidelberg, New York: Springer.

den Boer, J. H. G. W., Kroesen, G. M. W., Haverlag, M., and de Hoog, F. J. (1993). *Spectroscopic IR ellipsometry with imperfect components*. Thin Solid Films, **234**, pp. 323–326.

den Boer, J. H. W. G. (1995). "Spectroscopic Infrared Ellipsometry: Components, Calibration, and Application". PhD thesis. Eindhoven University of Technology.

den Boer, J. H. W. G., Kroessen, G. M. W., and de Hoog, F. J. (1995). *Measurenemt of the complex refractive index of liquids in the infrared using spectroscopic attenuated total reflection ellipsometry: correction for depolarization by scattering*. Applied Optics, **34**.(25), pp. 5708–5714.

Dence, C. W. and Reeve, D. W. (1996). *Pulp Bleaching - Principles and Practice*. Tech. rep. Atlanta, Georgia: TAPPI PRESS.

Dittmar, G., Offermann, V., Pohlen, M., and Grosse, P. (1993). *Extension of spectroscopic ellipsometry to the far infrared*. Thin Solid Films, **234**, pp. 346–351.

Djak, M. (2011). MA thesis. Graz University of Technology.

Djak, M., Gilli, E., Kontturi, E., and Schennach, R. (2011). *Thickness dependence of reflection absorption infrared spectra of supported thin Polymer films*. Macromolecules, **44**.(7), pp. 1775–1778.

Donoser, M., Wiltsche, M., and Bischof, H. (2005). "A New Automated Microtomy Concept for 3D Paper Structure Analysis". In: *Proceedings of the 9th IAPR Conference on Machine Vision Applications*, pp. 76–79.

Dressel, M., Gompf, B., Faltermeier, D., Tripathi, A. K., Pflaum, J., and Schubert, M. (2008). *Kramers-Kronig-consistent optical functions of anisotropic crystals: generalized spectroscopic ellipsometry on pentacene*. Optics Express, **16**.(24), pp. 19770–19778.

Duker, E and Lindström, T (2008). *On teh mechanisms behind the ability of CMC to enhance paper strength*. Nordic Pulp & Paper Research Journal, **23**.(1), pp. 57–64.

Fahlen, J and Salmen, L (2005). *Pore and Matrix Distribution in the Fiber Wall Revealed by Atomic Force Microscopy and Image Analysis*. Biomacromolecules, **6**, pp. 433–438.

Fujiwara, H. (2007). *Spectroscopic Ellipsometry - Principles and Applications*. Hoboken, NJ, USA: John Wiley & Sons.

Gilli, E. (2008). "IR spectroscopic investigations on the chemical surface properties of cellulose fibres". MA thesis. Institute for Solid State Physics, Graz University of Technology.

Gilli, E., Horvath, A. E., Horvath, A. T., Hirn, U., and Schennach, R. (2009a). *Analysis of CMC attatchment onto cellulosic fibers by infrared spectroscopy*. Cellulose, **16**.(5), pp. 825–832.

Gilli, E. and Schennach, R. (2009). *Detection of coatings on paper usinf infra red spectroscopy*. Lenzinger Berichte, **87**, pp. 162–167.

Gilli, E. and Schennach, R. (2010). *Determination of Noise-Free Optical Constants in the Infrared by Kramers-Kronig Troansformation of the Reflectance Ratio in s- and p-Polatization*. Applied Spectroscopy, **64**.(6), pp. 669–681.

Gilli, E. and Schennach, R. (2011). *Imaging ellipsometry based method and algorithm for the analysis of fiber-fiber bonds in a paper network*. Submitted to: Applied Optics,

Gilli, E., Kornschober, M., and Schennach, R. (Aug. 2009b). AT Patent Application No. AT 508 690 A1. Patent Application.

Gilli, E., Kappel, L., Hirn, U., and Schennach, R. (2009c). *An optical model for polarization microscopy analysis of pulp fibre-to-fibre bonds*. Composite Interfaces, **16**.(5), pp. 901–922.

Gilli, E., Kornschober, M., and Schennach, R. (Mar. 2011a). PCT Patent Application No. PCT/AT2010/000306. International Patent Application.

Gilli, E., Schmied, F., Diebald, S., Horvath, A. T., Teichert, C., and Schennach, R. (2011b). *Analysis of lignin precipitates on ozone treated kraft pulp by FTIR and AFM*. Submitted to: Cellulose,

Gilli, E., Kornschober, M., and Schennach, R. (2011c). *Optical arrangement and proof of concept prototype for mid infrared variable angle spectroscopic ellipsometry*. Submitted to: Infrared Physics & Technology,

Gilli, E., Schennach, R., and Kornschober, M. (2011d). *Optical arrangement for ellipsometry*. PCT Patent Application. WO 2011/022745 A1.

Gilli, E., Schennach, R., and Kornschober, M. (2011e). *Optische Anordnung für Ellipsometrie*. AT Patent Application. AT 508 690 A1.

Gombert, A., Köhl, M., and Weimar, U. (1993). *Broadband spectroscopic ellipsometry based on a Fourier transform spectrometer*. Thin Solid Films, **234**, pp. 352–355.

Grate, J. W. (2008). *Hydrogen-Bond Acidic Polymers for Vapor sensing*. Chemical Reviews, **108**.(2), pp. 726–745.

Gullichsen, J. and Paulapuro, H. (1999). *Papermaking Science and Technology*. Helsinki: Fapet Oy.

Gullichsen, J. and Paulapuro, H. (2000). *Forest Products Chemistry*. Helsinki: Fapet Oy, pp. 24–26.

Gustafsson, J, Ciovica, L, and Peltonen, J (2003). *The ultrastructure of spruce kraft pulps studied by atomic force microscopy (afm) and x-ray photoelectron spectroscopy (xps)*. Polymer, **44**.(3), pp. 661–670.

Hansen, W. N. (1968). *Electric Fields Produced by the Propagation of Plane Coherent Electromagnetic Radiation in a Stratified Medium*. Journal of the Optical Society of America, **58**.(3), pp. 380–390.

Harbecke, B., Heinz, B., and Grosse, P. (1985). *Optical Properties of Thin Films and the Berreman Effect*. Applied Physics A - Materials Science & Processing, **38**, pp. 263–267.

Hecht, E. (1987). *Optics*. Addison-Wesley.

Henrion, W., Röseler, A., Angermann, H., and Rebien, M. (1999). *Application of UV-VIS and FTIR Spectroscopic Ellipsometry to the Characterization of Wet-Chemically Treated Si Surfaces*. Physica Status Solidi A, **175**, pp. 121–128.

Hensler, D. H. (1972). *Light Scattering from Fused Polycrystalline Aluminum Oxide Surfaces*. Applied Optics, **11**.(11), pp. 2522–2528.

Hinrichs, K., Röseler, A., Roodenko, K., and Rappich, J. (2008). *Surface-Enhanced Infrared Absorption: Infrared Ellipsometry of Au Evaporated Ultrathin Organic Films*. Applied Spectroscopy, **62**.(1), pp. 121–124.

Hoffman, H., Mayer, U., and Krischanitz, A. (1995). *Structure of Alkylsiloxane Monolayers on Silicon Surfaces Investigated by External Reflection Infrared Spectroscopy*. Langmuir, **11**, pp. 1304–1312.

Hopfield, J. J. and Thomas, D. G. (1965). *Polariton absorption lines*. Physical Review Letters, **15**.(1), pp. 22–25.

Horvath, A. E. and Lindström, T (2007). *Intdirect polyelectrolyte titration of cellulosic fibers - surface and bulk charges of cellulosic fibers*. Nordic Pulp & Paper Research Journal, **22**.(1), pp. 87–92.

Horvath, A. E., Lindström, T, and Laine, J (2006). *On the indirect polyelectrolyte titration of cellulosic fibers. Conditions for charge stoichiometry and comparison with ESCA*. Langmuir, **22**.(2), pp. 824–830.

Jahoda, F. C. (1957). *Fundamental Absorption of Barium Oxide from Its Reflectivity Spectrum*. Physical Review, **107**.(5), pp. 1261–1265.

Jang, H., Weigel, G., Seth, R., and Wu, C. (2002). *The effect of fibril angle on the transverse collapse of papermakingfibers*. Paperi ja Puu-Paper and Timber, **84**.(2), pp. 112–115.

Jayme, G. and Hunger, G. (1961). "Electron Microscope 2- and 3-dimensional Classification of Fibre Bonding, Formation and Structure of Paper". In: *Transactions of the 2nd Fundamental Research Symposium Oxford*, pp. 135–170.

Jezierski, K. (1986). *Improvements in the Kramers-Kronig analysis of reflection spectra*. Journal of Physics C-Solid State Physics, **19**, pp. 2103–2112.

Johs, B. (1993). *Regression calibration method for rotating element ellipsometers*. Thin Solid Films, **234**, pp. 095–398.

Kappel, L. (2010). "Development and application of a method for fiber-fiber bonded area measurement". PhD thesis. Graz University of Technology.

Kappel, L., Hirn, U., Gilli, E., Bauer, W., and Schennach, R. (2010a). *Revisiting Polarized Light microscopy for fiber-fiber bond area measurement - Part I: Theoretical fundamentals*. Nordic Pulp & Paper Research Journal, **25**, pp. 65–70.

Kappel, L., Hirn, U., Gilli, E., Bauer, W., and Schennach, R. (2010b). *Revisiting polarized Light microscopy for fiber-fiber bond area measurement - Part II: Poroving the applicability*. Nordic Pulp & Paper Research Journal, **25**, pp. 71–75.

Karlsson, J. O., Andersson, M., Berntsson, P., Chihani, T., and Gatenholm, P. (1998). *Swelling behaviour of stimuli-responsive cellulose fibers*. Polymer, **39**.(16), pp. 3589–3595.

Kasic, A., Schubert, M., Einfeld, S., Hommel, D., and Tiwald, T. E. (2000). *Free-carrier and phonon properties of n- and p-type hexagonal GaN films maeasured by infrared ellipsometry*. Physical Review B, **62**, pp. 7365–7377.

Kattner, J. and Hoffmann, H. (2002). "External Reflection Spectroscopy of Thin Films on Dielectric Substrates". In: *Handbook of Vibrational Spectroscopy*. Ed. by J. M. Chalmers and P. R. Griffiths. Vol. 2. Chichester: John Wiley & Sons, pp. 1009–1027.

Katz, S, Beatson, R. P., and Scallan, A. M. (1984). *The determination of strong and weak acidic groups in sulfite pulps*. Svensk Papperstidning, **87**.(6), pp. 48–53.

Kawana, S. and Jones, R. A. L. (2001). *Character of the glass transition in thin supported polymer films*. Physical Review E, **63**, p. 021501.

Klemm, D, Philipp, B, Heinze, T, Heinze, U, and Wagenknecht, W (1998). "Comprehensive Cellulose Chemistry". In: vol. 1. Weinheim: Wiley-VCH. Chap. 3.

Koljonen, K., Österberg, M., Johansson, L.-S., and Stenius, P. (2003). *Surface chemistry and morphology of different mechanical pulps determined by ESCA and AFM*. Colloids and Surfaces A: Physiochem. Eng. Aspects, **228**, pp. 143–158.

Kondo, T. and Sawtari, C. (1996). *A Fourier transfornm infra-red spectroscopic analysis of the character of hydrogen bonds in amorphous cellulose*. Polymer, **37**, pp. 393–399.

Kontturi, E., Thüne, P. C., and Niemantsverdriet, J. W. (2003a). *Novel Method for preparing cellulose model surfaces by spin coating*. Polymer, **44**, pp. 3621–3625.

Kontturi, E., Thüne, P. C., and Niemantsverdriet, J. W. (2003b). *Cellulose Model Surfaces - Simplified Preparation by Spin Coating and Characterization by X-ray Photoelectron Spectroscopy, Infrared Spectroscopy, and Atomic Force Microscopy*. Langmuir, **19**, pp. 5735–5741.

Kontturi, E., Tammelin, T., and Österberg, M. (2006). *Cellulose-model flims and the fundamental approach*. Chemical Society Reviews, **35**, pp. 1287–1304.

Kontturi, E., Suchy, M., Penttilä, P., Jean, B., Pirkkalainen, K., Torkkeli, M., and Serimaa, R. (2011). *Amorphous Characteristics of an Ultrathin Cellulose Film*. Biomacromolecules, **12**.(3), pp. 770–777.

Kramers, H. A. (1927). "La diffusion de la lumiere par les atomes". In: *Atti Cong. Intern. Fiscia, Como*. Vol. 2, pp. 545–557.

Kramers, H. A. and de L. Kronig, R. (1928). *Zur Theorie der Absorption und Dispersion in den Röntgenspektren*. Zeitschrift für Physik, **48**.(3-4), pp. 174–179.

Laine, J, Lindström, T, Glad-Nordmark, G, and Risinger, G (2000). *Studies on topochemical modification of cellulosic fibres. Part 1. Chemical conditions for the attachment of carboxymethyl cellulose onto fibres.* Nordic Pulp & Paper Research Journal, **15**.(5), pp. 520–526.

Laine, J, Lindström, T, Bremberg, C, and Glad-Nordmark, G (2003). *Studies on topochemical modification of cellulosic fibres. Part 5. Comparison of the effects of surface and bulk chemical modification and beating of pulps on paper properties.* Nordic Pulp & Paper Research Journal, **18**.(3), pp. 326–333.

Letnes, P. A., Nerbø, I. S., Aas, L. M. S., Ellingsen, P. G., and Kildemo, M. (2010). *Fast and optimal broad-band Stokes/Mueller polarimeter design by the use of a genetic algorithm.* Optics Express, **18**.(22), pp. 23095–23103.

Levlin, J.-E. and Söderhjelm, L. (1999). *Pulp and Paper testing.* Helsinki: Fapet Oy.

Liebergott, N. (1972). *Sequential Treatment of Mechanical Pulps at High Consistency with H_2O_2 and O_3 - The Paprizone Process - Effect on Pulp Brightness and Strength.* Pulp Paper Mag. Can. **73**.(9), T214–T217.

Lindström, T (1980). *Influence of chemical factors on fiber swelling and paper strength.* Papier, **34**.(12), pp. 561–568.

Lindström, T (1989). "Some fundamental chemical aspects on paper forming." In: *Fundamentals of papermaking: transaction of the 9th fundamental research symposium.* Vol. 1. Cambridge, UK, pp. 311–412.

Lindström, T., Wågberg, L., and Larsson, T. (2005). "On the Nature of Joint Strength in Paper- A Review of Dry and Wet Strength Resins used in Paper Manufacturing". In: *13th Fundamental Research Symposium.* Cambridge, pp. 457–562.

Lorentz, H. A. (1916). *The Theory of Electrons and its Application to the Phenomena of Light and Radiant Heat.* Leipzig: Teubner.

Lucarini, V., Saarinen, J. J., Peiponen, K.-E., and Vartianen, E. M. (2005). *Kramers-Kronig Relations in Optical Materials Research.* Berlin, Heidelberg, New York: Springer.

Mamleeva, N. A., Autlov, S. A., Bazarnova, N. G., and Lunin, V. V. (2009). *Delignification of softwood by ozonation.* Pure Appl. Chem. **81**.(11), pp. 2081–2091.

McKelvey, R. D., Thompson, N. S., and Lyse, T. E. (1983). *The ozone oxidation of alkali-fiberized loblolly pine wood.* Cellulose Chem. Technol. **17**, pp. 355–361.

Mielczarski, J. A. and Mielczarsky, E. (1999). *Infrared External Reflection Spectroscopy of Adsorbed Monolayers in a Region of Strong Absorption of Substrate.* Journal of Physical Chemistry B, **103**, pp. 5852–5859.

Mielczarski, J. A. and Mielczarsky, E. (2005). *Monitoring Mineral Surface Phenomena by Infrared Reflection Spectroscopy.* Physicochemical Problems of Mineral Processing, **39**, pp. 33–46.

Milosevic, M., Harrick, N. J., and Berets, S. L. (1991). *The Seagull: A Multifunctional Variable-Angle Reflection Attatchment.* Applied Spectroscopy, **45**, pp. 126–131.

Milosevic, M. and Harric, N. J. (Sept. 1991). US Patent No. 5,048,970.

Napolitano, S. and Wübbenhorst, M. (2006). *Slowing Down of the Crystallization Kinetics in Ultrathin Polymer Films: A Size or an Interface Effect?* Macromolecules, **39**.(18), pp. 5967–5960.

Östenson, M. and Gatenholm, P. (2005). *Improvement of the Wetting and Absorption Properties of Lignocellulosic Fibers by Means of Gas Phase Ozonation*. Langmuir, **21**.(1), pp. 160–165.

Page, D. H. (1960). *Fibre-to-fibre bonds, Part 1 - A method for their direct observation*. Paper technology, **1**.(4), pp. 407–411.

Page, D. H. (1969). *A Theory for the Tensile Strength of Paper*. Tappi, **52**.(4), pp. 674–681.

Page, D. H. and Tydeman, P. A. (1960). *Fibre-to-fibre bonds, Part 2 - A preliminary study of their properties in paper sheets*. Paper technology, **1**.(5), pp. 519–530.

Palik, E. D., ed. (1985). *Handbook of Optical Constants of Solids*. Orlando: Academic Press, Inc.

Persson, B. N. J. (1998). *Sliding Friction*. Nanoscience and technology. Berlin Heidelberg: Springer.

Petridis, L., Pingali, S. V., Urban, V., Heller, W. T., O'Neill, H. M., Foston, M., Ragauskas, A., and Smith, J. C. (2011). *Self-Similar multiscale structure of lignin revealed by neutron scattering and molecular dynamics simulation*. Physical Review E, **83**, p. 061911.

Philipp, H. R. and Taft, E. A. (1959). *Optical Constants of Germanium in the Region 1 to 10 eV*. Physical Review, **113**.(4), pp. 1002–1005.

Plaskett, J. S. and Schatz, P. N. (1963). *On the Robinson and Price (Kramers-Kronig) Method of Interpreting Reflection Data Taken through a Transparent Window*. The Journal of Chemical Physics, **38**.(3), pp. 612–617.

Procter, A. R. (1974). *Ozone gas treatments of high Kappa kraft pulps*. Pulp Paper Mag. Can. **75**.(6), T210–T214.

Qazilbash, M. M., Burch, K. S., Whisler, D., Shrekenhamer, D., Chae, B. C., Kim, H. T., and Basov, D. N. (2006). *Correlated metallic state of vanadium dioxide*. Physical Review B, **74**, p. 205118.

Rappich, J. and Hinrichs, K. (2009). *In situ study of nitrobenzene grafting on Si(1 1 1)-H surfaces by infrared spectroscopic ellipsometry*. Electrochemistry Communications, **11**.(12), pp. 2316 –2319.

Roberts, M. E., Sokolov, A. N., and Bao, Z. (2009). *Material and device considerations for organic thin-film transistor sensors*. Journal of Materials Chemistry, **19**, pp. 3351–3363.

Robinson, T. S. (1952). *Optical Constants by Reflection*. Proceedings of the Physical Society. Section B, **65**.(11), pp. 910–911.

Robinson, T. S. and Price, W. C. (1953). *The Determination of Infra-Red Absorption Spectra from Reflection Measurements*. Proceedings of the Physical Society. Section B, **66**, pp. 969–974.

Roesseler, D. M. (1965a). *Kramers-Kronig analysis of non-normal incidence reflection*. British Journal of Applied Physics, **16**.(9), pp. 1359–1366.

Roesseler, D. M. (1965b). *Kramers-Kronig analysis of reflection data*. British Journal of Applied Physics, **16**.(8), pp. 1119–1123.

Röseler, A. (1993). *IR spectroscopic ellipsometry: instrumentation and results.* Thin Solid Films, **234**, pp. 307–313.

Röseler, A. and Korte, E. H. (2002). "Infrared Spectroscopic Ellipsometry". In: *Handbook of Vibrational Spectroscopy.* Ed. by J. M. Chalmers and P. R. Griffiths. Vol. 2. Chichester: John Wiley & Sons, pp. 1065–1090.

Schantl, J. (1971). *Charakteristische Gruppenschwingungen Organischer Moleküle im Infrarot-Spektrum.* Script for the lecture "Einführung in die Molekülspektroskopie", Institut für organische Chemie, Universität Innsbruck.

Schennach, R., Hirschmugl, C., Gilli, E., and Tysoe, W. T. (2009). *A New Method for Performing Polarization-Modulation Infrared Reflection-Absorption Spectroscopy of Surfaces.* Applied Spectroscopy, **63**.(3), pp. 369–372.

Schmied, F. J., Teichert, C, Kappel, L, Hirn, U, and Schennach, R (2011). *Quantitative analysis of precipitated lignin on kraft pulp fibers using atomic force microscopy.* submitted to Cellulose,

Schubert, M., Bundesmann, C., v. Weckstern, H., Jakopic, G., Haase, A., Persson, N.-K., Zhang, F., Arwin, H., and Inganäs, O. (2004). *Carrier redistribution in organic/inorganic (poly(3,4-ethylendioxy thiophene/poly(styrenesulfonate)polymer)-Si) heterojunction determined from infrared ellipsometry)).* Applied Physics Letters, **84**.(8), pp. 1311–1313.

Schubert, M. (2004). *Infrared Ellipsometry on Semiconductor Layer Structures. Phonons, Plasmons and Polaritons.* Berlin, Heidelberg, New York: Springer.

Schubert, M. (1996). *Polarization-dependent optical parameters of arbitrarily anisotropic homogeneous layered systems.* Physical Review B, **53**, pp. 4265–4274.

Serghei, A, Huth, H, Schick, C, and Kremer, F (2008). *Glassy Dynamics in Thin Polymer Layers Having a Free Upper Interface.* Macromolecules, **41**.(10), pp. 3636–3639.

Sharp, J. S. and Forrest, J. A. (2003). *Free Surfaces Cause Reductions in the Glass Transition Temperature of Thin Polystyrene Films.* Physical Review Letters, **91**, p. 235701.

Simola, J, Malkavaara, P, Aln, R, and Peltonen, J (2000). *Scanning probe microscopy of pine and birch kraft pulp fibres.* Polymer, **41**.(6), pp. 2121–2126.

Sixta, H., ed. (2006a). *Handbook of Pulp.* Vol. 1. Wiley-VCH Weinheim.

Sixta, H., ed. (2006b). *Handbook of Pulp.* Vol. 2. Wiley-VCH Weinheim.

Stagg, B. J. and Charalampopoulos, T. T. (1991). *Surface-roughness effects on the determination of optical properties of materials by the reflection method.* Applied Optics, **30**.(28), pp. 4113–4118.

Stettner, J., Frank, P., Griesser, T., Trimmel, G., Schennach, R., Gilli, E., and Winkler, A. (2008). *A study on the formation and thermal stability of 11-MUA SAMs on Au(111)/mica and on polycrystalline gold foils.* Langmuir, **25**.(3), pp. 1427–1433.

Terayama, H (1952). *Method of colloid titration (a new titration between polymer ions).* J Polymer Sci, **8**.(2), pp. 243–253.

Thomson, C. I. (2007). "Probing the Nature of Cellulosic Fibre Interfaces with Fluorescence Resonance Energy Transfer". PhD thesis. School of Chemistry and Biochemistry, Georgia Institute of Technology.

Tiwald, T. E., Thompson, D. W., Woolam, J. A., Paulson, W., and Hance, R. (1998a). *Application of IR variable angle spectroscopic ellipsometry to the determination of free carrier concentration depth profiles*. Thin Solid Films, **313-314**, pp. 661–666.

Tiwald, T. E., Thompson, D. W., Woolam, J. A., and Pepper, S. W. (1998b). *Determination of the mid-IR optical constants of water and lubricants using IR ellipsometry combined with an ATR cell*. Thin Solid Films, **313-314**, pp. 718–721.

Tiwald, T. E., Thompson, D. W., and Woolam, J. A. (1998c). *Optical determination of shallow carrier profiles using Fourier transform infrared ellipsometry*. Journal of Vacuum Science & Technology B, **16**, pp. 312–315.

Tiwald, T. E., Woolam, J. A., Zollner, S., Christiansen, J., Gregory, R. B., Wetteroth, T., Wilson, S. R., and Powell, A. R. (1999). *Carrier concentration and lattice absorption in bulk and epitaxial silicon carbide determined using infrared ellipsometry*. Physical Review B, **60**, pp. 11464–11474.

Toll, J. S. (1956). *Causality and the Dispersion Relation: Logical Foundations*. Physical Review, **104**.(6), p. 6.

Tolstoy, V. P., Chernyshova, I. V., and Skryshevsky, V. A. (2003). *Handbook of Infrared Spectroscopy of Ultrathin Films*. Hoboken, New Jersey: John Wiley and Sons, Inc.

Tompkins, H. G. and McGahan, W. A. (1999). *Spectroscopic Ellipsometry and Reflectometry*. New York: John Wiley & Sons.

Torgnysdotter, A. (2007). *The Link Between the Fiber Contact Zone and the Physical Properties of Paper: A Way to Control Paper Properties*. Journal of Composite Materials, **41**.(13), pp. 1619–1633.

Tousey, R. (1939). *On Calculating the Optical Constants from Reflection Coefficients*. Journal of the Optical Society of America, **29**.(6), pp. 235–239.

Trasferetti, B. C., Davanzo, C. U., Cruz, N. C. da, and Morales, M. A. B. de (2000). *Observation of the Berreman Effect in Infrared Reflection-Absorption Spectra of Amorpous Titanium Oxide Thin Filmf Deposited on Aluminum.* Applied Spectroscopy, **54**.(5). Berreman Minimum in amorphen Strukturen, simuliert mit Transition Matrix Formalismus und Fresnel, Daten aus KK-Transformation., pp. 687–691.

Tsankov, D., Hinrichs, K., Röseler, A., and Korte, E. H. (2001). *FTIR Ellipsometry as a Tool for Studying Organic Layers: From Langmuir-Blodgett Films to Can Coatings*. Physica Status Solidi A, **188**.(4), pp. 1319–1329.

Umemura, J. (2002). "Reflection-Absorption Spectroscopy of Thin Films on Metallic Substrates". In: *Handbook of Vibrational Spectroscopy*. Ed. by J. M. Chalmers and P. R. Griffiths. Vol. 2. Chichester: John Wiley & Sons, pp. 982–998.

Viitaharju, P. and Niskanen, K. (1994). *Chiral Curl in thin Papers*. Journal of Pulp and Paper Science, **20**.(5), J148–J152.

Wågberg, L, Ödberg, L, and Glad-Nordmark, G (1989). *Charge determination of porous substrates by polyelectrolyte adsorption*. Nordic Pulp & Paper Research Journal, **4**.(2), pp. 71–76.

Whangbo, M, Bar, G, and Brandsch, R (1998). *Qualitative relationships describing height and phase images of tapping mode atomic force microscopy. An application to micro-*

contact-printed patterned self-assembled monolayers. Appl. Phys. A: Mater. Sci. Process. **66**, pp. 1267–1270.

Wiltsche, M, Donoser, M, Kritzinger, J, and Bauer, W (2011). *Automated serial sectioning applied to 3D paper structure analysis*. Journal of Microscopy, **242**.(2), pp. 197–205.

Wiltsche, M. (2006). "Three Dimensional Analysis of Paper Structure Using Automated Microtomy". PhD thesis. Graz University of Technology.

Winter, L, Wågberg, L, Ödberg, L, and Lindström, T (1986). *Polyelectrolytes adsorbed on the surface on cellulosic materials*. J Colloid Interface Sci, **111**.(2), pp. 537–543.

Yamamoto, K. and Ishida, H. (1994a). *Kramers-Kronig analysis of infrared reflection spectra with parallel polarization for isotropic materials*. Spectrochimica Acta, **50A**.(12), pp. 2079–2090.

Yamamoto, K. (1994). "Optical theory applied to thin films". PhD thesis. Case Western Reverse University.

Yamamoto, K. and Ishida, H. (1994b). *Optical theory applied to infrared spectroscopy*. Vibrational Spectroscopy, **8**, pp. 1–36.

Yamamoto, K. and Masui, A. (1995). *Complex Refractive Index Determination of Bulk Materials from Infrared Reflection Spectra*. Applied Spectroscopy, **49**.(5), pp. 639–644.

Yamamoto, K., Masui, A., and Ishida, H. (1994). *Kramers-Kronig analysis of infrared reflection spectra with perpendicular polarization*. Applied Optics, **33**.(27), pp. 6285–6293.

Yang, C., Eusufzai, A. R. K., Sankar, R., Mark, R. E., and Perkins Jr., R. W. (1978). *Measurements of geometrical parameters of fiber networks, Part 1. Bonded surfaces, aspect ratios, fiber moments of inertia, bonding state probabilities*. Svensk Papperstidning, **13**, pp. 426–433.

Ye, C. (2006). *Spectroscopic imaging ellipsometry: real-time measurement of single, intact wood pulp fibers*. Applied Optics, **45**.(36), pp. 9092–9104.